Adam Wittek · Grand Joldes
Poul M.F. Nielsen · Barry J. Doyle
Karol Miller *Editors*

Computational Biomechanics for Medicine

From Algorithms to Models and Applications

Springer

Computational Biomechanics for Medicine

Adam Wittek • Grand Joldes • Poul M.F. Nielsen
Barry J. Doyle • Karol Miller
Editors

Computational Biomechanics for Medicine

From Algorithms to Models and Applications

Springer

Editors
Adam Wittek
Intelligent Systems for Medicine Laboratory
School of Mechanical
and Chemical Engineering
The University of Western Australia
Perth, WA, Australia

Poul M.F. Nielsen
Auckland Bioengineering Institute
The University of Auckland
Auckland, New Zealand

Department of Engineering Science
The University of Auckland
Auckland, New Zealand

Karol Miller
Intelligent Systems for Medicine Laboratory
School of Mechanical
and Chemical Engineering
The University of Western Australia
Perth, WA, Australia

Grand Joldes
Intelligent Systems for Medicine Laboratory
School of Mechanical
and Chemical Engineering
The University of Western Australia
Perth, WA, Australia

Barry J. Doyle
School of Mechanical
and Chemical Engineering
The University of Western Australia
Perth, WA, Australia

ISBN 978-3-319-54480-9 ISBN 978-3-319-54481-6 (eBook)
DOI 10.1007/978-3-319-54481-6

Library of Congress Control Number: 2017936220

Printed on acid-free paper

This Springer imprint is published by Springer Nature
The registered company is Springer International Publishing AG
The registered company address is: Gewerbestrasse 11, 6330 Cham, Switzerland

Preface

Extending the success of computational mechanics to fields outside traditional engineering, in particular to biology, the biomedical sciences, and medicine, has been recognised as one of the greatest challenges facing the computational engineering and computational mechanics communities. While advancements are being made towards clinically relevant computational biomechanics models and simulations, there is still much work ahead before personalised medicine underpinned by personalised computer simulations becomes a part of healthcare.

The first volume in the Computational Biomechanics for Medicine book series has been published in 2010. Since then, the book has become an annual forum for specialists in computational sciences to describe their latest results and discuss the possibility of applying their techniques to computer-integrated medicine. This eighth volume in the Computational Biomechanics for Medicine book series comprises 14 of the latest developments in solid biomechanics, vascular biomechanics, multi-level modelling and brain biomechanics, from researchers in Australia, New Zealand, China, Belgium, France, Germany, Greece, Poland, Sweden, United Kingdom and the USA. Some of the topics discussed are as follows:

- Tailored computational models
- Traumatic brain injury
- Soft tissue damage
- Soft tissue mechanics
- Medical image analysis
- Disease mechanisms and progression
- Clinically relevant simulations

The Computational Biomechanics for Medicine book series does not only provide the community with a snapshot of the latest state of the art, but more

importantly, when computational biomechanics and patient-specific modelling are a mainstay of personalised healthcare, it will serve as a key reminder of how the field has overcome one of its greatest challenges.

Crawley, Perth, WA, Australia — Adam Wittek
Crawley, Perth, WA, Australia — Grand Joldes
Auckland, New Zealand — Poul M.F. Nielsen
Crawley, Perth, WA, Australia — Barry J. Doyle
Crawley, Perth, WA, Australia — Karol Miller

Contents

The Effects of Geometric Variation from OCT-Derived 3D Reconstructions on Wall Shear Stress in a Patient-Specific Coronary Artery

Lachlan J. Kelsey, Carl Schultz, Karol Miller, and Barry J. Doyle

1 Introduction

In 2013, coronary artery disease (CAD) was the most common cause of death globally, resulting in 8.14 million deaths worldwide [1]. While the underlying mechanisms of CAD are not entirely understood, it is generally accepted that atherosclerosis is the main cause [2, 3]. The risk factors for atherosclerotic plaque formation in the coronary arteries are typically systemic in nature: i.e. diabetes, high

L.J. Kelsey
Vascular Engineering Laboratory, Harry Perkins Institute of Medical Research, Perth, WA, Australia

Intelligent Systems for Medicine Laboratory, School of Mechanical and Chemical Engineering, The University of Western Australia, Perth, WA, Australia

C. Schultz
Department of Cardiology, Royal Perth Hospital, Perth, WA, Australia

School of Medicine, The University of Western Australia, Perth, WA, Australia

K. Miller
Intelligent Systems for Medicine Laboratory, School of Mechanical and Chemical Engineering, The University of Western Australia, Perth, WA, Australia

Institute of Mechanics and Advanced Materials, Cardiff University, Cardiff, UK

B.J. Doyle (✉)
Vascular Engineering Laboratory, Harry Perkins Institute of Medical Research, Perth, WA, Australia

British Heart Foundation Centre for Cardiovascular Science, The University of Edinburgh, Edinburgh, UK

School of Mechanical and Chemical Engineering, The University of Western Australia, Perth, WA, Australia
e-mail: Barry.Doyle@uwa.edu.au

A. Wittek et al. (eds.), *Computational Biomechanics for Medicine*,
DOI 10.1007/978-3-319-54481-6_1

cholesterol and hypertension. However, the local site specificity of atherosclerotic plaques has been shown to depend on the local haemodynamic behaviour and shear stress experienced by an artery's endothelial layer. Plaques are generally located at regions of disturbed flow and low endothelial shear stress. The wall shear stress (WSS) experienced by endothelial cells ultimately influences their phenotype and therefore the inflammatory component of plaque progression [4, 5].

Modelling an arteries' haemodynamics with computational fluid dynamics (CFD) can be used to predict the blood flow behaviour in large arteries, such as the aorta, renal or carotid arteries (e.g. [6]). Common imaging methods such as computed tomography (CT) and magnetic resonance imaging (MRI) have enabled accurate reconstruction and modelling of the patient-specific human anatomy of these regions. However, imaging the coronary arteries is technically more challenging, as the spatial resolution of images limits our ability to reconstruct anatomically correct geometries [7]. In order to provide an evaluation of coronary artery stenosis severity in clinical practice, angiographic images are commonly used to create three-dimensional (3D) coronary artery reconstructions [8]. However, these reconstructions (which determine the vessel centreline from angiography) typically assume that the vessel is either circular or elliptical in cross-section, which results in an artificial smoothing of the lumen surface [7]. To increase the fidelity/lumen detail of these biplane angiography reconstructions, cross-sectional information may be acquired/derived from intravascular ultrasound (IVUS) or, more recently, intravascular optical coherence tomography (OCT), and registered along the vessel centreline. Aside from lumen detail, both IVUS and OCT imaging modalities provide useful diagnostic and prognostic information. OCT clearly shows high-risk features such as thin fibrous caps, inflammation and lipid pools, while IVUS allows for visualisation of atherosclerotic plaques [9].

Biplane angiography with IVUS was used in the PREDICTION study [10], which showed that CFD-computed low WSS regions correlated with regions of future plaque progression and lumen narrowing. While proven useful, the resolution of IVUS is an order of magnitude lower than OCT (i.e. 150 μm vs. 10 μm), and thus more likely to cause the loss of spatial information, important to accurate model reconstruction (particularly in stented arteries) [11–15]. However, both imaging modalities are limited by their axial/longitudinal resolution (≈200 μm distance between images). The level of artery wall detail is expected to underpin predictions of plaque deposition through better estimation of WSS. Therefore, coupling OCT data with image registration and vessel reconstruction methods to create 3D coronary artery models for CFD analysis is becoming more common [7, 9, 11, 14, 16]. However, in non-stented vessels, previous work has highlighted that simplifications to biplane angiographic models have had little impact on WSS estimation [8]. Furthermore, the benefit that intravascular imaging brings to WSS estimation, i.e. biplane angiography with IVUS [17], has been shown to be dependent on the geometry, as reasonably expected. Regarding this, CFD models based on coronary CT-derived geometries have emerged as a non-invasive means to estimate WSS fields which correlate with the site specificity of plaque (e.g. [18]). This is promising given the utility and availability of CT.

When compared to other methods, notably coronary CT, the imaging and reconstruction of OCT is relatively time-consuming, but provides the greatest level of wall detail. However, the presence of the guidewire shadow in OCT images is a limitation, and depending on the geometric features present, the segmentation of the artery lumen can require a high (or low) contour (point) resolution [19].

This study explores how changes to the resolution of an active contour model (or SNAKE [20]) affect the lumen-segmentation of an OCT-imaged left anterior descending (LAD) coronary artery. Similar to previous studies using biplane angiography (without IVUS or OCT) [8], the primary objective is to see how small variations in geometric detail affect the haemodynamics within the vessel (WSS computed from CFD) and provide comment on the merit of the reconstruction method used. The proximal end of the LAD coronary artery contains a stent, which may impact the performance of the active contour model, while the results are expected to change less in the distal end of the artery.

2 Method

2.1 Geometry Reconstruction

Three versions of a LAD coronary artery geometry were reconstructed from OCT image sets (acquired using Dragonfly OPTIS imaging catheters; St. Jude Medical, St. Paul, MN, USA). The in-plane pixel resolution of the OCT images was 10 μm, while the axial distance between OCT images was 200 μm. For each reconstruction, a different point resolution was used to trace the lumen contours. These resolutions contained 25, 50 and 100 points, respectively. The highest resolution reconstruction (100 Pts.) was considered to be geometrically accurate. The lumen contours were traced using an active contour function (MATLAB function Snake2D, copyright 2010, Dirk-Jan Kroon) previously used for OCT reconstruction [7], where a deformable spline is used to outline object contours using gradient vector flow [20]. This results in a non-uniform distribution of points discretising the lumen perimeters. For the 100 pt., high-resolution contours the average (in-plane) displacement between contour points was approximately 87 μm, however, at regions of extreme curvature the lumen discretisation reduced to OCT pixel size ($\approx$10 μm). The average displacement between contour points for the 50 and 25 pt. contours was two and four times greater than the 100 pt. contours, respectively. However, at regions of extreme curvature the minimum distances between points on the 50 and 25 pt. contours were larger than the OCT pixel size, with an average minimum discretisation size of 55 and 230 μm, respectively.

While the reconstruction method used here closely follows that of Kousera et al. [7], there are a few distinctions. Kousera et al. investigated single conduit geometries and registered their OCT-lumen contours along manually traced centrelines (using multiple angiography projections). However, in our study the OCT geometry is registered along a CT-derived centreline and merged with CT to include branching

arteries (such as the circumflex) and a distal bifurcation. The 3D CT-reconstruction (0.4 mm pixel size) and centreline calculation were performed using MIMICS v18 (Materialize, Belgium). The inclusion of side branches has been shown to improve the estimation of WSS [16]. The side branches also serve as landmarks which guide the orientation of the OCT-lumen contours along the vessel centreline. This approach follows previous work [16, 21], where the necessary rotations and longitudinal displacements were interpolated in the absence of local landmarks. Additionally, while not present in previous OCT-CFD models, idealised (circular) branching arteries have been included where visible on OCT but not visible on CT (or of insufficient CT-resolution to be reconstructed).

While calculating the OCT-lumen contours using the active contour algorithm, slight modifications to the previous method [7] were implemented to improve the success rate of the contour algorithm and reduce the need for image thresholding. This was done by altering the initial condition used by the contour algorithm. Instead of using a circle as the initial contour, the initial contour was calculated to more closely fit the lumen. To do this, the guidewire centre-point (stored during the guidewire removal; Fig. 1) was used as an initial estimate of a false lumen centroid, and the following steps were performed:

- Radially search the greyscale OCT image for the points of maximum brightness about the centroid.
- Remove any points whose radius is more than 1.5 standard deviations outside of the mean radial distance.
- Estimate a new centroid from the remaining points (the centroid of a polygon).
- Repeat this process until the change in the position of the new centroid is negligible.
- Smooth the point cluster with a moving average (11 nearest neighbours) and shrink its radii by 15%. This is the initial contour for the active contour algorithm (Fig. 1).

It should also be mentioned that, in order to completely reconstruct the LAD coronary artery, three OCT image sets were required as each OCT pullback is only 54 mm in length (270 images). The position of the patient's stent was a useful landmark which helped determine OCT contour orientations, and the nature of the connection between the OCT image sets (Fig. 2). A contour matching algorithm was implemented to find the rotational mismatch between overlapping contours. The mean and root-mean-square (RMS) of the difference in the magnitude of the radial vectors of each contour were minimised in this process.

2.2 CFD Mesh

The volume mesh was constructed within STAR-CCM+ v10.06 (CD-adapco Group) using a core unstructured polyhedral mesh and a prism-layer mesh near the wall boundary. The prism-layer mesh was progressively refined approaching

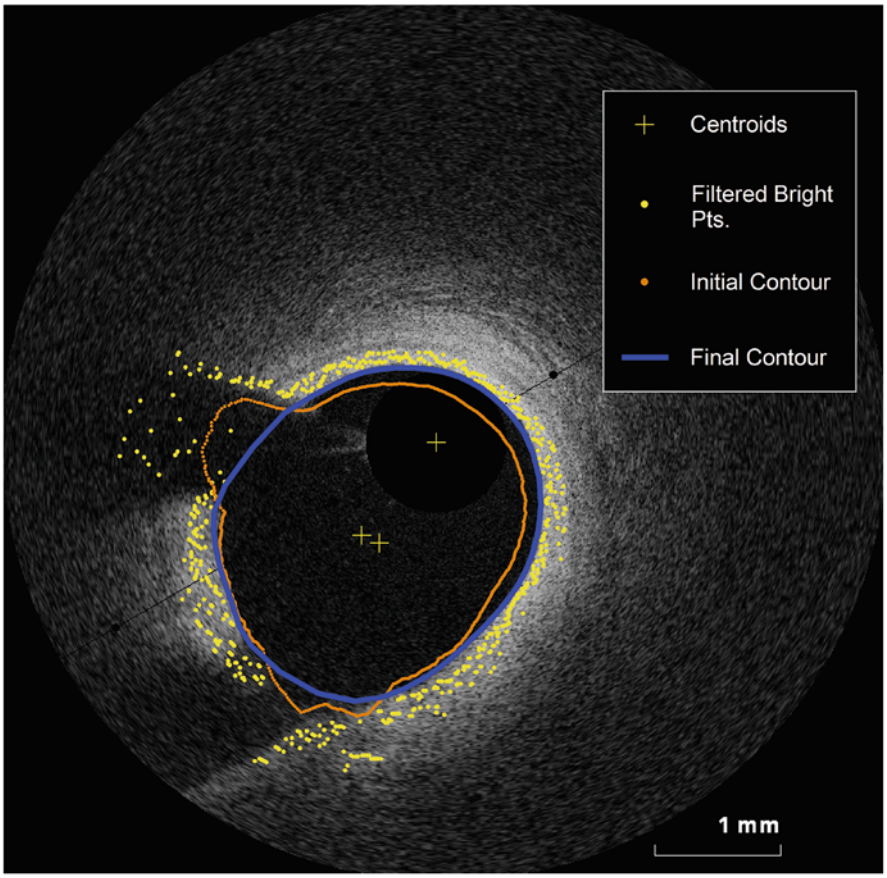

Fig. 1 Determining the lumen of an OCT image (*greyscale*). The two discontinuities in the artery wall are the guidewire shadow (*top left*) and a branching artery (*bottom left*)

the wall and the thickness of the prism-layer mesh and the surface size (edge length) were defined relative to the local lumen diameter. Curvature refinement was performed with a minimum surface size of 10 μm to ensure that details present in the geometries were not lost during meshing (Fig. 3). A conservative first-order Laplacian smoothing operation was applied to all three geometries before meshing to remove any unnatural transitions between neighbouring OCT contours, as well as attached branches. The outlets of the geometry were (normally) extruded by 11 times their diameter creating layers of prismatic cells to ensure that the outlets boundaries were isolated from the region of interest to avoid non-physical behaviour and instability in the numerical solution. Note that the polyhedral mesh was chosen over the more common tetrahedral mesh as it offers (finite-volume) solutions of similar accuracy at lower cost [22].

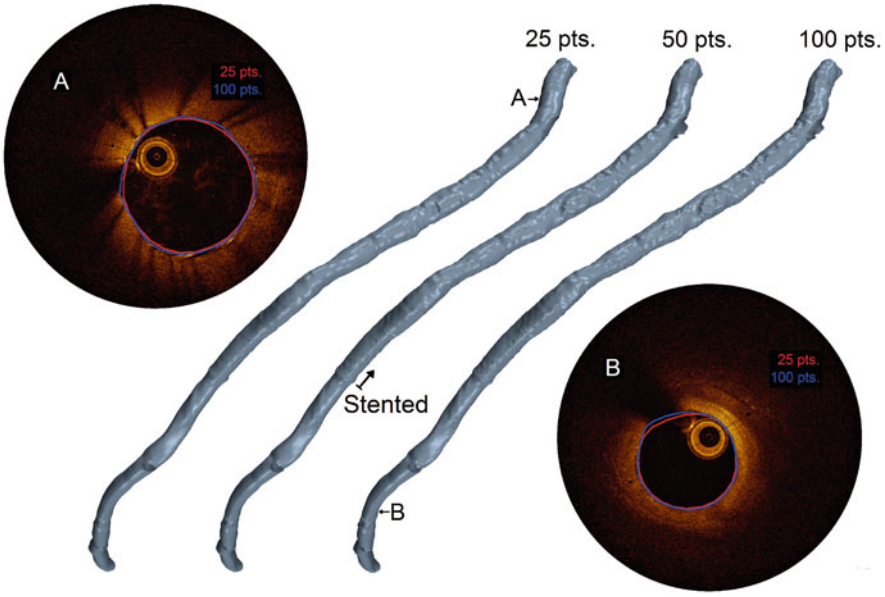

Fig. 2 Reconstructed LAD coronary artery geometries. The lower (distal) end of the stent is indicated on the medium-resolution geometry (the entire LAD coronary artery is stented above this point). OCT images (**a**) and (**b**) show the (similar) behaviour of the active contour model in the stented and non-stented regions of the geometry, respectively

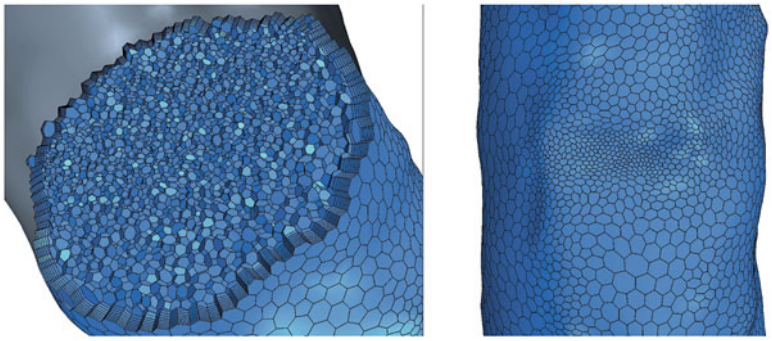

Fig. 3 Mesh cross-section and surface refinement (high-resolution geometry)

In order to determine a sufficient level of (uniform) mesh refinement, the Grid Convergence Index (GCI) [23] was investigated for the flow conditions outlined in Sect. 2.3, for both the low- and high-resolution geometries (derived from 25 pt. and 100 pt. active contours, respectively). The same meshing parameters were used for each of the geometries and the GCI was determined for the average WSS on the LAD surface, the pressure at the inlet and the velocity throughout the domain (sum of scattered probes). The meshes were deemed optimal when the GCI was less than

2% for all the variables considered [24]. This resulted in meshes of 0.9, 1.2 and 1.7 million cells, respectively, for the three geometries (low-, medium- and high-resolution). The greater number of cells in the high-resolution geometry mesh is attributable to the curvature refinement undertaken to preserve geometric features and a slow volumetric growth rate away from these regions.

2.3 Physical Assumptions and Boundary Conditions

The blood flow was approximated as laminar and was considered to be an isothermal, incompressible, (Carreau-Yasuda, generalised) non-Newtonian fluid with an infinite-shear viscosity of 0.0035 Pa s and a density of 1050 kg/m^3 [24–26]. The walls of the arteries were characterised by a no-slip, rigid wall boundary condition [27, 28] and the Navier–Stokes and continuity equations were solved using STAR-CCM+ (using a finite-volume discretisation and a second order upwind convection scheme). The convergence of each solution was considered to be achieved once the variables measured for determination of GCI were stable, and were supported by low (iterative) residuals (i.e. 10^{-12} RMS-absolute error for each direction of momentum and continuity).

As previous reports have shown that the WSS fields resulting from steady-state and transient simulations matched qualitatively [29], the geometries were compared for a steady-state flow field. The inlet flow (left main coronary artery) was set to an assumed mean diastolic flow-rate of 57 mL/min [30] (Reynolds Number = 130), which is half the maximum flow-rate. The flow-rate out the patient's circumflex was 29% of the inlet flow [31]. For the remaining (unquantified) LAD coronary artery outlets, the flow was split according to Murray's law, where the flow leaving each outlet is proportional to the cube of the outlet diameter (d) [32]. This is supported by the solution to the Poiseuille flow equation (1); as blood vessels are proven to regulate their size in order to maintain nominal levels of WSS ($\boldsymbol{\tau}_w$) [33]:

$$Q = (\pi/32\mu)\,\boldsymbol{\tau}_w\ d^3 \tag{1}$$

where Q is flow-rate, and μ is dynamic viscosity.

To ensure that the inlet velocity field was well developed, after each solver iteration the inlet velocity profile assumed the shape of the velocity profile three cell lengths downstream (while enforcing the desired mass-flow). This approach is similar to assumptions of fully developed parabolic flow and Womersley velocity profiles [34], but also accounts for the asymmetry induced by the downstream geometry. The inlet velocity profiles for each of the three geometries were the same, as the geometry immediately downstream from the inlet was CT-based and sufficiently far upstream from the OCT geometry sections to be influenced by changes to the geometry (Fig. 4).

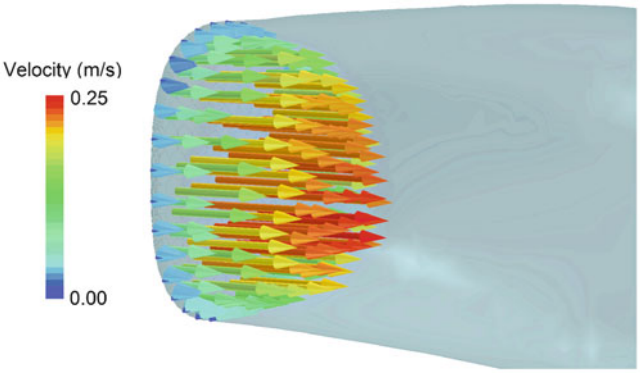

Fig. 4 Inlet velocity profile

2.4 Low WSS Analysis

Stent implantation causes changes in vascular geometry that alter local velocity and WSS distributions. These variations have been correlated with neointimal hyperplasia [35] and the ability of endothelial cells to migrate onto stent surfaces [36]. In relation to WSS, levels of 0.4 Pa or less has been associated with neointimal thickening in the coronary arteries [35, 37]. Time-averaged WSS values below this threshold have been used to quantify the impact of implanted stents (using OCT-derived geometries) [11]. Furthermore, previous work has shown that monocyte adhesion exponentially increases when WSS is below 0.4 Pa [38, 39]. Therefore, regions of WSS below 0.4 Pa are used in this study to identify areas of thrombotic susceptibility, and form a relevant basis for the comparison of the three geometries.

3 Results and Discussion

For the low-, medium- and high-resolution geometries, the LAD coronary artery surface-averaged WSS was 0.835 (+7%), 0.794 (+2%) and 0.78 Pa, respectively. This was inversely related to the differences in the surface area of the three OCT geometries: the surface areas were 9.27 (−4%), 9.58 (−1%) and 9.69 cm^2. Furthermore, the standard deviation of WSS across the LAD coronary artery increased with the resolution of the geometry; the values for the three geometries were 0.494 (−8%), 0.524 (−2%) and 0.537 Pa, respectively. These trends are not unexpected, and are not indicative of large variations in the WSS fields. This is supported by the circumferential averaging of WSS along the LAD coronary artery centreline (Fig. 5), as well as the qualitative agreement observed for the solutions to WSS (and velocity) throughout the LAD coronary artery (Fig. 6).

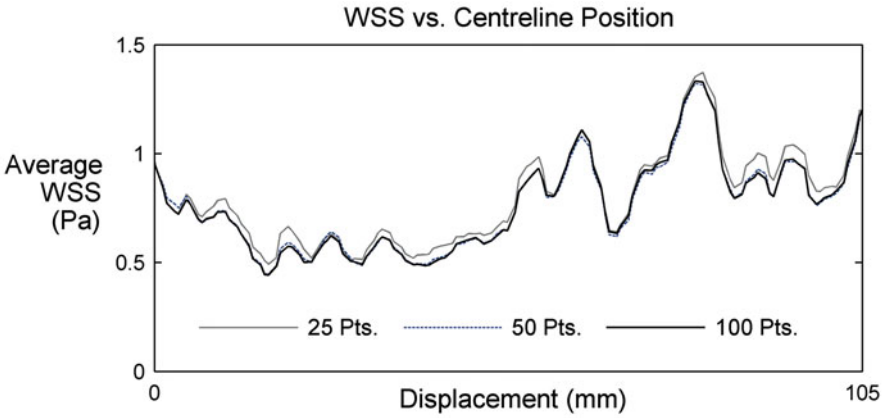

Fig. 5 Circumferential averaging of WSS along the LAD centreline

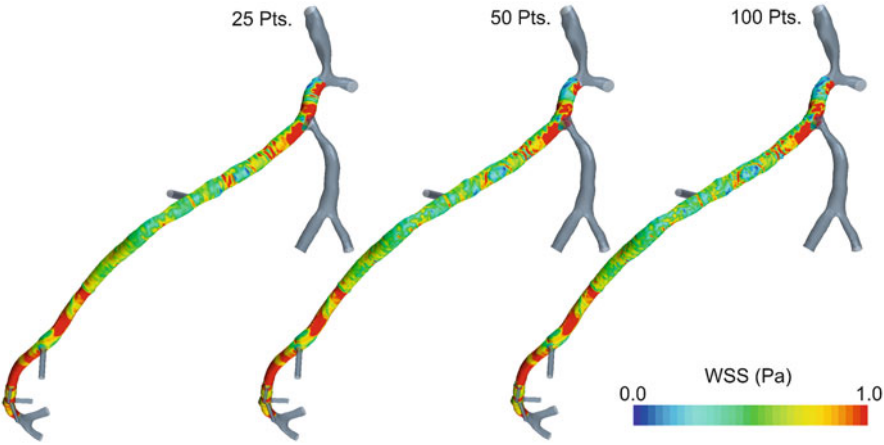

Fig. 6 Comparing the WSS fields for a wide range of values

However, the variation in the regions of low WSS, below 0.4 Pa, is much greater than the aggregate differences (discussed above). These differences occur in the proximal half of the LAD coronary artery where the artery is stented (Fig. 7). While not completely different to the low-resolution geometry, the walls of the medium- and high-resolution geometries contain a larger number of localised recesses that harbour low-velocity blood and therefore have low WSS (Fig. 7). For the low-, medium- and high-resolution geometries, the area of the LAD coronary artery surface below 0.4 Pa is 0.66 (−51%), 1.08 (−19%) and 1.34 cm^2, respectively. The low WSS analysis of the stented geometry appears to be very sensitive to the fidelity of the reconstruction. This is similar to previous observations of WSS field variation in a stented artery, which compared IVUS and OCT reconstructions. However, in

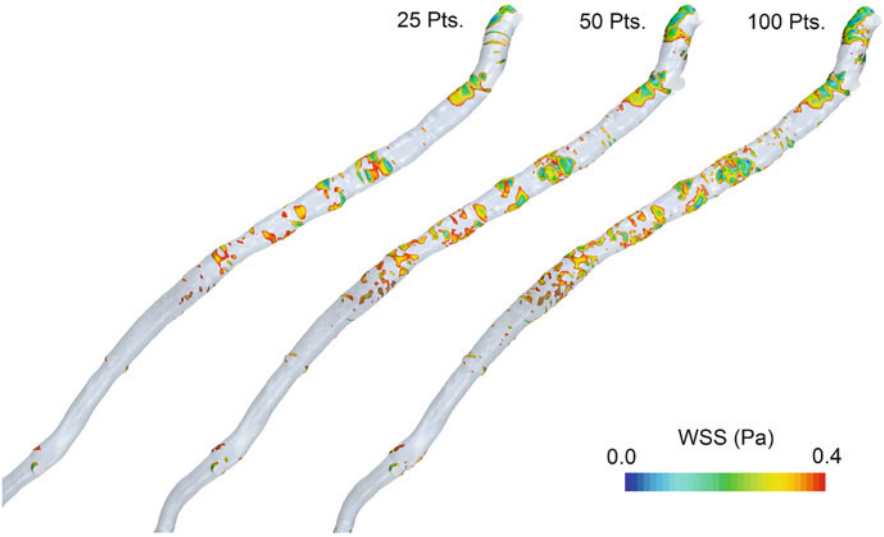

Fig. 7 Areas of WSS below 0.4 Pa

that study the differences were more extensive [14]. Furthermore, the similarity of the WSS fields in the distal half of the three geometries examined here concurs with results from the analyses of non-stented coronary arteries, reconstructed using a range of methods (including biplane angiography with OCT) [9].

There are a number of limitations to this study. This work only investigated one patient's geometry. Furthermore, the model depended on physical simplifications which are commonly implemented. Primarily, a steady-state flow field was used; whereas, a pulsatile flow field would likely increase the disparity in the results. Additionally, like other OCT reconstructions, it was assumed that the OCT images were orthogonal to the vessel centreline. This assumption is not suitable for tortuous vessels, as the guidewire does not follow the centreline path, but rather the path of lowest bend energy. It is recommended that the guidewire path is always taken into account to minimise the reconstruction error (i.e. [11]). This was not necessary for the geometry used here as the guidewire followed the vessel centreline and no longitudinal displacements had to be altered for the OCT image landmarks (branches) to agree with those shown on CT. Furthermore, while the high-resolution contour accurately segmented the lumen from the images, the stented geometry was not perfectly captured by OCT. Due to strut reflections; minor geometric details are missing where the stent struts are not embedded in the artery wall, as a neointimal layer has not yet developed in some areas of the stented LAD lumen.

4 Conclusion

Care should be taken when reconstructing geometries from OCT images to ensure that the final geometry closely represents the underlying imaging. This is particularly true for analyses of stented arteries (or complex geometries)—otherwise, poor reconstructions may produce misleading or incorrect results.

In this study, the high-resolution (100 pt. contour) reconstruction accurately represented the OCT images for the entire LAD coronary artery lumen. In the un-stented region of the artery, the lower-resolution reconstructions produced very similar geometries, and thus similar results when modelling the haemodynamics. However, the areas of low WSS in the stented portion of the artery depended greatly on the resolution of the geometric reconstruction. Compared to the high-resolution reconstruction, both the low- and medium- resolutions failed to accurately determine the areas of low WSS, as minor geometric features were inadequately represented.

While alternative OCT segmentation methods are available (e.g. [14]), the accuracy of the final geometry is limited by the ability of OCT to capture the in vivo geometry. In this regard, the axial distance between OCT images is more limiting than the pixel resolution (and cross-sectional information) of the images. Furthermore, the sensitivity of localised WSS to geometric differences is just as relevant in analyses using geometries derived from other imaging modalities.

References

1. Murray C et al (2014) Global, regional, and national age-sex specific all-cause and cause-specific mortality for 240 causes of death, 1990–2013: a systematic analysis for the Global Burden of Disease Study 2013. Lancet 385(9963):117–171. doi:10.1016/S0140-6736(14)61682-2
2. Libby P, Ridker PM, Maseri A (2002) Inflammation and atherosclerosis. Circulation 105(9):1135–1143. doi:10.1161/hc0902.104353
3. Hansson GK (2005) Inflammation, atherosclerosis, and coronary artery disease. N. Engl. J. Med. 352(16):1685–1695. doi:10.1056/NEJMra043430
4. Caro CG, Fitz-Gerald JM, Schroter RC (1969) Arterial wall shear and distribution of early atheroma in man. Nature 223(5211):1159–1160
5. Friedman MH et al (1981) Correlation between intimal thickness and fluid shear in human arteries. Atherosclerosis 39(3):425–436
6. Cheng Z et al (2010) Analysis of flow patterns in a patient-specific aortic dissection model. J. Biomech. Eng. 132(5):051007. doi:10.1115/1.4000964
7. Kousera CA et al (2014) Patient-specific coronary stenoses can be modeled using a combination of OCT and flow velocities to accurately predict hyperemic pressure gradients. IEEE Trans. Biomed. Eng. 61(6):1902–1913. doi:10.1109/tbme.2014.2310954
8. Wellnhofer E, Goubergrits L, Kertzscher U, Affeld K (2006) In-vivo coronary flow profiling based on biplane angiograms: influence of geometric simplifications on the three-dimensional reconstruction and wall shear stress calculation. Biomed. Eng. Online 5:39–39. doi:10.1186/1475-925X-5-39
9. Toutouzas K et al (2015) Accurate and reproducible reconstruction of coronary arteries and endothelial shear stress calculation using 3D OCT: comparative study to 3D IVUS and 3D QCA. Atherosclerosis 240(2):510–519. doi:10.1016/j.atherosclerosis.2015.04.011

10. Stone PH et al (2012) Prediction of progression of coronary artery disease and clinical outcomes using vascular profiling of endothelial shear stress and arterial plaque characteristics: the PREDICTION Study. Circulation 126(2):172–181. doi:10.1161/circulationaha.112.096438
11. Ellwein LM et al (2011) Optical coherence tomography for patient-specific 3D artery reconstruction and evaluation of wall shear stress in a left circumflex coronary artery. Cardiovasc. Eng. Technol. 2(3):212–227. doi:10.1007/s13239-011-0047-5
12. Otake H et al (2009) Local determinants of thrombus formation following sirolimus-eluting stent implantation assessed by optical coherence tomography. J. Am. Coll. Cardiol. Intv. 2(5):459–466. doi:10.1016/j.jcin.2009.03.003
13. Slager CJ et al (2000) True 3-dimensional reconstruction of coronary arteries in patients by fusion of angiography and IVUS (ANGUS) and its quantitative validation. Circulation 102(5):511–516
14. Bourantas CV et al (2014) Fusion of optical coherence tomographic and angiographic data for more accurate evaluation of the endothelial shear stress patterns and neointimal distribution after bioresorbable scaffold implantation: comparison with intravascular ultrasound-derived reconstructions. Int J Cardiovasc Imaging 30(3):485–494. doi:10.1007/s10554-014-0374-3
15. Goubergrits L et al (2009) Coronary artery WSS profiling using a geometry reconstruction based on biplane angiography. Ann. Biomed. Eng. 37(4):682–691. doi:10.1007/s10439-009-9656-7
16. Li Y et al (2015) Impact of side branch modeling on computation of endothelial shear stress in coronary artery disease: coronary tree reconstruction by fusion of 3D angiography and OCT. J. Am. Coll. Cardiol. 66(2):125–135. doi:10.1016/j.jacc.2015.05.008
17. J. Santos (2009) The influence of geometric factors on the wall shear stress distribution in realistic human coronary arteries. Dissertation, New University of Lisbon
18. Hetterich H et al (2015) Coronary computed tomography angiography based assessment of endothelial shear stress and its association with atherosclerotic plaque distribution in-vivo. PLoS One 10(1):e0115408. doi:10.1371/journal.pone.0115408
19. J.K. Hughey (2014) Computational evaluation of shear stress and restenosis in stented coronary arteries using optical coherence tomography. Master's Thesis, Marquette University
20. Chenyang X, Prince JL (1998) Snakes, shapes, and gradient vector flow. IEEE Trans. Image Process. 7(3):359–369. doi:10.1109/83.661186
21. Tu S et al (2013) In vivo flow simulation at coronary bifurcation reconstructed by fusion of 3-dimensional X-ray angiography and optical coherence tomography. Circ Cardiovasc Interv 6(2):15–17. doi:10.1161/circinterventions.112.000051
22. Spiegel M et al (2011) Tetrahedral vs. polyhedral mesh size evaluation on flow velocity and wall shear stress for cerebral hemodynamic simulation. Comput Methods Biomech Biomed Engin 14(1):9–22. doi:10.1080/10255842.2010.518565
23. Roache PJ (1994) Perspective: a method for uniform reporting of grid refinement studies. J. Fluids Eng. 116(3):405–413. doi:10.1115/1.2910291
24. Doyle BJ, McGloughlin TM, Kavanagh EG, Hoskins PR (2014) From detection to rupture: a serial computational fluid dynamics case study of a rapidly expanding, patient-specific, ruptured abdominal aortic aneurysm. In: Doyle BJ, Miller K, Wittek A, Nielsen MFP (eds) Computational Biomechanics for Medicine: Fundamental Science and Patient-specific Applications. New York, Springer, pp 53–68
25. Leuprecht A, Perktold K (2001) Computer simulation of non-newtonian effects on blood flow in large arteries. Comput Methods Biomech Biomed Engin 4(2):149–163. doi:10.1080/10255840008908002
26. Biasetti J, Spazzini PG, Swedenborg J, Gasser TC (2012) An integrated fluid-chemical model toward modeling the formation of intra-luminal thrombus in abdominal aortic aneurysms. Front. Physiol. 3:266. doi:10.3389/fphys.2012.00266
27. Steinman DA et al (2013) Variability of computational fluid dynamics solutions for pressure and flow in a giant aneurysm: the ASME 2012 Summer Bioengineering Conference CFD Challenge. J. Biomech. Eng. 135(2):021016. doi:10.1115/1.4023382

28. Torii R et al (2009) Fluid–structure interaction analysis of a patient-specific right coronary artery with physiological velocity and pressure waveforms. Commun. Numer. Methods Eng. 25(5):565–580. doi:10.1002/cnm.1231
29. Myers JG et al (2001) Factors influencing blood flow patterns in the human right coronary artery. Ann. Biomed. Eng. 29(2):109–120
30. Boutsianis E et al (2004) Computational simulation of intracoronary flow based on real coronary geometry. Eur. J. Cardiothorac. Surg. 26(2):248–256. doi:10.1016/j.ejcts.2004.02.041
31. Dong J, Sun Z, Inthavong K, Tu J (2015) Fluid–structure interaction analysis of the left coronary artery with variable angulation. Computer methods in biomechanics and biomedical engineering 18(14):1500–1508. doi:10.1080/10255842.2014.921682
32. Taylor CA, Fonte TA, Min JK (2013) Computational fluid dynamics applied to cardiac computed tomography for noninvasive quantification of fractional flow reservescientific basis. J. Am. Coll. Cardiol. 61(22):2233–2241. doi:10.1016/j.jacc.2012.11.083
33. Kamiya A, Togawa T (1980) Adaptive regulation of wall shear stress to flow change in the canine carotid artery. Am. J. Phys. 239(1):H14–H21
34. Campbell IC et al (2012) Effect of inlet velocity profiles on patient-specific computational fluid dynamics simulations of the carotid bifurcation. J. Biomech. Eng. 134(5):051001–051001. doi:10.1115/1.4006681
35. LaDisa JF Jr et al (2005) Alterations in wall shear stress predict sites of neointimal hyperplasia after stent implantation in rabbit iliac arteries. Am. J. Physiol. Heart Circ. Physiol. 288(5):H2465–H2475. doi:10.1152/ajpheart.01107.2004
36. Joner M et al (2008) Endothelial cell recovery between comparator polymer-based drug-eluting stents. J. Am. Coll. Cardiol. 52(5):333–342. doi:10.1016/j.jacc.2008.04.030
37. Malek AM, Alper SL, Izumo S (1999) Hemodynamic shear stress and its role in atherosclerosis. JAMA 282(21):2035–2042
38. Lawrence MB, McIntire LV, Eskin SG (1987) Effect of flow on polymorphonuclear leukocyte/endothelial cell adhesion. Blood 70(5):1284–1290
39. Hardman D et al (2013) On the prediction of monocyte deposition in abdominal aortic aneurysms using computational fluid dynamics. Proc Inst Mech Eng H 227(10):1114–1124. doi:10.1177/0954411913494319

Constitutive Modelling of Lamb Aorta

Ryley A. Macrae, Jane Pillow, Karol Miller, and Barry J. Doyle

1 Introduction

Vascular inflammation is an established marker of cardiovascular pathogenesis, but its role on arterial tissue biomechanics is not well understood. Inflammation has been identified as a risk factor for many adverse cardiovascular events [1], and is associated with increased risk even in apparently healthy individuals [2]. Inflammation is now widely regarded as a major contributing factor in the pathogenesis

R.A. Macrae
Vascular Engineering Laboratory, Harry Perkins Institute of Medical Research, Perth, WA, Australia

Intelligent Systems for Medicine Laboratory, School of Mechanical and Chemical Engineering, The University of Western Australia, Perth, WA, Australia

J. Pillow
School of Human Sciences, University of Western Australia, Australia

Centre for Neonatal Research and Education, School of Medicine, University of Western Australia, Australia

K. Miller
Intelligent Systems for Medicine Laboratory, School of Mechanical and Chemical Engineering, The University of Western Australia, Perth, WA, Australia

Institute of Mechanics and Advanced Materials, Cardiff University, Cardiff, UK

B.J. Doyle (✉)
Vascular Engineering Laboratory, Harry Perkins Institute of Medical Research, Perth, WA, Australia

British Heart Foundation Centre for Cardiovascular Science, The University of Edinburgh, Edinburgh, UK

School of Mechanical and Chemical Engineering, The University of Western Australia, Perth, WA, Australia
e-mail: Barry.Doyle@uwa.edu.au

A. Wittek et al. (eds.), *Computational Biomechanics for Medicine*,
DOI 10.1007/978-3-319-54481-6_2

of atherosclerosis [3, 4]. The inflammatory process is also associated with the development of aneurysms [5]. Furthermore, aneurysms with acute inflammation have been demonstrated to exhibit an increased rate of expansion [6–8].

These diseases involve extensive vascular remodelling changes to tissue biomechanics, but outside of gross changes to artery behaviour little work has been done on isolating the effect of inflammation on tissue biomechanics. There is a wealth of literature associating the presence of both acute and chronic inflammation with increased arterial stiffness as indicated by in-vivo measurements such as pulse-wave velocity (PWV) [9–12] but the mechanisms behind this remain unclear. Furthermore, while measurements such as pulse-wave velocity can illustrate the gross behaviour of arterial biomechanics under physiologic loading conditions, the precise effects of inflammation on the biomechanics of arteries remain relatively unexplored. The use of liposaccharides as a means for producing animal models of inflammation is well established. Intra-amniotic delivery of LPS to the fetus is widely used to model perinatal inflammation, though very few studies have examined the effect of this inflammation on cardiovascular biomechanics; though induced perinatal inflammation has been shown to alter haemodynamics and induce structural changes in the heart and small vessels [13–20].

The development of reliable constitutive models of the artery is necessary in order to better comprehend the mechanical component of cardiovascular disease pathogenesis [21], as well as providing insight into the complex biomechanical behaviours induced during therapeutical interventions such as arterial clamping and angioplasty [22]. The aim of this project was to develop constitutive models for the aorta of LPS-treated and non-treated lambs, so as to assess the impact of perinatal inflammation on arterial biomechanics. Changes in the arterial stiffness can lead to arterial remodelling and dysfunction, and so its characterization can provide insight into the nature of inflammatory processes, as well as being used to describe long term changes in arterial structure due to active vascular remodelling processes.

2 Methods

2.1 Subjects

Intra-amniotic LPS has been shown to impact the cardiovascular development of mouse [23] and rat [13] animal models, as well as impair function, alter the heart structure and induce expression of the inflammatory markers cytokine interleukin-1B and tumour necrosis factor in the myocardium of sheep [18, 24]. Foetal lambs were exposed to intra-amniotic injections of either saline (control group $n = 4$) or 4 mg *Escherichia coli* LPS (2 mg/mL: Sigma-Aldrich; 055:B5) (LPS group, $n = 6$) 2 days prior to operative operative preterm delivery at 129 days gestation. Lambs were then ventilated for 7 days, and then euthanized via 150 mg/kg of intravenous pentobarbitone (Valabarb, Jurox, Australia) for post-mortem. The aortas from each preterm lamb were excised for mechanical testing.

2.2 Test Protocol

Due to the small size of the excised specimens, mechanical testing was conducted via uniaxial loading of a ring-shaped specimen with a custom-built uniaxial test rig. While uniaxial tension experiments are insufficient to fully characterize the three-dimensional constitutive stress–strain relations of biological materials, these tests can provide useful descriptive information of the mechanical behaviour [25].

Testing was conducted within 24 h of excision. Ring-shaped samples were prepared by cutting the tubular specimen (i.e. the aorta) into smaller sections of an approximate width of 1.5 mm via circumferential cuts normal to the central axis (average of 8 rings per aortic specimen). Wall thickness (mean = 1.01 mm), sample width (mean = 1.58 mm) and ring circumference (mean = 12.8 mm) were measured optically via ImageJ. Average wall thickness was taken as the mean of 8 measurements, average wall width taken as the mean of 5 measurements and vessel circumference measured directly with the measurement tool. The sample was then mounted between two parallel metal wires and pre-stretched to the configuration shown in Fig. 1 and preconditioning applied via loading–unloading cycles until a repeatable displacement–force curve was obtained, as is standard for uniaxial testing of biological soft tissues [26]. Preconditioning was conducted to a maximum strain of 0.2 in all samples, and a repeatable mechanical response was noted after five loading–unloading cycles. Before testing, images of the sample were again taken to measure the initial distance between the pins (as shown in Fig. 1).

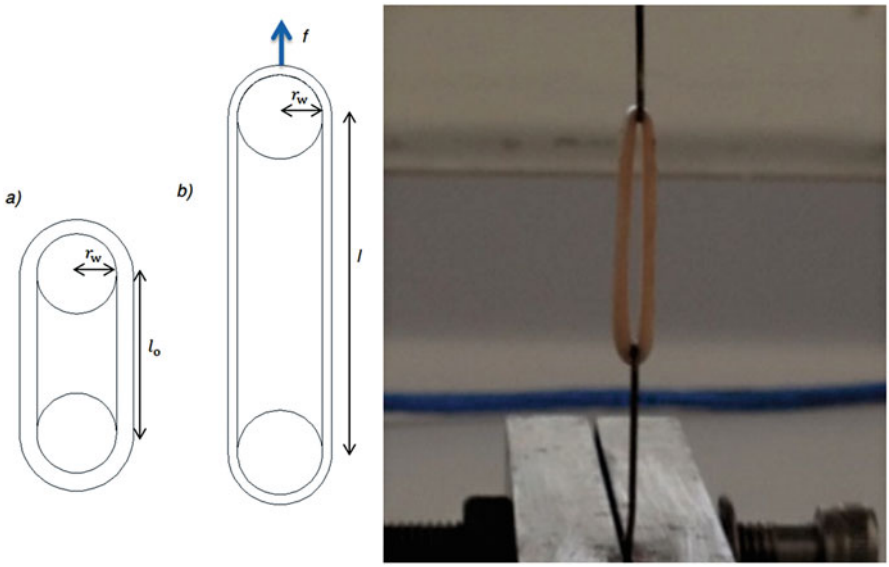

Fig. 1 Schematic of a uniaxial tension test of an arterial ring in the (**a**) reference and (**b**) deformed configuration, and corresponding photograph of loaded specimen. Reproduced from [25]

The approximate strain is calculated by measuring the displacement between the two wires [27, 28]. The average stretch ratio in the circumferential direction $\lambda_{\theta\text{avg}}$ is most simply determined by:

$$\lambda_{\theta\,\text{avg}} = \frac{l + \pi r_w}{l_o + \pi r_w} \tag{1}$$

where r_w is the radius of the cylindrical wire and l and l_o are the distances between the centres of the wires. Wires were coated in oil so as to minimize friction at the boundaries, and stress induced by friction was neglected from the analysis. The sample was then extended at a constant rate of 0.1 mm/s until failure whilst continuously measuring displacement and force.

2.3 Data Analysis

As the constitutive relations derived are intended to describe the mechanical behaviour and allow for comparison between LPS-treated and control specimens, data was processed in terms of the global stretch ratio consistently across specimens [29]. It was assumed that the effects of any friction and bending stiffness would be either negligible or relatively consistent across samples. Upon pre-loading the sample force was noted to be approximately 0.01 N, as compared to an average failure force of 2 N, indicating that the effect of bending stiffness was relatively low. Thus, assuming the ring is free to move along the wire boundary, nominal stress (S_{avg}) will be given by:

$$S_{\text{avg}} = \frac{F_{\text{exp}}}{2 \cdot A_{\text{avg}}} \tag{2}$$

where A_{avg} is the average cross-sectional area of the ring, assumed to be rectangular, $A_{\text{avg}} = t \cdot w$, and F_{exp} is the measured tension. However, while the width of each ring could be assumed constant, wall thickness around the ring was shown to vary significantly, with some rings showing a variation in wall thickness up to 30%. Thus, the assumption of constant cross-sectional area throughout the ring is invalid. Assuming the ring breaks at the smallest cross-sectional area, with the data of specimens which broke near the wires or in a region distinct from that of lowest cross-sectional area discarded, the nominal stress at the smallest cross-sectional area (S_b) can be determined from experimental data via:

$$S_{b\text{exp}} = \frac{F_{\text{exp}}}{2 \cdot A_b} \tag{3}$$

where A_b is the smallest initial cross-sectional area, as calculated at the smallest thickness. In order to derive a stress–strain relationship, it is necessary to relate the global average stretch (λ_{avg}) to a stretch local to the point of failure (λ_b). Assuming

circumferential force (F_θ) is constant throughout the ring, circumferential stress will be proportional to the initial cross-sectional area:

$$F_\theta = S_{\text{avg}} \cdot A_{\text{avg}} = S_b \cdot A_b \tag{4}$$

If we assume isotropy and incompressibility, the strain energy function can be expressed in terms of the first and second invariants of the Green strain tensor [30]:

$$W = \bar{W}(I_1, I_2) \tag{5}$$

Assuming no shear, under uniaxial tension the strain invariants are given by:

$$I_1 = {\lambda_1}^2 + \frac{2}{\lambda_1}, \; I_2 = 2\lambda_1 + \frac{1}{{\lambda_1}^2} \tag{6}$$

where λ_1 is the stretch in the direction of loading λ_θ. An Ogden model [31] with $N = 1$ proved a good fit ($R^2 \geq 0.97$) for the data while utilizing few parameters, given as follows:

$$W = \frac{\mu}{\alpha}\left(\lambda_1^\alpha + \lambda_2^\alpha + \lambda_3^\alpha - 3\right) \tag{7}$$

With nominal stress being given by:

$$S_1 = \frac{\mu}{\lambda_1}\left(\lambda_1^\alpha - \lambda_1^{\frac{-\alpha}{2}}\right) \tag{8}$$

where $[\mu, \alpha]$ are the particular coefficients of a given strain energy function. For the given strain levels, the use of higher order models is not warranted, as indicated by the goodness of fit. Determining the stretch ratio at the region of smallest cross-sectional area (λ_b) is a not entirely trivial matter. In this particular case, λ_b was determined via substituting Eq. (8) into the relation given by Eq. (4), such that:

$$\frac{\left(\lambda_b^\alpha - \lambda_b^{\frac{-\alpha}{2}}\right)}{\lambda_b} = \frac{A_{\text{avg}}}{A_b} \cdot \frac{\left(\lambda_{\text{avg}}^\alpha - \lambda_{\text{avg}}^{\frac{-\alpha}{2}}\right)}{\lambda_{\text{avg}}} \tag{9}$$

For the given measurements of A_b, A_{avg} and the range of values determined from displacement data [λ_{avg}], an initial guess was made of the constitutive parameters $[\mu, \alpha]$ and used to compute corresponding local stretch values [λ_b]. These values of stretch were then used to compute S_b as per Eq. (8). Model calibration was conducted via minimizing the error between this curve S_b–λ_b and the curve derived from experimental data $S_{\text{bexp}} - \lambda_\text{b}$, as determined from Eq. (3). Error was computed via a least squares method weighted towards the low-strain region:

$$\text{Error} = \sum \left(1 - \frac{S_{\text{model}}}{S_{\text{exp}}}\right)^2 \tag{10}$$

Error was weighted towards the low stress/strain region, as data in this region is of more physiological relevance than that in the very high strain region. In addition, data in the high stress–strain region is also influenced by factors not accounted for in the model, such as tissue damage occurring prior to tissue failure. The resultant fitted parameters $[\mu, \alpha]$ were then used to compute a new local stretch as described above which was then input into Eq. (9), and this approach iterated until successive error between computed constitutive parameters was negligible. All model calibration was conducted via a custom MATLAB script. While initial guesses for the constitutive parameters were at first selected arbitrarily, to reduce calibration time the initial guesses were then set to values approximate to those determined for early samples; $[\mu = 2 \times 10^{-4}, \alpha = 10]$.

Shear modulus in the undeformed state was derived from the Ogden model via:

$$\mu_o = \frac{1}{2}\mu\alpha \tag{11}$$

3 Results

Data from ten specimens (cut into approximately eight rings each) were utilized (control $n = 4$, LPS-treated $n = 6$). LPS-treated lambs demonstrated a trend towards higher wall thickness, though this finding was not significant ($p > 0.35$), with aortic specimens from the control group having an average of thickness of 0.977 ± 0.073 mm and LPS-treated group 1.076 ± 0.079 mm (see Fig. 2).

Force-extension data of rings cut from a single specimen showed high consistency (Fig. 3). Incorporation of the local stretch as determined by Eq. (9) affected the estimates of the Ogden parameter μ by up to 15%, and had no appreciable effect on determination of the parameter α ($\leq$0.1%). Fig. 4 illustrates the stress-stretch curve as assessed by taking a constant cross-sectional area compared to the stress-stretch curve computed with a locally determined stretch, for a representative sample.

The average constitutive parameters determined for the Ogden model were not significantly different between groups (see Table 1, Fig. 5), although μ

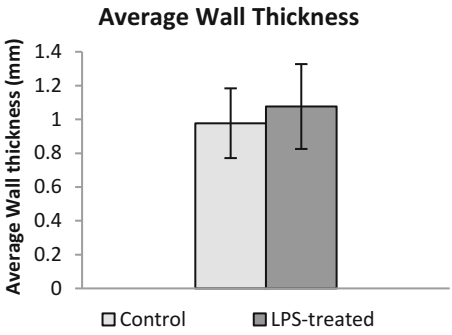

Fig. 2 Average wall thicknesses of the aorta for both the control and LPS-treated groups with standard deviations

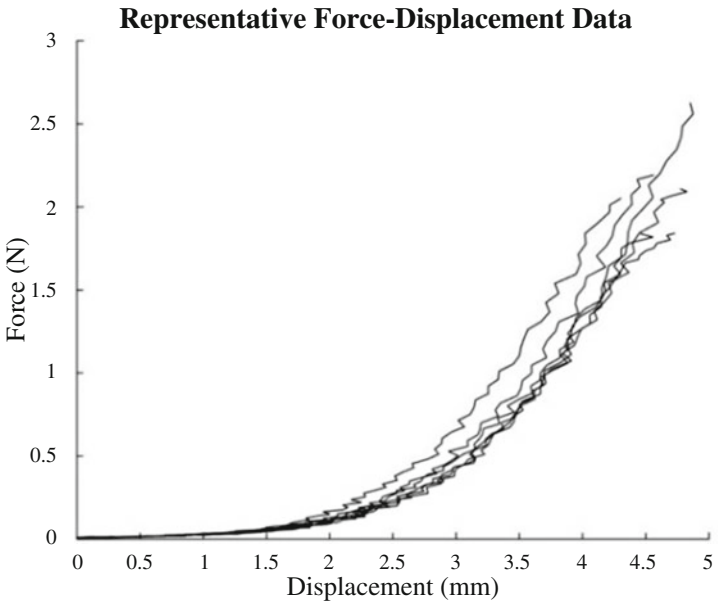

Fig. 3 Experimental force–displacement curves taken from a representative specimen (LPS-treated)

trended higher in the LPS-treated group ($\mu = 7.77 \times 10^{-4} \pm 6.96 \times 10^{-4}$ versus $4.43 \times 10^{-4} \pm 3.67 \times 10^{-4}$; $p > 0.4$). The α parameter showed no difference between groups ($p > 0.85$), with an average of 12.78 ± 0.58 MPa (control $= 12.96 \pm 2.145$, LPS-treated $= 12.65 \pm 3.378$). A difference was noted in the initial shear modulus, being higher in the LPS-treated group ($4.48 \times 10^{-3} \pm 3.71 \times 10^{-3}$ MPa versus $2.70 \times 10^{-3} \pm 2.23 \times 10^{-3}$ MPa), although again variation was high and the finding was non-significant ($p > 0.4$).

4 Discussion and Conclusion

The relation between inflammation and cardiovascular disease is widely researched, yet little data exists on the biomechanical impact of inflammation on the aorta. Previous studies suggest that inflammation stiffens the aorta [32, 33]; however, these previous studies use in-vivo pulse-wave velocity with inherent assumptions on aortic morphology, and not physical biomechanical ex-vivo testing. Our preliminary ex-vivo data suggests that LPS-induced systemic inflammation during foetal development does not greatly affect the biomechanical behaviour (i.e. stiffness) of the aorta, as assessed by vessel constitutive parameters. The development of these constitutive models provides valuable data on the precise

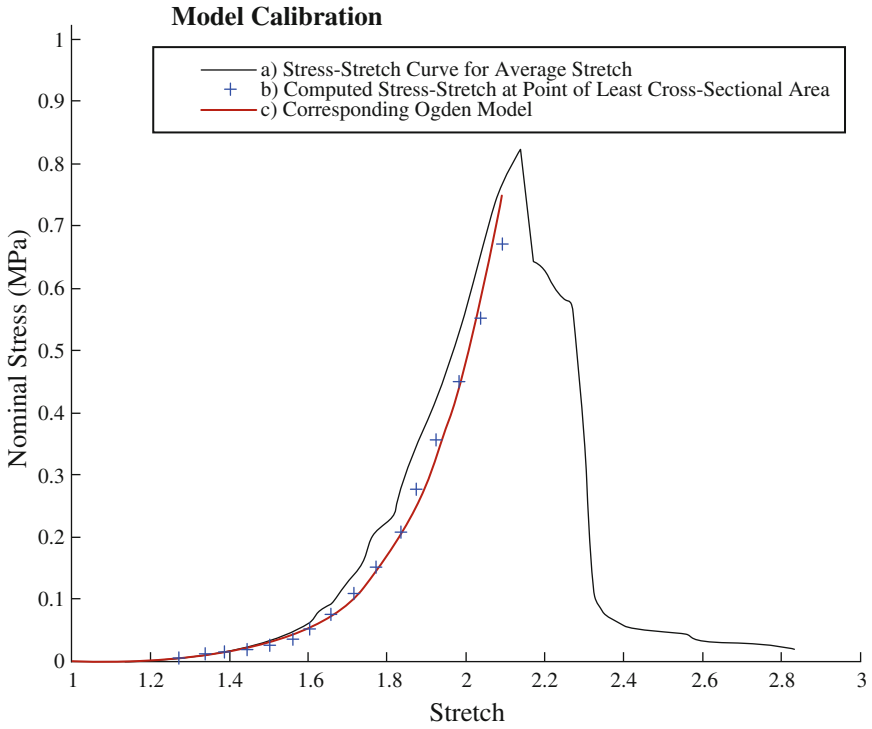

Fig. 4 Representative stress-stretch curves from a single sample (LPS-treated): (**a**) stress-stretch curve derived from the average stretch throughout the ring specimen; (**b**) stress-stretch curve at the smallest cross-sectional area as computed during model calibration and (**c**) the Ogden model fit to the computed stress-stretch curve at smallest cross-sectional area

Table 1 Collected values of constitutive parameters and initial shear modulus. Statistical significance was not reached in any case

Group	–	μ (MPa)	α	μ_o(MPa)
Control	Mean	4.43×10^{-4}	12.96	2.70×10^{-3}
	Standard Dev	$\pm 3.67 \times 10^{-4}$	± 2.145	$\pm 2.23 \times 10^{-3}$
LPS-treated	Mean	7.77×10^{-4}	12.65	4.48×10^{-3}
	Standard Dev	$\pm 6.96 \times 10^{-4}$	± 3.378	$\pm 3.71 \times 10^{-3}$

effects on mechanical behaviour of perinatal inflammation. Although there was on average a trend for LPS-treated arteries to be stiffer in the low-strain region, a significant change in stiffness expected was not demonstrated. The majority of prior studies employ pulse-wave velocity as an indicator of bulk stiffness, and thus care must be taken when comparing this data to the material stiffness given by the elastic modulus as measures of bulk stiffness are dependent on the thickness of the artery [34].

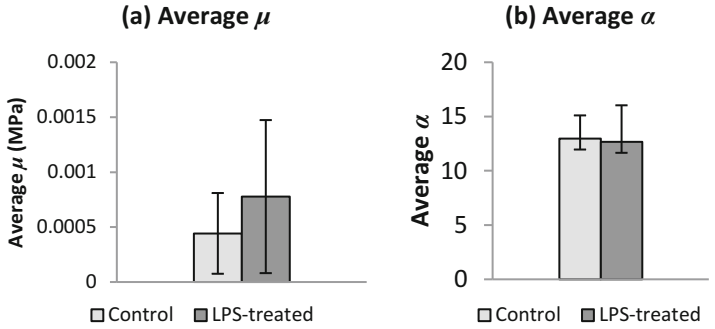

Fig. 5 Average constitutive parameters (**a**) μ and (**b**) α computed for both LPS-treated and control groups, with standard deviation

There are limitations to our work and it is possible the induced systemic inflammation was insufficiently present in the foetal cardiovascular system—either in severity or duration—to provoke a significant change in the biomechanics of the aorta. The constitutive parameters determined are primarily intended for comparison between treatment groups, and thus have not taken into account the potential impact of boundary friction on the parameter values. For a more precise determination of constitutive parameters, finite element method should be used [35]. The study was further limited by the number of specimens; due to the high variability in material properties between subjects, more data would be required to ascertain what, if any, correlation exists between systemic foetal inflammation and arterial biomechanics. This data represents a preliminary cohort, with testing of additional subjects currently underway. As this article is focussed on assessing the passive biomechanical response of the artery as an indication of structural remodelling, it necessarily neglects the active response of the artery, largely mediated via nitric oxide production [10].

In conclusion, this is the first study to assess the impact of inflammation on the biomechanical response of the aorta, using ex-vivo test methods. We show that in our preliminary cohort, inflammation does not significantly impact aortic stiffness, and the preterm lamb can be represented by a first order Ogden constitutive model. Further testing is needed to conclusively determine the effect of inflammation on aortic biomechanics.

References

1. Bhatt DL, Topol EJ (2002) Need to test the arterial inflammation hypothesis. Circulation 106(1):136–140
2. Rohde LE, Hennekens CH, Ridker PM (1999) Survey of C-reactive protein and cardiovascular risk factors in apparently healthy men. Am J Cardiol 84(9):1018–1022
3. Libby P (2002) Inflammation in atherosclerosis. Nature 420(6917):868–874

4. Ross R (1999) Atherosclerosis–an inflammatory disease. N Engl J Med 340(2):115–126
5. Rasmussen TE, Hallett JW Jr, Schulte S, Harmsen WS, O'Fallon WM, Weyand CM (2001) Genetic similarity in inflammatory and degenerative abdominal aortic aneurysms: a study of human leukocyte antigen class II disease risk genes. J Vasc Surg 34(1):84–89
6. Mosorin M, Juvonen J, Biancari F, Satta J, Surcel HM, Leinonen M, Saikku P, Juvonen T (2001) Use of doxycycline to decrease the growth rate of abdominal aortic aneurysms: a randomized, double-blind, placebo-controlled pilot study. J Vasc Surg 34(4):606–610
7. Pyo R, Lee JK, Shipley JM, Curci JA, Mao D, Ziporin SJ, Ennis TL, Shapiro SD, Senior RM, Thompson RW (2000) Targeted gene disruption of matrix metalloproteinase-9 (gelatinase B) suppresses development of experimental abdominal aortic aneurysms. J Clin Invest 105(11):1641–1649
8. Richards JM, Semple SI, MacGillivray TJ, Gray C, Langrish JP, Williams M, Dweck M, Wallace W, McKillop G, Chalmers RT, Garden OJ, Newby DE (2011) Abdominal aortic aneurysm growth predicted by uptake of ultrasmall superparamagnetic particles of iron oxide: a pilot study. Circ Cardiovasc Imaging 4(3):274–281
9. Aznaouridis KA, Stefanadis CI (2007) Inflammation and arterial function. Artery Research 1(1):32–38
10. Jain S, Khera R, Corrales-Medina VF, Townsend RR, Chirinos JA (2014) Inflammation and arterial stiffness in humans. Atherosclerosis 237(2):381–390
11. Mäki-Petäjä KM, Wilkinson IB (2012) Inflammation and large arteries: potential mechanisms for inflammation-induced arterial stiffness. Artery Res 6(2):59–64
12. Park S, Lakatta EG (2012) Role of inflammation in the pathogenesis of arterial stiffness. Yonsei Med J 53(2):258–261
13. Abdulkadir AA, Kimimasa T, Bell MJ, MacPherson TA, Keller BB, Yanowitz TD (2010) Placental inflammation and fetal hemodynamics in a rat model of chorioamnionitis. Pediatr Res 68(6):513–518
14. Galinsky R, Hooper SB, Wallace MJ, Westover AJ, Black MJ, Moss TJ, Polglase GR (2013) Intrauterine inflammation alters cardiopulmonary and cerebral haemodynamics at birth in preterm lambs. J Physiol 591(8):2127–2137
15. Kallapur SG, Bachurski CJ, Cras TDL, Joshi SN, Ikegami M, Jobe AH (2004) Vascular changes after intra-amniotic endotoxin in preterm lamb lungs. Am J Phys Lung Cell Mol Phys 287(6):L1178–L1185
16. Polglase GR, Hooper SB, Gill AW, Allison BJ, Crossley KJ, Moss TJ, Nitsos I, Pillow JJ, Kluckow M (2010) Intrauterine inflammation causes pulmonary hypertension and cardiovascular sequelae in preterm lambs. J Appl Physiol 108(6):1757–1765
17. Romero R, Espinoza J, Goncalves LF, Gomez R, Medina L, Silva M, Chaiworapongsa T, Yoon BH, Ghezzi F, Lee W, Treadwell M, Berry SM, Maymon E, Mazor M, DeVore G (2004) Fetal cardiac dysfunction in preterm premature rupture of membranes. J Matern Fetal Neonatal Med 16(3):146–157
18. Seehase M, Gantert M, Ladenburger A, Garnier Y, Kunzmann S, Thomas W, Wirbelauer J, Speer CP, Kramer BW (2011) Myocardial response in preterm fetal sheep exposed to systemic endotoxinaemia. Pediatr Res 70(3):242–246
19. Velten M, Hutchinson KR, Gorr MW, Wold LE, Lucchesi PA, Rogers LK (2011) Systemic maternal inflammation and neonatal hyperoxia induces remodeling and left ventricular dysfunction in mice. PLoS One 6(9):e24544
20. Yanowitz TD, Jordan JA, Gilmour CH, Towbin R, Bowen A, Roberts JM, Brozanski BS (2002) Hemodynamic disturbances in premature infants born after chorioamnionitis: association with cord blood cytokine concentrations. Pediatr Res 51(3):310–316
21. Holzapfel G, Gasser T, Ogden R (2000) A new constitutive framework for arterial wall mechanics and a comparative study of material models. J Elast Phys Sci Solids 61(1–3):1–48
22. Gasser TC, Schulze-Bauer CA, Holzapfel GA (2002) A three-dimensional finite element model for arterial clamping. J Biomech Eng 124(4):355–363

23. Rounioja S, Räsänen J, Glumoff V, Ojaniemi M, Mäkikallio K, Hallman M (2003) Intra-amniotic lipopolysaccharide leads to fetal cardiac dysfunction. A mouse model for fetal inflammatory response. Cardiovasc Res 60(1):156–164
24. Tare M, Bensley JG, Moss TJ, Lingwood BE, Kim MY, Barton SK, Kluckow M, Gill AW, De Matteo R, Harding R, Black MJ, Parkington HC, Polglase GR (2014) Exposure to intrauterine inflammation leads to impaired function and altered structure in the preterm heart of fetal sheep. Clin Sci (Lond) 127(9):559–569
25. Macrae RA, Miller K, Doyle BJ (2016) Methods in mechanical testing of arterial tissue: a review. Strain 52(5):380–399
26. Humphrey JD (2002) Cardiovascular solid mechanics: cells, tissues and organs. Springer-Verlag, New York
27. Cox RH (1983) Comparison of arterial wall mechanics using ring and cylindrical segments. Am J Phys 244(2):H298–H303
28. Stoiber M, Messner B, Grasl C, Gschlad V, Bergmeister H, Bernhard D, Schima H (2015) A method for mechanical characterization of small blood vessels and vascular grafts. Exp Mech 55(8):1591–1595
29. Shazly T, Rachev A, Lessner S, Argraves W, Ferdous J, Zhou B, Moreira A, Sutton M (2015) On the uniaxial ring test of tissue engineered constructs. Exp Mech 55(1):41–51
30. Fung YC (1993) Biomechanics: mechanical properties of living tissues. Springer-Verlag, New York
31. Ogden RW (1972) Large deformation isotropic elasticity-on the correlation of theory and experiment for incompressible rubberlike solids. Proc R Soc Lond A Math Phys Eng Sci 326(1567):565–584
32. Booth AD, Wallace S, McEniery CM, Yasmin J, Brown D, Jayne R, Wilkinson IB (2004) Inflammation and arterial stiffness in systemic vasculitis: a model of vascular inflammation. Arthritis Rheum 50(2):581–588
33. Wallace SML, Mäki-Petäjä KM, Cheriyan J, Davidson EH, Cherry L, McEniery CM, Sattar N, Wilkinson IB, Kharbanda RK (2010) Simvastatin prevents inflammation-induced aortic stiffening and endothelial dysfunction. Br J Clin Pharmacol 70(6):799–806
34. Greenwald SE (2007) Ageing of the conduit arteries. J Pathol 211(2):157–172
35. Morriss L, Wittek A, Miller K (2008) Compression testing of very soft biological tissues using semi-confined configuration—a word of caution. J Biomech 41(1):235–238

Quantifying Cytoskeletal Morphology in Endothelial Cells to Enable Mechanical Analysis

Yi Chung Lim, Detlef Kuhl, Michael T. Cooling, and David S. Long

1 Introduction

Blood-flow induced wall shear stress (WSS) is a focal risk factor for atherosclerosis [1]. Disturbed oscillatory WSS elicits an inflammatory endothelial cell (EC) response that contributes to the pathogenesis of atherosclerosis. Conversely, steady WSS results in a protective EC response [2]. A key EC response to WSS is the change in cell morphology: in particular, cytoskeletal morphology. Steady WSS results in cell elongation and alignment in the flow direction. In contrast, disturbed WSS causes greater shape variation in ECs (similar to cells grown in static conditions) [3–9].

Chien postulated that EC morphological dependency on WSS is caused by ECs maintaining an internal force homeostasis: cells adapt their morphology to keep internal forces within a "normal" range. In the case of disturbed WSS, the preferential flow direction cannot be sensed. This leads to internal force extremes causing endothelial dysfunction and an inflammatory response [10].

Computational models have already been used to quantify the stresses and strains within a single EC [11] or a population of ECs [12] in response to WSS (see [13] for a recent review). However, the effect of EC morphology on internal

Y.C. Lim (✉) • D. Kuhl
Department of Civil and Environmental Engineering, Institute of Mechanics and Dynamics, University of Kassel, Kassel, Germany
e-mail: yi.ch.lim@gmail.com

M.T. Cooling
Auckland Bioengineering Institute, University of Auckland, Auckland, New Zealand

D.S. Long
Auckland Bioengineering Institute, University of Auckland, Auckland, New Zealand

Department of Engineering Science, University of Auckland, Auckland, New Zealand

A. Wittek et al. (eds.), *Computational Biomechanics for Medicine*,
DOI 10.1007/978-3-319-54481-6_3

force transmission of WSS has only recently been examined. In particular, the effect of morphological variation in the nucleus and cell membrane on the internal force response to WSS has been quantified [14]. Further extension is required to include the cytoskeleton—a key component in cell mechanical stability [15]. One barrier to this is the lack of quantitative spatial descriptors (also known as shape/morphometric/summary descriptors) to define cytoskeletal morphology. Once this challenge has been overcome, it will be possible to test Chien's theory by quantifying the internal force distributions in populations of ECs with differing morphologies that are exposed to different WSS environments.

In this study, we have extended the spatial descriptor analysis to include the cytoskeleton and primary cilia. These descriptors were then used to recreate specific cells. Furthermore, our set of spatial descriptors were used to generate virtual cells characteristic of the entire population. Thus, the morphological variation of the entire population can be represented by a smaller set of virtual cells without a significant loss in information.

Our spatial descriptor analysis aims to provide a spatial domain suitable for future mechanical analysis. In doing so, we hope to enable future studies on the role of EC mechanics in atherosclerosis.

2 Materials and Methods

Human microvascular endothelial cells (HMEC-1s) were cultured using previously described methods [14, 16]. The primary cilia, acetylated α-tubulin, F-actin and the nuclei from 15 HMEC-1s were then co-imaged as previously described [14, 16].

2.1 Spatial Descriptors

The framework for spatial descriptors is based on the series of studies published by Murphy et al. [17–19].

Reference system, nucleus and cell membrane shape: The reference coordinate system of our model has previously been described [14]. Briefly, the nucleus centroid is the origin of coordinate system, the long axis of the nucleus forms the first axis, the apical-basal direction forms the second axis and the 3rd axis is perpendicular to the other two. Nuclei are chosen as the reference point as they are easily identified, and there is only one in every EC. The spatial descriptors of the nucleus and cell membrane have also been previously described [14]. Image processing and analysis was carried out in MATLAB (version 2013b), ImageJ (version 1.48o) and AMIRA (version 5.6).

Cytoskeleton—deconvolution: The acetylated α-tubulin and F-actin components of cytoskeleton were imaged and the morphology quantified. As a preliminary step, deconvolution was carried out to increase contrast of the cytoskeletal structures, thus allowing automatic segmentation. Image stacks of actin and tubulin were

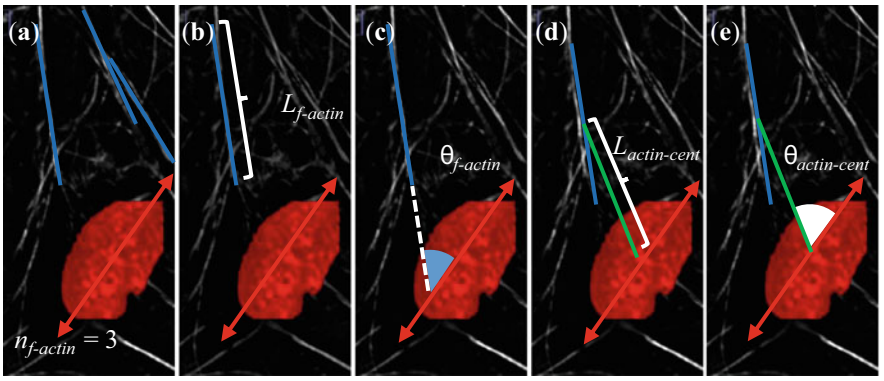

Fig. 1 Spatial descriptors used to quantify F-actin morphology: **(a)** $n_{\text{f-actin}}$, the number of actin fibres present in each cell, in this simplified example there are only three fibres (*blue*); (**b**) $L_{\text{f-actin}}$, fibre length; (**c**) $\theta_{\text{f-actin}}$, fibre orientation with respect to the nuclear axis; (**d**) $L_{\text{actin-cent}}$, the length between the actin fibre centroid and the nucleus centroid (shown in *green*) and (**e**) $\theta_{\text{actin-cent}}$, angle of the vector between actin fibre centroid and the nucleus centroid

deconvolved with an artificial point spread function (PSF) calculated using the Diffraction PSF 3D ImageJ plugin (http://www.optinav.com/Diffraction-PSF-3D.htm, [20]). Deconvolution was then carried out using the Iterative Deconvolve 3D ImageJ plugin (http://www.optinav.com/Iterative-Deconvolve-3D.htm, [20]).

F-actin: Each individual actin fibre was traced semi-automatically using the simple neurite tracer tool in ImageJ [21], hence the 3D coordinates of each fibre (at pixel resolution) were quantified. We found that nearly all stress fibres were within two slices (0.9 μm layer), in a layer one slice (0.45 μm) below the base of the nucleus. Hence the morphology of the actin fibre network can be captured by a 2D analysis. Five spatial descriptors were used to represent F-actin (see Fig. 1). The first is the number of actin fibres present in each cell, $n_{\text{f-actin}}$. All other F-actin spatial descriptors are arrays of size $n_{\text{f-actin}}$. The other descriptors are the fibre length, $L_{\text{f-actin}}$; the fibre orientation with respect to the nuclear axis, $\theta_{\text{f-actin}}$; the length between the centroid of the fibre and the nucleus centroid, $L_{\text{actin-cent}}$ and angle of the vector between actin fibre centroid and the nucleus centroid, $\theta_{\text{actin-cent}}$.

Acetylated α-tubulin: Acetylated α-tubulin migrates outward from the centrosome, and therefore can be modelled as a branching network, with straight segments. The centrosome was not explicitly imaged, but instead was estimated to be the voxel with maximum intensity in the tubulin images [22]. Again, the simple neurite tracer tool [21] was used to segment the acetylated *a*-tubulin morphology. The six spatial descriptors used to quantify α-tubulin morphology were: (1) the position of the centrosome with respect to the nucleus centroid; (2) number of microtubules in the cell, n_{tubule} (similar to F-actin, the remaining descriptors are arrays of size n_{tubule}); (3) the length of each microtubule, L_{tubule}; (4) the collinearity of a microtubule against its parent microtubule (the microtubule that it branched out from), θ_{cotubule}; (5) the change in height (z value) of the centroid microtubule compared to the height of the parent microtubule and (6) the ancestry number of the microtubule, which

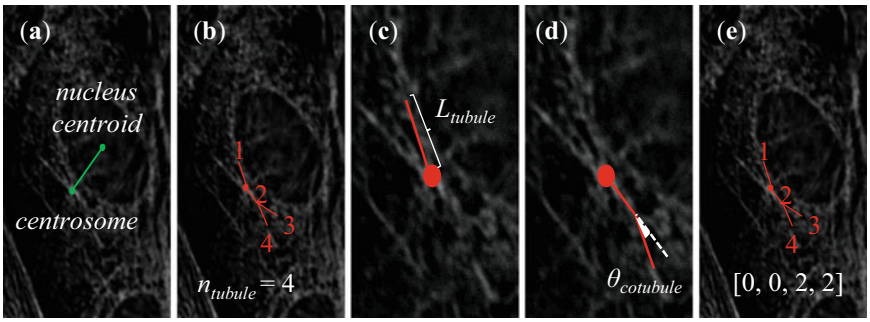

Fig. 2 Spatial descriptors used to quantify acetylated α-tubulin morphology: (**a**) the position of the centrosome relative to nuclear centroid; (**b**) number of microtubules in the cell, n_{tubule}; (**c**) the length of each microtubule, L_{tubule}; (**d**) the collinearity of a microtubule with its parent microtubule, θ_{cotubule}, note this consists of an in-plane angle and a z-direction change in slice and (**e**) the ancestry number of the microtubule, which identifies the number of its parent microtubule. In this example the ancestry numbers are 0, 0, 2, 2, indicating that the first two microtubules originate at the centrosome, and the third and fourth tubules originate from the second microtubule

identifies the number of its parent microtubule. These descriptors are illustrated in Fig. 2.

Primary cilium: Due to spectral overlap, a separate population ($n = 39$), from the population that was used in cell shape, nucleus and cytoskeleton analysis, of cells was used to examine primary cilium morphology using methods described in Lim et al. 2015 [16]. To avoid bias, every cilium in each image was analysed. Two spatial descriptors were formulated for primary cilia, cilia length and cilia-centroid position—the vector between the nucleus centroid and the base of the cilium.

2.2 Generating Virtual Cells

Virtual cells were generated from the complete population dataset of previously described morphological descriptors. Statistical boot-strapping was used to obtain a distribution for each of the descriptors: first, the n-sized vector (where n is $n_{\text{f-actin}}$ or n_{tubule}, respectively) of every spatial descriptor was resampled with replacement, to generate 1000 n-sized vectors. This large dataset is normal distributed. The F-actin and tubulin networks and primary cilia could then generated by sampling from these distributions. As the nucleus centroid is the reference point in the set of tubulin, actin and primary cilia descriptors, it is possible to generate a virtual cell with all of these components.

3 Results

3.1 F-Actin

The median of $n_{\text{f-actin}}$ was 20 fibres, with a maximum of 32 and a minimum of ten. There were fewer actin stress fibres than microtubules on average. $L_{\text{f-actin}}$ is right skewed, with a median value of 4.6 μm (see Fig. 3a). From the angle histogram of $\theta_{\text{f-actin}}$ (see Fig. 3b) there does not appear to be a preferential angle of orientation of actin fibres. Median $L_{\text{actin-cent}}$ was 13 μm (see Fig. 3c), suggesting that the majority of the actin stress fibres were beyond the *xy* area bounded by the nucleus. From the angle histogram of $\theta_{\text{actin-cent}}$ (see Fig. 3d), it appears that the centroid of actin fibres are preferentially to the left and right (270° and 90°) of the nucleus centroid, rather than above–below (0° and 180°) the nucleus centroid (nucleus axis is parallel to the above–below direction).

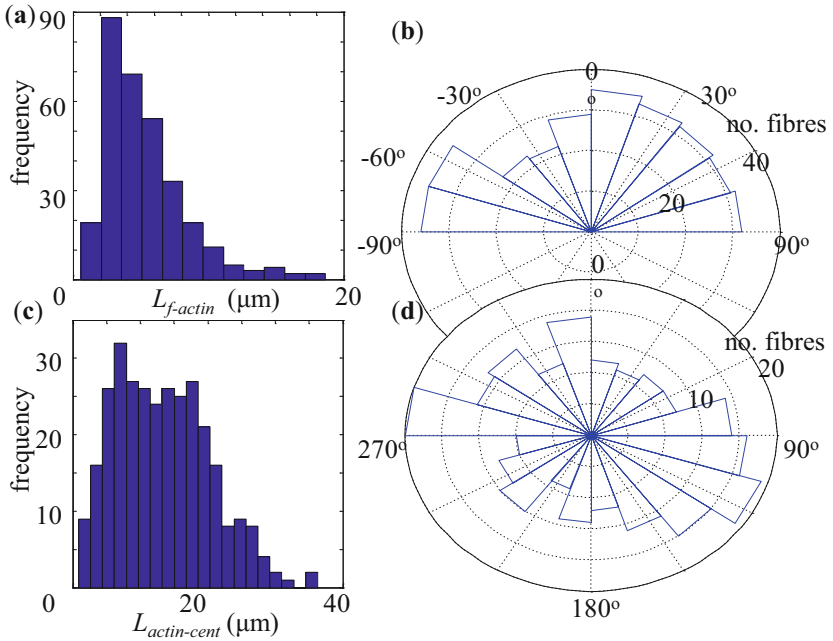

Fig. 3 Quantification of spatial descriptors of F-actin in the population. (**a**) The histogram of $L_{\text{f-actin}}$ shows $L_{\text{f-actin}}$ is right skewed and not normal (Shapiro–Wilk test, $p < 0.0001$). (**b**) The angle histogram of $\theta_{\text{f-actin}}$ with units in degrees: no preferential direction is evident. (**c**) The histogram of $L_{\text{actin-cent}}$. $L_{\text{actin-cent}}$ is not normal, (Shapiro–Wilk test, $p < 0.0001$). Most of the values of $L_{\text{actin-cent}}$ are above 5 μm, suggesting that actin fibres are far from the nucleus. (**d**) The angle histogram of $\theta_{\text{actin-cent}}$. Fibres are preferentially to the left and right (270° and 90°) of the nucleus centroid, rather than above–below (0° and 180°) the nucleus centroid

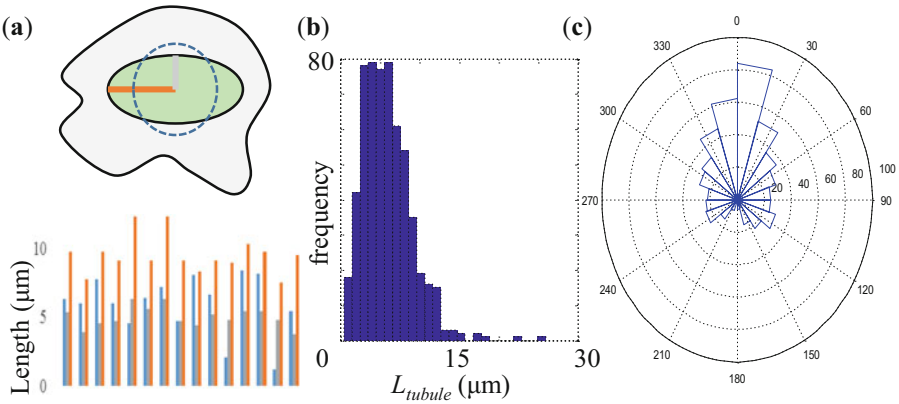

Fig. 4 Quantification of spatial descriptors of acetylated α-tubulin in the population. (**a**) Column graph of distance between centrosome and nucleus (*blue*), half of nucleus length (*orange*) and half of nucleus width (*grey*), *inset*: cartoon cell illustrating these lengths with nucleus in green. The centrosome distance is shown by the dashed blue circle. (**b**) The histogram of L_{tubule} shows microtubule length is right skewed and not normal (Shapiro–Wilk test, $p < 0.0001$). (**c**) Angle histogram of θ_{cotubule}, with units in degrees. The majority of microtubules are within 30° of their parent microtubule

3.2 *Acetylated α-Tubulin*

The distance in the *xy* plane between the centrosome and the nucleus centroid for all cells in the population are illustrated in Fig. 4a, with the nucleus length and width of that cell for comparison. The median of n_{tubule} was 38, with a maximum of 71 and minimum of 15. L_{tubule} was right skewed, with a median value of 5.9 μm (see Fig. 4b). The median of θ_{cotubule} was 3°, with the majority of microtubules within 30° of the parent microtubule (see Fig. 4c). The ancestry number and change in height are not shown here, but are stored to allow specific cells to be recreated. The actin filament and microtubule networks of a specific cell can also be recreated from its spatial description (see Fig. 5). The methods presented in this study result in straight actin filaments and straight microtubules. Nearly all actin filaments are captured, whereas the finer microtubule network cannot be resolved with our imaging technique. Note, these recreated images are in 2D. While actin filaments are mostly in plane, the microtubule network is not, hence further development is needed to extend these recreated models to 3D.

3.3 *Primary Cilium*

A histogram of primary cilium length is shown in Fig. 6a. The median ± interquartile range of primary cilium length was 3.0 μm ± 1.0 μm. The position of the base

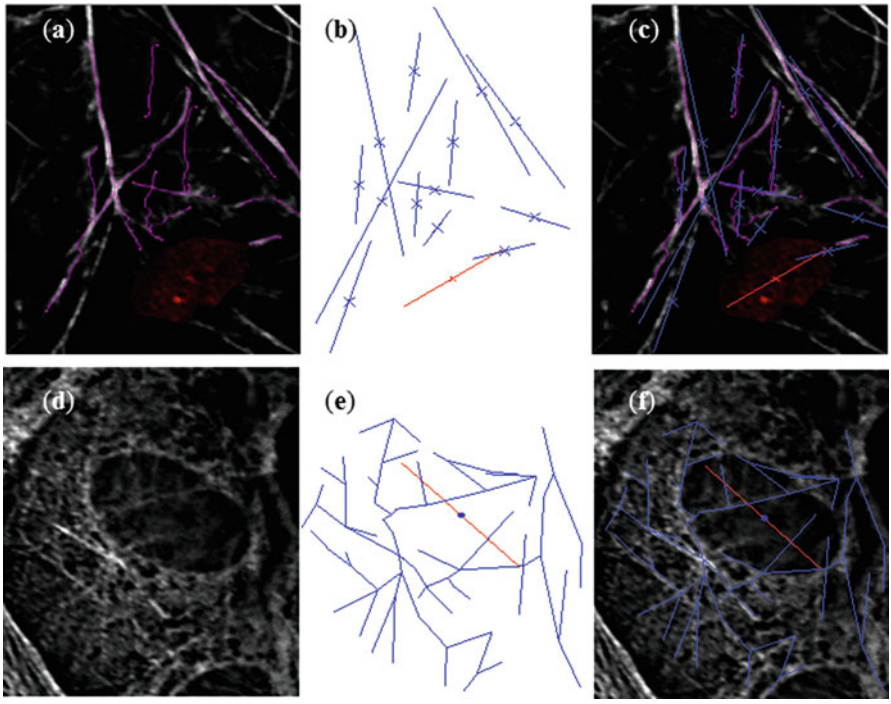

Fig. 5 Actin filament (**a–c**) and microtubule (**d–f**) morphology in a specific cell can be regenerated directly from its spatial descriptors. (**a**) F-actin (*pink*) and nucleus (*red*) in a HMEC-1. (**b**) Actin filament network recreated from spatial descriptors described in Fig. 1. Consisting of actin filaments (*blue*), nucleus axis (*red*) and filament centroids (*blue crosses*). (**c**) Overlap of the original image with the recreated geometry. While the recreated filaments are straighter than they appear in the original image, there is a close resemblance between the two. (**d**) Image slice of acetylated α-tubulin in a HMEC-1. The nucleus position is evident, as microtubules form a cage structure around it. (**e**) The geometry of the microtubule network (in 2D), recreated from spatial descriptors described in Fig. 2. The nucleus axis is shown in *red*, with the microtubules in *blue*. (**f**) Overlap of the original image with the recreated geometry. Similarly, recreated microtubules are straighter than the original image, and only the larger, thicker microtubules are detected

of the cilia relative to the nucleus centroid is shown in Fig. 6b. There does not appear to be a directional pattern in cilia location.

3.4 Generating Virtual Cell Components

To illustrate the ability to generate virtual cell components using our method, three 2D models of a single cell composed of a nucleus, cilium and cytoskeleton were created (see Fig. 7). These have a cytoskeletal network and primary cilium typical of the overall population of ECs.

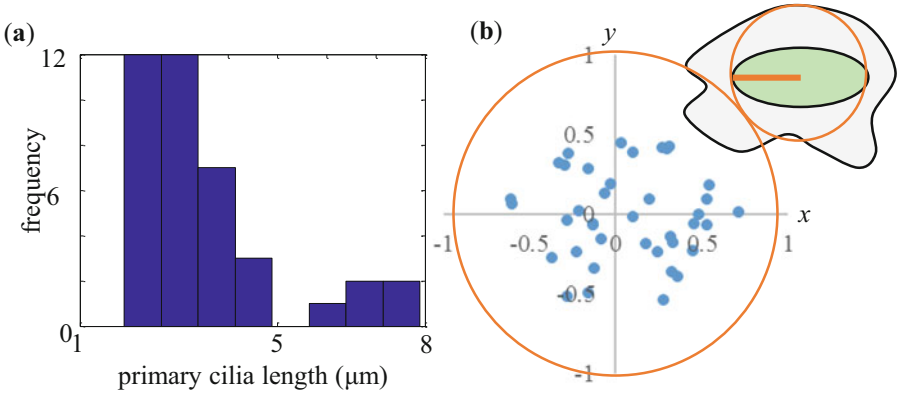

Fig. 6 Spatial descriptors of the primary cilium. (**a**) The histogram of primary cilium length ($n = 39$). The median ± interquartile range of primary cilium length was 3.0 μm ± 1.0 μm. (**b**) A scatter plot of the *xy* position of the base of the cilia with respect to the nucleus centroid, (units are normalised by nucleus length of each individual cell). *Orange circle* indicates a half nucleus length away from nucleus centroid. *Inset:* cartoon of cell giving context to the orange circle. The base of the cilium is generally very close to the nucleus centroid, with the majority within half a nucleus length (of that specific cell). There does not appear to be a predominant direction, with respect to the nucleus axis

These virtual models are at a preliminary stage. Further extension is needed to examine the co-dependency of spatial descriptors. For instance, the nucleus position and tubulin network are likely to be co-dependent, as the tubulin forms a cage around the nucleus. As this dependency is not measured in our current analysis, the virtual cells shown in Fig. 7 have a cage like tubulin network that is independent of nucleus position. Other less obvious co-dependencies may exist, and are best tested for using a regression analysis. Further extension is also required to generate 3D models.

4 Discussion and Conclusions

In this paper, we have quantified the morphological variation of the EC cytoskeleton and primary cilium using newly developed spatial descriptors. Our findings are in close agreement with a number of earlier studies: We found that actin occupies a planar layer in the cell (15–18% of the total cell height), which is in close agreement with Galbraith et al. finding of 20% (Fig. 7, from [5]). We also agree with the findings of Chiu et al. [3] that actin stress fibres tend to localise at the periphery of the cells. Our estimates for number of microtubules (median of 38) and collinearity (median of 3°, with the majority of values within 30°) is within the range of the findings of Li et al. [23] for a number of different cancer cell lines.

We found that centrosomes do not have to appear to have a directional bias in static cells (they are equally likely to occur at any angle around the nucleus centroid

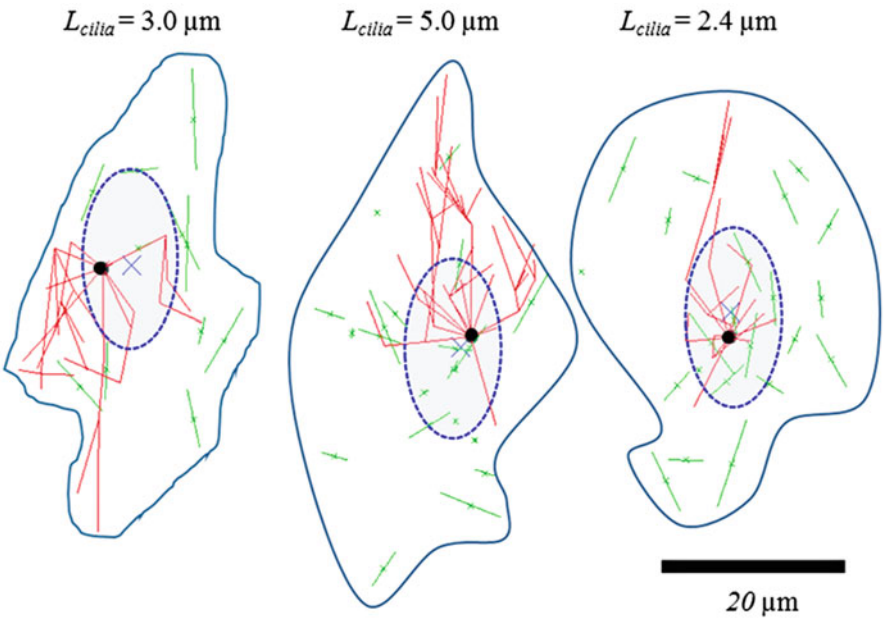

Fig. 7 Virtual cells generated using morphological descriptors, containing: actin stress fibres (*green lines*, with crosses at the centroid position); the microtubule network (in *red*), emerging from the centrosome (*black circle*) and the primary cilium (length, indicated, emerging from the centrosome). An idealised nucleus was also added (*blue dashed oval*), with length and width of the average nucleus calculated in [14]. Furthermore, the cells are enclosed by a cell membrane based on the smallest shape that can enclose the subcellular components

with respect to the nucleus centroid). Furthermore, we found that centrosomes occur near the nucleus centroid. Both these findings are in agreement with the qualitative findings of Galbraith et al. (Fig. 1a, $t = 0$; [5]). Furthermore, the base of the primary cilium is closely associated with centrosomes [24]: we also found a lack of preferential direction of the base of the cilia with respect to the nucleus centroid and nucleus axis. This is in agreement with Galbraith et al.'s finding that the centrosomes in static cells are distributed evenly upstream and downstream of the cell centroid (Fig. 1b, $t = 0$; [24]). Our estimated HMEC-1 primary cilium length of 3.0 μm is within the reported range of primary cilia lengths in other EC types [25–27].

Our spatial descriptor analysis is an improvement over existing descriptors because it can represent the geometry of a particular cell (Fig. 5) with sufficient accuracy to allow mechanical modelling: the most sophisticated cytoskeletonised EC models to date only represent the larger elements of the cytoskeleton as straight elements ($n < 50$) [12, 28], which our approach captures. Furthermore, our approach allows the creation of virtual cytoskeletonised cells that are characteristic of the entire population. Although at a preliminary stage, it is hoped that this virtual cell approach will reduce the computational cost of analysing the mechanics of an entire cell population.

We are in the process of developing a tensegrity-based mechanical cell model using the morphological data of the cytoskeleton obtained in this study. Our model consists of custom geometrically non-linear truss elements based on those developed by Crisfield [29, 30], modified to incorporate a prestress. A load controlled Newton–Raphson method is used to solve the static analysis of this model [31]. This modelling framework is suitable for modelling a cytoskeleton. Furthermore, we will use this model together with force-relaxation/force-minimisation methods [32–34] to determine force equilibrium. Forces acting on the membrane can be calculated using existing continuum methods [14] and mapped on to the nearest nodes in the pseudo-tensegrity model. It is anticipated that preliminary results of our model will be presented at the conference.

Acknowledgments HMEC-1s were kindly provided by Dr. Edwin Ades, Mr. Francisco J. Candal (CDC, Atlanta GA, USA) and Dr. Thomas Lawley (Emory University, Atlanta, GA, USA) NCEZID-R147589-00 [35]. The authors would also like to acknowledge Dr. Sue McGlashan, Ms. Hilary Holloway and Ms. Jacqui Ross from the Biomedical Imaging Research Unit, University of Auckland for assistance in microscope training and image acquisition. This work was supported by a University of Auckland Faculty Research Development Fund grant (3702516, D.S.L.). The first author is grateful for financial support from the University of Kassel.

References

1. Davies PF, Polacek DC, Shi C, Helmke BP (2002) The convergence of haemodynamics, genomics, and endothelial structure in studies of the focal origin of atherosclerosis. Biorheology 39(3):299–306
2. Davies PF (2009) Hemodynamic shear stress and the endothelium in cardiovascular pathophysiology. Nat Clin Pract Cardiovasc Med 6(1):16–26
3. Chiu J, Wang DL, Chien S, Skalak R, Usami S (1998) Effects of disturbed flow on endothelial cells. J Biomech Eng 120(1):2–8
4. Davies PF, Remuzzi A, Gordon EJ, Dewey CF, Gimbrone MA (1986) Turbulent fluid shear stress induces vascular endothelial cell turnover in vitro. Proc Natl Acad Sci U S A 83(7):2114–2117. doi:10.1073/pnas.83.7.2114
5. Galbraith CG, Skalak R, Chien S (1998) Shear stress induces spatial reorganization of the endothelial cell cytoskeleton. Cell Motil Cytoskeleton 40(4):317–330
6. Helmlinger G, Geiger RV, Schreck S, Nerem RM (1991) Effects of pulsatile flow on cultured vascular endothelial cell morphology. J Biomech Eng 113(2):123–131
7. Levesque MJ, Sprague EA, Schwartz CJ, Nerem RM (1989) The influence of shear stress on cultured vascular endothelial cells: the stress response of an anchorage-dependent mammalian cell. Biotechnol Prog 5(1):1–8
8. Nerem RM, Levesque MJ, Cornhill JF (1981) Vascular endothelial morphology as an indicator of the pattern of blood flow. J Biomech Eng 103(3):172–176
9. Rouleau L, Farcas M, Tardif J, Mongrain R, Leask RL (2010) Endothelial cell morphologic response to asymmetric stenosis hemodynamics: effects of spatial wall shear stress gradients. J Biomech Eng 132(8):081013–081013
10. Chien S (2007) Mechanotransduction and endothelial cell homeostasis: the wisdom of the cell. Am J Physiol Heart Circ Physiol 292(3):H1209–H1224

11. Ferko M, Bhatnagar A, Garcia M, Butler PJ (2007) Finite-element stress analysis of a multicomponent model of sheared and focally-adhered endothelial cells. Ann Biomed Eng 35(2):208–223
12. Dabagh M, Jalali P, Butler PJ, Tarbell JM (2014) Shear-induced force transmission in a multicomponent, multicell model of the endothelium. J R Soc Interface 11(98):20140431
13. Lim YC, Cooling MT, Long DS (2014) Computational models of the primary cilium and endothelial mechanotransmission. Biomech Model Mechanobiol 14:665–678
14. Lim YC, McGlashan S, Cooling MT, Long DS (2016) Mechanical models of endothelial mechanotransmission based on a population of cells. In: Joldes GR, Doyle B, Wittek A, PMF N, Miller K (eds) Computational biomechanics for medicine. Springer, New York
15. Chen TJ, Wu CC, Su FC (2012) Mechanical models of the cellular cytoskeletal network for the analysis of intracellular mechanical properties and force distributions: a review. Med Eng Phys 34(10):1375–1386
16. Lim YC, McGlashan S, Cooling MT, Long DS (2015) Culture and detection of primary cilia in endothelial cell models. Cilia 4(1):11
17. Buck TE, Li J, Rohde GK, Murphy RF (2012) Toward the virtual cell: automated approaches to building models of subcellular organization "learned" from microscopy images. BioEssays 34(9):791–799
18. Peng T, Murphy RF (2011) Image-derived, three-dimensional generative models of cellular organization. Cytometry A 79(5):383–391
19. Zhao T, Murphy RF (2007) Automated learning of generative models for subcellular location: building blocks for systems biology. Cytometry A 71(12):978–990
20. Dougherty R (2005) Extensions of DAMAS and benefits and limitations of deconvolution in beamforming. Am Inst Aeronaut Astronaut. doi:10.2514/6.2005-2961
21. Longair MH, Baker DA, Armstrong JD (2011) Simple neurite tracer: open source software for reconstruction, visualization and analysis of neuronal processes. Bioinformatics 27(17): 2453–2454
22. Shariff A, Murphy RF, Rohde GK (2011) Automated estimation of microtubule model parameters from 3-D live cell microscopy images. In: Anonymous biomedical imaging: from nano to macro, 2011 IEEE international symposium on, p. 1330
23. Li J, Shariff A, Wiking M, Lundberg E, Rohde GK, Murphy RF (2012) Estimating microtubule distributions from 2D immunofluorescence microscopy images reveals differences among human cultured cell lines. PLoS One 7(11):e50292
24. Hagiwara H, Ohwada N, Aoki T et al (2008) The primary cilia of secretory cells in the human oviduct mucosa. Med Mol Morphol 41(4):193–198
25. Iomini C, Tejada K, Mo W et al (2004) Primary cilia of human endothelial cells disassemble under laminar shear stress. J Cell Biol 164(6):811–817
26. Van der Heiden K, Groenendijk BCW, Hierck BP, Krams R, de Com R, Cheng C, Baiker M, Pourquie MJBM, Alkemade FE, deRuiter MC, Gittenberger-de Groot AC, Poelmann RE (2006) Monocilia on chicken embryonic endocardium in low shear stress areas. Dev Dyn 235(1):19–28
27. Geerts WJC, Vocking K, Schoonen N, Haarbosch L, van Donselaar EG, Regan-Klapisz E, Post JA (2011) Cobblestone HUVECs: a human model system for studying primary ciliogenesis. J Struct Biol 176(3):350–359
28. Khayyeri H, Barreto S, Lacroix D (2015) Primary cilia mechanics affects cell mechanosensation: a computational study. J Theor Biol 379:38–46
29. Crisfield MA (1991) Non-linear finite element analysis of solids and structures volume 1: essentials. Wiley, New York
30. Crisfield MA (1997) Non-linear finite element analysis of solids and structures volume 2: advanced topics. Wiley, New York
31. Zienkiewicz OC, Taylor RL (2000) The finite element method: the basis. Butterworth-Heinemann, Oxford
32. Bel Hadj Ali N, Rhode-Barbarigos L, Smith IFC (2011) Analysis of clustered tensegrity structures using a modified dynamic relaxation algorithm. Int J Solids Struct 48(5):637–647

33. Estrada GG, Bungartz H-J, Mohrdieck C (2006) Numerical form-finding of tensegrity structures. Int J Solids Struct 43(22–23):6855–6868
34. Paul C, Lipson H, Cuevas FJV (2005) Evolutionary form-finding of tensegrity structures. In: GECCO '05 Proceedings of the 7th annual conference on Genetic and evolutionary computation on, pp. 3–10
35. Ades EW, Candal FJ, Swerlick RA, George VG, Summers S, Bosse DC, Lawley TJ (1992) HMEC-1: establishment of an immortalized human microvascular endothelial cell line. J Investig Dermatol 99(6):683–690

Available Computational Techniques to Model Atherosclerotic Plaque Progression Implementing a Multi-Level Approach

Antonis I. Sakellarios, Georgia Karanasiou, Panagiotis Siogkas, Vasiliki Kigka, Themis Exarchos, George Rigas, Lampros K. Michalis, and Dimitrios I. Fotiadis

1 Introduction

Cardiovascular disease, and more specifically atherosclerosis, is considered as one of the most common causes of death in western societies. Atherosclerosis development initiates under the effect of several conditions such as the hemodynamics environment or the rapid accumulation of lipids and their oxidation. Nevertheless, atherosclerosis is characterized as an inflammatory disease which starts after the oxidation of low density lipoproteins (LDL) into the arterial wall and the migration of monocytes and macrophages at the lesion site [1]. Blood flow and especially low endothelial shear stress (ESS) and recirculations may cause injuries in the arterial wall [2]. These regions are usually located near bifurcations, curves, and branches. It has been shown that ESS affects in different ways the endothelial function altering the local gene expression and/or the permeability to molecules [2]. This affects endothelial permeability to LDL molecules and increases LDL accumulation in the arterial wall [3]. In high risk patients, an invasive treatment is followed, such as arterial bypass or Percutaneous Coronary Intervention. In coronary artery bypass grafting (CABG), arterial or vein conduits (grafts) are used to bypass the occluded arterial region. Stenting is a combination of angioplasty and stent implantation,

A.I. Sakellarios • G. Karanasiou • P. Siogkas • V. Kigka • T. Exarchos
G. Rigas • D.I. Fotiadis (✉)
Unit of Medical Technology and Intelligent Information Systems, Department of Materials Science and Engineering, University of Ioannina, Ioannina, Greece

A.I. Sakellarios • G. Karanasiou • P. Siogkas • V. Kigka • T. Exarchos • G. Rigas • D.I. Fotiadis
Department of Biomedical Research, Institute of Molecular Biology and Biotechnology – FORTH, University Campus of Ioannina, Ioannina, Greece
e-mail: fotiadis@cc.uoi.gr

L.K. Michalis
Department of Cardiology, Medical School, University of Ioannina, Ioannina, Greece

A. Wittek et al. (eds.), *Computational Biomechanics for Medicine*,
DOI 10.1007/978-3-319-54481-6_4

where the tubular wire mesh is positioned in the stenosed arterial region, inflated and permanently left in order to prevent arterial recoil and restenosis. The evolution of stents has resulted in improved clinical outcomes, however, there are still some issues that should be taken into consideration, such as the induced local arterial injury, the possibility of in-stent restenosis (ISR), as well as the risk for stent thrombosis (ST) [4].

Image processing algorithms and methodologies have been implemented for the accurate reconstruction of arteries and computational models have been employed utilizing the reconstructed arterial segments or trees. In the next sections a multi-level modeling approach is presented (Fig. 1). More specifically, the first level regards the arterial reconstruction using the available invasive and non-invasive vascular imaging modalities such as intravascular ultrasound, angiography, computed tomography, and magnetic resonance imaging. The second level is the modeling of blood flow and the estimation of ESS at the reconstructed arteries. The third level is the modeling of LDL and other molecules and cells in the arterial lumen

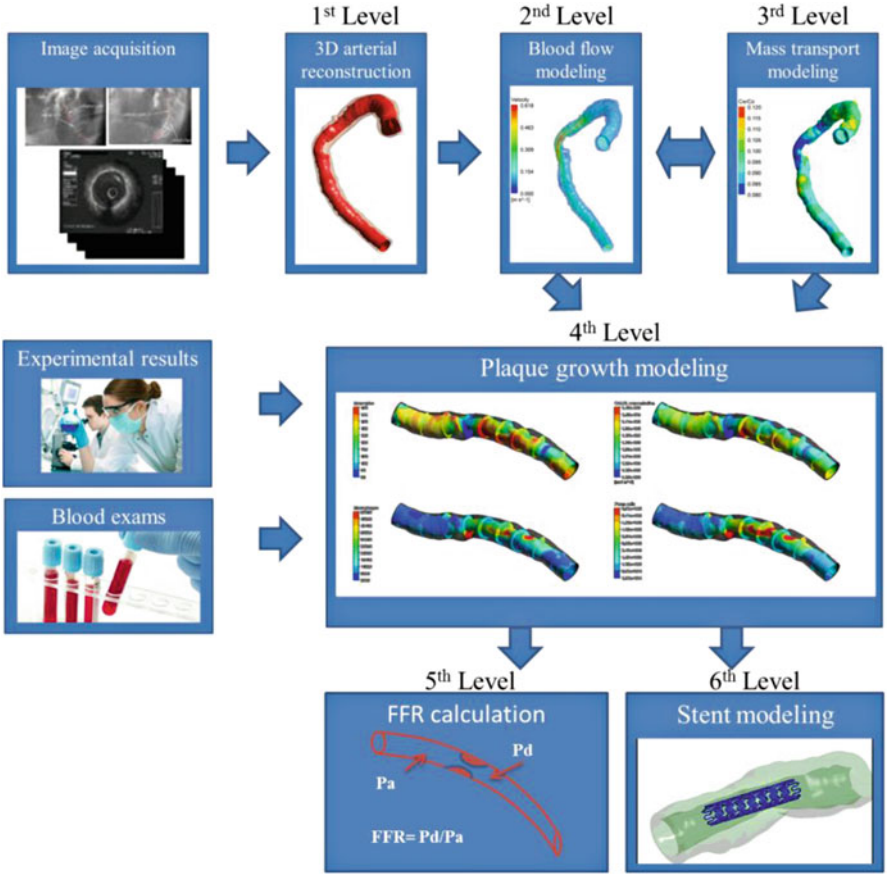

Fig. 1 Multi-level modeling approach of atherosclerotic plaque development

and their accumulation into the arterial wall. In the fourth level, plaque growth is modeled utilizing the results of the previous levels to model the inflammation in the arterial wall and the formation of foam cells. Data from experimental and animal studies have been used for the calculation of the parameters which are applied in the computational models. The fifth level consists of an innovative approach of FFR calculation, while in the sixth level, our stent deployment modeling approach, we studied the performance of the Leader Plus stent type expansion inside a patient specific coronary arterial segment focusing on the arterial stresses in the contact region with the stent.

2 Multi-Level Modeling of Atherosclerosis

2.1 Level 1: 3D Arterial Reconstruction Using Medical Images

The prerequisite of the modeling approaches which employ the finite element method is the use of geometries which represent the physical domain. Accurate modeling of biomechanical systems requires realistic description of the system geometry. Similarly, modeling approaches in atherosclerosis require an accurate representation of the arterial segments or arterial trees. The arteries were reconstructed utilizing various imaging modalities, e.g., intravascular ultrasound (IVUS), angiography, MRI, computed coronary tomography angiography (CCTA). In the following sections, the methodologies for 3D reconstruction of arteries based on the fusion of IVUS and angiography, CT, and MRI are presented.

3D Coronary Artery Reconstruction Using IVUS and Angiography

Coronary artery reconstruction was performed based on the fusion of bi-plane angiography and IVUS data [5]. Briefly, two orthogonal views of angiography are acquired and the catheter path is found. Using the orthogonal views, a 3D catheter path is generated. Active contours are implemented for the automate segmentation of IVUS frames and the detection of the lumen and media-adventitia borders. In the next step, the detected borders are placed perpendicularly onto the 3D catheter path after appropriate absolute orientation of the IVUS frames onto the path. The outcome of this process was two point clouds that represent the luminal and media-adventitia wall geometry.

3D Artery Reconstruction Using MRI

MRI imaging can be used for the imaging and consequently the reconstruction of arteries. Auer et al. introduced an active contour algorithm for the segmentation

of high-resolution MRI and then proposed a methodology that uses statistical information to characterize the plaque components [6]. Adame et al. [7] combined a model-based segmentation algorithm and fuzzy clustering in order to detect the vessel wall, lumen, and lipid core borders. An interesting study was performed by Hofman et al. who used Bayesian, K-Nearest neighbor, feed-forward neural networks, and a combination of Bayes classifier with the Parzen to characterize the type of the plaque in the carotid arteries [8]. Finally, Liu et al. [9] presented a Bayesian approach which used the pixel's intensity, the wall thickness, and the distance from the lumen to characterize plaque composition.

Our methodology includes four main steps [10]: (i) image acquisition and pre-processing of T1-Weighted, and Time-of-Flight (TOF) and T2-Weighted images, (ii) luminal border detection, (iii) outer vessel wall detection, and (iv) characterization of the composition of the plaque (hemorrhages, calcium, lipid cores, and fibrotic plaques). Active contours theory is implemented for lumen and outer vessel wall border detection in TOF and T1-Weighted images, respectively. Moreover, identification of the bifurcation is achieved using the theory of connecting components, while the different plaque types are classified into hemorrhages, calcium, lipid cores, and fibrotic plaques based on a knowledge-based algorithm. Validation of the proposed methodology was made using two experts' annotations (inter-observer variability for the lumen was -1.60 ± 6.70 and for the outer vessel wall was $0.56 \pm 6.28\%$) [10]. Plaque type is also accurately characterized after a validation in 591 images [10].

3D Artery Reconstruction Using CT

Several studies have demonstrated that CCTA provides an accurate analysis of coronary artery remodeling and is able to detect and quantify atherosclerotic plaque [11, 12]. Furthermore, different studies have proved the ability of CCTA to assess plaque burden and classify plaque composition [13]. Voros et al. [14] attempted to validate three-dimensional, quantitative measurements of coronary plaque by CCTA using IVUS. In a similar manner, Graaf et al. [15] correlated the metrics calculated using a fully automated CCTA methodology with those derived by VH-IVUS. Another study for the quantification of coronary arterial stenoses using CCTA was presented by Arbab et al. [16]. This approach indicated that CCTA in comparison with the conventional angiography is able to identify non-invasively patients with coronary artery disease. Recently, Athanasiou et al. [17] presented an innovative three-dimensional reconstruction methodology of coronary arteries and their plaque morphology, using CCTA images.

Our approach includes seven stages (Fig. 2). In the first stage the CCTA images are pre-processed using the Frangi Vesselness filter [18], which identifies tubular structures and limits the region of interest (ROI) to vessel candidate regions. In the second stage, a centerline extraction methodology is applied, using a minimum cost

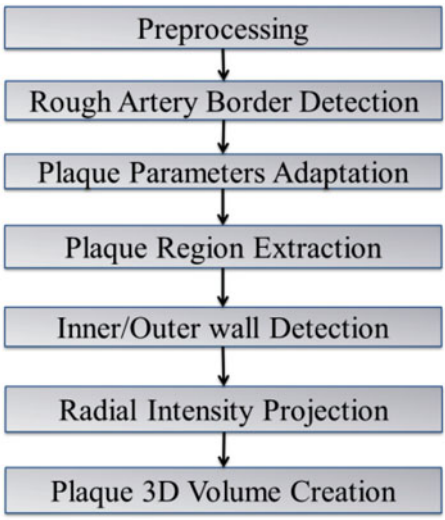

Fig. 2 The seven stages of the proposed artery reconstruction using CCTA

path approach [19]. In the third stage a weight function for lumen, outer wall, and calcified plaque is estimated, based on a membership function of Hounsfield Units (HU) values and the distance from the centerline. This function aims to compensate different protocols for discriminating lumen, outer wall, and calcified plaque. In the fourth stage, an extension of active contour models [20] for lumen segmentation is implemented. In the fifth stage, similar to the previous stage, a level set approach for outer wall segmentation is implemented. This approach uses as a prior shape for the outer wall the previously segmented lumen. In the sixth stage, a level set method is applied for plaque segmentation, taking into consideration calcium objects of significant size. Finally, in the seventh stage the 3D surfaces for the lumen, outer wall, and the calcified plaques are constructed.

2.2 Level 2: Blood Flow Modeling

Hemodynamics and especially, shear stress, found to play a considerable role in the development of atherosclerotic plaques [2]. Blood flow is modeled using the Navier–Stokes equations. The solution of the Navier–Stokes equations requires appropriate boundary conditions and in the case of the transient simulation initial conditions are also needed. We assume that the blood flow is laminar and incompressible. In addition the blood is considered to be Newtonian or non-Newtonian. The arterial wall is assumed to be rigid and non-deformable. The inflow boundary condition is defined by a constant velocity profile or a constant mass flow rate while at the outlet of the arterial segment we define a constant average pressure

profile. Finally, at the fixed walls all velocity components are set to be zero (no-slip boundary condition). In the case of transient flow the inflow is defined by the volumetric blood flow rate or a time dependent velocity profile. The flow rate is specified by a waveform, while three cardiac cycles are required as a general rule for accurate solution of pulsatile simulations. Blood flow modeling has been performed in several studies using mainly the finite element method [21–24]. Papafaklis et al. [25] studied the hemodynamics in coronary arteries bifurcation and investigated the influence of ESS to arterial wall thickening.

The ESS calculation is associated with the arterial geometry especially for regions of increased stenosis [26]. The presence of stenosis has a dramatic effect on the local ESS distribution, while tachycardia had a pronounced impact on ESS in the region of a stenosis with 3–5.7 fold decrease in time-averaged values during one cardiac cycle, compared to the normal heart rate profile [26]. ESS is also correlated with neointima formation after stent implantation [27]. In particular, in patients with bare metal stents (BMS) a negative association was noted between ESS and neointima burden ($p = 0.002$) as well as between ESS and the percentage of the neointimal necrotic core component ($p = 0.015$). In patients with biolimus eluting stents (BES), the suppression of neointimal formation did not allow evaluation of the effect of ESS on its tissue characteristics. Thus, ESS determines not only the amount but also the composition of the neointima in BMS. In the PROSPECT-CT study it was found that CCTA-derived variables had a moderate accuracy in detecting lesions that are likely to progress at follow-up [28]. Performing simulations at 17 bifurcations of the PROSPECT-CT database [29], we found that the Murray's law [30] provides the best accuracy to predict disease progression and also that the use of the side branch in the calculations of ESS is necessary for accurate results. More specifically, low ESS is an independent predictor of lumen reduction and necrotic core increase.

2.3 Level 3: LDL Transport Modeling

The third level is the modeling of LDL transport and its accumulation in the arterial wall. The same principles apply for the HDL transport as well as other cells transport such as monocytes. The rationale is that LDL is transferred in the arterial lumen not only by the blood flow (convection) but also by diffusion due to the concentration difference. Furthermore, LDL/HDL molecules penetrate the endothelial membrane and accumulate into the arterial wall. In order to model macromolecular transport in arteries the convection-diffusion equation is employed.

Prosi et al. [31] have classified mass transfer models into three major categories: (a) the wall-free models, (b) the lumen-wall models, and (c) the multi-layer models. In wall-free models the arterial wall is non-permeable and the wall thickness is not taken into account. Hong et al. [32] presented a numerical simulation of pulsatile flow and macromolecular transport in complex blood vessels. The arterial wall was assumed rigid and the low density lipoprotein (LDL) molecule was too large to penetrate the arterial wall. The lumen-wall models are a more realistic approach since the transport within the lumen is coupled with that in the arterial wall. In these models, the arterial wall is simplified as a homogeneous porous monolayer. Sun et al. [33] and Olgac et al. [34] investigated the influence of the ESS on the arterial mass transport by modeling the blood flow and the solute transport in the lumen and the arterial wall. The most realistic models are the multilayer models, in which the arterial wall consists of more than one layers. Mass transport is made in each layer and interaction between these layers exists. Prosi et al. [31] introduced several mathematical models, based on partial differential equations, to study the coupled transport of macromolecules in the blood stream and in the arterial wall.

We have implemented two LDL transport models. The first one has been proposed by Sun et al. [35]. The second approach enhances the effect of LDL accumulation in the luminal side assuming that endothelial permeability increases when the local luminal LDL concentration is high [26]. Finally, another approach has also been developed which describes a permeability model based on the local endothelial dysfunction caused by the expression of nitric oxide [36]. Results of these studies are summarized below. The endothelial permeability is modeled assuming that the endothelium is a semi-permeable biological membrane. The Kedem–Katchalsky equations [37] are employed. The permeability term of these equations is of utmost importance and several experiments and studies attempted to define it [38]. However, pathological conditions such as hypertension or diabetes could increase endothelial permeability. Besides the constant endothelial permeability model, a variable permeability model which depends on the local luminal LDL concentration [39] has been developed.

Regarding the LDL transport modeling, we showed in one coronary artery that hypertension and tachycardia affect LDL accumulation [26]. The model of endothelial permeability which is based on the local LDL concentration showed that the clinical impact of LDL in real life is simulated more accurately with this model. LDL transport modeling was implemented in large arterial datasets in order to show LDL's effect to plaque growth using baseline and retrospective imaging data. The results show that there is a correlation of high LDL accumulation with plaque growth and especially with plaque burden increase. This finding is observed first in 58 coronary arteries acquired from the PROSPECT database [40]. It was also shown using a dataset of 12 carotid arteries where for the first time MRI examinations from three time points are used [41]. However, the accuracy to predict regions of plaque growth is similar with low ESS leading us to use more sophisticated LDL transport models, as the one based on the local luminal LDL concentration or the proposed endothelial dysfunction model which is based on the production of nitric oxide.

2.4 Level 4: Plaque Growth Modeling

The fourth level of multi-level modeling of atherosclerotic plaque growth is the modeling of the major mechanisms which underlie the initiation and the formation of plaque into the arterial wall. The first two studies were presented by Filipovic et al. [42] and Parodi et al. [43]. Another plaque growth model was presented by Cilla et al. [44]. It was applied in an artificial axisymmetric geometrical coronary artery model. The results though it was not implemented into realistic arteries show that the presented model can simulate the atheromatic plaque growth despite the use of an artificial geometry.

In this level, we first model the oxidation of LDL. It is the first time that such a model for the atheroprotective effect of HDL in the oxidation of LDL has been presented. Thus, experimental data are used to develop a novel LDL oxidation model [45]. In the next step, the effect of cytokines, the transport of monocytes and their differentiation to macrophages, and finally the absorption of oxidized LDL by them to form the foam cells are simulated [46]. The computational model has been implemented in proof-of-concept studies of animal or human data recruited during the ARTREAT project or using data from the databases of PROSPECT and IBIS studies. The first version of the model includes only the modeling of the LDL oxidation. More specifically, we assume that LDL is oxidized when it gets inside the arterial wall. However, this mechanism is affected by the existence of local concentration of HDL which plays an atheroprotective role to plaque development. The proposed model was based on experimental studies. The model was implemented in an arterial segment using pig data [47] and the results have shown that the calculated oxidized concentration of LDL correlates well with the lipid plaque components found in histological images. In the most complex form of the plaque growth model, we model monocytes migration but also their differentiation to macrophages into the arterial wall to finally estimate the formation of foam cells. This model has been implemented in human arteries (coronaries and carotids). In both cases the major conclusion is that advanced modeling of plaque growth is necessary to increase the accuracy to predict the regions which are prone for disease progression. More specifically, in the carotid artery we found that the oxidized LDL and macrophages are correlated with lumen reduction and thickness change, while the prediction accuracy of using all calculated variables in a multivariate model increases against of using only the low ESS as a predictor of disease progression [48]. In a recent proof-of-concept case we demonstrated a validation scenario of plaque growth modeling using follow-up virtual histology IVUS and optical coherence tomography data from a human coronary arterial segment. In this case the prediction accuracy is over 75% when using all variables [46]. The overall multi-level approach results are shown in Fig. 3.

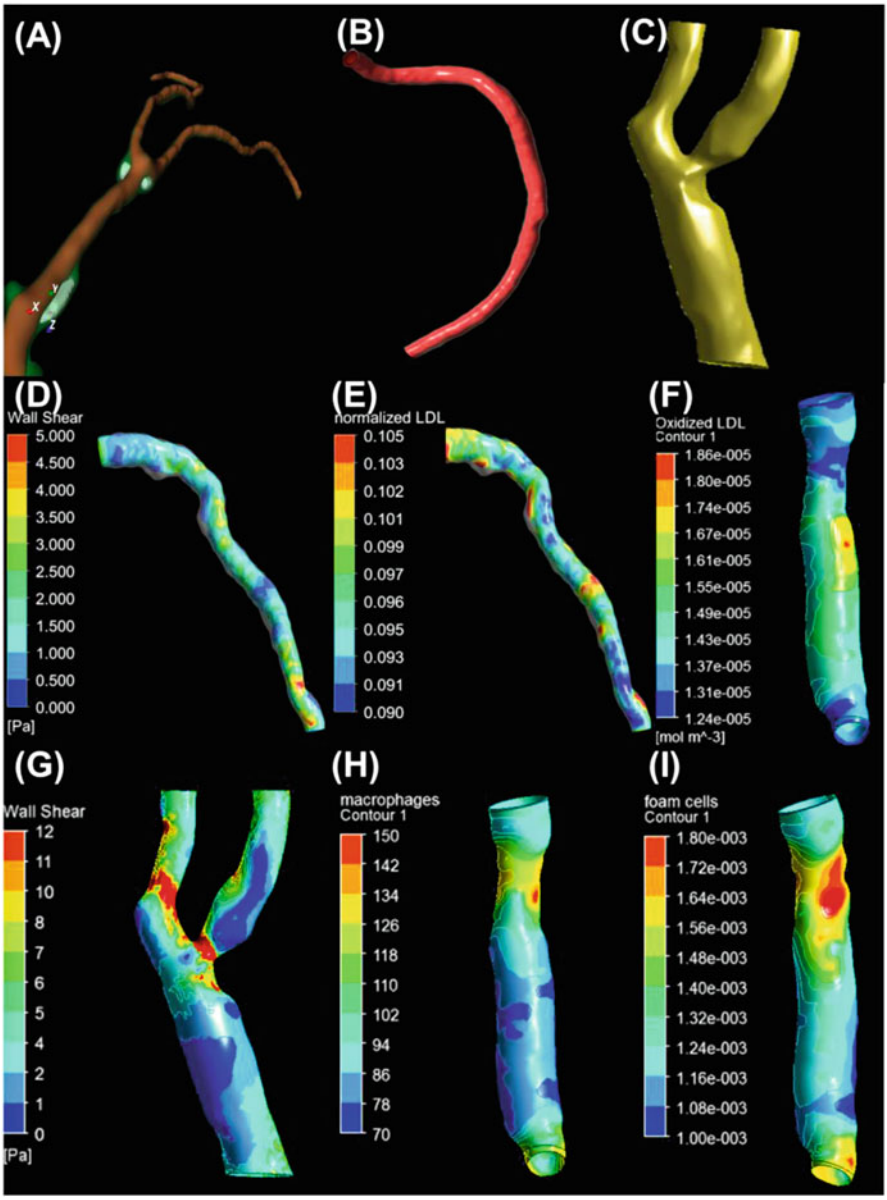

Fig. 3 Multi-level rationale of plaque growth modeling. (**A**–**C**) 3D reconstruction of coronary and carotid arteries, (**D**, **G**) ESS distribution coronary and carotid artery, (**E**) LDL accumulation in the arterial wall in the LDL transport modeling level, and (**F**, **H**, **I**) oxidized LDL, macrophages, and foam cells accumulation in the arterial wall in plaque growth modeling level

2.5 Level 5: Computational Prediction of FFR

Fractional Flow Reserve (FFR) is considered the gold standard in every day clinical practice for the evaluation of the severity of coronary lesions. However, it requires the use of a dedicated pressure-flow wire, thus increasing the total cost of the whole examination, as well as the discomfort of the patient. In order to tackle this issue, several approaches have been reported in literature that combine non-invasive imaging techniques (CCTA) and the use of computational fluid dynamics to provide an estimation of the invasively measured FFR [49, 50]. Virtual functional assessment index (vFAI) has been proposed as an accurate and valid equivalent to the invasively measured FFR, allowing the evaluation of the hemodynamic status of an existing coronary lesion in short time. Our method utilizes three-dimensional (3D) anatomical data from the coronary vasculature and performs blood flow modeling to calculate the ratio of pressures distal and proximal over the lesion for flows ranging from 0 to 4 mL/s, normalized by the same ratio for a totally healthy artery, offering an insight in CAD hemodynamic significance that is numerically equal to the invasively measured FFR. In coronary angiography derived 3D models, close correlation ($r = 0.78$, $p < 0.0001$) and agreement of vFAI compared to wire-FFR (mean difference: -0.0039 ± 0.085, $p = 0.59$) was found [51]. Diagnostic accuracy, sensitivity, and specificity for the optimal vFAI cut-point (≤ 0.82) were 88%, 90%, and 86%, respectively. Regarding CCTA derived 3D models, very good correlation ($r = 0.88$, $p < 0.001$) and strong agreement between vFAI and invasively measured FFR (mean difference: -0.0039 ± 0.04) were also found [52]. The respective diagnostic accuracy, sensitivity, and specificity for the optimal vFAI cut-point (≤ 0.84) were 91.7%, 75%, and 96.4%. Finally, in hybrid IVUS-angiography 3D models, a modest correlation ($r = 0.84$, $p = 0.073$) was found [53].

2.6 Level 6: Stent Modeling

Computational simulations might be an effective tool for investigating the mechanical performance of stents and evaluating the arterial implications such as in stent restenosis coming from different stent designs and materials, a process that cannot be fully assessed in experimental studies [54]. Towards this direction, several research teams have provided valuable information, either by performing computational simulations of stent deployment inside idealized arteries, or even utilizing patient specific imaging data for the reconstruction of arterial segments [55, 56].

The unexpanded configuration of the 3D finite element model consisted of one 3D reconstructed coronary arterial segment and the Leader Plus stent geometry (Fig. 4). The mesh was created with 3D higher order ten node elements. The mesh sensitivity was implemented with a convergence criterion of the maximum von Mises stresses being within 5%. Stent deployment was performed following a

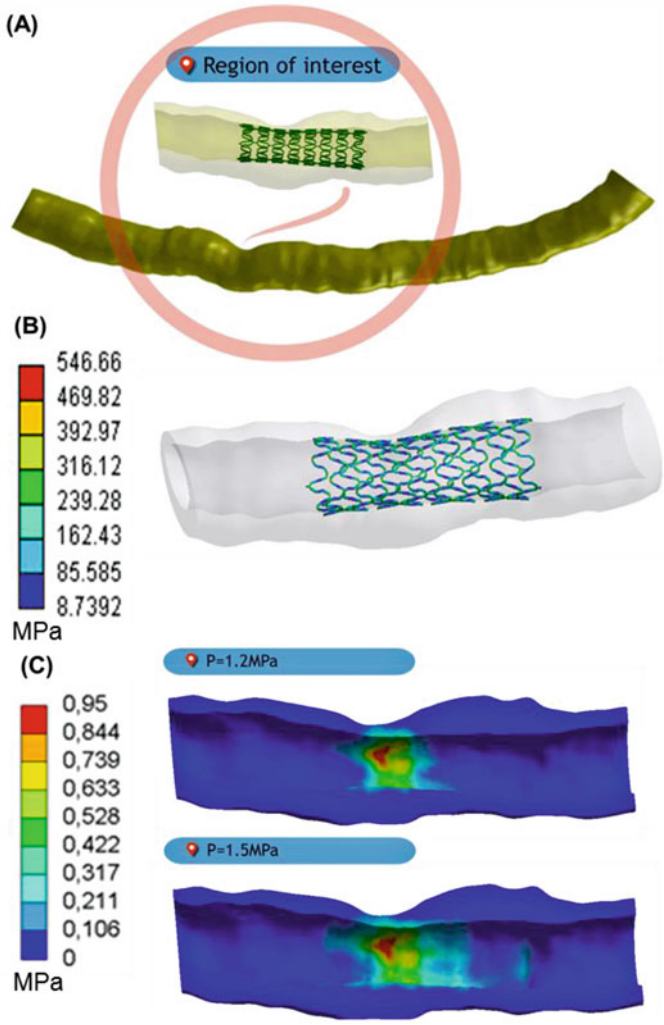

Fig. 4 (**a**) The reconstructed artery and the LeaderPlus stent. (**b**) Von Mises stress distribution in the deformed Leader Plus Stent. (**c**) Von Mises stress at the arterial wall (MPa) during stent expansion for the applied pressure of 1.2 MPa and 1.5 MPa

pressure driven approach through the application of a pressure directly to the inner stent surface. To represent the performance of the human tissue, several material models can be utilized. In our model, the artery was assumed homogeneous with nonlinear behavior. A polynomial form of the Mooney–Rivlin hyperelastic material model was used for the arterial wall [57], with the strain energy density function based on Maurel et al. [58], whereas a bilinear elasto-plastic material model was employed for the stent. The stent was initially placed in the arterial stenosis region.

The ends of the artery were not allowed to move or rotate, appropriate boundary conditions allowed the movement in the axial and radial directions of the stent, whereas stent inflation was enabled by a pressure of 1.5 MPa. Stent expansion was achieved under uniform pressure, however, due to the asymmetry of the stenosed arterial region, stent struts deformed non-uniformly (Fig. 4). The investigation of the stent response is of great importance since high stent stresses can result in stent fracture and consequently in arterial injury. High stresses, approximately 550 MPa, were observed in the stent connectors. During stent deployment, the von Mises stresses were increasing (Fig. 4) and high von Mises stresses occurred in the arterial-stent surface.

3 Discussion and Conclusions

A methodological approach for the computational modeling of the major mechanisms of atherosclerotic plaque development has been presented in this work. Until recently 3D reconstruction and blood flow were only utilized to estimate disease progression. In the current work we propose a multi-level modeling scheme consisting of the 3D reconstruction level, the blood flow modeling and ESS estimation level, the LDL transport modeling level, the plaque growth modeling level but also the stent deployment modeling. Regarding the level of blood flow modeling, first, we prove the effect of geometry and existed stenosis to ESS distribution as well as the effect of tachycardia and hypertension. Second, we associate ESS with disease progression utilizing the CT imaging modality and for the first time we prove that CT imaging can accurately be used for the calculation of ESS and disease progression. Third, for the first time we present an analysis of ESS and neointima formation in arterial segments with deployed stent. Going beyond the state of the art in LDL transport modeling we presented several novel models for endothelial permeability as well as different analyses of the effect of LDL concentration at plaque progression. More specifically, we developed a model of endothelial permeability and LDL transport which is based on the local concentration of LDL concentration. The developed model has been applied to different datasets of arteries demonstrating the ability to predict regions which are prone for plaque growth.

The major innovation is the development of plaque growth computational models. This work starts with the development of an LDL oxidation model. The proposed LDL oxidation model is based not only on the LDL accumulation in the arterial wall, but also on the HDL concentration which has an atheroprotective role on disease progression. The last part is the development of a plaque growth model which simulates the major mechanisms of the atherosclerotic plaque growth process. These mechanisms beside the LDL oxidation are the migration of monocytes into the arterial wall under the effect of cytokines expression and their consequent transformation to macrophages. The appearance of macrophages into the arterial wall with the existence of oxidized LDL leads to the formation of foam cells.

In this model we included all these mechanisms. We applied the proposed model in several cases (one carotid artery and three coronary arteries) and the comparison of the simulation results with the retrospective follow-up data prove that our model is highly promising for a new kind of thinking in the field of atherosclerotic plaque development. More specifically, until now low ESS is considered as a predictor of disease progression without, however, accurate results. Complex modeling of plaque growth increases the accuracy of disease prediction.

Acknowledgements This work is partially funded by the European Commission (Project SMARTOOL, GA number: 689068, H2020).

References

1. Libby P, Ridker PM, Hansson GK (2011) Progress and challenges in translating the biology of atherosclerosis. Nature 473(7347):317–325
2. Chatzizisis YS, Coskun AU, Jonas M, Edelman ER, Feldman CL, Stone PH (2007) Role of endothelial shear stress in the natural history of coronary atherosclerosis and vascular remodeling – molecular, cellular, and vascular behavior. J Am Coll Cardiol 49(25):2379–2393
3. Chien S (2003) Molecular and mechanical bases of focal lipid accumulation in arterial wall. Prog Biophys Mol Biol 83(2):131–151
4. Surdell D, Shaibani A, Bendok B, Eskandari MK (2007) Fracture of a nitinol carotid artery stent that caused restenosis. J Vasc Interv Radiol 18(10):1297–1299
5. Bourantas CV, Kalatzis FG, Papafaklis MI, Fotiadis DI, Tweddel AC, Kourtis IC, Katsouras CS, Michalis LK (2008) ANGIOCARE: an automated system for fast three-dimensional coronary reconstruction by integrating angiographic and intracoronary ultrasound data. Catheter Cardiovasc Interv 72(2):166–175
6. Auer M, Stollberger R, Regitnig P, Ebner F, Holzapfel GA (2006) 3-D reconstruction of tissue components for atherosclerotic human arteries using ex vivo high-resolution MRI. IEEE Trans Med Imaging 25(3):345–357
7. Adame IM, van der Geest RJ, Wasserman BA, Mohamed MA, Reiber JH, Lelieveldt BP (2004) Automatic segmentation and plaque characterization in atherosclerotic carotid artery MR images. MAGMA 16(5):227–234
8. Hofman JM, Branderhorst WJ, ten Eikelder HM, Cappendijk VC, Heeneman S, Kooi ME, Hilbers PA, ter Haar Romeny BM (2006) Quantification of atherosclerotic plaque components using in vivo MRI and supervised classifiers. Magn Reson Med 55(4):790–799
9. Liu F, Xu D, Ferguson MS, Chu B, Saam T, Takaya N, Hatsukami TS, Yuan C, Kerwin WS (2006) Automated in vivo segmentation of carotid plaque MRI with morphology-enhanced probability maps. Magn Reson Med 55(3):659–668
10. Sakellarios AI, Stefanou K, Siogkas P, Tsakanikas VD, Bourantas CV, Athanasiou L, Exarchos TP, Fotiou E, Naka KK, Papafaklis MI, Patterson AJ, Young VE, Gillard JH, Michalis LK, Fotiadis DI (2012) Novel methodology for 3D reconstruction of carotid arteries and plaque characterization based upon magnetic resonance imaging carotid angiography data. Magn Reson Imaging 30(8):1068–1082
11. Papadopoulou S-L, Neefjes LA, Schaap M, Li H-L, Capuano E, van der Giessen AG, Schuurbiers JCH, Gijsen FJH, Dharampal AS, Nieman K, van Geuns RJ, Mollet NR, de Feyter PJ (2011) Detection and quantification of coronary atherosclerotic plaque by 64-slice multidetector CT: a systematic head-to-head comparison with intravascular ultrasound. Atherosclerosis 219(1):163–170

12. Divakaran S, Cheezum M, Hulten E, Bittencourt M, Silverman M, Nasir K, Blankstein R (2015) Use of cardiac CT and calcium scoring for detecting coronary plaque: implications on prognosis and patient management. Br J Radiol 88(1046):20140594
13. Saremi F, Achenbach S (2015) Coronary plaque characterization using CT. Am J Roentgenol 204(3):W249–W260
14. Voros S, Rinehart S, Qian Z, Vazquez G, Anderson H, Murrieta L, Wilmer C, Carlson H, Taylor K, Ballard W (2011) Prospective validation of standardized, 3-dimensional, quantitative coronary computed tomographic plaque measurements using radiofrequency backscatter intravascular ultrasound as reference standard in intermediate coronary arterial lesions: results from the ATLANTA (assessment of tissue characteristics, lesion morphology, and hemodynamics by angiography with fractional flow reserve, intravascular ultrasound and virtual histology, and noninvasive computed tomography in atherosclerotic plaques) I study. J Am Coll Cardiol Intv 4(2):198–208
15. de Graaf MA, Broersen A, Kitslaar PH, Roos CJ, Dijkstra J, Lelieveldt BP, Jukema JW, Schalij MJ, Delgado V, Bax JJ (2013) Automatic quantification and characterization of coronary atherosclerosis with computed tomography coronary angiography: cross-correlation with intravascular ultrasound virtual histology. Int J Card Imaging 29(5):1177–1190
16. Arbab-Zadeh A, Hoe J (2011) Quantification of coronary arterial stenoses by multidetector CT angiography in comparison with conventional angiography methods, caveats, and implications. J Am Coll Cardiol Img 4(2):191–202
17. Athanasiou L, Rigas G, Sakellarios AI, Exarchos TP, Siogkas PK, Bourantas CV, Garcia-Garcia HM, Lemos PA, Falcao BA, Michalis LK (2016) Three-dimensional reconstruction of coronary arteries and plaque morphology using CT angiography–comparison and registration with IVUS. BMC Med Imaging 16(1):1
18. Frangi AF, Niessen WJ, Vincken KL, Viergever MA (1998) Multiscale vessel enhancement filtering. In: Wells WM, Colchester A, Delp S (eds) Medical image computing and computer-assisted intervention — MICCAI'98: first international conference Cambridge, MA, USA, October 11–13, 1998 proceedings. Springer, Berlin Heidelberg, pp 130–137. doi:10.1007/BFb0056195
19. Metz C, Schaap M, Weustink A, Mollet N, van Walsum T, Niessen W (2009) Coronary centerline extraction from CT coronary angiography images using a minimum cost path approach. Med Phys 36(12):5568–5579
20. Chan TF, Vese LA (2001) Active contours without edges. IEEE Trans Image Process 10(2):266–277
21. Taylor CA, Steinman DA (2010) Image-based modeling of blood flow and Vessel Wall dynamics: applications, methods and future directions. Ann Biomed Eng 38(3):1188–1203
22. Saad Y, Schultz MH (1986) Gmres – a generalized minimal residual algorithm for solving nonsymmetric linear-systems. SIAM J Sci Stat Comput 7(3):856–869
23. Perktold K, Hofer M, Rappitsch G, Loew M, Kuban BD, Friedman MH (1998) Validated computation of physiologic flow in a realistic coronary artery branch. J Biomech 31(3):217–228
24. Steinman DA, Thomas JB, Ladak HM, Milner JS, Rutt BK, Spence JD (2002) Reconstruction of carotid bifurcation hemodynamics and wall thickness using computational fluid dynamics and MRI. Magn Reson Med 47(1):149–159
25. Papafaklis MI, Vergallo R, Jia HB, Bourantas C, Yonetsu T, Lakkas L, McNulty I, Kotsia A, Lee H, Antoniadis A, Yu B, Naka KK, Fotiadis DI, Feldman C, Michalis L, Jang IK, Stone P (2013) Longitudinal distribution of endothelial shear stress along culprit lesions and association with plaque characteristics in patients with acute coronary syndromes: a three-dimensional frequency-domain optical coherence tomography study. J Am Coll Cardiol 62(18):B198–B198
26. Sakellarios AI, Papafaklis MI, Siogkas P, Athanasiou LS, Exarchos TP, Stefanou K, Bourantas CV, Naka KK, Michalis LK, Parodi O, Fotiadis DI (2013) Patient-specific computational modeling of subendothelial LDL accumulation in a stenosed right coronary artery: effect of hemodynamic and biological factors. Am J Physiol Heart C 304(11):H1455–H1470

27. Bourantas CV, Raber L, Zaugg S, Sakellarios A, Taniwaki M, Heg D, Moschovitis A, Radu M, Papafaklis MI, Kalatzis F, Naka KK, Fotiadis DI, Michalis LK, Serruys PW, Garcia Garcia HM, Windecker S (2015) Impact of local endothelial shear stress on neointima and plaque following stent implantation in patients with ST-elevation myocardial infarction: a subgroup-analysis of the COMFORTABLE AMI-IBIS 4 trial. Int J Cardiol 186:178–185
28. Bourantas CV, Papadopoulou SL, Serruys PW, Sakellarios A, Kitslaar PH, Bizopoulos P, Girasis C, Zhang YJ, de Vries T, Boersma E, Papafaklis MI, Naka KK, Fotiadis DI, Stone GW, Reiber JH, Michalis LK, de Feyter PJ, Garcia-Garcia HM (2015) Noninvasive prediction of atherosclerotic progression: the PROSPECT-MSCT study. JACC Cardiovasc Imaging 9(8):1009–1011
29. Papadopoulou SL, Neefjes LA, Garcia-Garcia HM, Flu WJ, Rossi A, Dharampal AS, Kitslaar PH, Mollet NR, Veldhof S, Nieman K, Stone GW, Serruys PW, Krestin GP, de Feyter PJ (2012) Natural history of coronary atherosclerosis by multislice computed tomography. JACC Cardiovasc Imag 5(3):S28–S37
30. Murray CD (1926) The physiological principle of minimum work applied to the angle of branching of arteries. J Gen Physiol 9(6):835–841
31. Prosi M, Zunino P, Perktold K, Quarteroni A (2005) Mathematical and numerical models for transfer of low-density lipoproteins through the arterial walls: a new methodology for the model set up with applications to the study of disturbed lumenal flow. J Biomech 38(4):903–917
32. Hong J, Wei L, Fu C, Tan W (2008) Blood flow and macromolecular transport in complex blood vessels. Clin Biomech 23(Suppl 1):S125–S129
33. Sun N, Wood NB, Hughes AD, Thom SA, Xu XY (2006) Fluid-wall modelling of mass transfer in an axisymmetric stenosis: effects of shear-dependent transport properties. Ann Biomed Eng 34(7):1119–1128
34. Olgac U, Knight J, Poulikakos D, Saur SC, Alkadhi H, Desbiolles LM, Cattin PC, Kurtcuoglu V (2011) Computed high concentrations of low-density lipoprotein correlate with plaque locations in human coronary arteries. J Biomech 44(13):2466–2471
35. Sun N, Wood NB, Hughes AD, Thom SAM, Xu XY (2006) Fluid-wall modelling of mass transfer in an axisymmetric stenosis: effects of shear-dependent transport properties. Ann Biomed Eng 34(7):1119–1128
36. Sakellarios AI, Siogkas P, Exarchos T, Stefanou K, Bourantas CV, Athanasiou L, Fotiou E, Papafaklis M, Naka KK, Michalis LK, Fotiadis DI (2011) Modelling LDL accumulation in the case of endothelial dysfunction. J Serbian Soc Comput Mech 5(2):90–100
37. Kedem O, Katchalsky A (1958) Thermodynamic analysis of the permeability of biological membranes to non-electrolytes. Biochim Biophys Acta 27(2):229–246
38. Stangeby DK, Ethier CR (2002) Coupled computational analysis of arterial LDL transport – effects of hypertension. Comput Methods Biomech Biomed Engin 5(3):233–241
39. Guretzki HJ, Gerbitz KD, Olgemoller B, Schleicher E (1994) Atherogenic levels of low density lipoprotein alter the permeability and composition of the endothelial barrier. Atherosclerosis 107(1):15–24
40. Sakellarios A, Bourantas CV, Papadopoulou SL, Tsirka Z, de Vries T, Kitslaar PH, Girasis C, Naka KK, Fotiadis DI, Veldhof S, Stone GW, Reiber JH, Michalis LK, Serruys PW, de Feyter PJ, Garcia-Garcia HM (2016) Prediction of atherosclerotic disease progression using LDL transport modelling: a serial computed tomographic coronary angiographic study. Eur Heart J Cardiovasc Imaging 18(1):11–18. doi:10.1093/ehjci/jew035
41. Sakellarios AI, Bizopoulos P, Papafaklis MI, Athanasiou L, Exarchos T, Bourantas CV, Naka KK, Patterson AJ, Young VE, Gillard JH, Parodi O, Michalis LK, Fotiadis DI (2016) Natural history of carotid atherosclerosis in relation to the hemodynamic environment: a low-density lipoprotein transport modeling study with serial magnetic resonance imaging in humans. Angiology 68(2). doi:10.1177/0003319716644138
42. Filipovic N, Nikolic D, Saveljic I, Milosevic Z, Exarchos T, Pelosi G, Parodi O (2013) Computer simulation of three-dimensional plaque formation and progression in the coronary artery. Comput Fluids 88:826–833

43. Siogkas P, Sakellarios A, Exarchos TP, Athanasiou L, Karvounis E, Stefanou K, Fotiou E, Fotiadis DI, Naka KK, Michalis LK, Filipovic N, Parodi O (2011) Multiscale – patient-specific artery and atherogenesis models. IEEE T Biomed Eng 58(12):3464–3468
44. Cilla M, Pena E, Martinez MA (2014) Mathematical modelling of atheroma plaque formation and development in coronary arteries. J R Soc Interface 11(90):1–16
45. Kunitake ST, Jarvis MR, Hamilton RL, Kane JP (1992) Binding of transition-metals by apolipoprotein-a-I-containing plasma-lipoproteins-inhibition of oxidation of low-density lipoproteins. In: Proceedings of the National Academy of Sciences of the United States of America, 1992. pp 6993-6997
46. Sakellarios A, Raeber L, Bourantas C, Exarchos T, Athanasiou L, Pelosi G, Parodi O, Koskinas K, Naka K, Michalis L, Serruys PW, Garcia-Garcia H, Windecker S, Fotiadis D (2016) Prediction of atherosclerotic plaque development in an in vivo coronary arterial segment based on a multi-level modeling approach. IEEE Trans Biomed Eng. doi:10.1109/TBME.2016.2619489
47. Puccinelli E, Gervasi PG, Trivella MG, Vornoli A, Viglione F, Pelosi G, Parodi O, Sampietro T, Puntoni M (2015) Modulation of lipid homeostasis in response to continuous or intermittent high-fat diet in pigs. Animal 9(6):1000–1007
48. Sakellarios AI, Bizopoulos P, Stefanou K, Athanasiou LS, Papafaklis MI, Bourantas CV, Naka KK, Michalis LK, Fotiadis DI (2015) A proof-of-concept study for predicting the region of atherosclerotic plaque development based on plaque growth modeling in carotid arteries. Conf Proc IEEE Eng Med Biol Soc 2015:6552–6555
49. Koo BK, Erglis A, Doh JH, Daniels DV, Jegere S, Kim HS, Dunning A, DeFrance T, Lansky A, Leipsic J, Min JK (2011) Diagnosis of ischemia-causing coronary stenoses by noninvasive fractional flow reserve computed from coronary computed tomographic angiograms. Results from the prospective multicenter DISCOVER-FLOW (diagnosis of ischemia-causing stenoses obtained via noninvasive fractional flow reserve) study. J Am Coll Cardiol 58(19):1989–1997
50. Kruk M, Wardziak L, Demkow M, Pleban W, Pregowski J, Dzielinska Z, Witulski M, Witkowski A, Ruzyllo W, Kepka C (2016) Workstation-based calculation of CTA-based FFR for intermediate stenosis. JACC Cardiovasc Imaging 9(6):690–699
51. Papafaklis MI, Muramatsu T, Ishibashi Y, Lakkas LS, Nakatani S, Bourantas CV, Ligthart J, Onuma Y, Echavarria-Pinto M, Tsirka G, Kotsia A, Nikas DN, Mogabgab O, van Geuns RJ, Naka KK, Fotiadis DI, Brilakis ES, Garcia-Garcia HM, Escaned J, Zijlstra F, Michalis LK, Serruys PW (2014) Fast virtual functional assessment of intermediate coronary lesions using routine angiographic data and blood flow simulation in humans: comparison with pressure wire – fractional flow reserve. EuroIntervention 10(5):574–583
52. Siogkas PK, Anagnostopoulos CD, Exarchos TP, Liga R, Knuuti J, Scholte AJHA, Papafaklis MI, Parodi O, Michalis LK, Neglia D, Fotiadis DI (2016) Computational Hemodynamic Assessment of coronary lesions from Computed Tomography Angiography. A novel approach. In: ESC Congress 2016, Rome, Italy
53. Siogkas PK, Athanasiou LS, Sakellarios AI, Stefanou KA, Exarchos TP, Papafaklis MI, Naka KK, Parodi O, Michalis LK, Fotiadis DI (2015) Validation study of a 3D-QCA coronary reconstruction method using a hybrid intravascular ultrasound and angiography reconstruction method and patient-specific fractional flow reserve data. Conf Proc IEEE Eng Med Biol Soc 2015:973–976
54. Azaouzi M, Makradi A, Petit J, Belouettar S, Polit O (2013) On the numerical investigation of cardiovascular balloon-expandable stent using finite element method. Comput Mater Sci 79:326–335
55. Gervaso F, Capelli C, Petrini L, Lattanzio S, Di Virgilio L, Migliavacca F (2008) On the effects of different strategies in modelling balloon-expandable stenting by means of finite element method. J Biomech 41(6):1206–1212
56. Karanasiou GS, Sakellarios AI, Tripoliti EE, Petrakis EGM, Zervakis ME, Migliavacca F, Dubini G, Dordoni E, Michalis LK, Fotiadis DI (2013) Modeling of stent implantation in a human stenotic artery. In: LMR R (ed) XIII mediterranean conference on medical and biological engineering and computing, Seville, Spain, 2013. Springer International Publishing, Cham, pp 1045–1048

57. Lally C, Reid AJ, Prendergast PJ (2004) Elastic behavior of porcine coronary artery tissue under uniaxial and equibiaxial tension. Ann Biomed Eng 32(10):1355–1364
58. Maurel W (1998) Biomechanical models for soft tissue simulation. ESPRIT basic research series, vol 18155. Springer, Berlin, New York

Reduced Order Model of a Human Left and Right Ventricle Based on POD Method

Piotr Przybyła, Witold Stankiewicz, Marek Morzyński, Michał Nowak, Dominik Gaweł, Sebastian Stefaniak, and Marek Jemielity

1 Introduction

According to the World Health Organization, chronic diseases are responsible for 63% of all deaths in the world, with cardiovascular disease as the leading cause of death. Magnetic resonance imaging technologies have advanced rapidly in recent years enabling both radiologists and cardiologists to perform evaluated studies for assessment of the functional parameters of the heart, such as myocardial wall motion, volumetric parameters, ejection fraction, and stroke volume across both the left and right ventricles. In theory the term cardiomyopathy could apply to almost any disease affecting the heart, in practice it is usually reserved for severe myocardial disease leading to heart failure [1]. Clinical biomechanists are confronted with various challenges. One of them is the task of reducing the amount of data from clinical datasets [2, 3].

Recently computer methods and programs are being implemented throughout all aspects of biomedical research and medical practice. Many of them are concentrated on biomechanics of particular movement disorders, as in the case of hip joint dysplasia [4], Parkinson disease [5], or cardiac motion [6]. In the last case, to mark the deteriorations, clinical biomechanists record kinematic and electromyographic signals, which are both analyzed statistically and in terms of an explicit inverse dynamic model [7]. These analyses, on the other hand, may grant insight into proper relevant biomechanical aspects of particular movement disorders and, in some cases, elemental motor deteriorations. Nevertheless, magnetic resonance imaging brings

P. Przybyła • W. Stankiewicz (✉) • M. Morzyński • M. Nowak • D. Gaweł
Division of Virtual Engineering, Poznan University of Technology, Poznań, Poland
e-mail: witold.stankiewicz@put.poznan.pl

S. Stefaniak • M. Jemielity
Cardio-Surgery Department in Clinical Hospital of University of Medical Sciences Poznan, Poznań, Poland

A. Wittek et al. (eds.), *Computational Biomechanics for Medicine*,
DOI 10.1007/978-3-319-54481-6_5

a large amount of data which is difficult to elaborate and process. The design of the model of heart motion is difficult as the movement interweaves with several factors such as muscle contraction, blood flow, calcification, fiber orientation, and nerve impulses. Each of those aspects can be designed separately and is challenging as well. The example of computational model combining all the aforementioned factors is given in [8].

Another solution can be a "Black Box" model based on statistical analysis. An overview of these methods, combining different types of models over a global shape model and promising for other medical segmentation problems, especially if local anatomical abnormalities (e.g., a tumor) appear, is presented in [9].

In [10] clinical diagnosis is based upon global modes of motion, measurement of longitudinal displacement of the LV may be critical, and thus an increased emphasis on acquiring sufficient long axis image data may be warranted. They also suggest that methods sensitive to transmural differences in displacement may offer a clinical advantage for diagnosis of functional abnormality. Finally, the creation of a kinematic mode database can greatly increase reconstruction efficiency in healthy hearts by eliminating modes which contribute little to the reconstruction accuracy [11].

We can create a "black box model" based only on movement observation, which could be applied in, for example, flow control. Mathematical models for human ventricles contain large amounts of data. Their numerical solution is based on appropriate space/time discretizations which requires computational times that even utilizing state-of-the-art algorithmic solvers are far from being acceptable. A means to overcome this difficulty is to use reduced order models (ROMs) where the dimension of the ROM is, by at least one order of magnitude, smaller than the dimension of the full order model while still separating the effects of the essential dynamics of the underlying physiological processes. Suitable model order reduction techniques include balanced truncation (BT) [12], Proper Orthogonal Decomposition (POD) [13], and reduced basis methods (RBM) [14].

This paper is structured as follows. In Sect. 2 we describe the method of generating a model of left and right ventricle. In Sect. 3 we present Proper Orthogonal Decomposition. Decomposition of left and right ventricle and decomposition of left ventricles are presented in Sects. 4 and 5, respectively. Finally, discussion and conclusions are presented in Sect. 6.

2 Generation of a Patient-Specific Cardiac Model

Choosing an optimal medical image visualization method always raises many questions. With a choice between CT, ultrasonography, Spectral CT, and MRI, the Magnetic Resonance Imaging seems to be the most suitable—while CT slices are more dense, they are related with radiation.

Initial clinical data consists of a cine-MRI sequence of the cardiac cycle of an adult patient. Images are in short axis, covering both ventricles (ten slices; slice

thickness: 8 mm, temporal resolution: 25 frames). Images were made isotropic and contrast was enhanced by clamping the tails of the grey-level histogram. DICOM examinations were loaded into the program, in particular, dynamic information on a cardiac study is automatically extracted.

To build a patient-specific model of the heart from the DICOM data resulting from MRI, it is crucial to segment the different parts of the organ. That implies segmenting the left and right endocardia, as well as the epicardium.

In this paper, we demonstrate our methodology on commonly available datasets. They consist of left and right ventricle data by Toussaint et al. [7], and a set of left ventricle models from the Sunnybrook Cardiac Data, SCD [15]. In the first case, interactive surface generation using implicit functions was used. Segmentation is started on the first frame of the MRI cardiac sequence, corresponding to end diastole. Interactive segmentation is based on variational implicit surfaces [16], which consists of computing an implicit function whose zero-level set passes through defined control points (landmarks). In order to calibrate the physiological parameters of the model, segmentation operation is repeated throughout the entire cardiac sequence, in order to estimate—for instance—the blood pool volume. The semi-automatic process described above, in which the user empirically specifies landmarks and filters, is to ensure the visual compliance of the myocardium area in the MRI and the determined mask. Then, nonlinear image registration based on diffeomorphic demons is performed [17]. The resulting deformation fields are then used to propagate the myocardium mask throughout further frames of cardiac sequence. Finally, the dynamic mesh of the myocardium is obtained by performing successive isosurface extractions on the aforementioned binary masks.

3 Proper Orthogonal Decomposition

Modal decomposition is a powerful and popular tool in model reduction techniques [18] and biomechanics [13]. In the case of the empirical approach, where the modes are obtained from the analysis of measured data or simulation, a number of methods may be distinguished. The most popular of them, Proper Orthogonal Decomposition (POD) (also known as PCA—Principal Component Analysis) [19–21] is based on the eigenanalysis of the autocorrelation matrix computed for the input signal [22]. There are many variants of this method designed for certain purposes. For example, method of snapshots [23] is used when the number of snapshots is much smaller than the dimension of the single snapshot. Sparse PCA [24] finds modes that are sparse vectors, that facilitates further interpretation. Kernel PCA [25] is the extension of PCA using kernel functions for the mapping of input data onto higher-dimensional feature space and multilinear PCA [26] is based on the linear transformations of each dimensional separately.

Another decomposition methods used in biomechanics include Independent Component Analysis [27] and Linear Discriminant Analysis (LDA) [28].

In the case of global analysis of cyclic data, snapshot POD of Sirovich is the best approach. This method is based on the assumption that there is a correlation between sampled data and it decomposes the data into uncorrelated modes that are optimal for energy representation by construction.

In this method, the M snapshots v_i of size N (number of Degrees of Freedom) are centered using time-averaged solution u_0. Resulting M fluctuation vectors $v_i' = v_i - u_0$ form a matrix V'. POD modes used in model reduction are the eigenvectors u_i of standard eigenproblem $Cu_i = \lambda_i \cdot u_i$ of the autocorrelation matrix C. In snapshot POD, this matrix (of size $M \times M$) is defined as:

$$C = \frac{1}{M} V'^T V',$$

and the POD modes w_i are computed by the projection of eigenvectors u_i, related to eigenvalues λ_i of largest magnitude and representing mode amplitudes, onto a set of initial snapshots V:

$$w_i = \frac{Vu_i}{\|Vu_i\|}.$$

4 Proper Orthogonal Decomposition of Left and Right Ventricle

A set of meshes was created with the help of CardioViz [29, 30], containing the 85 frames of the cardiac cycle. Vertex positions at each time frame are assigned to the corresponding frame mesh. As the topology of the mesh does not change along the sequence, a single VTK object explaining the topology is given to all the frames. Scalar data are also associated with each time frame. Linear interpolation is used to map scalar information on the mesh object [7]. Proper orthogonal decomposition was implemented to one cardiac cycle. The cycle was decomposed to 85 modes, which should represent 100% energy of heart motion. The Table 1 presents individual and joint information transferred by modes. We note the first five modes only, by virtue of little percentage of information being transferred by further modes, assuming that they can be neglected. It can be seen that just the first three modes represent 99% of information concerning the cardiac cycle. Using this data we can judge, which modes seem to be the important.

The first three modes, multiplied by maximal and minimal values of coefficients and superimposed on the time-average geometry of the heart, are presented in Fig. 1. In order to strengthen the visual effect, the results are scaled twice. The first mode represents systole of both left and right ventricles, with no twist.

The twist and movement along long axis are described by the second and third POD modes (Figs. 2 and 3, respectively).

Table 1 Information transferred by modes

Mode number	Information transferred [%]	Information transferred (jointly) [%]
1	73.55	73.55
2	22.14	95.70
3	3.43	99.13
4	0.49	99.63
5	0.14	99.77

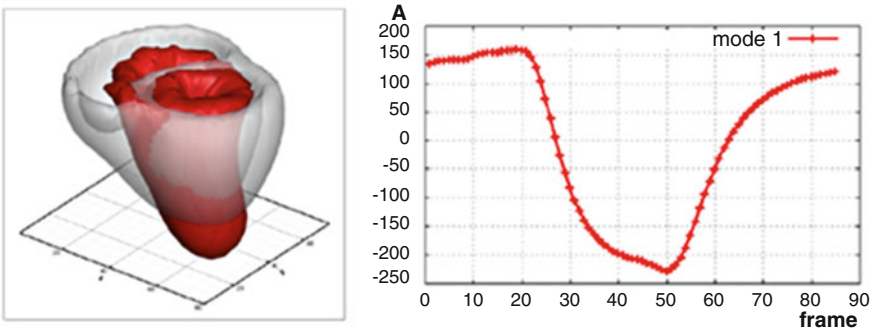

Fig. 1 The First POD mode superimposed on averaged geometry, depicted using doubled min. and max. values of corresponding time coefficient (dimensionless mode amplitude A)

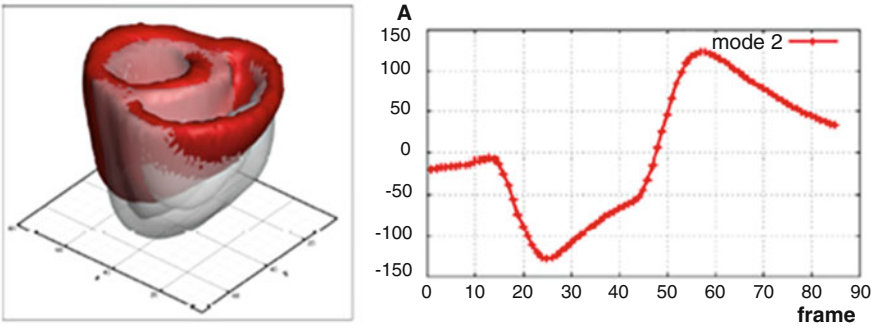

Fig. 2 Same as Fig. 1, but for the second POD mode

The figures above display slight discrepancy in amplitude at the beginning and end of the cycle. We assume that the reason for this is the absence of snapshots for one or two time steps. Diagrams of specific modes are distinctive to a factual, individual heart model [7], in this case left and right ventricle with no pathologies. Pathological ventricles will have differing, individual diagrams.

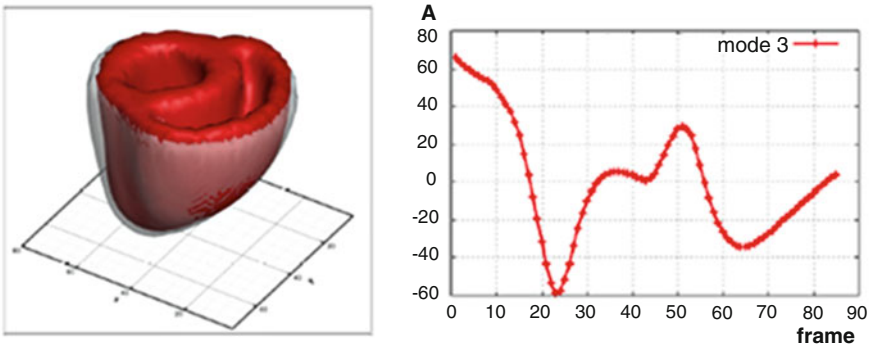

Fig. 3 Same as Fig. 1, but for the third POD mode

5 Proper Orthogonal Decomposition of Left Ventricles

Proper Orthogonal Decomposition was performed on models from The Sunnybrook Cardiac Data (SCD) [15], also known as the 2009 Cardiac MR Left Ventricle Segmentation Challenge data, consisting of models from a mixed groups of patients and pathologies. The data contributor is the Imaging Research, Sunnybrook Health Sciences Centre, Toronto, Canada. The subset of the data was first used for automated myocardium segmentation challenge from short-axis MRI, held by a MICCAI workshop in 2009. The data has already been registered [15]. The study description indicates the pathology. The patient datasets were classified into four groups representing diverse morphologies, based on the following clinical criteria [31]:

I. Heart failure with infarction (SC-HF-I) group had EF < 40% and evidence of late gadolinium (Gd) enhancement (12 patients)
II. Heart failure with no infarction (SC-HF-NI) group had EF < 40% and no late Gd enhancement (12 patients)
III. LV hypertrophy (SC-HYP) group (EF > 55%, 12 patients)
IV. Healthy (SC-N) group had EF > 55% and no hypertrophy (nine patients).

Three groups of patients (I, II, and IV) were chosen for further analysis of modal decomposition. The results were presented for the most exemplary of them.

5.1 Ventricle Models with Heart Failure with Infarction

Modal distribution of the same pathology seems to be comparable between different patients. Proportional information of mode I does not exceed 60%. As proportional information we understand the shared information of movement carried by mode. The same phenomena applies to mode II and III. Mode II holds on the level between

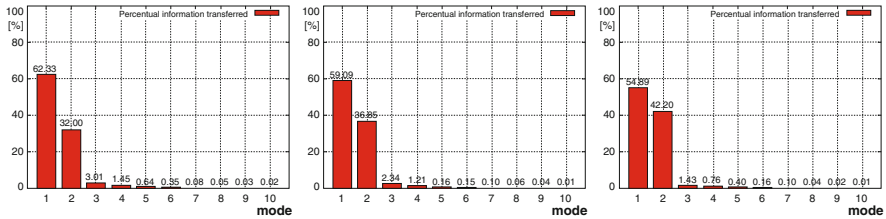

Fig. 4 Proportional information transferred by the modes. Three different patients with heart failure with infarction presented from left to right

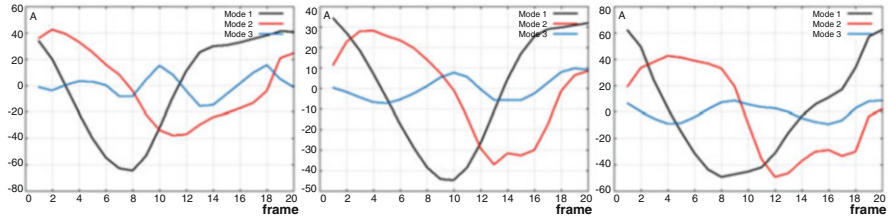

Fig. 5 Mode amplitudes A in time, for three different patients with heart failure with infarction

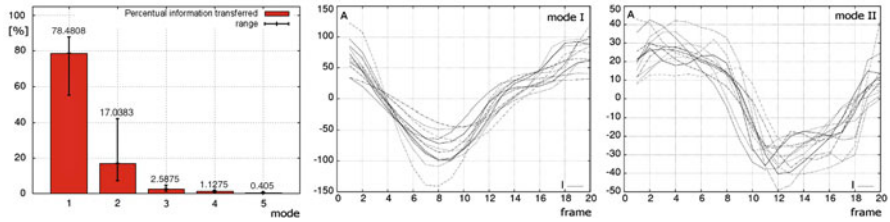

Fig. 6 Amplitude range overview through modal distributions of mode I, II, III for all test cases. Mode amplitudes A in time (frames of cycle), presented for every test case, mode I and mode II

30% and 42%, while mode III does not exceed 3%. Proportional distribution for three exemplary patients: men aged 48, 57, 69 is shown in Fig. 4.

Changes of amplitudes in time for the first three modes in Fig. 5 for exemplary patients are congenial. Transition of graphs appears almost simultaneously (mode I and III) showing little differences between mode II (patient II and III has similar progress; the curve of patient I is flattened at the beginning of the cycle).

Figure 6 displays the amplitudes of mode I and II in time for every test case of the presented group. Thorough analysis will require full medical history of every single patient, which was not provided in the data. However it is noticeable, that changes of amplitude are congenial.

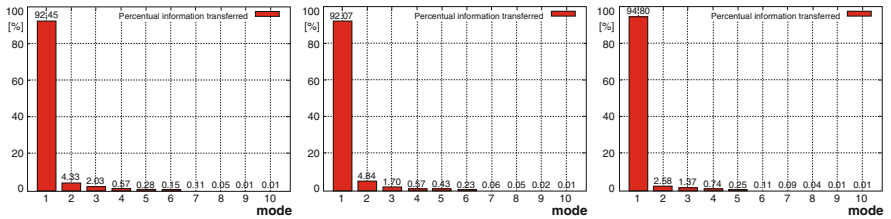

Fig. 7 Proportional information transferred by the modes. Three different patients with healthy hearts presented from left to right

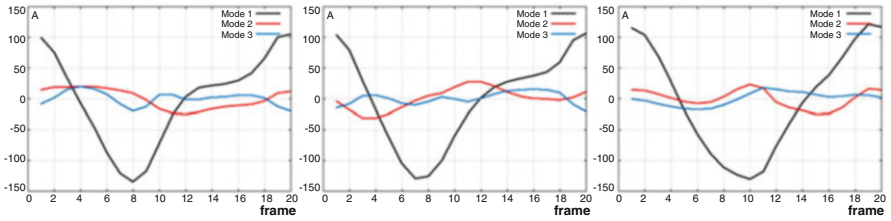

Fig. 8 Mode amplitudes A in time, presented for three different patients with healthy hearts

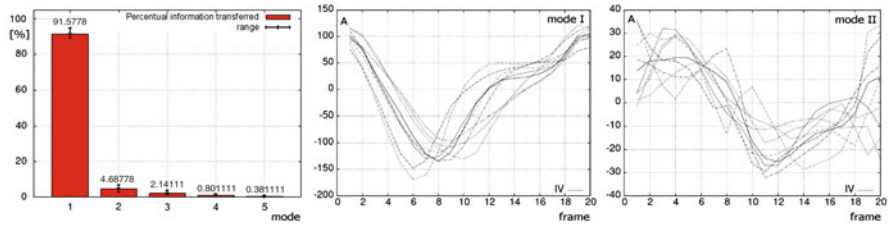

Fig. 9 Amplitude range overview through modal distributions of mode I, II, III for all test cases. Mode amplitudes A in time (frames of cycle), presented for every test case, mode I and mode II

5.2 Healthy (SC-N) Group, no Hypertrophy

Exemplary distributions of healthy patients: 63 aged male, 53 aged female, 77 aged female, is presented in Fig. 7. In this case, mode I substantially dominates in proportional information distribution. There is little influence of modes II and III. Similar phenomena appeared in the model of left and right ventricle in Sect. 4.

Range of amplitude in time for first three modes in Fig. 8 for healthy patients is almost identical, even though we compare patients from differing ages and gender. The averaged value of mode I from acquired dataset is 91.35%.

In Fig. 9 we have presented the amplitudes of mode I and II in time for every test case of the presented group. The shape of amplitudes is similar, and the tendency is maintained for every test case in both modes.

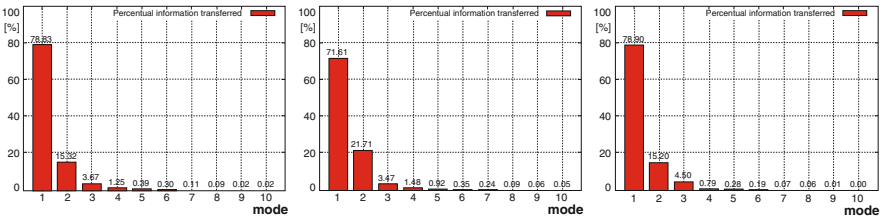

Fig. 10 Proportional information transferred by the modes. Three different patients with heart failure without infarction presented from left to right

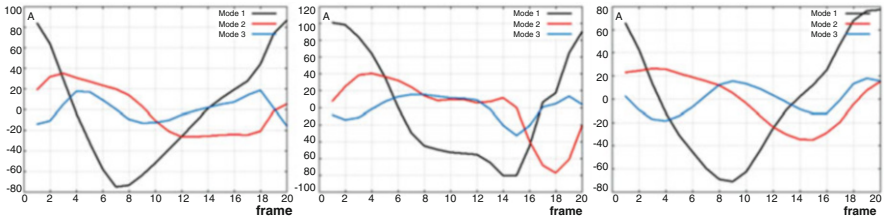

Fig. 11 Mode amplitudes A in time, presented for three different patients; heart without infarct

5.3 Heart Failure with no Infarction

The third group of patients analyzed in this paper were having heart failure without infarct. In these cases, achieved data indicates greater influence for mode II in pathological hearts than for healthy ones. However, it was still less than for patients with heart failure with infarct. Three exemplary test cases (77 aged male, 82 aged male, 77 aged female) are presented in Figs. 10 and 11.

Mode amplitude is fluctuating in mode II and III, while mode I is similar in all presented cases. Average value of mode I for patients with no infarction fluctuates between 70% and 80%, while mode II exceeds 15%, which is rather unique, and characteristic for this pathology.

In Fig. 12 we have presented the amplitudes of mode I and II in time for every test case of the presented group. It is notable, that amplitudes are similar to these presented in Sect. 5.1. As mentioned before, thorough analysis could be performed with closer information about patients pathology. However, general trend of amplitudes is maintained.

6 Discussion and Conclusions

This article concerns the analysis of the motion of the left and right ventricle, captured from MRI examination. We have proven that such a complex motion might be modeled with a few degrees of freedom—POD modes and their amplitudes.

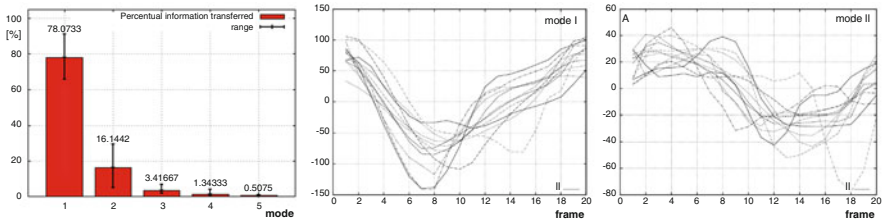

Fig. 12 Amplitude range overview through modal distributions of modes for all test cases. Mode amplitudes A in time (frames of cycle), presented for every test case, mode I and mode II

Modal decomposition gives more insight into the heart than 2D analysis of MRI slices. This approach is in line with the recent works. Principal Component Analysis has been already used to analyze the electrocardiogram signals for detection of heart arrhythmia [32], reduced order modeling [33], and automated diagnosis of cardiac health [34]. Recently, 4D models are used as an input. Wu et al. [35] use POD to analyze time-varying, three-dimensional data from ECG-gated multislice cardiac CT images of human right ventricle and classify pulmonary hypertension. They state that such approach might provide "new metrics to improve the diagnosis and understanding of cardiovascular diseases." Similar approach for cardiac MR and CT image sequences is used by Perperidis et al. [29].

In our study, already three modes allow to reproduce 99% of the original properties of the heart motion, to analyze it and compare to the real motion of systole and diastole. It will make possible the correlation of modal data (modes, amplitudes, and eigenvalues) with the corresponding pathologies. As the change in the cardiac cycle will be visible after the spatio-temporal decomposition as well, the designed model makes the proper diagnosis, preparation for invasive procedures and future treatment much easier, more cost effective and requiring less time.

The analyzed set is quite small, but preliminary conclusions may be drawn. It seems that the increased eigenvalue of second mode (related to higher amplitudes) might be correlated with the aforementioned heart failures. The order of the higher modes might vary for different subjects. The first modes always represent the contraction of the ventricles. The differentiation between failing and healthy hearts is done by comparing ratios of the first mode (failing below 89–91%) and second mode (failing above 5.1–6.7%), no matter what motion it describes. Unfortunately, myocardial infarction does not affect noticeably the modal amplitudes and eigenvalues. This case requires further study, performed on a larger patients group.

The POD analysis can show abnormalities which cannot be observed in live time diagnostics, before any dysfunction or symptoms arise. This would allow the prevention of changes in cardiac muscle by early diagnosis and treatment either pharmacologically or surgically. A major significance of this work is that we would be able to diagnose various hearts, including the prenatal heart. MRI examination is both suitable and safe for in utero scans of the fetal heart. As an example, let us consider the left ventricle ejection fraction. The normal value is more than 50%,

when it falls below, it is identified as left ventricle dysfunction. As we know from its movement we are able to "switch off or disregard" this specific part of the muscle and we will not receive any important information about the disease, because the LVEF will remain >50%. This could present in heart infarct, cardiomyopathy, dangerous heart infections, and other states. The use of POD can show that despite the normal ejection fraction, another underlying disease may be present. The cardiac movement preceding the heart conduction system has been known to have been misdiagnosed. The conductive system leads the impulse to start the systole from the apex to the bases. Conduction problems with the impulse may not been seen as a delay of diastole or systole within the muscle segment. The large more obvious issues are easily appreciated, however, the smaller more subtle issues are not easily perceived and unfortunately they often go unnoticed. The POD method is ideally suited for quick diagnosis of these types of abnormalities. Last but not least this is an excellent tool for the presentation and teaching of cardiac abnormalities, for both medical students and as a tool for Cardiac specialists.

An important limitation of the method is the need of registration of the data resulting from medical imaging. While there are software tools for such handling available, they still do not allow full automation. The quality of the data, like the resolution of MRI slices, is related to the above—it might influence the order of (further) modes, their shapes, and eigenvalues.

Acknowledgments This work was supported by The National Centre for Research and Development under the grant PBS3/B9/34/2015.

References

1. Baguet JP, Barone-Rochette G, Tamisier R, Levy P, Pépin JL (2012) Mechanisms of cardiac dysfunction in obstructive sleep apnea. Nat Rev Cardiol 9(12):679–688
2. Bouvy ML, Heerdink ER, Leufkens HGM, Hoes AW (2003) Predicting mortality in patients with heart failure: a pragmatic approach. Heart 89(6):605–609
3. Bassingthwaighte J, Hunter P, Noble D (2009) The cardiac Physiome: perspectives for the future. Exp Physiol 94(5):597–605
4. Rychlik M, Józwiak M, Idzior M, Chen PJ, Szulc A, Woźniak W (2010) Acetabular direction and capacity of hip joint dysplasia in cerebral palsy–counterpoint option of morphology understanding. In 6th World Congress of Biomechanics (pp. 1546–1549), Springer
5. Fasano A, Daniele A, Albanese A (2012) Treatment of motor and non-motor features of Parkinson's disease with deep brain stimulation. Lancet Neurol 11(5):429–442
6. Glass L, Hunter P, McCulloch A (eds) (2012) Theory of heart: biomechanics, biophysics, and nonlinear dynamics of cardiac function. Springer, New York
7. Toussaint N, Mansi T, Delingette H, Ayache N, Sermesant M (2008) An integrated platform for dynamic cardiac simulation and image processing: application to personalised tetralogy of fallot simulation. In: Eurographics Workshop on Visual Computing and Biomedicine. (pp.21–28).
8. Vazquez M, Arís R, Houzeaux G, Aubry R et al (2011) A massively parallel computational electrophysiology model of the heart. Int J Num Meth Biomed Eng 27(12):1911–1929

9. Heimann T, Meinzer HP (2009) Statistical shape models for 3D medical image segmentation: a review. Med Image Anal 13(4):543–563
10. O'Dell W, McVeigh ER (1998) A modal description of LV motion during ejection, In: Proceedings of the International Society for Magnetic Resonance in Medicine
11. Hoppe RHW (2002) Model reduction by proper orthogonal decomposition, NSF-I/UCRC 288 grant, University of Houston
12. Antoulas AC (2005) Approximation of large scale dynamical systems. Advances in design and control, vol 6. SIAM, Philadelphia
13. Rychlik M, Stankiewicz W, Morzyński M (2008) Application of modal analysis for extraction of geometrical features of biological objects set. Biodevices 2008(2):227–232
14. Fischer SL, Hampton RH, Albert WJ (2014) A simple approach to guide factor retention decisions when applying principal component analysis to biomechanical data. Comput Methods Biomech Biomed Engin 17(3):199–203
15. Radau P, Lu Y, Connelly K, Paul G, Dick AJ, Wright GA (2009) Evaluation framework for algorithms segmenting short axis cardiac MRI. MIDAS J 49. http://hdl.handle.net/10380/3070
16. Turk G, O'Brien JF (1999) Variational implicit surfaces. Tech. Rep. Georgia Institute of Technology, Georgia
17. Vercauteren T, Pennec X, Perchant A, Ayache N (2007) Non-parametric diffeomorphic image registration with the demons algorithm. In International Conference on Medical Image Computing and Computer-Assisted Intervention MICCAI (pp. 319–326).
18. Toussaint N, Sermesant M, Fillard P (2007) vtkinria3d: A VTK extension for spatiotemporal data synchronization, visualization and management. In: Proceedings of Workshop on Open Source and Open Data for MICCAI.
19. Daffertshofer A, Lamoth CJ, Meijer OG, Beek PJ (2004) PCA in studying coordination and variability: a tutorial. Clin Biomech 19(4):415–428
20. Lumley JL (1967) The structure of inhomogeneous turbulent flows. Atmospheric turbulence and radio wave propagation, pp 166–178
21. Chandrashekara R et al (2003) Construction of a statistical model for cardiac motion analysis using nonrigid image registration. Inf Process Med Imaging 18:599–610
22. Zhang X, Cowan BR, Bluemke DA, Finn JP, Fonseca CG et al (2014) Atlas-based quantification of cardiac remodeling due to myocardial infarction. PLoS One 9(10):e110243
23. Sirovich L (1987) Turbulence and the dynamics of coherent structures. Parts I–III. Q Appl Math 45(3):561–590
24. Zou H, Hastie T, Tibshirani R (2006) Sparse principal component analysis. J Comput Graph Stat 15(2):265–286
25. Hoffmann H (2007) Kernel PCA for novelty detection. Pattern Recogn 40(3):863–874
26. Lu H, Plataniotis KN, Venetsanopoulos AN (2008) MPCA: multilinear principal component analysis of tensor objects. IEEE Trans Neural Netw 19(1):18–39
27. Stone JV (2005) A brief introduction to independent component analysis. In: Everitt BS, Howell DC (eds) Encyclopedia of statistics in behavioral science. Wiley, Chichester
28. Yu H, Yang J (2001) A direct LDA algorithm for high-dimensional data - with application to face recognition. Pattern Recogn 34(10):2067–2070
29. Perperids D, Mohiaddin R, Edwards P, Rueckert D (2007) Segmentation of cardiac MR and CT image sequences using model-based registration of a 4D statistical model. In: Medical Imaging (p 65121D). International Society for Optics and Photonics
30. Stankiewicz W, Roszak R, Morzyński M (2011) Genetic algorithm-based calibration of reduced order Galerkin models. Math Model Anal 16(2):233–247
31. Alfakih K, Plein S, Thiele H, Jones T et al (2003) Normal human left and right ventricular dimensions for MRI as assessed by turbo gradient echo and steady-state free precession imaging sequences. J Magn Reson Imaging 17(3):323–329
32. Ghorbanian P, Ghaffari A, Jalali A, Nataraj C (2010) Heart arrhythmia detection using continuous wavelet transform and principal component analysis with neural network classifier. Comput Cardiol 37:669–672

33. Boulakia M et al (2012) Reduced-order modeling for cardiac electrophysiology. Application to parameter identification. Int J Numer Meth Biomed Engng 28:727–744
34. Martis RJ et al (2012) Application of principal component analysis to ECG signals for automated diagnosis of cardiac health. Expert Syst Appl 39(14):11792–11800
35. Wu J, Wang Y, Simon MA, Brigham JC (2012) A new approach to kinematic feature extraction from the human right ventricle for classification of hypertension: a feasibility study. Phys Med Biol 57(23):7905–7922

Estimation of the Permeability Tensor of the Microvasculature of the Liver Through Fabric Tensors

Rodrigo Moreno, Patrick Segers, and Charlotte Debbaut

1 Introduction

Liver diseases represent a big burden for health systems. As an example, the prevalence of chronic liver conditions in Europe has been reported as high as 5.7% [1]. A full understanding of the circulatory system of the liver and how it is affected by different liver diseases can be used for designing better treatments. This knowledge can also be used in liver transplantation for both improving surgery planning and increasing the viability of the liver graft through hypothermic machine perfusion [6].

At the microscale, a promising procedure for studying the structure of the vasculature of the liver in vitro is to analyze vascular corrosion casts imaged through micro-computed tomography (micro-CT). At this scale, the liver is organized in functional units often referred to as lobules [9]. Blood flows in the lobule from vessels located at the corners towards the central vein in the center through microvessels called sinusoids. The boundaries of the lobules are referred to as vascular septa. Figure 1 shows a schematic representation of a lobule.

A strategy that has been followed by some researchers is to describe the lobules as a porous media which can be characterized through different parameters such as porosity, pore size, and permeability. Such models can be used to predict the microperfusion at a micro-level [2, 5].

R. Moreno (✉)
School of Technology and Health, KTH Royal Institute of Technology, Hälsovägen 11C, 14157 Huddinge, Stockholm, Sweden
e-mail: rodrigo.moreno@sth.kth.se

P. Segers • C. Debbaut
Biofluid, Tissue and Solid Mechanics for Medical Applications (bioMMeda), Institute Biomedical Technology (IBiTech), Ghent University, De Pintelaan 185, Block B, B-9000 Gent, Belgium
e-mail: patrick.segers@ugent.be; charlotte.debbaut@ugent.be

A. Wittek et al. (eds.), *Computational Biomechanics for Medicine*,
DOI 10.1007/978-3-319-54481-6_6

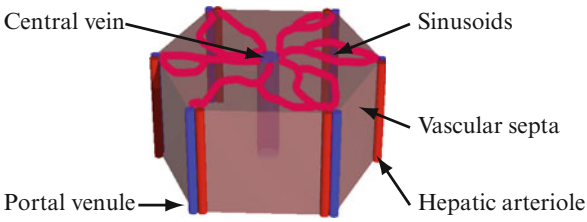

Fig. 1 Schematic representation of a liver lobule

One of the most important parameters in those models is the permeability, which measures how easy it is for a fluid to traverse a porous material. The discharge per unit area q (given in m/s) is related to the gradient of the pressure ∇p (given in Pa/m) in porous media through the Darcy's law:

$$q = \frac{-\mathsf{K}}{\mu}\nabla p, \tag{1}$$

where K is the permeability given in m^2 and μ is the dynamic viscosity given in Pa s. It is known that the permeability is not isotropic inside the lobules, which means that accurate models must consider second-order tensorial estimates of this parameter [4]. The permeability tensor is a symmetric positive definite second-order tensor, which can be represented by a 3×3 matrix. Basically, the permeability tensor depends on the geometry of the microvasculature, the properties of the vessel walls, the fluid dynamics properties of the blood, and properties of the parenchymal matrix.

Although it is possible to compute the permeability tensor through computational fluid dynamics (CFD) simulations in vascular corrosion casts imaged through micro-CT [4, 14], this approach has two main issues. On the one hand, the simulations require boundary conditions that are not straightforward to design. On the other hand, the computations are usually restricted to relatively small samples due to the expensive computational cost of the simulations. Thus, with this approach, the computation of the permeability tensor for a complete lobule usually requires averaging several permeability tensors computed from subsamples of the lobule.

CFD simulations require certain assumptions. It is well known that blood is a complex non-Newtonian fluid whose behavior varies depending on the diameter of the vessels. However, it is common to assume that blood behaves as a Newtonian fluid for computing the permeability tensor provided that the range of diameters of sinusoids inside the lobules is relatively reduced (8–20 μm) and blood flows at low velocities within those vessels. An important consequence of these assumptions is that the anisotropy and orientation of the permeability tensor mostly depends on the geometric arrangement of sinusoids of the lobule. This opens the door to approximating the permeability tensor through image processing-based methods for tackling the aforementioned issues of CFD simulations.

Fabric tensors are geometric features that describe the anisotropy and orientation of porous media [12]. In biomechanics, especially in trabecular bone research and material mechanics, fabric tensors have been used for two different purposes. First, different anisotropy measurements, e.g., fractional anisotropy (FA), can directly be extracted from tensors, which can potentially be used as quantitative imaging biomarkers. Second, fabric tensors can be combined with other parameters for predicting biomechanical tensors. For example, fabric tensors can be used for accurately estimating the stiffness tensor of trabecular bone in a few seconds [13]. Indeed, fabric tensors can also be applied to describe the microarchitecture of the microvessels in the lobules, considering that they can also be modeled as porous media. Although, the potential of this approach has recently been pointed out in [8], to the best of our knowledge, this is the first attempt of using fabric tensors in this context. Hence, the main aim of this paper is to explore the use of fabric tensors for approximating the permeability tensor of the liver lobules.

The paper is organized as follows. Section 2 describes the materials and methods. Section 3 compares the results with CFD. Finally Sect. 4 discusses the results and makes some concluding remarks.

2 Materials and Methods

2.1 Image Acquisition

A normal human liver which was discarded for transplantation after failed reallocation was used in this study.[1] A vascular corrosion cast was created for the liver using the standard procedure used in our lab [4]. First, a polymer resin was injected from the hepatic artery and portal vein to the liver until the resin reached the vena cava inferior. Second, the tissue surrounding the vessels was dissolved using potassium hydroxide.

Once the corrosion casts were obtained, a sample of size $1.1 \times 1.9 \times 1.5$ mm was taken for imaging through an in-house developed micro-CT scanner. The resolution of the images is $2.6\,\mu$m isotropic. This sample contains approximately three lobules of the liver, which were manually separated from each other. The images were segmented using Otsu's threshold. Vessels with diameters beyond $20\,\mu$m were discarded by just considering vessels that are filtered out by the opening operator of mathematical morphometry as described in [3, 10]. Figure 2 shows a rendering of the normal liver containing approximately three lobules.

[1]Ethical approval was obtained from the Ethical Committee of the University Hospitals Leuven (Belgium) and by the Belgian Liver and Intestine Committee.

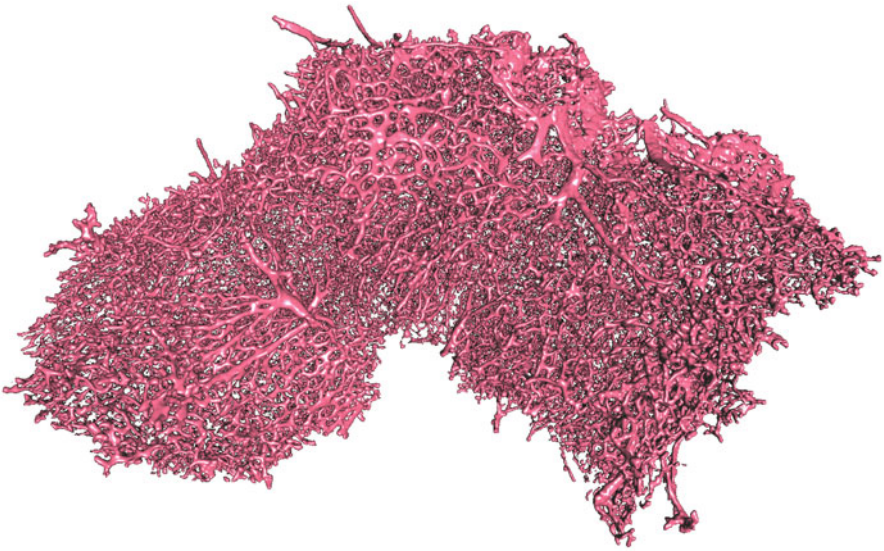

Fig. 2 Rendering of the micro-CT image of a sample taken from the normal liver containing three lobules

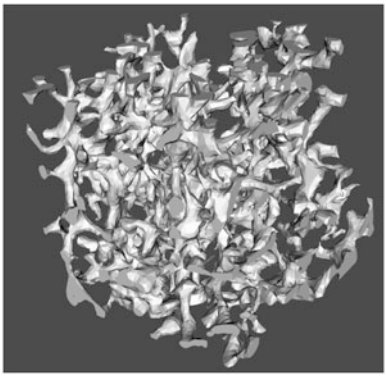

Fig. 3 Rendering of the section used for computing the permeability tensor through CFD

2.2 CFD Simulations

The CFD simulations were performed as described in [4]. A sample of 150 × 150 × 150 μm was cut from one of the three lobules. The z axis of the sample was aligned to the central vein. A surface mesh of the sample was used to create the volume meshes used in the simulations. Figure 3 shows the sample used for the CFD simulations.

Three simulations were performed, one per axis. In order to facilitate setting the boundary conditions for the simulations, two slabs of 15 μm were put perpendicular to the axis of interest before and after the sample in every simulation. A typical fluid

velocity was set at one slab and a zero pressure was set at the end of the opposite slab. CFD simulations were performed to estimate local velocities and pressures. By applying the Darcy's law, these values were used to compute the different entries of the permeability tensor for 15 subsamples of size $50 \times 50 \times 50\,\mu\text{m}$ taken from the original sample. Finally, these entries were averaged and the resulting tensors were symmetrized to get a single permeability tensor for the complete sample. A detailed description of the computations is given in [4].

2.3 Estimation of the Permeability Tensor Through Fabric Tensors

Methods for computing fabric tensors can roughly be classified into boundary- and volume-based [12]. Boundary-based fabric tensors have the advantage of being very efficient. From these, the generalized mean intercept length (GMIL) tensor [11] was chosen for this study since it has been proven versatile for predicting biomechanical tensors [13].

The GMIL tensor is computed in three steps. The mirrored extended Gaussian image (EGI) [7] is computed either from a robust estimation of the gradient or from a surface mesh. Second, the EGI is convolved with a kernel in order to obtain an orientation distribution function (ODF). Finally, a second-order fabric tensor is computed from the ODF. More formally, the generalized MIL tensor is computed as:

$$\mathsf{GMIL} = \int_{\Omega} \frac{v\, v^T}{C(v)}\, d\Omega\,, \tag{2}$$

where v are vectors on the unitary sphere Ω, and C is given by $C = H * E$: that is, the angular convolution $(*)$ of a kernel H with the mirrored EGI E. In particular, the von Mises–Fisher kernel, which is a function on the polar angle ϕ in spherical coordinates, is given by:

$$H(\phi) = \frac{\kappa}{4\pi \sinh(\kappa)}\, e^{\kappa \cos(\phi)}. \tag{3}$$

The advantage of using this kernel is that it has a parameter κ that can be used to control its smoothing action. A value of $\kappa = 8$ yielded the best results in the experiments of Sect. 3.

Fabric tensors are dimensionless descriptors, which means that they must be combined with other features for predicting the size of the permeability tensor. In this paper, we used the density of sinusoids ϵ for this purpose. In particular, we used a linear regression model between the Frobenius norm of the tensors obtained through CFD from the 15 subsamples used for computing the permeability tensor and their respective density $\epsilon (R^2 = 0.89)$.

3 Results

Figure 4 depicts the permeability tensor computed through CFD and fabric tensors. As shown, the shape of the two tensors is very similar and the main difference between them is their orientation.

Table 1 shows the eigenvalues of the two tensors before and after normalization as well as the FA.

The table shows that the shape of both tensors is very similar. Moreover, they tend to be orthotropic with respect to the central vein, which is consistent with the shape of the lobule shown in Fig. 1 and with the findings in [15]. Furthermore, the anisotropy in the axis parallel to the central vein is approximately twice the one in plane. Notice that the differences in the non-normalized eigenvalues are related to the linear model used to predict the size of the tensors and not with the use of fabric tensors.

The normalized difference of the norm D_N, the normalized difference of the FA D_{FA}, and the angle between the main eigenvectors D_A were computed to compare the permeability tensor computed through CFD and fabric tensors, which are referred to as $\mathsf{K}_{\mathrm{CFD}}$ and K_{FT}, respectively. These measurements are given by:

$$D_N = \frac{|\,||\mathsf{K}_{\mathrm{CFD}}||_F - ||\mathsf{K}_{\mathrm{FT}}||_F\,|}{||\mathsf{K}_{\mathrm{CFD}}||_F}, \tag{4}$$

$$D_{\mathrm{FA}} = \frac{|\mathrm{FA}(\mathsf{K}_{\mathrm{CFD}}) - \mathrm{FA}(\mathsf{K}_{\mathrm{FT}})|}{\mathrm{FA}(\mathsf{K}_{\mathrm{CFD}})}, \tag{5}$$

$$D_A = \arccos(|e1_{\mathrm{CFD}} \cdot e1_{\mathrm{FT}}|), \tag{6}$$

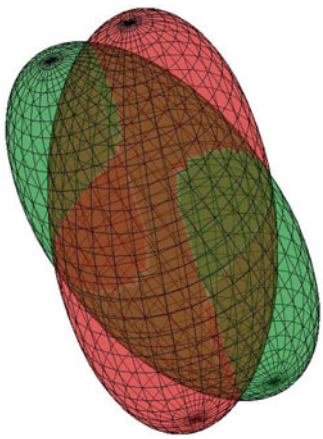

Fig. 4 Permeability tensor computed on a sample taken from a lobule. Results from CFD and fabric tensors are depicted in *green and red*, respectively

Table 1 Eigenvalues before and after normalization for a sample of a lobule

Tensor	λ_1 (f m^2)	λ_2 (f m^2)	λ_3 (f m^2)	λ_2/λ_1 (%)	λ_3/λ_1 (%)	FA (%)
K_{CFD}	32.01	17.26	14.27	53.91	44.56	42.12
K_{FT}	26.15	14.92	11.07	57.05	42.32	42.32

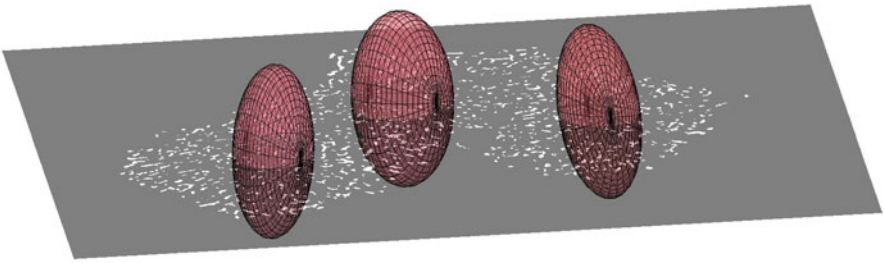

Fig. 5 Results for the three lobules. The tensors are plotted with a slice of the micro-CT image approximately where the central veins are located

Table 2 Eigenvalues after normalization for the complete lobules shown in Fig. 5

Lobule	λ_2/λ_1 (%)	λ_3/λ_1 (%)	FA (%)
Left	35.02	30.91	60.82
Center	31.40	25.21	66.69
Right	37.62	33.81	57.44

where $||\cdot||_F$ is the Frobenius norm, FA is the fractional anisotropy, and $e1$ is the eigenvalue corresponding to the largest eigenvalue of the tensor. These measurements are 17.9%, 0.2%, and 19.62° for the tested sample.

Figure 5 shows the results for the three lobules with the proposed method. As shown, the resulting tensors are approximately aligned with the orientation of the central veins. The corresponding CFD-based tensors were not available for comparison due to the high computational complexity of the simulations.

Table 2 shows the normalized eigenvalues and the FA for the three tensors. Similarly to the previous experiment, they exhibit orthotropic symmetry, but they have larger anisotropy.

As for computational effort, the new method took 330 ms for processing the result shown in Fig. 4 and 7.5 s per lobule for the results shown in Fig. 5. The CFD counterpart for Fig. 4 took several hours.

4 Discussion

A new method for estimating the permeability tensor of the microvasculature of the liver based on fabric tensors was presented. The main advantage of the new method is that it is very efficient and does not require to set boundary conditions. The results are promising, in particular with respect to the shape of the tensor, where the new method was able to reproduce the one obtained through CFD.

The results of this paper suggest that the permeability tensor is mostly related to the geometrical arrangement of the sinusoids. However, this finding must be validated with a larger dataset. Actually, the main limitation of this study is that,

due to ethical restrictions, it is difficult to have access to more data. One way to circumvent this problem is to work with animal models, something that will be tested in our lab.

Additional ongoing research include improving the estimation of the size of the tensors and improving the CFD simulations in order to consider the non-linear dependency of the permeability tensor on the gradient of the pressure as reported in [16].

References

1. Blachier M, Leleu H, Peck-Radosavljevic M, Valla DC, Roudot-Thoraval F (2013) The burden of liver disease in Europe. J Hepatol 58:593–608
2. Bonfiglio A, Leungchavaphongse K, Repetto R, Siggers JH (2010) Mathematical modeling of the circulation in the liver lobule. J Biomech Eng 132(11):111011
3. Coeurjolly D (2010) Fast and accurate approximation of the Euclidean opening function in arbitrary dimension. In: IEEE International Conference on Pattern Recognition (ICPR), pp 229–232
4. Debbaut C, Vierendeels J, Casteleyn C, Cornillie P, Van Loo D, Simoens P, Van Hoorebeke L, Monbaliu D, Segers P (2012) Perfusion characteristics of the human hepatic microcirculation based on three-dimensional reconstructions and computational fluid dynamic analysis. J Biomech Eng 134(1):011003
5. Debbaut C, Vierendeels J, Siggers JH, Repetto R, Monbaliu D, Segers P (2014) A 3D porous media liver lobule model: the importance of vascular septa and anisotropic permeability for homogeneous perfusion. Comput Methods Biomech Biomed Eng 17(12):1295–1310
6. Debbaut C, Monbaliu DRL, Segers P (2014) Validation and calibration of an electrical analog model of human liver perfusion based on hypothermic machine perfusion experiments. Int J Artif Organs 37(6):486–498
7. Horn BKP (1984) Extended Gaussian images. Proc IEEE 72(12):1671–1686
8. Jiřík M, Tonar Z, Králíčková A, Eberlová L, Mírka H, Kochová P, Gregor T, Hošek P, Svobodová M, Rohan E et al (2016) Stereological quantification of microvessels using semiautomated evaluation of X-ray microtomography of hepatic vascular corrosion casts. Int J Comput Assist Radiol Surg 11(10):1803–1819
9. Marieb EN, Hoehn K (2008) Anatomy & physiology. Pearson Education, San Francisco
10. Moreno R, Borga M, Smedby Ö (2012) Estimation of trabecular thickness in gray-scale images through granulometric analysis. In: Proceedings of SPIE. Medical Imaging 2012: Image Processing, vol 8314, p 831451
11. Moreno R, Borga M, Smedby Ö (2012) Generalizing the mean intercept length tensor for gray-level images. Med Phys 39(7):4599–4612
12. Moreno R, Borga M, Smedby Ö (2014) Techniques for computing fabric tensors: a review. In: Westin CF, Vilanova A, Burgeth B (eds) Visualization and processing of tensors and higher order descriptors for multi-valued data. Springer, Berlin, pp 271–292
13. Moreno R, Smedby Ö, Pahr DH (2016) Prediction of apparent trabecular bone stiffness through fourth-order fabric tensors. Biomech Model Mechanobiol 15(4):831–844
14. Peeters G, Debbaut C, Cornillie P, De Schryver T, Monbaliu D, Laleman W, Segers P (2015) A multilevel modeling framework to study hepatic perfusion characteristics in case of liver cirrhosis. J Biomech Eng 137(5):051007

15. Ricken T, Dahmen U, Dirsch O (2010) A biphasic model for sinusoidal liver perfusion remodeling after outflow obstruction. Biomech Model Mechanobiol 9(4):435–450
16. Rohan E, Lukeš V (2015) Modeling nonlinear phenomena in deforming fluid-saturated porous media using homogenization and sensitivity analysis concepts. Appl Math Comput 267:583–595

Motion Estimation with Finite-Element Biomechanical Models and Tracking Constraints from Tagged MRI

Arnold D. Gomez, Fangxu Xing, Deva Chan, Dzung L. Pham, Philip Bayly, and Jerry L. Prince

1 Introduction

Soft tissue deformation elicits vital transport processes throughout the body, and is a key determinant in widespread conditions and diseases. For example, systemic circulatory deficiencies may arise from impaired myocardial contraction, and acceleration-induced axonal overstretching has been linked to traumatic brain [1, 2] and can be investigated using MRI. Thus, noninvasive motion estimation is of clinical and investigational interest. However, the acquisition and processing of tagged MRI has been problematic due to long scan times, artifacts, and challenges in obtaining accurate 3D estimates of displacement and strain. It has been shown that integration of an organ's geometry (and fiber orientations if relevant) and use of material constitutive information can increase estimation accuracy, reduce artifacts, and improve one's ability to estimate dense displacements and strains from sparsely acquired imaging data [1, 3].

Motivated by versatile contrast and unparalleled soft tissue sensitivity, several motion estimation approaches have been developed within the MRI framework,

A.D. Gomez (✉) • J.L. Prince
Electrical and Computer Engineering Department, Johns Hopkins University, Baltimore, MD, USA
e-mail: adgomez@jhu.edu

F. Xing
Department of Radiology, Massachusetts General Hospital/Harvard Medical School, Boston, MA, USA

D. Chan • D.L. Pham
Center for Neuroscience and Regenerative Medicine, The Henry M. Jackson Foundation, Bethesda, MD, USA

P. Bayly
Mechanical Engineering Department, Washington University in St. Louis, St. Louis, MO, USA

A. Wittek et al. (eds.), *Computational Biomechanics for Medicine*,
DOI 10.1007/978-3-319-54481-6_7

as well as dedicated motion encoding pulse sequences, image postprocessing, or both [4]. Analysis of tagged MRI is one of the most well-established approaches which, from early implementations targeting the cardiovascular system, has expanded to include other organs [5–7].

Best results in 3D motion estimation generally require consistent repetition of movement and relatively high resolution, but these are constrained by scan time [8, 9]. Traditionally, displacement information has been reconstructed in the imaging planes first and then propagated to a 3D domain with the help of interpolation methods, such as splines, or finite elements [3, 10]. These approaches enable preemptive reduction of artifacts via smoothing or refinement, and enforce incompressibility during the interpolation process [10]. However, the imaging raster rarely aligns with the geometry or fiber structure of an organ; thus, smoothing or interpolation may introduce fictitious edge tractions, or violate other mechanical characteristics such as tissue anisotropy.

In this research, the tracking process is realized by enforcing image phase conservation in material points within the field of view (FOV), but not coincident with the spatial imaging raster. The proposed tracking kernel is based on the classic harmonic phase (HARP) analysis of tagged MRI [11], combined with hyperelastic model registration methods [1], according to a phase conservation principle parallel to intensity conservation in optical flow [12]. Thus, the results are *mechanically representative,* in that they are diffeomorphic, have traction free surfaces, and are otherwise consistent with continuum mechanics, but the phase vector formulation increases sensitivity in texture-free regions, and provides a more objective similarity metric.

We demonstrate our implementation in three scenarios. The first two consist of forward displacement reconstruction where the goal is to obtain deformation fields. These include: measurement of impact-induced deformation in a Sylgard™ brain phantom and quantification of fiber strain in residually stressed myocardium. The third scenario consists of displacement-based inverse parameter identification of intrinsic tongue muscle activation. Our results indicate that, in forward displacement reconstruction, the approach is robust to artifacts (edges and large displacements) and to material stiffening due to residual stress. In the inverse problem, we show that evaluating fiber stretch enables approximation of muscle activation without the need for iterative minimization.

2 Background

2.1 Harmonic Phase Analysis

Tagged MRI contains artificial magnetic patterns (lines or sinusoidal profiles) that are imposed near the beginning of a CINE sequence and deform with moving tissue. HARP analysis focuses on harmonic peaks in the Fourier domain, which arise from

the periodic nature of tag patterns. The harmonic phase vector, $\boldsymbol{\phi} = [\phi_1 \ \phi_2 \ \phi_3]^T$, where each term is the phase of the inverse Fourier transform of a harmonic peak in an image whose tag direction is orthogonal to the other two directions, carries information about local components of tissue motion. In particular, the phase at a reference location, $\boldsymbol{X}$, at $t = t_0 = 0$ will be the same as tissue moves to a new spatial location, $\boldsymbol{x}$, at a later time. In other words,

$$\boldsymbol{\phi}\,(\boldsymbol{X}, t_0) = \boldsymbol{\phi}\,(\boldsymbol{x}, t)\,. \tag{1}$$

Thus, 3D motion estimation can be thought of as the solution of a multidimensional, nonlinear, root-finding problem: given phase distributions at two time points, find $\boldsymbol{x}$ for a given $\boldsymbol{X}$, or vice versa.

We note that a practical application of HARP analysis deals not with the true real-valued phase, but rather with the *harmonic phase* whose range is the interval $[-\pi\,, \pi)$. Nevertheless, it is possible to use the expressions herein without loss of generality by adopting local phase unwrapping in the final implementation [11].

2.2 Deformations in Continuum Mechanics

Tissue deformation can be modeled as a boundary problem seeking to minimize an energy functional $E(\boldsymbol{\varphi})$, where the deformation map $\boldsymbol{\varphi}$ contains admissible deformations evaluated at material points, i.e., $\boldsymbol{\varphi}(\boldsymbol{X}) = \boldsymbol{x} = \boldsymbol{X} + \boldsymbol{u}(\boldsymbol{X})$ [1]. Given an integration domain, $\mathcal{R} \in \mathbb{R}^3$, the Euler–Lagrange equations necessary to minimize E are obtained by taking the directional derivative with respect to a small variation (or virtual displacement) in the spatial coordinates. This yields the weak form of the so-called virtual work equation,

$$\delta W = \int_{\mathcal{R}} \boldsymbol{P} : \delta \dot{\boldsymbol{F}}\, dV - \int_{\mathcal{R}} \boldsymbol{f}_0 \cdot \delta \boldsymbol{v}\, dV + \int_{\mathcal{S}} \boldsymbol{t}_0 \cdot \delta \boldsymbol{u}\, dS. \tag{2}$$

At equilibrium, $\delta W = 0$ describes a static momentum balance between body or boundary forces (respectively $\boldsymbol{f}_0$ and $\boldsymbol{t}_0$), and internal stresses defined by the material-dependent first Piola–Kirchhoff stress tensor, $\boldsymbol{P}(\boldsymbol{F})$, and the spatial gradient of the deformation map, $\boldsymbol{F} = \frac{d\boldsymbol{x}}{d\boldsymbol{X}}$ [13, 14].

One of the most popular approaches for solving the boundary problem associated with (2) is FE analysis. This process generally involves extracting discretized geometry from MRI via delineation and meshing, assigning a suitable constitutive model, and defining boundary conditions. The FE method has experienced considerable expansion in biomechanics, thanks to several improvements geared to handle complex biological geometries, and nonlinear material models [13, 15].

3 Tracking Tagged MRI with Deformable Models

3.1 Conservation of Harmonic Phase Vector

The basis of HARP analysis, (1), can also be described through physical conservation principles. Let $\boldsymbol{\phi}$ represent a vectorial angular quantity (per unit mass), which is conserved. Then, the net change in phase density can be expressed as a mass transport process defined in weak form by

$$\frac{D}{Dt}\int_{\mathcal{R}} \boldsymbol{\phi}\rho \, dV = \int_{\mathcal{R}} \frac{\partial (\boldsymbol{\phi}\boldsymbol{\rho})}{\partial \boldsymbol{t}} \, dV + \int_{\mathcal{S}} \rho\boldsymbol{\phi} \otimes \boldsymbol{v} \cdot \boldsymbol{n} \, dS, \tag{3}$$

where the right-hand side contains generative and advection terms dependent on mass density ρ and velocity $\boldsymbol{v}$ across a boundary surface with local normal $\boldsymbol{n}$ [16]. Application of Gauss' theorem and the continuity equation reduces the phase conservation relationship to

$$\frac{D\boldsymbol{\phi}}{Dt} = \frac{\partial \boldsymbol{\phi}}{\partial \boldsymbol{t}} + \nabla \boldsymbol{\phi} \cdot \boldsymbol{v}. \tag{4}$$

The left side of the equation corresponds to the material description, which yields the deformable model tracking constraint discussed in the next section. The middle expression is equivalent to the spatial description, and is the harmonic phase equivalent of the familiar optical flow equation used in intensity-based image registration [12].

3.2 Nonlinear Tracking Constraint

We now focus on obtaining displacements using the material description of harmonic phase conservation noting that direct application of (1) has two key limitations: First, harmonic phase vector pairs are not unique as a consequence of phase wrapping, thus tracking may converge at erroneous locations after large displacements; second, without regularization, tracking points near edges will result in spurious displacements due to partial volume artifacts.

Definition

Using integration with respect to time, the total derivative in (4) can be formulated as a difference between two phase images, acquired at the reference and at a subsequent time, evaluated at a material point and its corresponding location in the deformed configuration, i.e., $\boldsymbol{x} = \boldsymbol{x}(\boldsymbol{X}, t)$. This difference defines the nonlinear tracking constraint to be imposed on (2),

$$\boldsymbol{f}_{harp} = \lambda(t)\left(\boldsymbol{\phi}\left(\boldsymbol{x}\left(\boldsymbol{X},\boldsymbol{t}\right),\boldsymbol{t}\right) - \boldsymbol{\phi}\left(\boldsymbol{X},\boldsymbol{t}_0\right)\right), \tag{5}$$

where $\lambda(t)$ is a Lagrange multiplier that enforces phase consistency in tracking. In essence, the constraint introduces an additional body force whose purpose is to deform the model according to the temporal changes in the tag patterns.

Implementation

Given the nonlinear nature of (5), implementation within a Newton–Raphson (or similar) iterative solver requires consistent linearization of the virtual work contribution from the constraint to be applied on (2). In other words, linearizing $\delta W_{\text{harp}}\left(\boldsymbol{x},\delta\boldsymbol{v}\right) = \int_{\mathcal{R}} \boldsymbol{f}_{\text{harp}}\cdot\delta\boldsymbol{v}\, dV$ yields the tangent stiffness aggregate to be passed along to the solver, i.e.,

$$D\delta W_{harp}\left(\boldsymbol{x},\delta\boldsymbol{v}\right)[\boldsymbol{u}] = \int_{\mathcal{R}} \lambda(t)\nabla\boldsymbol{\phi}\left(\boldsymbol{x}\left(\boldsymbol{X},\boldsymbol{t}\right),\boldsymbol{t}\right)\ \delta\boldsymbol{v}\cdot\delta\boldsymbol{u}\, dV. \tag{6}$$

The tracking constraint was implemented as a plug-in extension to the FE solver within the FEBio Software Suite [15].

Image Preprocessing

In (5), it is assumed that the harmonic phase images are defined everywhere, which typically is not the case. Therefore, an image interpolation step must be built into the implementation. In fact, we propose upsampling tagged images prior to harmonic peak extraction (effective bandwidth remains limited by the original acquisition). We used grid-based cubic spline interpolation to achieve isotropic resolution based on the in-plane slice resolution. As with conventional HARP analysis, band-pass filtering is necessary to extract harmonic peaks. In this research, each 2D slice was filtered one image at a time, with a circular band-pass filter centered at the tagging frequency with a radius equal to half of the center frequency [11].

Solution Strategy

Two main approaches for enforcement of tracking constraints are available in this implementation. The first consists of applying a global, linearly increasing, penalty $\lambda(t)$ function (penalty method), and the second consists of using an iterative approximation to its local values to a given tolerance (augumented Lagrangian) [17]. Both the maximum penalty $\lambda_{\max}$ and tolerance λ_{tol} were adjusted according to a desired tracking residual $\varepsilon = \int \boldsymbol{\phi}(\boldsymbol{x}(\boldsymbol{X},t),t) - \boldsymbol{\phi}(\boldsymbol{X},t_0)\, dV$.

4 Experiments and Results

4.1 Measuring Impact-Induced Deformation in Brain Phantom

The goal of this experiment was to demonstrate our approach against traditional HARP analysis, i.e., application of (1) with a fixed-point algorithm, for reconstructing the motion of a Sylgard™ phantom, Fig. 1(a). The phantom's base was subject to a sudden rotational acceleration and consequently imaged (3T scanner, 13 frames, 18 ms TR, 13 axial slices, 160 ×160 px, 1.5 ×1.5 mm, SPAMM sequence). Two FE models of the phantom were constructed: one consisting of 4250 linear (fully integrated) brick elements, and the other used the same number of elements using a quadratic 20-node formulation. In both, the material was modeled as a Neo-Hookean solid ($C_1 = 1.0$ kPa, $\kappa = 120$ kPa). Tracking was performed to $\varepsilon = 0.05$ rad, with $\lambda_{\max} = 0.2$, and $\lambda_{\text{tol}} = 0.1$. Both algorithms ran for ten iterations per time frame.

Representative displacements at $t = 54$ ms appear in Fig. 1(c) and (d), for conventional HARP and our method, respectively. As expected, using a fixed-point algorithm results in two types of artifacts: spurious displacements near the edges, and erroneous tracking due to large displacements. In contrast, the proposed methodology results in smooth (traction-free) displacements at the boundaries, and consistent tracking of rotation. Both linear and quadratic meshes yielded identical qualitative results with minor quantitative differences (less than 0.1%).

4.2 Quantifying Fiber Stretch in Residually Stressed Myocardium

Most tissues, even in the absence of loading, exhibit some level of residual stress, which becomes apparent by recoil following an incision, suggesting that fibers in situ are prestretched [18]. Here, we (a) demonstrate that our approach may include

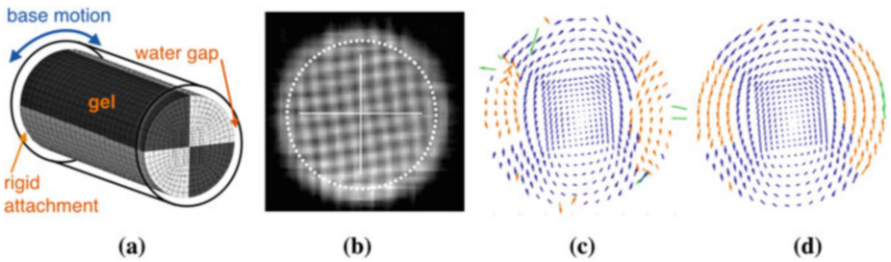

Fig. 1 Acceleration-induced brain phantom deformation. As shown in the schematic (**a**), motion of the base causes deformation into a new configuration (**b**). Conventional HARP analysis (**c**) shows large-displacement artifacts (*orange*), and spurious displacements at the edges (*green*). The problematic areas in proposed method (**d**) are largely artifact-free

modeled prestretch via interstitial growth [19], and (b) evaluate changes in tracking results due to prestretch-induced stiffness variations. To this end, the left ventricle of a healthy volunteer was imaged (3T scanner, 12 long slices, eight long slices, 256 ×256, 1.25 ×1.25 mm, CSPAMM sequence), and images at early diastole (lowest pressure load) were used to generate an FE model consisting of 6500 linear brick elements. Simulated contraction, with parameters available in [1, 18], was used as ground truth displacements, and to create synthetic deformed images for tracking.

Two displacement results were obtained with a stress-free reference (SFR) and a prestretched reference (PSR), which included −5\% mean fiber prestretch [18, 19]. In both, tracking was performed to $\varepsilon = 0.2$ rad. Tracking from SFR terminated after 17 iterations using $\lambda_{\max} = 0.2 \times 10^{-2}$ and $\lambda_{\text{tol}} = 5 \times 10^{-2}$. The same values for PSR after ten iterations were 1.4×10^{-2} and 7×10^{-2}, respectively. Compared to the ground truth, the displacement residuals were 0.6±0.3 mm and 0.9±0.3 mm (SFR and PSF, respectively). This similarity in residuals shows that prestretch-induced variations can be compensated by tracking parameters. Thus, although the image-derived deformed configurations are similar, the PSF relates to a reference state consistent with experimental evidence of residual stress, Fig. 2(a), and results in visibly higher systolic fiber shortening, Fig. 2(b) and (c).

4.3 Estimating Activation of Intrinsic Tongue Muscles

In this experiment, we estimate the magnitude of activation stress responsible for an observed deformation in the tongue. To this end, motion was first tracked based on a stack of images from a healthy volunteer at two time frames (3T scanner, ten coronal slices, eight sagittal slices, 256×256, 1.9×1.9 mm, CSPAMM

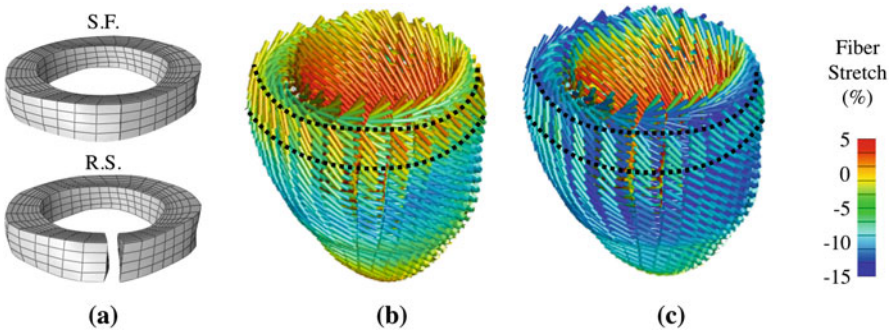

Fig. 2 Comparison between SFR and PSR. A radial cut (**a**) on a ring-like section shows no change in the SFR, but the same cut causes separation of edges in the PSR, similar to experimental observations [18]. Comparable deformed configurations exhibit different fiber stretches with respect to the SFR (**b**) or the PSR (**c**)

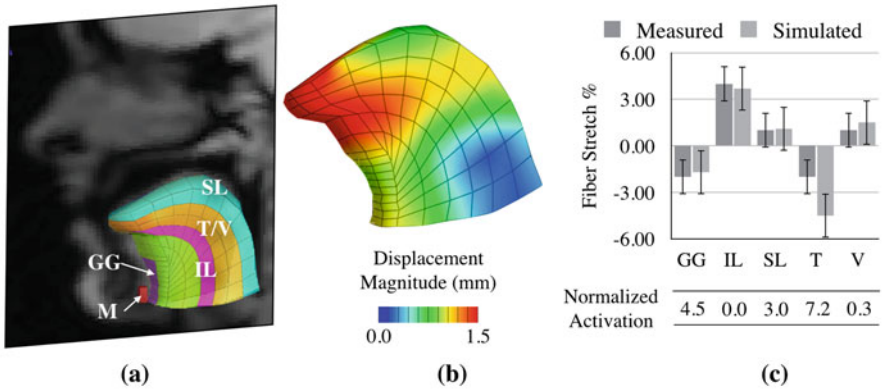

Fig. 3 Motion estimation in the tongue. Five muscles from MRI (**a**) are used within an FE model to extract deformations (**b**), and to simulate activation stresses. Measured and simulated fiber stretches (**c**) show qualitative agreement with those extracted from the tagged images. Key: *GG* genioglossus, *IL* inferior longitudinal, *SL* superior longitudinal, *T* transverse, *V* verticalis *M* mandible insertion

sequence) using an FE model consisting of 280 quadratic brick elements, and the tracking constraint set to $\varepsilon = 0.05$ rad. To obtain contractile stress normalized to material stiffness, the tissue was modeled as a Neo-Hookean solid ($C_1 = 1.0$ kPa, $\kappa = 120$ kPa). Fiber directionality and muscle definitions were based on the literature [7]. Unlike previous work, which relied on numerical optimization—where multiple simulations were run to find the closest match between simulated and observed tongue deformation—our strategy was to directly approximate the contractile stresses from the image-derived fiber shortening according to the active contraction model presented in [1] (solving for $T_{\max}$ in Eq. 4). These approximations were applied uniformly over each of the muscles in Fig. 3(a).

Image tracking, the basis of the observed tongue deformation, terminated after ten iterations $\lambda_{\max} = 1.0$ and $\lambda_{\text{tol}} = 0.1$. Displacement results appear in Fig. 3b. Experimental and simulated fiber stretches averaged over the muscle region appear in Fig. 3c, and show qualitative agreement. Comparison between the image-based deformation and activation simulation allows direct estimation of contractile stress, avoiding numerical optimization, which may converge at local minima [7]. Note that both, forward simulations and image tracking via the proposed phase tracking constraint, occur in the same geometrical model; thus, comparison between experimental and simulated behavior can be done on an element-per-element basis.

5 Discussion

This study extends fundamental concepts used for motion estimation based on scalar intensity images to the vectorial phase domain, which allows application of tagged images for mechanically regularized motion estimation. One immediate

advantage of this type of regularization is the reduction of artifacts present at the edges where image information is affected by partial volume. The use of tagged images disambiguates similarity metrics associated with intensity in areas of low texture. This improves motion tracking, and adds robustness to material parameter uncertainty.

As shown in previous literature featuring intensity-based motion estimation in FE models [1], displacements can be made consistent despite changes in material parameters by scaling the tracking penalty. The idea is that, within a range, a stiffer material will simply require larger forces to produce the same deformation. In the proposed method, we take advantage of the vectorial nature of phase to extract a similarity metric, ε, that serves as a stopping criteria for motion estimation; the tracking penalty continues to be scaled until the criteria is met. This basic principle was demonstrated when tracking deformation in residually stressed ventricular tissue, where the tracking parameters associated with the PSR were much larger than the SFR, even though the tracking metric and displacement accuracy were identical.

In terms of implementation, the proposed method effectively reduces to calculating body forces derived from phase images, i.e., the application of nodal forces where each (xyz) component is equal to scaled differences between template and target phase image in each corresponding tagging direction. The stiffness contribution, evaluated once per element, is defined similarly to the contribution of the material model but is defined as described in (6). From an image processing standpoint, upsampling of images enables the use of advantageous interpolation techniques that would be computationally expensive to evaluate along with the FE tracking constraint.

6 Conclusion

The main goal of this paper was to introduce and demonstrate unique features associated with this motion estimation strategy, including artifact reduction, robustness to material parameters, and interaction between observed motion and mechanical features like realistic geometry and fibers. Future research directions will focus on the relative performance of its different components, both from an imaging standpoint (the effects of image quality, upsampling, and filtering) and from a modeling perspective (the consequences of constitutive modeling and geometrical representation), and with respect to other motion estimation techniques.

Acknowledgments This research was funded by NIH Grant R01-NS055951, supplement PA12-149, and support by the Center for Neuroscience and Regenerative Medicine.

References

1. Phatak NS, Maas SA, Veress AI, Pack NA, Di Bella EVR, Weiss JA (2009) Strain measurement in the left ventricle during systole with deformable image registration. Med Image Anal 13:354–361
2. Wright RM, Ramesh KT (2012) An axonal strain injury criterion for traumatic brain injury. Biomech Model Mechanobiol 11:245–260
3. Haber I, Metaxas DN, Axel L (2000) Three-dimensional motion reconstruction and analysis of the right ventricle using tagged MRI. Med Image Anal 4:335–355
4. Ibrahim E-SH (2011) Myocardial tagging by cardiovascular magnetic resonance: evolution of techniques-pulse sequences, analysis algorithms, and applications. J Cardiovasc Magn Reson 13:36
5. Bayly PV, Clayton EH, Genin GM (2012) Quantitative imaging methods for the development and validation of brain biomechanics models. Annu Rev Biomed Eng 14:369–396
6. Moerman KM, Sprengers AMJ, Simms CK, Lamerichs RM, Stoker J, Nederveen AJ (2012) Validation of tagged MRI for the measurement of dynamic 3D skeletal muscle tissue deformation. Med Phys 39:1793–1810
7. Harandi, N.M., Woo, J., Farazi, M.R., Stavness, L., Stone, M., Fels, S., Abugharbieh, R. (2015) Subject-specific biomechanical modelling of the oropharynx with application to speech production. IEEE ISBI, pp 1389–1392
8. Knutsen AK, Magrath E, McEntee JE, Xing F, Prince JL, Bayly PV, Butman JA, Pham DL (2014) Improved measurement of brain deformation during mild head acceleration using a novel tagged MRI sequence. J Biomech 47:3475–3481
9. Spottiswoode BS, Zhong X, Hess AT, Kramer CM, Meintjes EM, Mayosi BM, Epstein FH (2007) Tracking myocardial motion from cine DENSE images using spatiotemporal phase unwrapping and temporal fitting. IEEE Trans Med Imaging 26:15–30
10. Liu X, Abd-Elmoniem KZ, Stone M, Murano EZ, Zhuo J, Gullapalli RP, Prince JL (2012) Incompressible deformation estimation algorithm (IDEA) from tagged MR images. IEEE Trans Med Imaging 31:326–340
11. Osman NF, McVeigh ER, Prince JL (2000) Imaging heart motion using harmonic phase MRI. IEEE Trans Med Imaging 19:186–202
12. Horn, B.K., Schunck, B.G. (1981) Determining optical flow. In: Technical Eymposium East. pp. 319–331
13. Bonet J, Wood RD (1997) Nonlinear continuum mechanics for finite element analysis. Cambridge University Press, Cambridge
14. Bathe KJ (1996) Finite element procedures. Prentice-Hall, Upper Saddle River
15. Maas SA, Ellis BJ, Ateshian GA, Weiss JA (2012) FEBio: finite elements for biomechanics. J Biomech Eng 134(1):011005
16. Spencer AJM (1985) Continuum mechanics. Dover Books, Essex
17. Guo H, Nickel JC, Iwasaki LR, Spilker RL (2012) An augmented Lagrangian method for sliding contact of soft tissue. J Biomech Eng 134:084503
18. Genet M, Rausch MK, Lee LC, Choy S, Zhao X, Kassab GS, Kozerke S, Guccione JM, Kuhl E (2015) Heterogeneous growth-induced prestrain in the heart. J Biomech 48:2080–2089
19. Ateshian GA, Ricken T (2010) Multigenerational interstitial growth of biological tissues. Biomech Model Mechanobiol 9:689–702

Subpixel Measurement of Living Skin Deformation Using Intrinsic Features

Amir HajiRassouliha, Andrew J. Taberner, Martyn P. Nash, and Poul M.F. Nielsen

1 Introduction

Characterising the behaviour of skin is important in a number of applications. For example, quantification of skin properties can provide a better understanding of the wound healing process [1], the effects of ageing [2], the process of wrinkle formation [3], as well as improved methods for surgical planning [4]. Skin is a complex tissue that is anisotropic, heterogeneous, nonlinear, and viscoelastic [5]. Several methods have been developed to characterise the complex mechanical behaviour of skin in-vivo or in-vitro, such as during biaxial [6], compression [7], suction [8], or indentation [9] tests on tissues. Measuring the skin surface deformation is an essential part of all these methods. To address this, various devices have been designed and built for measuring skin deformations in-vivo. Some use sensor technologies, such as three-degree-of-freedom tactile devices [10], microrobots [11], motion capture systems [12], while others use image processing techniques for measuring deformations, such as single cameras [13, 14], multi-view stereo [15], and hand-held stereoscopic devices [16].

Digital image correlation (DIC) is the main image processing method used for measuring skin deformation with subpixel accuracy. DIC is a technique in which images are divided into many smaller overlapping subimages, and the displacement is found for each individual subimage separately [17]. The DIC technique typically

A. HajiRassouliha (✉)
Auckland Bioengineering Institute, The University of Auckland, Auckland, New Zealand
e-mail: ahaj975@aucklanduni.ac.nz

A.J. Taberner • M.P. Nash • P.M.F. Nielsen
Auckland Bioengineering Institute, The University of Auckland, Auckland, New Zealand

Department of Engineering Science, The University of Auckland, Auckland, New Zealand
e-mail: p.nielsen@auckland.ac.nz

A. Wittek et al. (eds.), *Computational Biomechanics for Medicine*,
DOI 10.1007/978-3-319-54481-6_8

includes two main steps for first finding the integer shift, and then the subpixel shift between two subimages. The integer part of most of the existing DIC algorithms uses cross-correlation (CC) to find the shift between two subimages. However, CC frequently fails on images that are poorly textured. Therefore, speckled patterns or markers are often added to the surface of the skin to enable the shift to be estimated using CC [13–15]. Furthermore, the accuracy and efficiency of the subpixel part of most of the existing algorithms are limited. To address these limitations, we have recently proposed a new method for subpixel image registration. This method is based on a phase-based algorithm that uses Savitzky–Golay differentiators in gradient correlation (P-SG-GC) [18]. It has been shown that the P-SG-GC algorithm can achieve accuracies better than 0.0002 pixel (60 times better than the state-of-the-art algorithms) in finding synthetically applied shifts to 2400 standard subimages of size 128 pixel × 128 pixel [18]. Furthermore, P-SG-GC is computationally efficient and performs well in low-textured images, where most of the existing algorithms fail to find the displacement [18].

This study investigates the performance of P-SG-GC for finding the deformation of living skin. First, an experimental setup was arranged to measure the accuracy of P-SG-GC in finding translational shifts of a target ranging from subpixel values to large shifts. Then, P-SG-GC was used to measure the deformation of skin using only intrinsic features.

2 Method

The accuracy of P-SG-GC in measuring translational shifts was evaluated by the experimental setup shown in Fig. 1. A photographic stand was used to hold a single monochrome CMOS USB 3 camera (Flea3 FL3-U3-13Y3M-C, Point Grey, Canada) in a position perpendicular to the surface of a flat object (target). The camera was equipped with a 12.5 mm lens (Fujinon) and the target was attached to a ball bearing manual linear stage with an accuracy of 2 μm over a 25 mm travel range (M-423 (https://www.newport.com/p/M-423), Newport, USA.).

A series of translational shifts (approximately 5, 10, 100, 500, 1000, 1500, and 2000 μm) were applied to the target using the translational stage. The camera captured images from the initial and shifted positions of the target. These were divided into approximately 2700 subimages of size 64 pixel × 64 pixel, which were distributed uniformly across the surface of the target with a step increment of 10 pixel. The P-SG-GC algorithm was used to measure displacements between all the subimages of the initial and shifted images in the x and y directions (d_x and d_y). The total displacement for each subimage was calculated using Eq. 1:

$$D_t(i) = \sqrt{{d_x}^2 + {d_y}^2} \ \text{(pixel)} \quad (i \leq n) \tag{1}$$

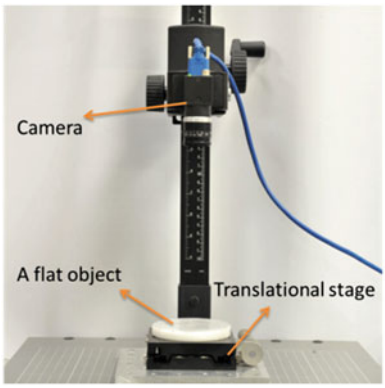

Fig. 1 The experimental setup used to evaluate the accuracy of P-SG-GC in measuring translational shifts. A photographic stand was used to hold the camera in a position perpendicular to the surface of a flat object attached to a linear translational stage

where i is the subimage number, and n is the total number of subimages. The mean of the $D_t(i)$ values (MD) (Eq. 2) was chosen as the estimation of the P-SG-GC algorithm for that translational shift of the target.

$$MD = \frac{\sum_{i=1}^{n} D_t(i)}{n} \quad \text{(pixel)} \tag{2}$$

If we assume an ideal condition at each applied translational shift, including a perfect perpendicular position of the camera and a completely flat target, all the $D_t(i)$ values should be equal. Therefore, the standard deviation of the $D_t(i)$ values at each translational shift was considered as an indication of the accuracy of the P-SG-GC algorithm in measuring the shift. In addition, the linearity between the set of applied physical shifts (in μm) and the MD values was considered as an indication of the linearity of measurements.

The estimation of physical shifts using a camera system is subject to various sources of error. One of the error sources that can be compensated for is the effect of optical distortions of the camera lens, especially the radial distortion (also known as barrel distortion) [19]. The lens radial distortion causes straight lines to become curved in the camera images (similar to being mapped around a sphere), thus changing the estimates of displacements from the images. To minimise this effect, we compensated for lens distortion in the images and repeated the computations. The lens distortion removal (i.e. undistortion of the images) was performed using radial and tangential lens distortion coefficients estimated through a camera calibration process.

After the P-SG-GC algorithm was tested, this algorithm was used to measure deformations of living skin. For this purpose, two images were taken of the skin on the back of a volunteer's hand at two different deformation states due to the movement of the volunteer's thumb. To provide a similar condition to that used in the evaluation step, the volunteer's hand was positioned at the same location as the target used for the validation experiments.

3 Results and Discussion

Figure 2 shows the difference between the $D_t(i)$ values (Eq. 1) and the *MD* values (Eq. 2) estimated using the P-SG-GC algorithm applied to original (distorted) image in the left column and undistorted images in the right column for shifts of 500, 1000, 1500, and 2000 μm. The difference values are colour-coded and are in units of pixel. As can be seen in Fig. 2, the *MD* values were all larger than 1 pixel for all these shifts and a distinct pattern is evident for the original (distorted) images in the left column. This pattern is indicative of a lens radial distortion effect that compresses the periphery of the image towards the optical centre (i.e. the principal point) [19]. Because of this effect, the measured shifts around the edges of the original (distorted) images were smaller than their actual values. The shift independent effect of lens distortion is shown in Fig. 3, where the P-SG-GC algorithm was applied to determine the displacement field between one of the images and its undistorted version.

The comparison between the left and right columns of Fig. 2 illustrates the improvement in the displacement estimates by correcting for lens distortion. Not only were the spatial distributions more uniform in the images of the right column compared with the left column, but the degree of underestimation of the displacement magnitudes was also reduced. The values in undistorted images revealed a distribution of displacements that is likely to be related to a relative tilt between the camera sensor and the target surface. This is an issue because the displacement measurements were performed in 2D by assuming that the camera axis was perpendicular to the surface of the flat object, the accuracy of which was difficult to determine using our experimental setup. Furthermore, the camera calibration error in finding the lens distortion coefficients was not considered in these measurements.

Figure 4 shows the linearity of the relation between translational shift (5, 10, 100, 500, 1000, 1500, and 2000 μm) and the *MD* values for the original (distorted) and undistorted images. As illustrated in Fig. 4, the estimates from the P-SG-GC algorithm show a linear correlation with the physical shift for both the original (distorted) and undistorted images ($(1-R^2) = 5.2 \times 10^{-4}$ for the original images and $(1-R^2) = 5.6 \times 10^{-4}$ for undistorted images).

Figure 5 shows the standard deviation of the estimated $D_t(i)$ values (Eq. 1) at the different translational shifts estimated from the original images and undistorted images. The standard deviation of the estimates based on the undistorted images was approximately half that estimated using the original (distorted) images. This illustrates that the removal of the lens distortion helped to increase the measurement accuracy.

The standard deviations of the measurements in Fig. 5 were less than 0.01 pixel for shifts less than 1 pixel (at 5 μm, 10 μm, and 100 μm shifts it was 0.008 pixel, 0.008 pixel, and 0.009 pixel, respectively). The standard deviation increased for displacements larger than 1 pixel, but the values were small compared with the displacement. For example, the standard deviation of the P-SG-GC measurements

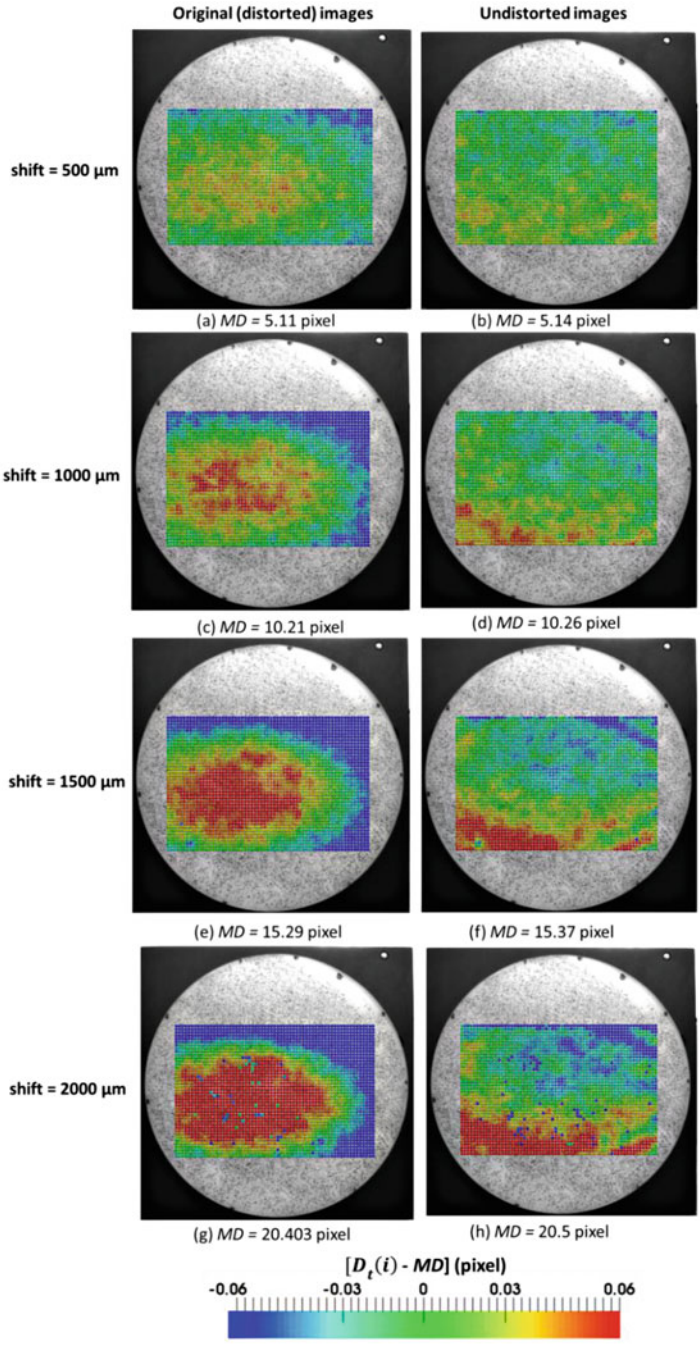

Fig. 2 The ($D_t(i)$–MD) values measured using the P-SG-GC algorithm applied to the original and undistorted images. The values are colour-coded and are in units of pixel. The target was moved downward using the linear translational stage, and the shift magnitudes are indicated at the left

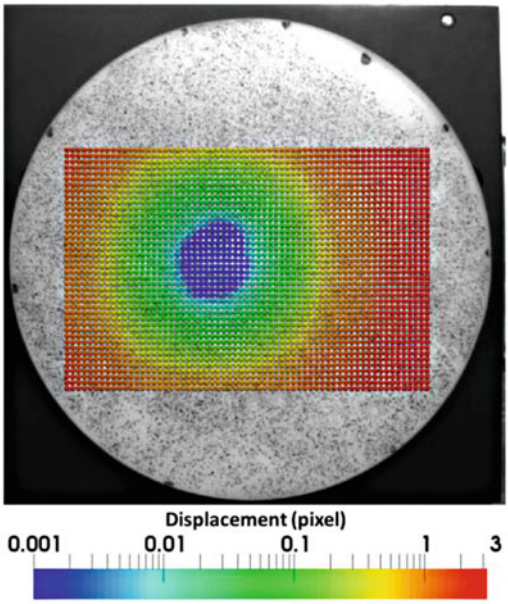

Fig. 3 The displacement map caused by the lens distortion model on the same area as of the images in Fig. 2. The displacement values were estimated applying the P-SG-GC algorithm to one of the images and its undistorted version. Displacement magnitudes are colour-coded in a logarithmic scale and values are in units of pixel

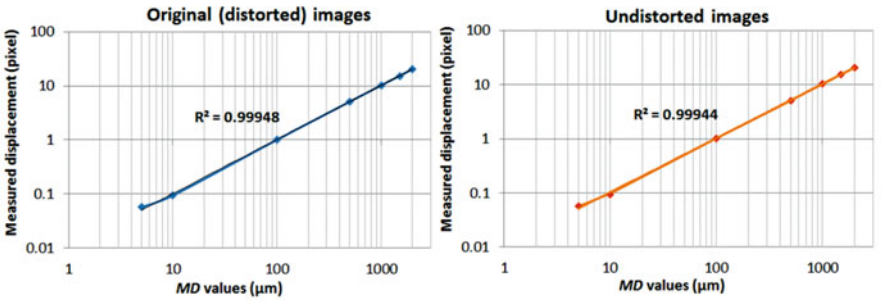

Fig. 4 The linearity between the *MD* values estimated using the P-SG-GC algorithm, and the translational shifts of the target using the linear translational stage

for the estimation of the 2000 µm shift was 0.0735 pixel for the original (distorted) images and 0.0456 pixel for undistorted images (0.36% and 0.22% of the *MD* values, respectively). The low standard deviation of the measurements (Fig. 5) and the high degree of linearity between the estimated values and actual physical shifts (Fig. 4) demonstrate that the P-SG-GC algorithm could measure small and large displacements to a good level of accuracy.

We next used the P-SG-GC algorithm to measure skin deformation on a volunteer's hand. As shown in Fig. 6, the volunteer's hand was placed at a similar location to that of the target, and an image was taken of the initial state of the skin of the back of the hand (Fig. 6a). The volunteer then moved his thumb to deform the skin of the back of his hand (Fig. 6b). As evident in Fig. 6, the skin in this test did

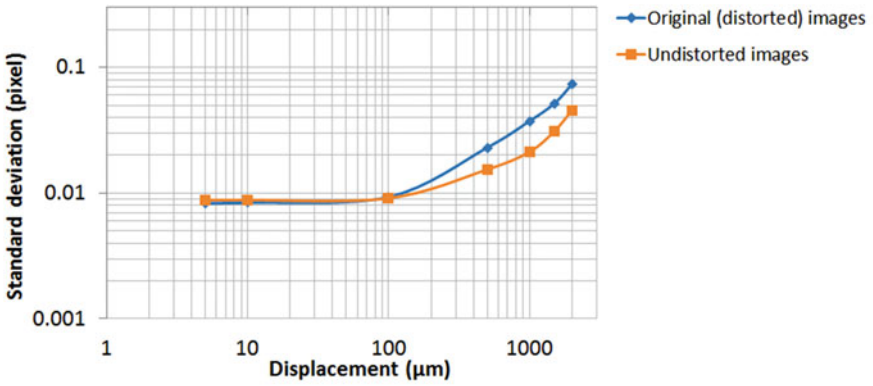

Fig. 5 The standard deviation of displacements estimated for subimages of the original (distorted) and undistorted images using the P-SG-GC algorithm

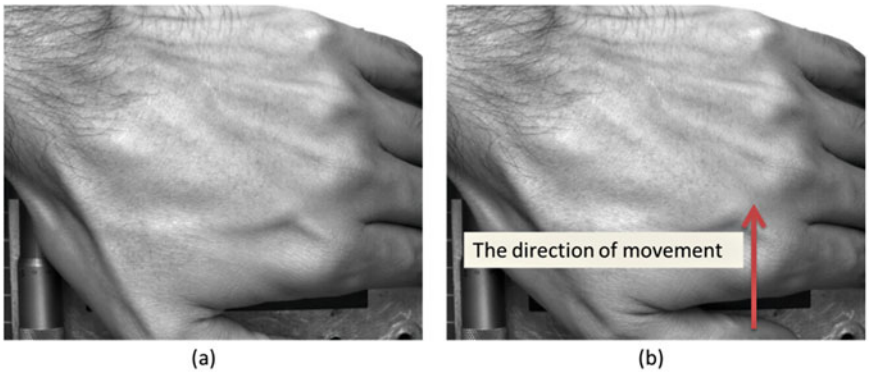

Fig. 6 The images of a volunteer's hand used in this study to test the capability of the P-SG-GC algorithm in finding the skin displacements using intrinsic features. The volunteer was asked to move his thumb in (**b**) to deform the skin of the back of his hand

not have obvious intrinsic features, and no extra pattern was applied to the skin. The P-SG-GC algorithm was used to estimate the skin deformations from Fig. 6a and Fig. 6b. The result of the measurements for subimages of size 64 pixel × 64 pixel is shown in Fig. 7. The magnitude of the displacements is colour-coded, and the arrows indicate the localised direction of skin movement. The skin displacements ranged from subpixel values (0.01 pixel) to values larger than 18 pixels. As can be seen in Fig. 7, the displacement fields show a continuous gradient over the surface of the skin. The result illustrates that the P-SG-GC algorithm could successfully estimate the skin deformation using only intrinsic features. These measurements cannot be validated directly with currently available methods, since most of them fail to measure skin deformation using intrinsic features.

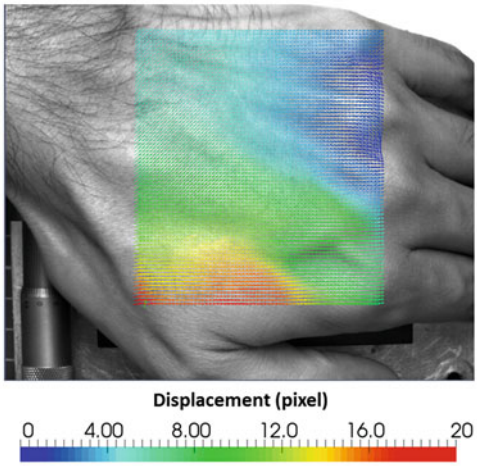

Fig. 7 The estimation of the skin deformation from the images of Fig. 6 using the P-SG-GC algorithm and subimages of size 64 × 64 pixel. The magnitude of the displacements is colour-coded and the arrows show the directions of displacement

4 Conclusion

Measuring skin deformation is an important step for developing biomechanical models of skin. Existing methods cannot provide sufficient accuracy [10–12], or require the addition of textured patterns to the skin [13–15]. In this paper, we have addressed these limitations using a novel subpixel image registration algorithm (P-SG-GC) [18]. An experimental setup was created (Fig. 1) for validating P-SG-GC with a flat target and a linear translational stage. A series of translational shifts (5, 10, 100, 500, 1000, 1500, and 2000 μm) were applied to the target, which were then measured by comparing the original and undistorted initial and shifted images using P-SG-GC with subimages of size 64 × 64 pixel. The lens distortion effects (Fig. 3) were corrected in the images, which resulted in more accurate displacement measurements (Fig. 2).

The results showed a high degree of linearity between the physical and estimated shifts (Fig. 4). Furthermore, the measurements had small standard deviation values compared to the applied displacements (Fig. 5). These results indicate the high accuracy of the P-SG-GC algorithm. Increasing the subimage size from 64 to 128 pixel would further decrease this error, although this would also decrease the localised spatial resolution of the displacement estimates.

The P-SG-GC algorithm was used to find the deformation of the skin of a volunteer's hand (Fig. 6). The result showed that P-SG-GC could measure the skin displacements from subpixel values (0.01 pixel) to values larger than 18 pixels (Fig. 7) using subimages of size 64 × 64 pixel. Even though the skin in this example did not have obvious image features, P-SG-GC could estimate the displacements using only intrinsic textures.

The measurements of this study were all performed in 2D using a single camera. In future, a stereoscopic system will be used to measure 3D skin deformations, and the measurements will be compared with the estimation of finite element models of skin.

References

1. Junker JPE, Philip J, Kiwanuka E, Hackl F, Caterson EJ, Eriksson E (2014) Assessing quality of healing in skin: review of available methods and devices. Wound Repair Regen 22(Suppl 1):2–10
2. Pawlaczyk M, Lelonkiewicz M, Wieczorowski M (2013) Age-dependent biomechanical properties of the skin. Postępy Dermatol Alergol 30:302–306
3. Miura N, Arikawa S, Yoneyama S, Koike M, Murakami M, Tanno O (2012) Digital image correlation strain analysis for the study of wrinkle formation on facial skin. J Solid Mech Mater Eng 6:545–554
4. Flynn C, Taberner A, Nielsen P (2011) Modeling the mechanical response of in vivo human skin under a rich set of deformations. Ann Biomed Eng 39:1935–1946
5. Jor JWY, Parker MD, Taberner AJ, Nash MP, Nielsen PMF (2013) Computational and experimental characterization of skin mechanics: identifying current challenges and future directions. Wiley Interdiscip Rev Syst Biol Med 5:539–556
6. Kvistedal YA, Nielsen PMF (2009) Estimating material parameters of human skin in vivo. Biomech Model Mechanobiol 8:1–8
7. Li J, Liu H, Althoefer K, Seneviratne LD (2012) A stiffness probe based on force and vision sensing for soft tissue diagnosis. Proc Annu Int Conf IEEE Eng Med Biol Soc EMBS 1:944–947
8. Diridollou S, Patat F, Gens F, Vaillant L, Black D, Lagarde JM, Gall Y, Berson M (2000) In vivo model of the mechanical properties of the human skin under suction. Skin Res Technol 6:214–221
9. Pailler-Mattei C, Bec S, Zahouani H (2008) In vivo measurements of the elastic mechanical properties of human skin by indentation tests. Med Eng Phys 30:599–606
10. Fan Z, Samuel Q, Ilana BS, William N, Allison RP (2014) Sensory substitution using 3-Degree-of-Freedom tangential and normal skin deformation feedback. 2014 IEEE Haptics Symposium. 1–1
11. Flynn C, Taberner AJ, Nielsen PMF, Fels S (2013) Simulating the three-dimensional deformation of in vivo facial skin. J Mech Behav Biomed Mater 28:484–494
12. Mahmud J, Evans SL, Holt CA (2012) An innovative tool to measure human skin strain distribution in vivo using motion capture and delaunay mesh. J Mech 28:309–317
13. Sasaki A, Hashimoto H (2013) Measurement of hand skin deformation in dexterous manipulation. In: IECON 2013-39th Annual Conference of the IEEE Industrial Electronics Society, pp 8306–8311
14. Kacenjar S, Chen S, Jafri M, Wall B, Pedersen R, Bezozo R (2013) Near real-time skin deformation mapping. SPIE-IS&T 8655, pp 86550G-1–86550G-14
15. Tepole AB, Gart M, Gosain AK, Kuhl E (2014) Characterization of living skin using multi-view stereo and isogeometric analysis. Acta Biomater 10:4822–4831
16. Hajirassouliha A, Taberner AJ, Nash MP, Nielsen PMF Subpixel phase-based image registration using Savitzky-Golay differentiators in gradient-correlation. IEEE Trans Image Process (Under Review)
17. Pan B, Qian K, Xie H, Asundi A (2009) Two-dimensional digital image correlation for in-plane displacement and strain measurement: a review. Meas Sci Technol 20:62001
18. Hajirassouliha A, Taberner AJ, Nash MP, Nielsen PMF Subpixel Phase-based image registration using Savitzky-Golay differentiators in gradient-correlation. IEEE Trans Image Process (Under Review)
19. Wöhler C (2013) 3D computer vision: efficient methods and applications. Springer, London, p 5

Three-Dimensional Glenohumeral Joint Kinematic Analyses from Asynchronous Biplane Fluoroscopy Using an Interpolation Technique

Mohsen Akbari-Shandiz, Joseph D. Mozingo, David R. Holmes III, and Kristin D. Zhao

1 Introduction

The use of biplane fluoroscopic systems has become increasingly popular for evaluating joint kinematics in vivo [1–6]. Glenohumeral joint kinematics can be quantified from biplane fluoroscopic images using radiostereometric analysis (RSA) or a 3D–2D registration approach. *Custom* biplane fluoroscopic systems, which are not FDA-approved for clinical use, have been commonly used for these approaches [2, 7]. *Clinical* biplane systems are FDA-approved but are inherently not well-suited for biplane analyses due to the fact that images are acquired asynchronously. Asynchrony in image acquisition has the advantage of reducing cross-scattering effects of one X-ray source onto the other [8]; however, asynchronous acquisition introduces errors into the registration process, as there is joint movement between the two asynchronous images. Moreover, the magnitude of the error depends on the speed of movement which is not known prior to the scan and the fluoroscopy frame rate. Thus, achieving accurate 3D kinematics using conventional techniques on temporally offset data sets is challenging.

In the present study, our goal was to improve the accuracy of image registration by generating simulated corresponding fluoroscopy images. We introduce an interpolation algorithm to generate missing images in biplane image sequences thus producing interpolated-synchronous image pairs. The main objective of this study

M. Akbari-Shandiz • J.D. Mozingo • K.D. Zhao (✉)
Assistive and Restorative Technology Laboratory, Rehabilitation Medicine Research Center, Department of Physical Medicine and Rehabilitation, Mayo Clinic, Rochester, MN, USA
e-mail: Zhao.Kristin@mayo.edu

D.R. Holmes III
Biomedical Imaging Resource, Department of Physiology and Biomedical Engineering, Mayo Clinic, Rochester, MN, USA

A. Wittek et al. (eds.), *Computational Biomechanics for Medicine*,
DOI 10.1007/978-3-319-54481-6_9

was to validate the proposed approach using an artificial shoulder model and clinical biplane fluoroscope. We performed a quantitative comparison of 3D–2D registration using (a) asynchronous biplane image registration and (b) interpolated-synchronous biplane image registration.

2 Methods

2.1 Image Acquisition

We imaged radiopaque humerus and scapula bone models (Reference part #1020-100-1, Sawbones, Pacific Research Laboratories) with radiopaque beads rigidly attached to the surface of each. Seven and nine beads were fixed on the humerus and scapula, respectively. A clinical flat-panel biplane fluoroscope (Siemens Artis Zee; Forchheim Germany) was used for all 2D imaging. The scapula was fixed in a custom apparatus that allowed free movement of the humerus (Fig. 1), and the glenohumeral joint was centered in the imaging volume of the biplane fluoroscope. Biplane radiographic images of the shoulder were acquired at 30 frames/s (15 frames/s temporally offset for each source; an oscilloscope was used to check the offset for the biplane system and to ascertain if it was constant), while manually elevating the humerus relative to the scapula in the frontal plane (approximately 2.66 s from rest to full elevation).

Fluoroscopic images were also acquired at multiple static humeral elevation angles (73 kVp, plane 1: 39 mA, plane 2: 92 mA) using the custom apparatus to evaluate the effect of calibration error. This will be explained in more detail below.

The flat-panel detectors remained stationary and were positioned 90° from each other for all image acquisitions. A custom calibration cube was imaged using the fluoroscopic setup to define the orientation of the X-ray sources and detectors. Following fluoroscopic imaging, CT imaging was acquired on a clinical CT scanner

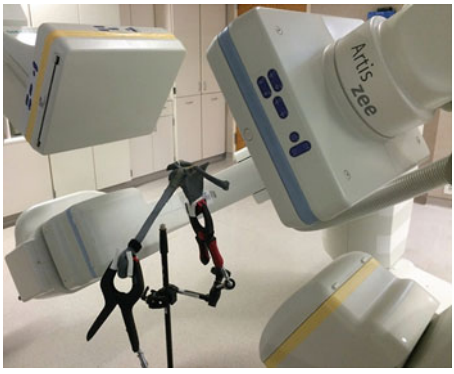

Fig. 1 Sawbones radiopaque shoulder bone model, fixed in a custom apparatus, was imaged using a clinical biplane fluoroscope, while manually elevating the humerus relative to the scapula

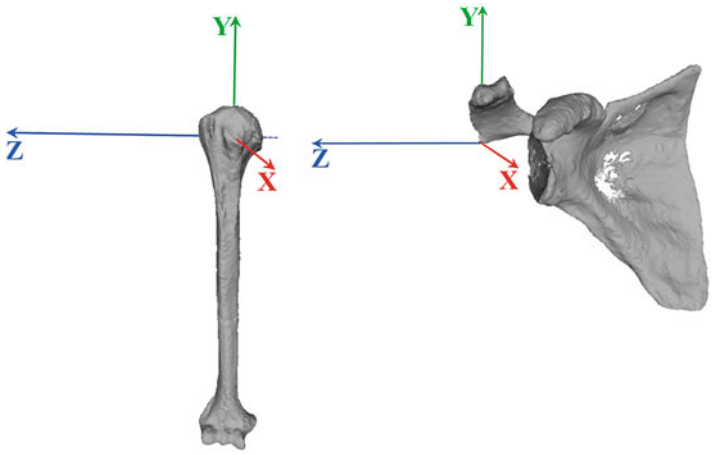

Fig. 2 Humerus and scapula coordinate systems based on ISB recommendations

(Siemens Definition FLASH; Forchheim, Germany), with slice thickness: 1 mm; kVp: 140; FOV: 426 mm; and pixel image size: 512 × 512, to obtain the 3D bone models and 3D positions of the beads.

2.2 Image Analysis

3D models of the humerus and scapula were manually segmented from reconstructed CT volumes (AnalyzePro; Mayo Clinic). Coordinate systems were computed for each 3D bone model using anatomical features as recommended by the International Society of Biomechanics (ISB) as shown in Fig. 2 [9]. Forty paired biplane digital fluoroscopic images, corresponding to one elevation movement, were analyzed.

To quantify bone rotations and translations, the 3D–2D image registration was performed using open-source software (JointTrack Biplane, sourceforge.net/projects/jointtrack/) [10]. To perform a comparison between 3D–2D registration and RSA analysis, the 3D positions of the beads were determined relative to the bone coordinate systems by segmenting them directly from the CT volumes.

The 3D positions of the beads were tracked from the biplane fluoroscopy images using a freely available software (XMA Lab; Brown University) [11], and then used to calculate frame-by-frame motion for each bead set and thus the corresponding bone model.

Asynchronous Biplane Registration

To quantify bone rotations and translations, the 3D bone models were registered to each set of two biplane images under the assumption that they were synchronous, despite the joint movement between the two asynchronous images (Fig. 4a). The 3D positions of the beads were also determined from the asynchronous biplane images using the RSA technique.

Generating Interpolated Images

Since the proposed method relies on generating interpolated images from the 3D data, a contour projection algorithm was developed. Following the segmentation of the CT image volumes, the 3D bone models are defined as a set of vertices and triangle meshes. The silhouette of the 3D bone models were identified by the contour edges, which are common sides of triangle meshes that have the normal pointing in opposite directions from the X-ray source (Fig. 3) [12]. The silhouette was then projected on the image plane to create the missing images. A Matlab script (version 9.0.0.341360 (R2016a), The Mathworks Inc., Natick, Massachusetts) was used to identify the silhouette of each bone model and project it onto the image plane to create the missing images. Since JointTrack software uses a contour-based registration technique, the projection of the silhouette of the bone models is enough for the image registration.

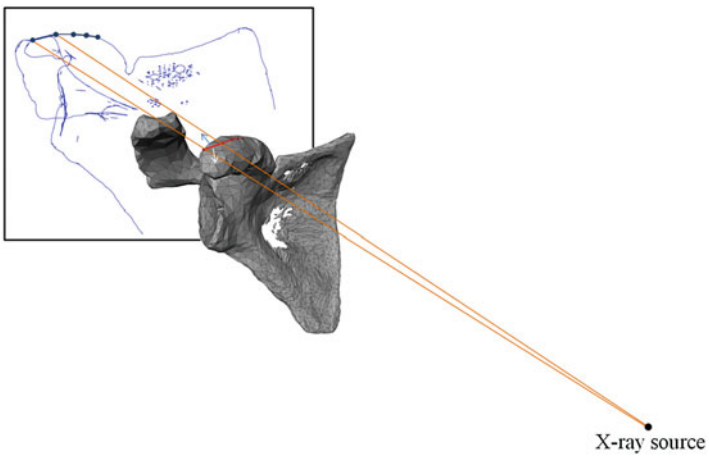

Fig. 3 2D perspective silhouette of bone models was projected to create simultaneous corresponding fluoroscopy images

Semi-Synchronous Biplane Registration

In the proposed interpolation algorithm, the bone models were registered independently to each view from two X-ray sources. The bone kinematics from sets of two successive images for view 1 (X-ray source 1) were measured using single plane image registration and then interpolated to determine the bone pose at the time between the two acquisition times (Fig. 4b). Pose interpolation was performed as the interpolation of rigid body transformations between two registrations. First, the rigid body transformations were converted to kinematic parameters (three translations along and three rotations around X, Y, and Z axes). Then each kinematic parameter was averaged between two registrations, assuming the bone models moved with no acceleration during each time interval to determine the interpolated pose.

Since the single plane registration accuracy for in-plane bone translation and rotation is much higher than the registration accuracy for the out-of-plane motions, the interpolated pose is only reliable in the in-plane direction for the corresponding view (view 1 in this case). We can therefore project the bone model with the new interpolated pose, given the known position of the view 1 source and detector and the surface geometry of the bone models. This generates the missing image which coincides with the corresponding fluoroscopy images from view 2 (Fig. 4b). The same process was repeated for view 2 (Fig. 4c). The 3D bone models were then matched to each set of interpolated-synchronous biplane images in order to determine the joint movement (Fig. 4d). The same technique was used for the RSA analysis in order to generate interpolated-synchronous biplane images of the beads.

2.3 Comparison Analysis

Since our RSA (gold standard) results were also determined from the interpolated-synchronous biplane images, we first needed to evaluate the accuracy of the RSA results. We measured reprojection error as an indication of the accuracy of the RSA for the two registration methods. The reprojection error is a geometric error corresponding to the image distance between a projected point and a measured one and is used to quantify how closely an estimate of a 3D point recreates the point's true projection. However, the reprojection error contains the calibration error, in addition to the error due to the asynchronous acquisition. To measure the reprojection error due to the calibration error alone, we analyzed images that were acquired statically at multiple static humeral elevation angles. Static images can be assumed as synchronous biplane images, considering no object motion occurs between the acquisitions.

We evaluated the accuracy of the 3D–2D registration by computing the absolute error between the 3D–2D registration results and the RSA analysis, for each of six poses (three positions and three orientations) of the humerus and scapula, in each image pair.

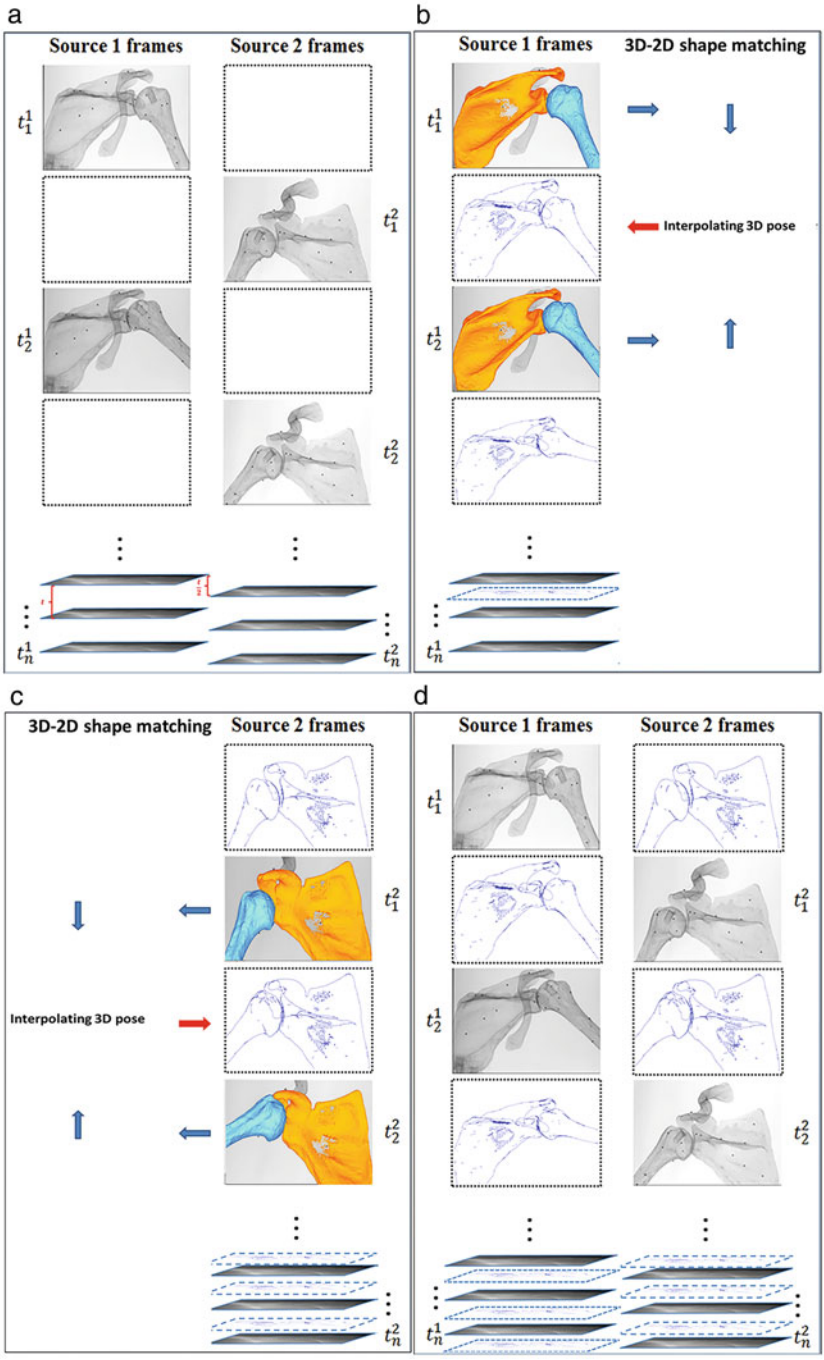

Fig. 4 An interpolation algorithm was used to generate the missing images in biplane image sequences to produce interpolated-synchronous image pairs: (**a**) asynchronous biplane images; (**b**) generate missing images in view 1; (**c**) generate the missing images in view 2; (**d**) interpolated-synchronous biplane images

3 Results

For the asynchronous RSA analysis, mean reprojection error of all the beads was 1.0 ± 0.7 pixel (max 4 pixels), compared to the 0.4 ± 0.3 pixel (max 1.7 pixels) error for the interpolated-synchronous RSA analysis. The average reprojection error due to the calibration error alone was 0.06 ± 0.05 pixel (max 0.2 pixels).

For the asynchronous biplane acquisition, the mean absolute error between the 3D–2D registration approach and the RSA analysis were 0.42 ± 0.03 mm and 1.03 ± 0.22° (max error: 1.24 mm and 5.73°) for the humerus, and were 0.37 ± 0.04 mm and 0.28 ± 0.03° (max error: 1.43 mm and 1.11°) for the scapula.

For the interpolated-synchronous biplane acquisition, the mean absolute error between the 3D–2D registration approach and the RSA analysis were 0.18 ± 0.01 mm and 0.4 ± 0.13° (max: 0.6 mm and 1.7°) for the humerus and were 0.25 ± 0.02 mm and 0.17 ± 0.02° (max: 0.9 mm and 0.7°) for the scapula. The absolute error for all frames is shown for each kinematic variable in Fig. 5.

4 Discussion

The notion of registering fluoroscopic images to 3D data has been studied for several decades. Early findings are reported in [13]. Many approaches have been proposed; however, nearly all of them assume synchrony between images. Single plane approaches have been proposed where the third dimension is geometrically modeled [14]; however, errors were high [15]. Moreover, when motion is introduced the accuracy of 3D bone pose, reconstructed from either the RSA technique or the 3D–2D image registration, is even more influenced by the synchronicity of the biplane images.

Our studies showed that the introduced interpolation algorithm improves this accuracy by creating interpolated-synchronous biplane images. The interpolated-synchronous biplane registration was expected to perform superiorly. With 3D–2D image registration, movement of the bone models along the out of plane axis produces relatively little change in the model projection. By using the simultaneous image pair, registration in one view serves to correct the depth estimate in the other, and vice versa. The reprojection error in the RSA analysis due to asynchronous biplane acquisition was also reduced using the same interpolation technique. The interpolated-synchronous biplane registration technique produced average errors (0.18 mm and 0.4° for the humerus and 0.25 mm and 0.17° for the scapula) that are in the range of published results of other studies that have validated the 3D–2D registration technique at the shoulder using custom biplane (synchronous biplane) fluoroscopes [2, 3, 7]. Therefore, our interpolation approach is able to provide acceptable accuracy for shoulder kinematics. The difference between the two approaches becomes more pronounced with faster bone movement. This is suggested by the greater improvements in accuracy seen in humerus tracking

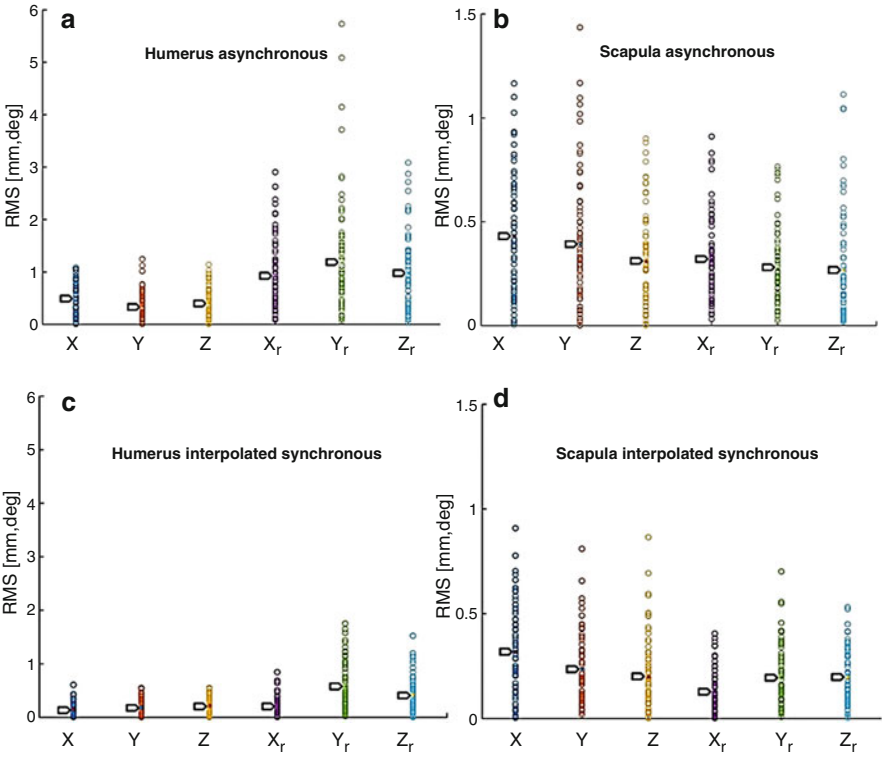

Fig. 5 The frame-to-frame absolute error (*circles*) and mean absolute error (*arrows*) for each kinematic variable (X: anterior–posterior translation; Y: superior–inferior translation; Z: medial–lateral translation; X_r: elevation (abduction–adduction); Y_r: axial rotation, Z_r: flexion–extension) at different elevation angles: (**a**) humerus kinematics from asynchronous; (**b**) scapula kinematics from asynchronous; (**c**) humerus kinematics from interpolated-synchronous; (**d**) scapula kinematics from interpolated-synchronous registration

compared to the scapula, which underwent slower movement. One limitation of the study is that we assumed the bone models moved with no acceleration in each time interval. However, this was an acceptable assumption for the small time intervals between two successive frames and the movement velocity examined in this study.

In order to quantitatively demonstrate the accuracy of the proposed method, this study was conducted with artificial bone models and a single shoulder activity. Results may differ for a human shoulder joint with surrounding soft tissue, and with different shoulder motions. To address some of these issues an intensity-based registration scheme may be used where a CT image is registered to the X-ray images by comparison of the pixel intensity between digitally reconstructed radiographs (DRR) and the X-ray image [2]. The use of an intensity-based registration approach also reduces the dependency of registration on the accuracy of segmentation [16].

Future work includes the investigation of accuracy of the proposed technique in different shoulder activities using a cadaveric model and the addition of digitally reconstructed radiographs (DRRs) to our protocol for intensity-based 3D–2D image registration. The introduced interpolation algorithm would be applicable to a variety of 3D–2D registration applications, and is of interest to activities with fast bone movements.

Acknowledgments We wish to thank Mark Hindal for his assistance with the study. We gratefully acknowledge funding from the Minnesota Partnership for Biotechnology and Medical Genomics (MNP IF #14.02).

References

1. Brainerd EL, Baier DB, Gatesy SM, Hedrick TL, Metzger KA, Gilbert SL, Crisco JJ (2010) X-ray reconstruction of moving morphology (XROMM): precision, accuracy and applications in comparative biomechanics research. J Exp Zool 313:262–279
2. Bey MJ, Zauel R, Brock SK, Tashman S (2006) Validation of a new model-based tracking technique for measuring three-dimensional, in vivo glenohumeral joint kinematics. J Biomech Eng 128:604–609
3. Zhu Z, Massimini DF, Wang G, Warner JJP, Li G (2012) The accuracy and repeatability of an automatic 2D-3D fluoroscopic image-model registration technique for determining shoulder joint kinematics. Med Eng Phys 34:1303–1309
4. Li G, Suggs J, Hanson G, Durbhakula S, Johnson T, Freiberg A (2006) Three-dimensional tibiofemoral articular contact kinematics of a cruciate-retaining total knee arthroplasty. J Bone Joint Surg Am 88:395–402
5. Iaquinto JM, Tsai R, Haynor DR, Fassbind MJ, Sangeorzan BJ, Ledoux WR (2014) Marker-based validation of a biplane fluoroscopy system for quantifying foot kinematics. Med Eng Phys 36:391–396
6. Miranda DL, Schwartz JB, Loomis AC, Brainerd EL, Fleming BC, Crisco JJ (2011) Static and dynamic error of a biplanar videoradiography system using marker-based and Markerless tracking techniques. J Biomech Eng 133:121002
7. Massimini DF, Warner JJP, Li G (2011) Non-invasive determination of coupled motion of the scapula and humerus-an invitro validation. J Biomech 44:408–412
8. Cross JA, McHenry B, Schmidt TG (2015) Quantifying cross-scatter contamination in biplane fluoroscopy motion analysis systems. J Med Imaging 2:043503
9. Wu G, Van Der Helm FCT, Veeger HEJ, Makhsous M, Van Roy P, Anglin C, Nagels J, Karduna AR, McQuade K, Wang X, Werner FW, Buchholz B (2005) ISB recommendation on definitions of joint coordinate systems of various joints for the reporting of human joint motion – part II: shoulder, elbow, wrist and hand. J Biomech 38:981–992
10. Mu S (2007) JointTrack: an open-source, easily expandable program for skeletal kinematic measurement using model-image registration. http://ufdc.ufl.edu/UFE0021784/00001
11. Knorlein BJ, Baier DB, Gatesy SM, Laurence-Chasen JD, Brainerd EL (2016) Validation of XMALab software for marker-based XROMM. J Exp Biol 219(Pt 23):3701–3711
12. Valenti M, de Momi E, Yu W, Ferrigno G, Akbari Shandiz M, Anglin C, Zheng G (2015) Fluoroscopy-based tracking of femoral kinematics with statistical shape models. Int J Comput Assist Radiol Surg 11(5):1–9
13. Lavallee S, Szeliski R, Brunie L (1993) Matching 3D smooth surfaces with their 2D projections using 3D distance maps. Geom Reason Percept Action 708:217–238

14. Fregly BJ, Rahman HA, Banks SA (2005) Theoretical accuracy of model-based shape matching for measuring natural knee kinematics with single-plane fluoroscopy. J Biomech Eng 127:692–699
15. Banks SA, Hodge WA (1996) Accurate measurement of three-dimensional knee replacement kinematics using single-plane fluoroscopy. IEEE Trans Biomed Eng 43:638–649
16. Chang CJ, Lin GL, Tse A, Chu HY, Tseng CS (2015) Registration of 2D C-arm and 3D CT images for a C-arm image-assisted navigation system for spinal surgery. Appl Bionics Biomech 2015:1–9

An Evaluation of Adaptive Biomechanical Non-Rigid Registration for Brain Glioma Resection Using Image-Guided Neurosurgery

Fotis Drakopoulos, Chengjun Yao, Yixun Liu, and Nikos Chrisochoides

1 Introduction

Malignant gliomas are the most common primary brain tumors, accounting for approximately 70% of the 22,500 new cases of primary brain tumors annually diagnosed in adults in the USA [1]. The heterogeneity and infiltrative nature of gliomas suggests that a resection within or adjacent to the eloquent areas is challenging and carries a risk of post-operative neurologic deficit [2]. Therefore, the main challenge for neurosurgeons in glioma surgery is to achieve a maximal tumor resection while still preserving eloquent areas.

Image-guided neurosurgery (IGNS) has yielded faster, safer, and more effective minimally invasive procedures [3–8]. During the procedure (i.e., after the opening of the skull and dura), the shape of the brain changes because of the cerebrospinal fluid drainage, gravity, the application of dehydrolyzing agent, and other operations (i.e., resection, retraction), introducing discrepancies in relation to the pre-operative configuration. Interventional MRI can compensate for the intra-operative brain deformation. However, the acquisition of other image modalities (fMRI, DT-MRI) is impractical due to long processing time (e.g., a 3T MAGNETOM Verio scanner requires about 20 min to acquire a DT-MRI and more than 30 min to acquire a BOLD fMRI).

Commonly, commercial systems exclusively use rigid registration to project the pre-operatively acquired imaging (MRI, fMRI, and DT-MRI) into the navigational system; however, a number of studies have tracked surface points in the brain

F. Drakopoulos • Y. Liu • N. Chrisochoides (✉)
The Department of Computer Science, Old Dominion University, Norfolk, VA, USA
e-mail: npchris@gmail.com

C. Yao
The Department of Neurosurgery, Huashan Hospital, Shanghai, China

A. Wittek et al. (eds.), *Computational Biomechanics for Medicine*,
DOI 10.1007/978-3-319-54481-6_10

and reported that movements on the order of a centimeter or more can occur intra-operatively [9]. Additionally, shift can occur in deep subcortical white matter because of tissue retraction, lateral ventricle, and the application of a dehydrolyzing agent. Therefore, a non-rigid registration is necessary to accurately capture the soft tissue deformation induced by tumor resection.

A commonly used non-rigid transformation model is based on the finite element method (FEM). FE biomechanical models allow more principled control of localized deformations and have been applied to improve the efficacy and efficiency of brain surgery [3–8, 10–13]. An FE model is represented by a series of Partial Differential Equations (PDEs), which describe the physical deformation of the underlying tissues. The tissues are delineated in the image by using a segmentation technique [14, 15]. The segmented image is tessellated into a volumetric mesh and each element is assigned to a local physical description of the anatomical structure to which it belongs. To find the numerical solution of the PDEs, constraints are applied to the model, and a linear system of equations is solved to compute the displacements on the mesh vertices. A dense deformation field can be estimated by interpolating the computed mesh displacements at each image voxel.

Meshless methods have been presented as alternatives to FE methods. A Meshless Total Lagrangian Explicit Dynamics (MTLED) algorithm was developed to compute soft tissue deformation in surgical simulation [16]. This method was accurate in terms of overall reaction forces but not quite as good with individual displacements or forces. In [17] a MTLED-based suite of algorithms was used to perform a comprehensive patient-specific surgical simulation. The results obtained using MTLED were as useful and accurate as those obtained with the FE method.

The produced non-rigid transformation can be useful to create augmented reality visualizations of pre-operative multi-modal imaging (MRI, fMRI, DT-MRI) with iMRI, and thus to facilitate real-time resection guidance in glioma surgery involving language areas and neighboring subcortical motor pathways (e.g., Pyramid Tracts). Figure 1a depicts such a visualization. The DTI tractography is shown in real-time together with a tumor model (red) during the neurosurgical resection.

The augmented reality visualization helps neurosurgeon to achieve an appropriate volumetric resection while preserving neighboring subcortical motor pathways.

The aim of this paper is to evaluate the efficiency (i.e., accuracy, robustness) of two adaptive biomechanical non-rigid registration methods [3, 4] to compensate for the brain deformation induced by cerebral glioma resection. The first method employs a point/element outlier rejection scheme integrated into a Nested Expectation and Maximization framework to simultaneously resolve the point correspondence, the deformation field, and the resection region. The second approach iteratively estimates a dense deformation field by inclemently and accurately incorporating small changes in the geometry of the domain resulted by tumor resection. The evaluation performed on MRI data from ten patients who underwent partial, complete, and extended glioma resection at Huashan Hospital. Structural MRI (SPGR, MP-RAGE, FLAIR, T2w) were acquired prior and during each surgery

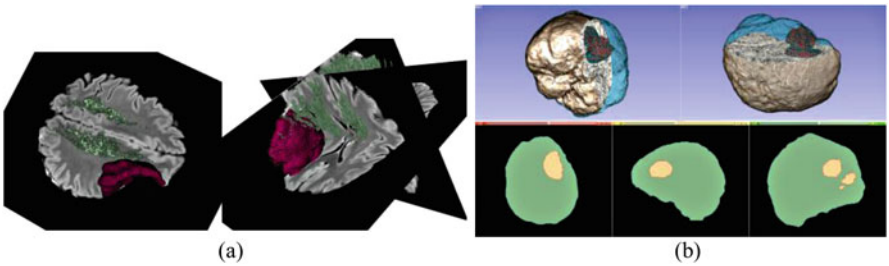

Fig. 1 (**a**) Non-rigid alignment of pre-operative DTI tractography with iMRI. The fused image shows that the partially resected tumor is directly adjacent to the Pyramid Tracts. (**b**) Multi-tissue mesh (number of tetrahedra: 160,179; minimum dihedral angle: 4.41°). Top row: mesh superimposed on MRI. *Cyan* and *red* represent the surface of the brain parenchyma mesh and the tumor mesh, respectively. Bottom row: mesh fidelity illustrated on an axial, sagittal, and coronal slice. Each slice depicts an intersection between the mesh surface (*cyan and red lines*) and the segmented volume (*green and yellow regions*). The closer the mesh surface to the physical image boundaries, the higher the mesh fidelity

with a 3T movable scanner. The registration accuracy was assessed on totally 40 volumetric alignments by: (i) a visual inspection, (ii) a Hausdorff Distance (HD)-based error metric, and (iii) a landmark-based error measured by neurosurgeon.

2 Materials and Methods

2.1 Patient Population

Ten patients with an age range of 19–75 years underwent surgery on a single, unilateral, and supratentorial primary glioma from September 2010 to August 2013. The lesions involved in Pyramid Tracts (PTs) were in cortical regions in the motor or somatosensory areas, cortical regions adjacent to the central gyrus, subcortical regions with an infiltrative progression along the PTs, and/or deep temporal or insular regions in relation to the internal capsule. Pre- and intra-operative brain images were obtained in the integrated neurosurgical suite (IMRIS, Winnipeg, Manitoba, Canada) using a ceiling-mounted movable 3.0 T MAGNETOM Verio scanner (Siemens AG, Erlangen, Germany) with a 70 cm working aperture. A neurosurgeon categorized the image data as: (i) Partial Tumor Resection (PTR), (ii) Complete Tumor Resection (CTR), and (iii) Extensive Tumor Resection (ETR). Table 1 lists the clinical data.

Table 1 Clinical MRI data

			Image Size (voxels)		Image Spacing (mm)	
#	Genre	Type	Pre-op	Intra-op	Pre-op	Intra-op
1	M	PTR	448 × 512 × 176	512 × 448 × 176	0.488 × 0.488 × 1	0.488 × 0.488 × 1
2	M	PTR	448 × 512 × 80	512 × 456 × 66	0.468 × 0.468 × 2	0.468 × 0.468 × 2
3	M	PTR	448 × 512 × 176	512 × 448 × 176	0.488 × 0.488 × 1	0.488 × 0.488 × 1
4	M	CTR	512 × 448 × 176	512 × 448 × 176	0.488 × 0.488 × 1	0.488 × 0.488 × 1
5	F	CTR	448 × 512 × 176	448 × 512 × 176	0.488 × 0.488 × 1	0.488 × 0.488 × 1
6	M	CTR	448 × 512 × 176	384 × 512 × 144	0.488 × 0.488 × 1	0.488 × 0.488 × 1
7	M	ETR	448 × 512 × 144	448 × 512 × 144	0.488 × 0.488 × 1	0.488 × 0.488 × 1
8	F	ETR	512 × 456 × 66	456 × 512 × 66	0.468 × 0.468 × 2	0.468 × 0.468 × 2
9	F	ETR	512 × 456 × 66	512 × 456 × 68	0.468 × 0.468 × 2	0.468 × 0.468 × 2
10	M	ETR	448 × 512 × 176	448 × 512 × 176	0.488 × 0.488 × 1	0.488 × 0.488 × 1

PTR partial tumor resection, *CTR* complete tumor resection, *ETR* extensive tumor resection

2.2 Segmentation

The biomechanical non-rigid registration in this study requires a pre-operative segmentation. Pre-operative imaging is usually acquired few days before the first intra-operative acquisition, therefore any computational requirements of a pre-operative segmentation are easily satisfied. Before the segmentation, the brain is extracted from the skull using the BET tool [14]. Then a combination of automatic operators implemented in 3D Slicer (i.e., region growing and level-set filters) [15] and a slice-by-slice manual segmentation is performed to correct any erroneously included regions. An evaluation on how the segmentation accuracy affects the registration accuracy is beyond the scope of this paper, however, it will be included in our future work.

2.3 Rigid Registration

The first intra-operative scan is acquired after the head of the patient is positioned for the craniotomy and fixed but before the opening of the skull. At this stage no brain shift occurs. A Rigid Registration (RR) was performed with the BRAINSFit module in 3D Slicer v4.4.0 [18] to compensate for any translations or rotations between the pre- and the intra-operative image. RR uses a Versor Rigid 3D Transform (VR3DT) to apply a rotation and translation to the space. RR relies on histogram bins and spatial samples to estimate a Mattes Mutual Information (MMI) cost metric for the alignment. The larger the number of samples, the slower and more precise the fit. In order to achieve higher accuracy, we set 100 histogram levels and 5% sampling percentage (50 and 0.2% are the default values, respectively). For the rest of the RR parameters we used the default values.

2.4 Adaptive Non-Rigid Registration

The last 10 years we explored the feasibility of three biomechanical non-rigid registration methods to compensate for the brain deformation induced by tumor resection: (i) A Physics-Based Non-Rigid Registration (PBNRR) integrated on ITK and 3D Slicer [19]; (ii) A Nested Expectation-Maximization Non-Rigid Registration (NEMNRR) [3, 20]; (iii) An Adaptive Physics-Based Non-Rigid Registration (APBNRR) [4, 21]. NEMNRR, and APBNRR are adaptive; PBNRR is non-adaptive.

The above non-rigid registration methods do not simulate the skull or an interaction between the brain parenchyma and the skull. Before the registration, the pre-operative and the intra-operative intracranial brain cavities are extracted from the skull [14]. A sparse displacement field is computed from the distances between features in the pre-operative intracranial cavity and their corresponding features in the intra-operative intracranial cavity. PBNRR and APBNRR rely on a cross correlation metric to compute the corresponding features. NEMNRR relies on a Gaussian distribution function. A tetrahedral mesh of the brain parenchyma is generated from a segmented pre-operative intracranial cavity and the sparse displacement field is applied on the mesh nodes. The prescribed displacement field implicitly accounts for a brain–skull interaction in the case where corresponding features are located on the surface of the brain parenchyma. In this study, the nodes on the parenchyma surface are free to translate in three-dimensions as no explicit interaction between the brain and the skull is assumed.

A linear assumption is used for the displacements and the materials of the model. The values of the mechanical properties of the isotropic materials (i.e., Young's modulus, Poisson ratio) were obtained from [8]. These values were extrapolated from best-fit data obtained in porcine studies. For tumor, a value ten times stiffer than that for normal tissue is used (Table 2). The adaptive methods employ a heterogeneous model (brain parenchyma, tumor). The non-adaptive method employs a homogeneous model (brain parenchyma). The quality of the tetrahedral mesh (e.g., dihedral angle) influences the accuracy of the numerical solution of a linear system of equations and thus, the correctness of the estimated transformation. The higher the quality of the elements (e.g., the larger the minimum dihedral angle), the better the conditioning of the coefficient matrix and, consequently, the convergence of the linear solver. Figure 1b depicts a multi-tissue mesh used for biomechanical non-rigid registration. Parameter δ (Table 2) determines the size of the mesh ($\delta > 0$).

NEMNRR formulates the registration as a three-variable (point correspondence, deformation field, and resection region) functional minimization problem, in which point correspondence is represented by a fuzzy assign matrix, deformation field is represented by a piecewise linear function regularized by the strain energy of a heterogeneous biomechanical model, and resection region is represented by a maximal connected tetrahedral mesh. This method utilizes a point/element outlier rejection incorporated into a Nested Expectation and Maximization framework to simultaneously resolve these three variables. Figure 2 illustrates the NEMNRR framework.

Table 2 Parameters for non-rigid registration

Parameter	Value	Description	Method
Connectivity pattern	face	Pattern for block selection	PBNRR, APBNRR
F_s	5%	% selected blocks from total number of blocks	PBNRR, APBNRR
$B_{s,x} \times B_{s,y} \times B_{s,z}$	$3 \times 3 \times 3$	Block size (in voxels)	PBNRR, APBNRR
$W_{s,x} \times W_{s,y} \times W_{s,z}$	$9 \times 9 \times 3$ (PTR), $13 \times 13 \times 3$ (CTR, ETR)	Block matching window size (PBNRR, APBNRR) or Search range (NEMNRR) (voxels).	All
R	0.93	Annealing factor	NEMNRR
δ	5	Mesh size	All
E_b , ν_b	2.1 KPA, 0.45	Young's modulus, Poisson ratio for brain parenchyma	All
E_t , ν_t	21 KPA, 0.45	Young's modulus, Poisson ratio for tumor	NEMNRR, APBNRR
F_r	25%	% of rejected outlier blocks	PBNRR, APBNRR
N_{rej}	10	Number of outlier rejection steps	PBNRR, APBNRR
$N_{iter,.max}$	10	Max number of iterations	APBNRR
$N_{b0,min}$	1% of the total number of blocks	Minimum number of blocks without a correspondence	APBNRR

All: PBNRR, NEMNRR, APBNRR

APBNRR iteratively estimates a dense deformation field by inclemently and accurately incorporating small changes in the geometry of the domain resulted by tumor resection. The computation of the dense field is facilitated by a sparse displacement vector associated with highly discriminant blocks inside the cranial cavity, and a heterogeneous biomechanical model which describes the physical deformation of the brain. After each deformation, the quality of the elements deteriorates, and thus the model is globally re-meshed in real-time using a Delaunay meshing algorithm [22] to avoid the heavily distorted elements, and to recover the anatomical boundaries with geometric guarantees. Figure 3 illustrates the APBNRR framework. The model is globally re-meshed from a warped segmented image to capture not only the brain deformations but also the complex geometric changes nearby the tumor margins, while maintaining throughout the process meshes with good quality elements—critical for the accuracy and convergence rate of the solver.

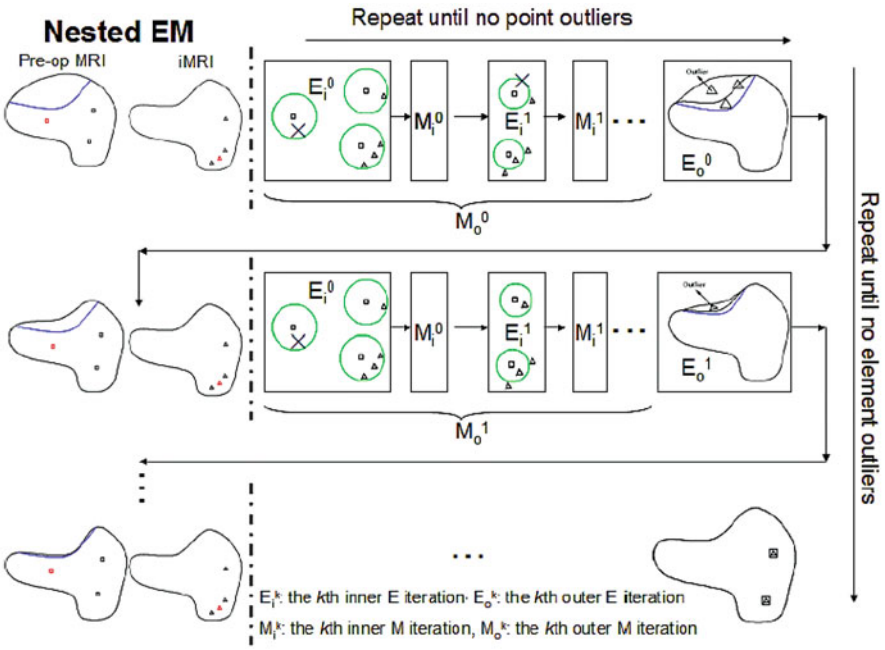

Fig. 2 Nested Expectation Maximization framework [3]. In the horizontal direction, the inner EM iteratively estimates the correspondence and the deformation field until no point outliers are detected. In the vertical direction the outer EM rejects the element outliers and computes the resected region

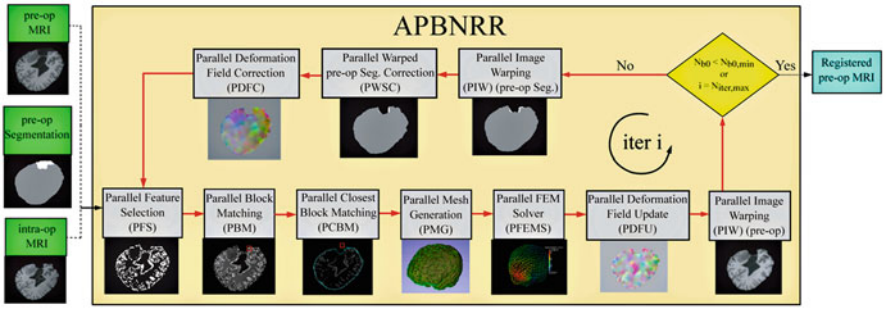

Fig. 3 APBNRR framework [4]. The red arrows show the execution order of the different modules in the loop. The loop breaks when the number of blocks without correspondence is less than a threshold or when the maximum number of iterations has been reached

3 Results

We performed an evaluation on imaging data from ten patients underwent partial, complete, and extended glioma resection. We assessed the registration accuracy with a visual inspection, a Hausdorff Distance (HD)-based error metric, and a landmark-based error measured by a neurosurgeon. Table 2 presents the parameters used for the non-rigid registration. More details about the parameters of each method are given in [3, 4, 19].

3.1 Visual Assessment

In most applications, careful visual inspection remains the first and most important validation check available for previously unseen data. Figure 4 depicts a qualitative assessment for six patients of this study. For each patient, we depict an intra-operative MRI, a registered pre-operative MRI, and a subtraction between the intra-operative and the registered pre-operative MRI. Based on Fig. 4, APBNRR aligns more accurately the MR images and preserves the brain morphology during the neurosurgical resection, especially near the tumor margins. The assessment shows that the quality of the alignments is not significantly affected by the volumetric resection (partial, complete, or extended). In contrast, the other methods show significant misalignments near the tumor cavities.

3.2 Quantitative Assessment with the HD Metric

We employed a publicly available implementation of the Hausdorff Distance (HD) metric [23] to quantitatively evaluate the registration accuracy. This metric is a measurement of the degree of mismatch between two point sets. The first set is extracted from the pre-operative volume, and then it is transformed according to the estimated deformation field. The second point set is extracted from the intra-operative volume. The HD metric is computed between the transformed point set and the fixed point set. For the point extraction, we employed a Canny edge detection implemented in ITK. Compare to a previous evaluation of the registration accuracy [5], this study uses the 100% HD metric. The smaller the HD value, the more precise the alignment ($HD \geq 0$). The ideal case with perfect alignment is when HD is equal to 0. The ratio $= HD_X/HD_Y$ denotes how many times more accurate one method is when compared to another. When ratio > 1 then method Y is ratio times more accurate than method X. Table 3 presents the results. We computed a total of 40 HD errors. APBNRR achieved the smallest error in each individual case, and the smallest average error (3.69 mm) among all the methods. APBNRR is on average, 6.83, 6.41, and 6.34 times more accurate compared to RR, PBNRR, and NEMNRR, respectively.

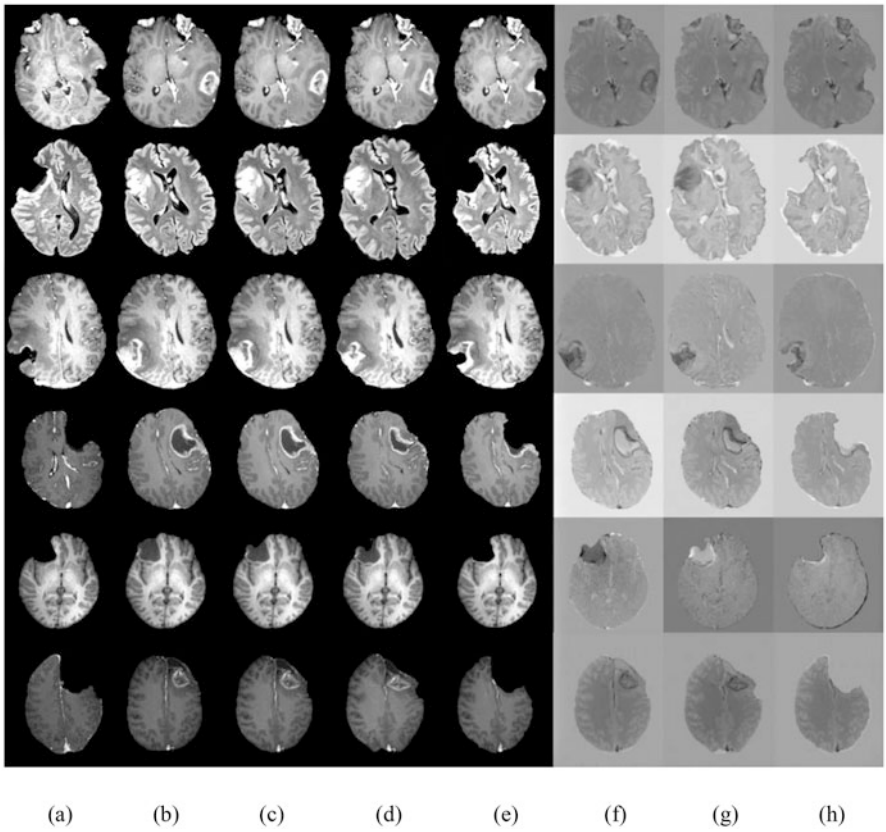

Fig. 4 Qualitative evaluation of the registration accuracy. *Each row* represents a single case. We depict the same representative slice for all the images belonging to the same row. The results were confirmed by a neurosurgeon who inspected the full registered volumes. From top to bottom row: PTR cases 1, 2; CTR cases: 4, 5; ETR cases: 7, 9. From left to right column: (**a**) intra-op MRI; (**b**) RR pre-op MRI; (**c**) PBNRR pre-op MRI; (**d**) NEMNRR pre-op MRI; (**e**): APBNRR pre-op MRI; (**f**): (**a**) subtracted from (**c**); (**g**): (**a**) subtracted from (**d**); (**h**): (**a**) subtracted from (**e**)

3.3 Quantitative Assessment with Anatomical Landmarks

A neurosurgeon quantitatively evaluated the alignment accuracy on six anatomical locations, as suggested in [24]. The neurosurgeon selected six landmarks in the pre-operative volume and identified their correspondent locations in the intra-operative volume. Two landmarks were selected at the cortex near the tumor depending on the shift of the brain surface; other two landmarks were selected at the anterior horn and at the triangular part of the lateral ventricle; the last two landmarks were selected at the junction between the pons and mid-brain and at the roof of fourth ventricle. For each landmark, the error was calculated as the distance between the physical location of the point in the intra-operative volume and its transformed location in

Table 3 Quantitative evaluation of the registration accuracy with a HD metric

Case	Type	HD_{RR}	HD_{PBNRR}	HD_{NEMNRR}	HD_{APBNRR}	$\frac{HD_{RR}}{HD_{APBNRR}}$	$\frac{HD_{PBNRR}}{HD_{APBNRR}}$	$\frac{HD_{NEMNRR}}{HD_{APBNRR}}$
1	PTR	16.15	15.12	15.08	4.60	3.51	3.29	3.28
2	PTR	26.89	26.89	23.87	4.00	6.72	6.72	5.97
3	PTR	29.93	27.76	28.11	2.83	10.58	9.81	9.93
4	CTR	17.90	15.56	16.84	4.11	4.36	3.79	4.10
5	CTR	30.37	28.96	28.96	3.13	9.70	9.25	9.25
6	CTR	23.22	21.44	21.27	3.08	7.54	6.96	6.91
7	ETR	17.59	16.63	15.20	4.19	4.20	3.97	3.63
8	ETR	32.32	30.13	30.20	3.45	9.37	8.73	8.75
9	ETR	18.48	18.15	17.86	3.97	4.65	4.57	4.50
10	ETR	27.07	24.91	25.16	3.54	7.65	7.04	7.11
Average		*23.99*	*22.56*	*22.26*	*3.69*	*6.83*	*6.41*	*6.34*

HD_{RR}, HD_{PBNRR}, HD_{NEMNRR}, and HD_{APBNRR} are the alignment error after an RR, PBNRR, NEMNRR, and APBNRR registration, respectively
PTR partial tumor resection, *CTR* complete tumor resection, *ETR* extensive tumor resection. All errors are in mm

Table 4 Quantitative evaluation of the registration accuracy with six anatomical landmarks identified by a neurosurgeon

Method	Average min error	Average max error	Average mean error
RR	3.49	11.96	7.27
PBNRR	1.72	9.94	5.38
NEMNRR	2.31	11.76	6.01
APBNRR	1.52	9.05	4.71

The values are the average minimum, maximum, and mean errors computed on the six anatomical locations, from ten patients. All errors are in mm

the registered volume. For each patient, we calculated a minimum, a maximum, and a mean error based on six landmarks. We then calculated their corresponding average errors for ten patients. Table 4 presents the results. The landmark-based assessment confirms that the APBNRR provides the most accurate alignments on the specific anatomical locations. APBNRR exhibits the lowest average mean error (4.71 mm) which may be clinically useful.

4 Conclusion

A retrospective study was carried out on volumetric MRI data acquired from ten patients. The patients underwent an incomplete, complete, and extensive glioma resection at Huashan Hospital. The accuracy of the alignments was assessed with a: (i) robust HD metric, (ii) anatomical points identified by a neurosurgeon, and (iii) visual assessment inspected by a neurosurgeon.

The experimental evaluation confirmed that a geometric-based adaptive deformable registration approach exhibits the most accurate alignments among all the methods in this study, independently of the volumetric resection (PTR, CTR, or ETR). This method significantly reduces the error due to rigid registration commonly used by commercial neuronavigators within the time constraints imposed by neurosurgery. Indeed, it completes a volumetric alignment, on the average, in 137.90 s (including I/O) on a Linux workstation with 12 Intel Xeon X5690@3.47 GHz CPU cores and 96 GB of RAM.

We observed differences between the alignment errors measured with a Hausdorff Distance metric and manually identified anatomical landmarks. We believe that, this is because the HD approach computes the degree of mismatch between two point sets A , B by measuring the distance of the point of A that is farthest from any point of B and vice versa, but there is no explicit pairing of points of A with points of B [25]. On the other hand, the landmark-based approach measures the Euclidian distance between two but corresponding points, though in some applications (e.g., inter-subject brain registration) the true point-to-point correspondence can never be known and may not even exist.

Acknowledgments Research reported in this publication was supported in part by the Modeling and Simulation Fellowship at Old Dominion University, CCF-1439079, John Simon Guggenheim Foundation, and by the Richard T. Cheng Endowment.

References

1. Louis David N, Hiroko O, Wiestler Otmar D, Cavenee Webster K, Burger Peter C, Anne J, Scheithauer Bernd W, Paul K (2007) The 2007 WHO classification of tumors of the central nervous system. J Acta Neuropathol 114(2):97–109
2. Evren Keles G, Chang EF, Lamborn KR, Tihan T, Chang C-J, Chang SM, Berger MS (2006) Volumetric extent of resection and residual contrast enhancement on initial surgery as predictors of outcome in adult patients with hemispheric anaplastic astrocytoma. J Neurosurg 105(1):34–40
3. Yixun L, Chengjun Y, Fotis D, Wu J, Liangfu Z, Nikos C (2014) A nonrigid registration method for correcting brain deformation induced by tumor resection. Med Phys 41(101710)
4. Drakopoulos F, Chrisochoides NP (2015) Accurate and fast deformable medical image registration for brain tumor resection using image-guided neurosurgery. Comput Methods Biomech Biomed Eng Imaging Visual 4(2):112–126
5. Archip N, Clatz O, Whalen S, Kacher D, Fedorov A, Kot A, Chrisochoides N, Jolesz F, Golby A, Black PM, Warfield SK (2007) Non-rigid alignment of pre-operative MRI, fMRI, and DT-MRI with intra-operative MRI for enhanced visualization and navigation in image-guided neurosurgery. NeuroImage 35(2):609–624
6. Clatz O, Delingette H, Talos IF, Golby A, Kikinis R, Jolesz F, Ayache N, Warfield S (2005) Robust non-rigid registration to capture brain shift from intraoperative mri. IEEE Trans Med Imaging 24(11):1417–1427
7. Michael MI (2015) Computational modeling for enhancing soft tissue image guided surgery: an application in neurosurgery. Ann Biomed Eng 44(1):1–11
8. Miga MI, Roberts DW, Kennedy FE, Platenik LA, Hartov A, Lunn KE et al (2001) Modeling of retraction and resection for intraoperative updating of images. Neurosurgery 49:75–84

9. Dorward NL, Olaf A, Velani B, Gerritsen FA, Harkness WFJ, Kitchen ND, Thomas DGT (1998) Postimaging brain distortion: magnitude, correlates, and impact on neuronavigation. J Neurosurg 88:656–662
10. Mostayed A, Garlapati R, Joldes G, Wittek A, Roy A, Kikinis R, Warfield S, Miller K (2013) Biomechanical model as a registration tool for image-guided neurosurgery: evaluation against bspline registration. Ann Biomed Eng 41(11):2409–2425
11. Wittek A, Miller K, Kikinis R, Warfield SK (2007) Patient-specific model of brain deformation: application to medical image registration. J Biomech 40(4):919–929
12. Ferrant M, Nabavi A, Macq B, Black PM, Jolesz FA, Kikinis R, Warfield SK (2002) Serial registration of intraoperative MR images of the brain. Med Image Anal 6(4):337–359
13. Ferrant M, Nabavi A, Macq B, Jolesz FA, Kikinis R, Warfield SK (2001) Registration of 3-d intraoperative MR images of the brain using a finite-element biomechanical model. IEEE Trans Med Imaging 20(12):1384–1397
14. Smith SM (2002) Fast robust automated brain extraction. Hum Brain Mapp 17(3):143–155
15. Antiga L, Piccinelli M, Botti L, Ene-Iordache B, Remuzzi A, Steinman D (2008) An image-based modeling framework for patient-specific computational hemodynamics. Med Biol Eng Comput 46(11):1097–1112
16. Horton A, Wittek A, Joldes GR, Miller K (2010) A meshless Total Lagrangian explicit dynamics algorithm for surgical simulation. Int J Num Methods Biomed Eng 26(8):977–998
17. Miller K, Horton A, Joldes GR, Wittek A (2012) Beyond finite elements: a comprehensive, patient-specific neurosurgical simulation utilizing a meshless method. J Biomech 45(15):2698–2270
18. Johnson H, Harris G, Williams K. 2007. Brainsfit: mutual information registrations of whole-brain 3d images, using the insight toolkit.
19. Liu Y, Kot A, Drakopoulos F, Yao C, Fedorov A, Enquobahrie A, Clatz O, Chrisochoides NP (2014) An itk implementation of a physics-based non-rigid registration method for brain deformation in image-guided neurosurgery. Front Neuroinfo 8:33
20. Yixun L, Chrisochoides N (2013) Heterogeneous biomechanical model on correcting brain deformation induced by tumor resection. In: Computational biomechanics for medicine. Springer, New York, pp 115–126
21. Drakopoulos F, Liu Y, Foteinos P, Chrisochoides NP (2014) Towards a real time multi-tissue adaptive physics based non-rigid registration framework for brain tumor resection. Front Neuroinfo 8:11
22. Foteinos P, Chrisochoides N (2014) High quality real-time image-to-mesh conversion for finite element simulations. J Parallel Distrib Comput 74(2):2123–2140
23. Commandeur F, Velut J, Acosta O (2011) A VTK algorithm for the computation of the Hausdorff distance. VTK J 839
24. Hastreiter P, Rezk-Salama C, Soza G, Bauer M, Greiner G, Fahlbusch R, Ganslandt O, Nimsky C (2004) Strategies for brain shift evaluation. Med Image Anal 8(4):447–464
25. Huttenlocher DP, Klanderman GA, Rucklidge WJ (1993) Comparing images using the hausdorff distance. IEEE Trans Pattern Anal Mach Intell 15(9):850–863

Registration of Prone and Supine Breast MRI for Breast Cancer Treatment Planning

Thiranja P. Babarenda Gamage, Habib Y. Baluwala, Martyn P. Nash, and Poul M.F. Nielsen

1 Introduction

Breast cancer is the leading cause of cancer-related death in females, affecting 1 in every 10 women worldwide. Breast conserving therapy (BCT) is the most common procedure used for treating early stage invasive breast cancers, and involves localized excision of tumorous lesions followed by radiotherapy. Clinical imaging modalities used for diagnosing the disease (e.g., MRI) are acquired with the patient positioned differently to that assumed during the actual treatment procedures. Since such procedures are not performed under image guidance, localization of tumors is challenging, especially when the stiffness of the tumor is similar to the stiffness of the surrounding tissue. This represents a significant challenge for clinicians, with the majority of studies in the literature reporting incomplete excision of tumors in 20–40% of the patients who underwent BCT [1]. This study therefore aimed to register regions of interest between diagnostic prone MRI and pre-operative supine MRI to help clinicians localize tumors during treatment procedures.

Such registration problems have typically been solved using image intensity-based non-rigid registration algorithms in a number of different organs [2]. In such approaches, a transformation is applied to one image in order to best match image intensity values in another image, using nonlinear optimization [3, 4]. However, these methods have proven to be unreliable when attempting to account for large changes in tissue motion in highly deformable organs, such as that observed in the

T.P.B. Gamage • H.Y. Baluwala
Auckland Bioengineering Institute, The University of Auckland, Auckland, New Zealand

M.P. Nash • P.M.F. Nielsen (✉)
Auckland Bioengineering Institute, The University of Auckland, Auckland, New Zealand

Department of Engineering Science, The University of Auckland, Auckland, New Zealand
e-mail: p.nielsen@auckland.ac.nz

A. Wittek et al. (eds.), *Computational Biomechanics for Medicine*,
DOI 10.1007/978-3-319-54481-6_11

breast between the prone and supine positions. The failure of these approaches is usually due to poor registration initialization, which can cause the locally convergent optimization algorithms used for maximizing voxel correspondence to diverge, especially if physically based constraints are not used to help constrain the problem [5].

Previous studies have therefore aimed to develop biomechanical models of the breast to provide an estimate of the tissue displacement observed between the prone and supine MRI for initializing non-rigid registration algorithms [6]. However, recent studies have observed relatively large errors in tissue displacement estimates from the biomechanical models. For example, [7] observed mean model errors between 11.5 and 39.2 mm when simulating prone to supine breast deformation, even with a model that accounted for the mechanical behavior of multiple tissues in the breast (skin, fat, fibroglandular tissues), and the pectoral muscle, on which these breast tissues sit.

These large errors may be due to the simplified frictionless boundary conditions that were applied on the posterior surface of model during the simulation. These boundary conditions were used for approximating sliding of the pectoral muscle over the ribcage that occurs due to relative changes in the position of the arm between the prone and supine positions. However, frictionless boundary conditions may not be suitable, as the extent to which the pectoral muscle slides over the breast tissues is then largely dependent on the stiffness of the breast tissues (with stiffer parameters resulting in less sliding and less stiff parameters resulting in a greater extent of sliding). In this study we aimed to determine the accuracy to which prone and supine MRI could be registered using an initial estimate of tissue displacement from a biomechanical model that directly prescribes the observed motion of the pectoral muscle between the prone and supine positions.

Section 2 describes the methodology used for solving prone-to-supine breast mechanics, and using this initial estimate for non-rigidly registering the prone and supine MRI. Section 3 describes the results of the registration procedure, and provides an analysis of the accuracy of the initial estimate of tissue displacement provided by the mechanics simulation. Potential approaches for improving the accuracy of the mechanics simulations are then discussed in Section 4.

2 Methodology

2.1 Modeling Breast Anatomy

Prone and supine MR images were acquired from two volunteers using a Siemens 1.5 T Magnetom Avanto MRI system. T2-weighted imaging sequences were acquired for each volunteer with an axial (transversal) slice orientation, and a 0.684 mm × 0.684 mm × 2.5 mm voxel size.

Subject-specific finite element (FE) models of the left breast were created from the prone MR images of each volunteer considered in this study. In each model,

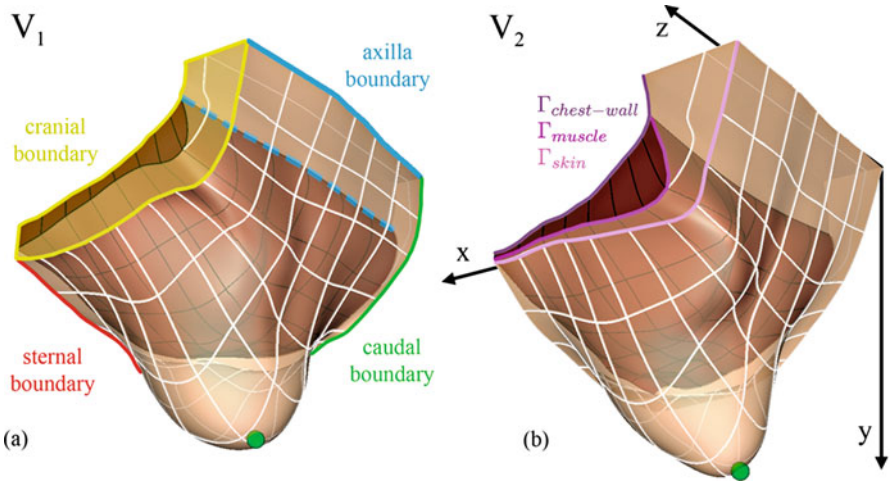

Fig. 1 FE model geometric fits are shown in (**a**) and (**b**) for volunteers 1 and 2, respectively. The *dashed blue line* indicates the axilla boundary of the muscle tissue

separate FE meshes were created to represent the geometry of the breast tissue and pectoral muscle. The meshes were created by fitting cubic Hermite basis functions to manually segmented skin, muscle, and chest wall boundaries seen in the prone MRI (denoted as Γ_{skin}, Γ_{muscle}, and $\Gamma_{\text{chest-wall}}$, respectively), using an iterative closest point algorithm. The skin and chest wall root-mean-squared errors (RMSE) following the fitting were 1.19 mm, 0.98 mm, and 1.20 mm, respectively, for volunteer 1 and 0.74 mm, 1.02 mm, 1.17 mm, respectively, for volunteer 2. The fitted meshes are shown in Fig. 1.

2.2 *Modeling Breast Mechanics*

Finite elasticity theory was used to simulate the large deformations observed during prone-to-supine breast repositioning [8]. These governing equations were solved using the finite element method in the OpenCMISS computational modeling software package [9]. The mechanical responses of the breast tissues were assumed to be isotropic and were modeled using an ideally incompressible, hyperelastic neo-Hookean constitutive relation. A linear Lagrange hydrostatic pressure field was used to enforce incompressibility of the breast tissues.

The breast and muscle tissues were each described by a different neo-Hookean stiffness parameter, namely θ_{breast} (a homogeneous representation of the stiffness of the breast tissues, composed mainly of adipose, fibroglandular, and skin tissues) and θ_{muscle} (representing the stiffness of the pectoral muscles). These parameters were assigned to their respective mesh elements.

Since the breast was imaged under gravity loading conditions, either the regional stress-state of the breast, or its stress-free reference configuration, is required for accurate mechanics simulations. The importance of determining this stress-free reference configuration was highlighted for the breast in [10]. In this study, a stress-free reference configuration was numerically determined, by implementing the algorithm described in [11], in the OpenCMISS numerical software package. Once the reference configuration was identified, the breast could be re-orientated to simulate the supine position.

Boundary and Loading Conditions

An important aspect of simulating breast tissue movement involves accounting for any relative motion between the pectoral muscles and the chest wall. This relative motion arises due to a relative change in position of the shoulder joint and the arm, to which the pectoral muscles attach, when an individual is repositioned. Previous studies have attempted to indirectly account for this sliding behavior by introducing frictionless [7] or frictional [12] contact constraints, at the muscle and chest wall interface. However, this assumes that the observed degree of sliding depends mainly on the stiffness of the breast tissues and not the actual motion of the shoulder joint and arm (which is dependent on the orientation in which the subject is positioned during imaging). Such an assumption can therefore introduce large modeling errors.

The lateral insertion points of the pectoralis major muscle or the shoulder joint were not visible within the field of view of either the prone or supine MR images of each volunteer. Therefore, the amount of sliding due to shoulder and arm motion could only be approximated in this study. This was achieved by first aligning the anterior sternocostal articulation junctions in both the prone and supine images. The axillary boundary of the pectoral muscle (defined by the dashed blue line in Fig. 1) was then identified in both the prone and supine MR images, and used to estimate the degree of sliding. Kinematic constraints were then applied on the posterior surface of the muscle to enforce the observed sliding motion along the curvature of the chest wall. A linear gradient was used to determine the amount of sliding at any point along this posterior surface, from a fixed edge at the sternal boundary of the model (representing the medial insertion point of the pectoralis major muscles) to the observed degree of sliding at the axillary boundary of the pectoral muscle.

Gravity loading was applied as a body-force acting in the direction determined from the alignment of the prone and supine MR images. The density of the breast tissue was defined as the volume weighted combination of the adipose (928 kg/m^3) and fibroglandular (1035 kg/m^3) tissue densities [13]. A density of 1060 kg/m^3 [14] was used for the muscle tissue.

Mesh Convergence Analysis

An FE displacement convergence analysis was performed to ensure the simulation results were mesh resolution independent. Six geometric points were randomly embedded within the fibroglandular region of the prone breast model. The simulated positions of these material points were compared with successive refinements to the mesh. This convergence analysis was performed using the breast geometry of volunteer 2, with neo-Hookean stiffness parameters $\theta_{\text{muscle}} = 106$ Pa and $\theta_{\text{breast}} = 190$ Pa. From this analysis, a 7756 degree of freedom (DOF) mesh resolution was chosen for generating the results in the remainder of the study, as it produced a 0.14 mm maximum displacement difference of the embedded points compared with a 14,404 DOF mesh.

2.3 Registering Prone and Supine MRI

As described in Sect. 1, image intensity-based registration techniques alone are incapable of successfully registering the large degree of breast tissue deformation observed between the prone and supine MR images, unless a suitable initial estimate of the tissue motion is provided. In this study, the nonlinear transformation, $\boldsymbol{T_m}(\boldsymbol{\theta})$, obtained from simulating prone-to-supine repositioning using the FE mechanics model (where $\boldsymbol{\theta}$ are the constitutive parameters of the FE model) was used as this initial estimate. This was achieved by embedding prone MRI pixels into the prone model, allowing each to be assigned a unique material point. These material points were subsequently transformed using $\boldsymbol{T_m}$, and re-sampled to generate a model-simulated supine MRI. The model-simulated supine MRI and the independently acquired supine MRI were then registered using image intensity-based registration techniques. This procedure defined another nonlinear and invertible transformation, $\boldsymbol{T_r}$, which maps material points between these two images. The total tissue motion was therefore described by $\boldsymbol{T} = \boldsymbol{T_r} \cdot \boldsymbol{T_m}$.

Implementation

In this study, the registration framework developed by [3] was used to determine the transformation $\boldsymbol{T_r}$ using a NMI similarity metric. This was performed using the IRTK software package [3, 4].

The IRTK registration procedure involved both rigid and non-rigid components. The rigid component of the registration was parameterized using a 12 DOF, affine transformation (which allowed translation, rotation, shear, and anisotropic scaling). The non-rigid component of $\boldsymbol{T_r}$ was represented by a multi-resolution free-form-deformation (FFD), parameterized using a lattice of control point vectors, to allow linear interpolation of the MR images. The NMI similarity metric was maximized with a conjugate gradient descent optimization algorithm to determine the optimal

parameters of the rigid and non-rigid components of $\boldsymbol{T_r}$. The muscle tissue was not registered during this procedure due to the low signal quality and lack of visible features within the tissue.

Verifying Implementation Accuracy

The accuracy of the registration framework was verified by applying a known deformation field from a mechanics solution to the prone MR image [15]. The extent to which the applied deformation could be recovered using the registration framework was then analyzed. This approach was also used to tune the numerical parameters of the registration framework (such as the spacing between control points and number of registration iterations) to ensure the framework was suitable for registering the MR images used in this study. The results of the MRI registration verification tests indicated that the framework was capable of recovering the simulated deformation with a 3D RMSE of 0.45 mm.

2.4 Identifying Subject-Specific Mechanical Properties

The registered displacements (described by $\boldsymbol{T_r}$) can be used to indicate the discrepancy between the model-simulated supine MRI and the independently acquired supine MRI. The constitutive parameters of the model ($\boldsymbol{\theta}$) could therefore be optimized to minimize these discrepancies. The optimal constitutive parameters ($\boldsymbol{\theta}^*$) identified from this procedure therefore allow the breast model to provide the best estimate of tissue motion in the supine position, for optimally registering the model-simulated supine MRI and the independently acquired supine MRI.

A nonlinear, least squares optimization procedure was implemented to minimize the mean-squared registered displacements, Φ_{MSE}, and thus to determine subject specific $\boldsymbol{\theta}^*$ as shown below:

$$\min_{\theta} \phi_{\boldsymbol{T_r}}^{\mathrm{MSE}} = \frac{1}{N} \sum_{i=1}^{N} \left\| \widetilde{\boldsymbol{I}_s}(\boldsymbol{\theta}, \boldsymbol{x}_i) - \boldsymbol{T_r}(\widetilde{\boldsymbol{I}_s}(\boldsymbol{\theta}, \boldsymbol{x}_i), \boldsymbol{I}_s) \right\|^{2.}$$

where $\boldsymbol{x_i}$ denotes the geometric location of the ith breast tissue voxel in the model-simulated supine MRI ($\widetilde{\boldsymbol{I}_s}(\boldsymbol{\theta}, \boldsymbol{x_i})$) and its corresponding registered location in the independently acquired supine MRI ($\boldsymbol{T_r}(\widetilde{\boldsymbol{I}_s}(\boldsymbol{\theta}, \boldsymbol{x_i}), \boldsymbol{I}_s)$). While the registration was performed over the entire breast tissue region, only the pixels representing the fibroglandular tissue were used for evaluating Φ_{MSE}. This was because many features were present in the fibroglandular tissue region, compared with the relatively featureless adipose tissue.

The optimization procedure was implemented in Matlab using the *lsqnonlin* optimization function. Box constraints, defining upper and lower bounds on the parameters, were manually defined during the optimization procedure to describe a feasible range of parameters.

3 Results

The optimal constitutive parameters ($\boldsymbol{\theta}^*$) that minimized the registered displacements are shown in Table 1. These results indicated that the breast tissue of volunteer 2 was stiffer than volunteer 1. However, similar muscle stiffness parameters were identified for both volunteers. These parameters are similar to those obtained in a similar study that modeled only the breast and muscle tissues ($\theta_{\text{breast}}{}^* = 50$ Pa, and $\theta_{\text{muscle}}{}^* = 260$ Pa) [16].

The supine shape determined using the biomechanical model with the optimal set of model constitutive parameters ($\boldsymbol{\theta}^*$) is shown in Fig. 2a. Figure 3a shows an example of axial slice of the model-simulated supine MRI obtained from transforming the prone MRI using $\boldsymbol{T_m}(\boldsymbol{\theta}^*)$. Figure 3b–f shows the results of the procedure used to register the model-simulated supine MRI and the independently acquired supine MRI. The differences in image intensities before and after registration are shown in Fig. 3e, f, respectively. These results showed good agreement between the registration-simulated supine MRI and the independently acquired supine MRI. A quantitative comparison between these images was also performed by comparing distances between the centroid of eight manually segmented landmarks identified in these images that were distributed throughout the breast tissue. The results of this analysis are shown in Table 2, and also indicated good agreement between the images.

The displacements described by $\boldsymbol{T_r}$ were then used to provide an indication of the accuracy of the models. These displacements are described in Table 3. The magnitudes of these displacements are also shown on the simulated supine geometry in Fig. 4 to indicate the distribution of the errors within the breast tissue.

The results in Fig. 4 indicate large 3D registered displacement magnitudes were observed near the nipple position of the model. This was identified to be due to the model over-estimating the tissue motion near the nipple in both volunteers (as seen

Table 1 Optimal constitutive parameters ($\boldsymbol{\theta}^*$) that minimized the registered displacements between the model-simulated supine MRI and the independently acquired supine MRI

Volunteer	$\theta_{\text{breast}}{}^*$ (Pa)	$\theta_{\text{muscle}}{}^*$ (Pa)
1	106	190
2	377	242

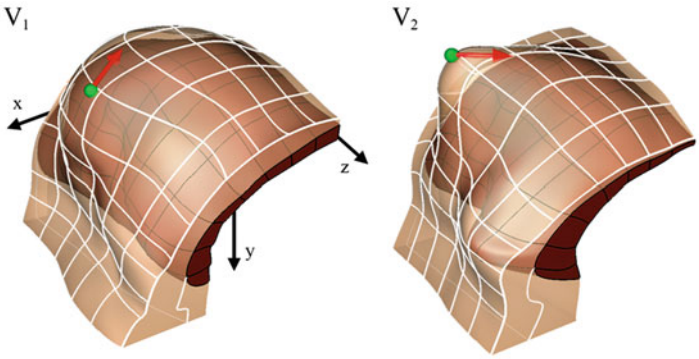

Fig. 2 The simulated supine shape of the breast from the mechanics solution solved using the optimal constitutive parameters ($\boldsymbol{\theta}^*$). Each *red arrow* indicates the error between the model-simulated nipple position (indicated by the *green sphere*) and its location identified from the independently acquired supine MRI

in Figs. 2 and 3c) in the axial (x–y) plane. The results in Table 3 also indicate that the registered displacements were the largest along the caudal-cranial direction (z-axis). Registered displacements of up to 12 mm were observed towards the caudal boundary ($-z$) in volunteer 1, and up to 23 mm towards the cranial boundary ($+z$) in volunteer 2.

4 Discussion

The results described in this study indicated that the two parameter models with the improved boundary conditions provided a good initial estimate of the tissue motion for registering the prone and supine MRI. These models showed mean modeling errors (identified from MRI registration) of 9.1 and 19.4 mm for volunteer 1 and 2, respectively, compared with mean modeling errors between 11.5 and 39.2 mm for the six parameter model considered in [7] (identified by tracking the displacement of nine fiducial markers placed on the breast surface). However, the results in this study highlighted that relatively large errors were present in certain regions of the model.

The largest registered displacements between the model-simulated supine MRI and the independently acquired supine MRI were along the cranial-caudal axis (z-axis). The RMS alignment errors between the sternum landmarks in the prone and supine MRI (2.29 mm and 2.40 mm for volunteers 1 and 2, respectively) were an order of magnitude smaller than these registered displacements. It was therefore unlikely that these discrepancies were due to errors in aligning the prone and supine MR images. Furthermore, the direction of the registered displacements along the z-axis for volunteer 1 was different to that observed in volunteer 2. These additional

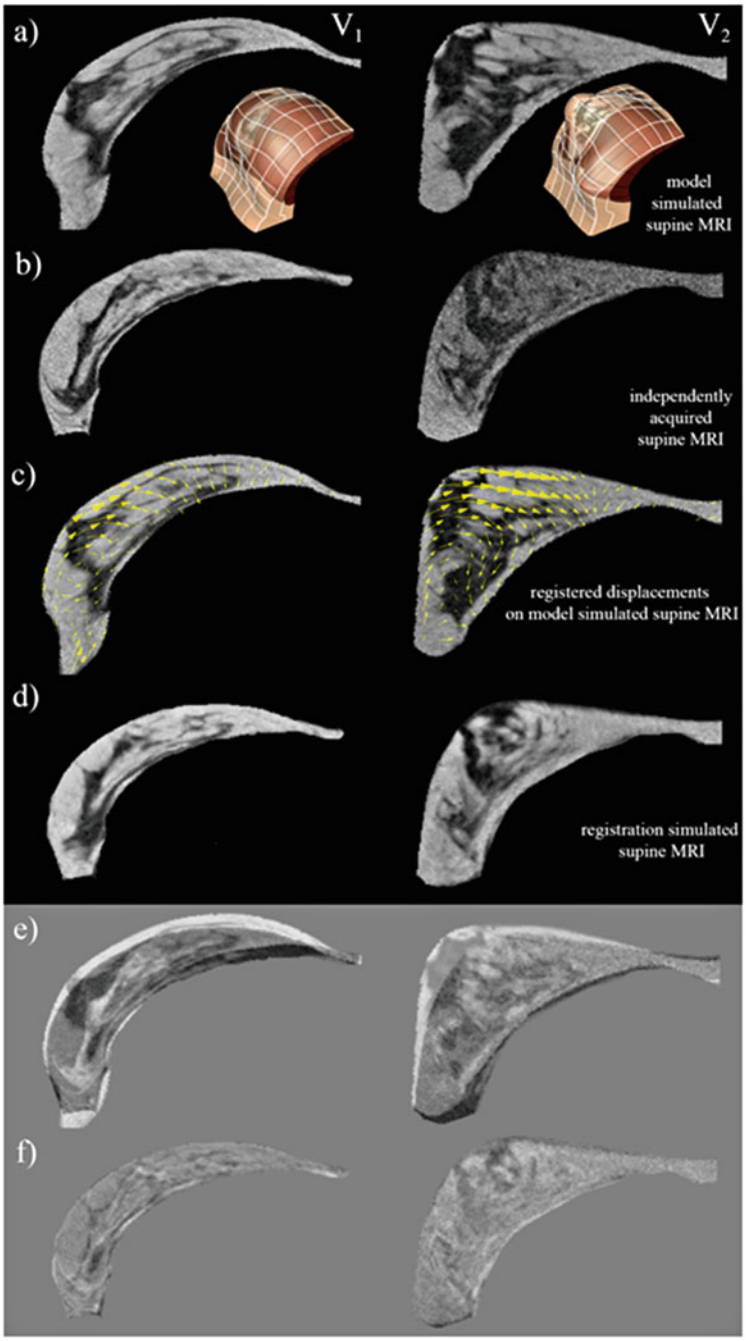

Fig. 3 MRI registration results for a transverse section of the FE model, simulated with the optimal tissue parameters ($\boldsymbol{\theta}^*$). The FE model-simulated supine MRI and independently acquired supine MRI are shown in (**a**) and (**b**), respectively. The registered displacements described by $\boldsymbol{T_r}$ are indicated by the *yellow arrows* in (**c**), and the resulting registration-simulated MRI is shown in (**d**). The differences in image intensities before registration and after registration are shown in (**e**) and (**f**), respectively

Table 2 The quantification of the registration errors using the mean (μ), standard deviation (σ), and maximum (max) difference in the centroid of six manually labelled landmarks in the model-simulated supine MRI and the independently acquired supine MRI

Volunteer	μ (mm)	σ (mm)	Max (mm)
1	1.61	1.24	3.37
2	1.10	0.50	1.67

Table 3 Total tissue displacement (**T**) between the registered prone and supine MRI ($\boldsymbol{T} = \boldsymbol{T_r} \cdot \boldsymbol{T_m}$). $\boldsymbol{T_m}$ describes the estimate of the prone-to-supine displacements from the mechanics model using the optimal constitutive parameters. $\boldsymbol{T_r}$ describes the additional displacements required to match the deformation observed in the independently acquired supine MRI

Volunteer	Component	T (mm) μ ± σ	T_m (mm) μ ± σ	T_r (mm) μ ± σ
1	Magnitude	61.8 ± 14.6	61.8 ± 16.0	9.1 ± 3.9
	x	38.7 ± 6.1	41.7 ± 7.6	−3.0 ± 5.1
	y	47.2 ± 15.0	44.4 ± 16.1	2.8 ± 3.8
	z	1.2 ± 6.7	5.6 ± 4.0	−4.4 ± 4.6
2	Magnitude	51.9 ± 7.9	49.7 ± 9.8	19.4 ± 4.8
	x	24.4 ± 4.1	33.6 + 6.1	−9.2 ± 7.1
	y	42.9 ± 8.9	36.2 ± 9.2	6.7 ± 2.6
	z	14.0 ± 5.0	−0.1 ± 1.7	14.1 ± 3.7

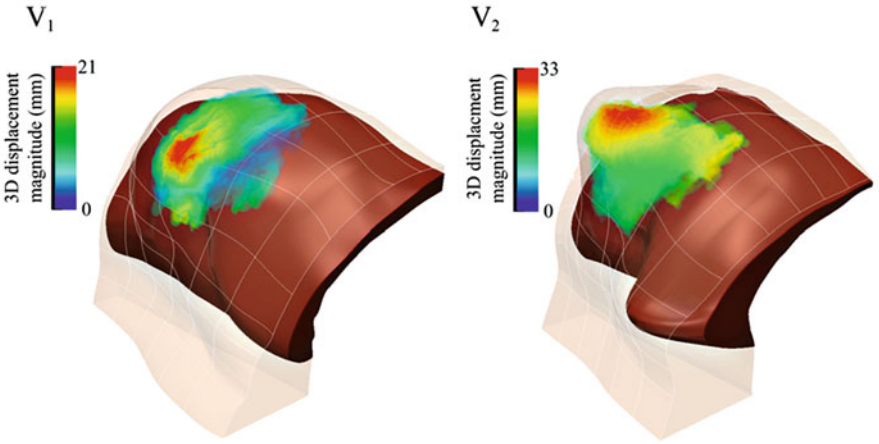

Fig. 4 The 3D magnitude of the registered displacements, describing by the discrepancy between the model-simulated supine MRI and the independently acquired supine MRI

displacements may be due to different motion of the shoulders in the z-axis (cranial-caudal direction), during repositioning from the prone-to-supine positions, which could not be accounted for in the model. However, further investigation is required to confirm this hypothesis.

Large errors were also observed near the nipple position of the model. This observation maybe due to the lack of a stiffer skin layer in the model which, if present, may resist motion of the nipple towards the axilla, and help improve the accuracy of the models.

The tissue landmarks used for assessing the accuracy of the registration were only labelled by one human rater. Obtaining labels from multiple raters would allow the accuracy of the segmentation to be estimated using probabilistic methods such as Simultaneous Truth And Performance Level Estimation (STAPLE) [17]. The use of Hausdorff distance-based automatic segmentation approaches may also help assess the alignment of structures within the breast, particularly in the regions where fibroglandular tissue is present [18].

The breast is supported by Cooper's ligaments that extend from the skin into the pectoral muscle fascia. It is unclear if these structures contribute significantly when simulating the supine position as the ligaments would likely be in compression and therefore unable to carry load. However, their influence is likely more significant when determining the unloaded state of the breast from the prone position (where the ligaments are in tension). Further investigations are required to determine the influence of these ligaments during prone to supine repositioning.

5 Conclusions

This chapter describes a biomechanical modeling framework for simulating breast tissue motion from the prone-to-supine orientation to help clinicians register tissue motion between diagnostic prone MRI and pre-operative supine MRI, for example, for treatment of planning procedures. The framework was demonstrated using MR images from two volunteers. A relatively large displacement of the pectoral muscle was observed between the prone and the supine positions in both volunteers. This motion was accounted for in the models by directly prescribing the observed motion of the muscle during the prone-to-supine simulations. The results showed that a two parameter breast model provided good initial estimates of tissue displacement for registering the prone and supine MRI, with registration errors less than 5 mm for mean tissue displacement magnitudes of up to 61.8 mm.

Acknowledgements The authors are grateful for financial support from the New Zealand Government Ministry for Business, Innovation and Employment (MBIE) and the University of Auckland Foundation. The authors thank Duane Malcolm for his contributions to this study.

References

1. Pleijhuis RG et al (2009) Obtaining adequate surgical margins in breast-conserving therapy for patients with early-stage breast cancer: current modalities and future directions. Ann Surg Oncol 16(10):2717–2730

2. Sotiras A, Davatzikos C, Paragios N (2013) Deformable medical image registration: a survey. IEEE Trans Med Imaging 32(7):1153–1190
3. Rueckert D et al (1999) Nonrigid registration using free-form deformations: application to breast MR images. IEEE Trans Med Imaging 18(8):712–721
4. Schnabel J et al (2001) A generic framework for non-rigid registration based on non-uniform multi-level free-form deformations. In: Niessen W, Viergever M (eds) Medical image computing and computer-assisted intervention 2001. Springer, Berlin Heidelberg, pp 573–581
5. Lee AWC et al (2010) Breast image registration by combining finite elements and free-form deformations. In: Martí J et al (eds) Digital mammography. Springer, Berlin/Heidelberg, pp 736–743
6. Hipwell JH et al (2016) A review of biomechanically informed breast image registration. Phys Med Biol 61(2):R1
7. Han L et al (2014) A nonlinear biomechanical model based registration method for aligning prone and supine MR breast images. IEEE Trans Med Imaging 33(3):682–694
8. Babarenda Gamage TP et al (2012) Patient-specific modeling of breast biomechanics with applications to breast cancer detection and treatment. In: Gefen A (ed) Patient-specific modeling in tomorrow's medicine. Springer, Berlin Heidelberg, pp 379–412
9. Bradley C et al (2011) OpenCMISS: a multi-physics & multi-scale computational infrastructure for the VPH/Physiome project. Prog Biophys Mol Biol 107(1):32–47
10. Eiben B, Vavourakis V, Hipwell JH, Kabus S, Lorenz C, Buelow T, Hawkes DJ (2014) Breast deformation modelling: comparison of methods to obtain a patient specific unloaded configuration. In: Proceedings of SPIE 9036, Medical Imaging 2014: image-guided procedures, robotic interventions, and modeling, pp 903615-1–903615-8. doi:10.1117/12.2043607
11. Rajagopal V et al (2007) Determining the finite elasticity reference state from a loaded configuration. Int J Numer Methods Eng 72(12):1434–1451
12. Lee AWC (2011) Breast image fusion using biomechanics. PhD thesis, University of Auckland
13. Johns PC, Yaffe MJ (1987) X-ray characterisation of normal and neoplastic breast tissues. Phys Med Biol 32(6):675–695
14. Urbanchek MG et al (2001) Specific force deficit in skeletal muscles of old rats is partially explained by the existence of denervated muscle fibers. J Gerontol A Biol Sci Med Sci 56(5):B191–B197
15. Schnabel JA et al (2003) Validation of nonrigid image registration using finite-element methods: application to breast MR images. IEEE Trans Med Imaging 22(2):238–247
16. Babarenda Gamage TP et al (2012) Modeling prone to supine breast deformation under gravity loading using heterogeneous finite element models. In: Nielsen PMF, Wittek A, Miller K (eds) Computational biomechanics for medicine. Springer, New York, pp 29–38
17. Warfield SK, Zou KH, Wells WM (2004) Simultaneous truth and performance level estimation (STAPLE): an algorithm for the validation of image segmentation. IEEE Trans Med Imaging 23(7):903–921
18. Garlapati RR et al (2015) Towards measuring neuroimage misalignment. Comput Biol Med 64:12–23

Evaluation of Strains on Levator Ani Muscle: Damage Induced During Delivery for a Prediction of Patient Risks

Olivier Mayeur, Estelle Jeanditgautier, Jean-François Witz, Pauline Lecomte-Grosbras, Michel Cosson, Chrystele Rubod, and Mathias Brieu

1 Introduction

The pelvic floor mobility is linked to a complex equilibrium related to the mechanical properties of tissues and the geometry of the related organs [1]. Different anatomical structures seem to play a major contribution in such balance and life events, such as aging, pregnancy, or delivery that could affect the physiologic mobility and induces pathology such as genital prolapse (POP). As POP concerns 30% of the women population [2], understanding of these diseases is a major health issue. Multiparity related to vaginal delivery is now identified as a significant risk factor [3]. In addition, modification of the pelvic floor during pregnancy is also reported as a change of organs equilibrium, leading to an alteration of POP-Q (POP quantification system) [4]. The main hypothesis of the changes highlighted previously was the change in biomechanical properties of the pelvic tissues [5]. These observations bring us to study the sustainable structures such as muscles and ligaments for a better understanding of the involved phenomena.

Furthermore, many studies are interested in perineal avulsion that could be classified into four categories, with first-degree corresponding to laceration on superficial perineal skin and fourth-degree is used for the most critical form [6]. These different forms of perineal trauma occurred on 85% of women having vaginal

O. Mayeur • J.-F. Witz • P. Lecomte-Grosbras • M. Brieu
Centrale Lille, Villeneuve-d'Ascq, France

Laboratoire de Mécanique de Lille, CNRS FRE-3723, Villeneuve-d'Ascq, France
e-mail: olivier.mayeur@ec-lille.fr

E. Jeanditgautier • M. Cosson • C. Rubod
Laboratoire de Mécanique de Lille, CNRS FRE-3723, Villeneuve-d'Ascq, France

CHU Lille, Service de Chirurgie Gynécologique, 59000 Lille, France

Université Lille Nord de France, Faculté de Médecine, 59000 Lille, France

A. Wittek et al. (eds.), *Computational Biomechanics for Medicine*,
DOI 10.1007/978-3-319-54481-6_12

birth and 60% receive stitches [7]. Literature reveals also a link between occurrence of levator ani muscle (LAM) trauma and POP pathology [8, 9]. It is interesting to notice also significant differences on LAM defects between nulliparous patient and primiparous women with vaginal delivery [10]. No LAM defects are observed on nulliparous against 20% on primiparous women with vaginal delivery (71% of women with LAM trauma present incontinence).

Finite element method, coupled with mechanical behavior models of biological structures, is commonly used in biomechanics to investigate strains and stresses occurred on human body. In gynecology/obstetric, FE simulation allows us to analyze the mobility of the pelvic system in physiological and pathological conditions [1, 11]. Further studies are also reported in the literature concerning the pelvic system during childbirth and more precisely the deformations that occurred on muscle of the pelvic floor [12, 13]. However, these studies are often represented by simplified models of anatomy and rarely focused on the local geometry of pelvic structures. It would be interesting to develop an FE model of the whole pelvic system with refined geometry on sustainable structure such as LAM to access to precise quantifiable measurements. Such a tool will help to evaluate the behavior of anatomical structures under different loading conditions and appears to be relevant to assess the damages and predict the risk of perineal lesions during delivery following different scenarios.

2 Materials and Methods

The approach engaged in this study follows a classical protocol involving the data acquisition from pregnant woman through clinical MRI, modeling the anatomical structures involved and generating an FE model. We have focused on several relevant parameters to better understand the strain levels induced on the pelvic floor during childbirth; this model is set to match different delivery scenarios or morphology of the patient and fetus.

2.1 MRI Protocol to 3D Representation

Different MRI sequences were performed on four pregnant primiparous women (institutional ethical approval CEROG OBS 2012-05-01 R1), without noticeable medical history and presenting a normal gynecologic examination (Fig. 1a). The MRI are performed on T1, T2, and proton density sequences under medical supervision. For each patient, five MRI are performed, distributed at different weeks of gestation (e.g., 16, 32, and 38) and 2 months and 1 year after delivery. These sequences allow us to obtain images in different incidences (axial, coronal, and sagittal). Thanks to the AVIZO Standard edition 7® (Visualization Sciences Group VSG, SAS) software, a manual thresholding is applied on these data to generate

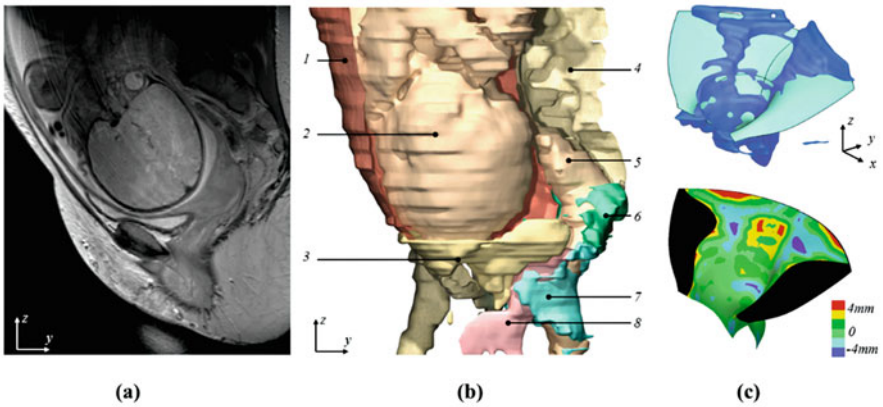

Fig. 1 (**a**) MRI at 38 weeks, (**b**) 3D reconstruction at 38 weeks with principal anatomic structure: (1) uterus, (2) fetal head, (3) bladder, (4) sacrum, (5) rectum, (6) uterosacral ligaments, (7) levator ani muscle, (8) vagina, (**c**) Comparison between LAM data from MRI and fitted surface, deviation analysis (*black surface* represents the interpolated geometry)

a 3D pelvic models composed by bone structures, organs, muscles, ligaments, and fetus (Fig. 1b).

Eighteen structures are identified individually for each term in order to have representative models of pelvic system during pregnancy and on post-partum. Based on the four women, this applied protocol brings us to the opportunity to create 20 3D reconstruction of the entire pelvic to analyze the geometrical evolution during pregnancy and after, and to take into account the geometrical modification close to delivery time.

2.2 Geometrical Surfaces to FE Model

A protocol is developed to represent the geometrical changes such as cervical dilation which must be taken into consideration for FE simulation. Using a reconstruction software from the MRI is not sufficiently adapted to use the geometries in FE simulations. Manual work is needed to make geometric reconstructions compatible with the FE method. This intermediate step is performed using CATIA software (Dassault Systèmes) and consists in transforming each anatomical structure into a viable surface model for the FE meshing (Fig. 2a).

This step involves B-Spline curves on which surfaces can be interpolated to match with the geometry of the organs or muscles. An analysis of the deviation between these surfaces and reconstructions resulting from AVIZO was established to validate the process and guarantee the representativeness of the patient. The average deviation is about −0.06 mm, which allows us to have a relevant precision, in accordance with the tolerance induced by the voxel size ($0.53 \times 0.53 \times 4.8$ mm). Some geometries with thin structures, difficult to detect on MRI, are interpolated to avoid the holes (Fig. 1c). Imperfections from operator-dependent segmentation,

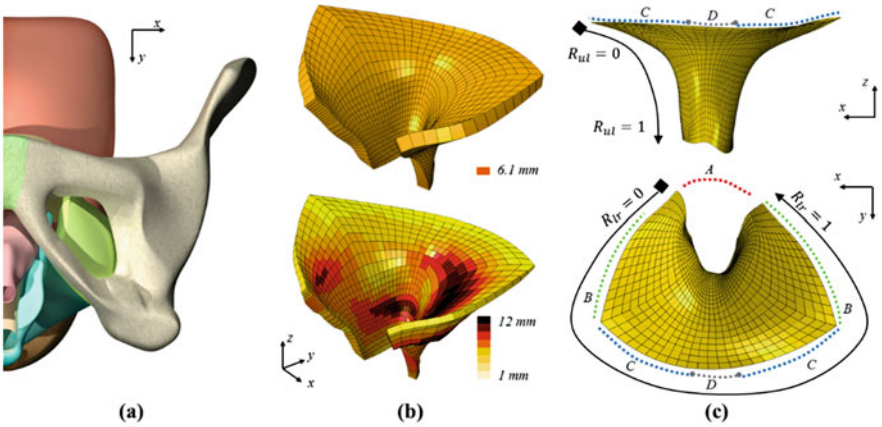

Fig. 2 (**a**) Surface model reconstruction, (**b**) mapping of the LAM thicknesses at 38 weeks, with constant value and refinement with eight groups, (**c**) illustration of the points of reference on the LAM (R_{ul} and R_{lr}, related to the upper/lower and left/right directions, respectively) and boundary conditions on LAM (A—link with the pubic symphysis, B–link with obturator muscle, C—link with sacrospinous ligament, and D—link with the coccyx)

reconstruction algorithms or software, are removed especially the stair-step artifact induced by the voxel size, a phenomenon commonly observed in such type of reconstruction method.

In order to develop an FE model, we used the 38 weeks models corresponding to the geometry 2 or 3 weeks before childbirth. Analysis of the geometry of each patient was made according to the term as well as to the fetal head. No significant differences have been observed on the bone structure. For muscle structures, the levator ani muscle (LAM) was individualized to consider each muscle structure (puborectalis, pubococcygeus, and iliococcygeus). During segmentation, observations on the MRI images revealed a change in the size of LAM. This observation was confirmed during the reconstruction and analysis of the geometrical model with an increase in thickness close to the delivery followed by a decrease during postpartum. As LAM is one of the anatomical structures impacted during delivery [14], this structure could highly damage and represents a priority analysis area to evaluate the risk of lesion. The thickness of the structures has been investigated during surface model definition. Special attention is paid to the creation of LAM geometry (Fig. 2b). In literature, many studies use surfaces with a constant thickness [12, 13] and few used a thickness variation [15, 16]. Since the principal aim is to analyze the areas where deformations are critical, consequently strongly influenced by the geometry of the model, it was necessary to develop a method to refine the geometry locally by increasing the mesh definition. A Python routine has been developed in order to attribute the real thickness in a shell formulation by computing the distance between each gravity center of element and external surface of muscle (Fig. 2b).

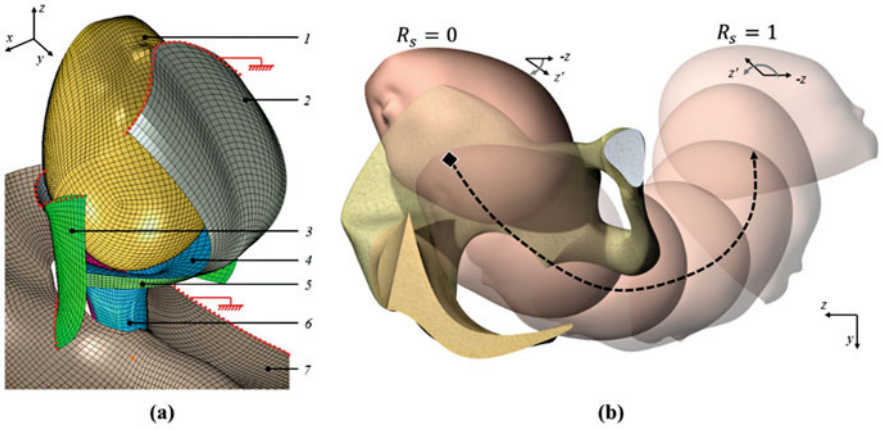

Fig. 3 (**a**) FE model with anatomical sustainable structures with boundary conditions; (*1*) fetal head, (*2*) sacrum, (*3*) obturator internus muscle, (*4*) LAM iliococcygeus muscle, (*5*) sacrospinous ligament, (*6*) LAM pubococcygeus muscle, (*7*) skin limit, (**b**) illustration of the reference trajectory corresponding to a left occipitoanterior cephalic presentation (R_s ratio related to the time of simulation)

2.3 FE Simulation and Scenario

These models lead us to perform simulations with FE method into Abaqus/CAE 6.12–2 software (Dassault Systèmes Simulia Corp.). We generate an FE mesh of the geometrical model derived from MRI to 38 weeks. This model is established with 15,000 elements and a convergence study was performed to guarantee the quality of the mesh (Fig. 3a). We assign mechanical properties from preliminary works to organs and ligaments [17, 18]. One of the conclusions of these publications is to show that despite the intra and inter dispersions, the mechanical properties can be differentiated in the old women but remain statistically equivalent among young people. So we assume that the ligament properties were similar in a parturient. We favored a hyperelastic behavior on our simulation to compute strain more accurately than with linear elastic models [1]. In accordance with the mechanical properties of pelvic cavity, a C0 (0.24) and C1 (0.19) coefficients are employed to defined a hyperelastic behavior with large strain into ABAQUS (second order Yeoh model [19]). The bone structures are considered as a stiff deformable part ($E = 10$ GPa).

Boundary conditions (Figs. 2c and 3a) for each structure suspension are equivalent to previous works already published [1]. During delivery, uterine contraction occurred but such a phenomenon is "poorly" described in literature and hard to quantify with experimental test. This lack of information leads to difficulties to consider muscle activation in our FE method approach. We decided to impose trajectory of the fetal head descent and not focus on the uterine contractions. The advantage of this approach is to employ parameter path to correspond to different scenarios and cephalic presentations.

The imposed trajectories allow to compare to one to each other and investigate their influence on the pelvic floor. The most common cephalic presentation is the left occipitoanterior (LOA), which occurred in 57% of delivery scenarios and is related to a longitudinal vertex presentation where the occiput is close to the pubis and faces to the left (Fig. 3b). A first internal rotation is performed at the beginning of the simulation to align the occiput to the pubic symphysis. The head then performs an important rotation (axis normal to the sagittal plane) during passage into the LAM. We decided to study this trajectory as a reference in the following parts. This presentation will be compared with a posterior position (occiput faces posteriorly) and more precisely the right occipitoposterior (ROP), occurred in 33% of delivery.

3 Result

3.1 Strain Analysis on Levator Ani Muscle

First part evaluates the influence of the muscle thickness on the computed strain level. Since a relationship between strain and material damage has been observed on experimental tests on pelvic organs [20], strain level is a relevant criterion to evaluate the avulsion risk. The first simulation is performed with a constant thickness on the LAM. The protocol of thickness allocation is applied to increase the representativeness of the model. To optimize the computing time, we chose to gather the elements with closed thicknesses by groups. Refinement groups used in this study correspond to 5, 8, and 12. Variable thicknesses influence the strain levels locally and are relevant to access to critical strain level (Fig. 4a). Maximal strain with constant thickness is about 81%, on the right side of muscle ($R_{lr} = 0.67$),

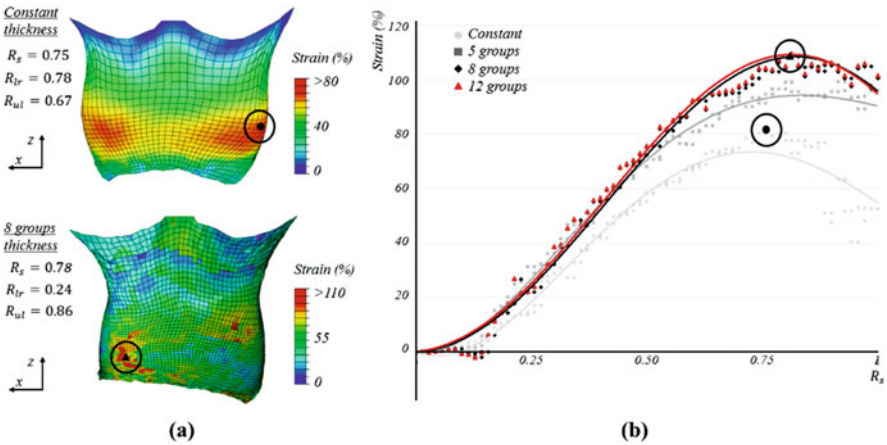

Fig. 4 (**a**) Comparison of strain mapping at the maximal step between constant thickness model and variable model with 12 groups of refinement, (**b**) Evolution of critical area of each model during head descent

while 109% with variable model with 12 groups of refinement, located on the other side ($R_{lr} = 0.24$). In addition with this result, we may notice that the zones mostly impacted change with the descent of fetal head in the birth canal. Obviously, the upper part (R_{ul}<0.2) is more impacted at the beginning of the simulation than during the extraction of fetal head where lower part (R_{ul}>0.6) suffers largest strain. This argument brings us to identify, thanks to the R_{ul}, R_{lr}, and R_s ratio (Fig. 2c), the location of the critical position of the head which is configuration and time dependent.

Strain distribution on LAM depends on the thickness mapping. The comparison between constant and different groups of thickness shows that the simulation results converge in function of the number of employed groups. A configuration with eight groups of refinement is sufficient to take into account the precise level of strain (Fig. 4b). Since the global geometry and local distribution are not symmetric, taking account of the LAM thickness shows that some complications may occur rather on one side than another (R_{lr} ratio). As expected, the higher strain occurs in the thinner regions (Figs. 2b and 4a). The first conclusion reveals the necessity of FE refinement of the thickness to evaluate the lesion risk with a better precision. The application of this mapping in patient-specific is strongly advised. The following simulations take this configuration as reference to assess the influence of head size, parturient morphology at different terms or descent scenario (Fig. 5).

3.2 *Fetal Head and Term*

Secondly, we investigated morphological parameters with the FE parametric model such as the size of fetal head. To estimate the impact on the strain levels, the cranial perimeter varies from ±5%, corresponding to the percentile classes. In accordance

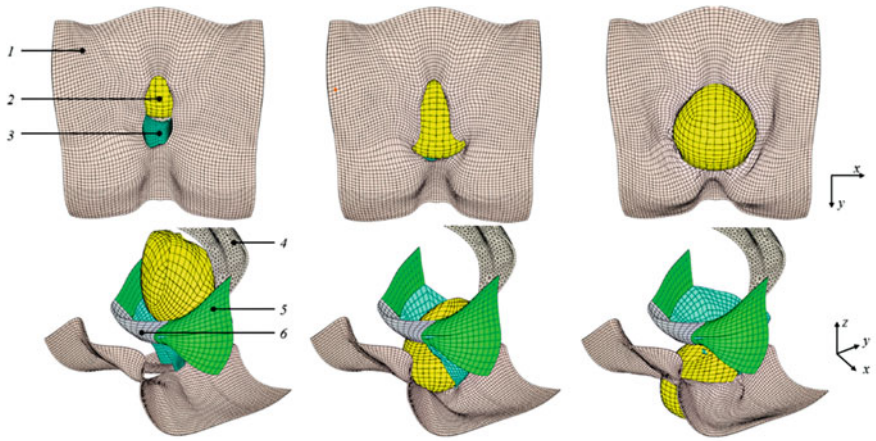

Fig. 5 FE simulation of the left occipitoanterior presentation: (*1*) skin, (*2*) fetal head, (*3*) LAM, (*4*) sacrum, (*5*) obturator internus muscle, (*6*) pubic symphysis

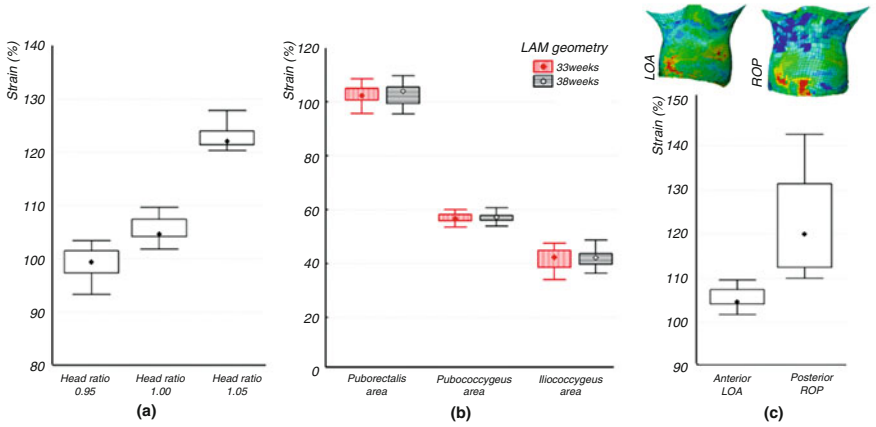

Fig. 6 (**a**) Influence of the fetal head size on LAM strains, (**b**) Influence of the weeks of gestation on the maximal strain level area, comparison on the different anatomical structures of LAM (geometry of parturient), (**c**) Influence of the head position, comparison between LOA and ROP

with the LAM refinement study, some differences of the maximal strain location are observed (Fig. 6a). The critical areas are also positioned on the lower part of LAM but with few differences of location between the three configurations (1 mm^2 zone). The simulation allows us to predict that the most important damage area depends on the duration of the head descend in the LAM. Since the trajectory is unchanged in this study, it helps to show that strain levels follow the same trend at the beginning of simulation but become higher with large head before the delivery, when the fetal head arrives at the vulva. Maximum strain levels observed for the 0.95, 1, and 1.05 head ratios rise to 103%, 109%, and 128% respectively. In Fig. 6, the box-plot representation is used by taking the principal strain value of the eight elements close to the most impacted one.

MRI reconstructions on the four pregnant women at different weeks allow us to show that the thickness on LAM increases during pregnancy with a mean difference about 12% between 33 (5.4 mm) and 38 weeks (6.1 mm). This difference in LAM thickness has been implemented on the model to correspond to a premature scenario. In order to separate the effect of the geometry of the parturient from the geometry of the fetal head that evolved also during the term, we chose to keep the same head size for this simulation. At equivalent head size, we can see that the strain levels are quite similar between 33 and 38 weeks (Fig. 6b). The individualization of each muscle structure reveals that this trend matches with the localizations, dispersions, and maximum strain values. The modification of the fetal head size has a stronger impact than the morphological change of mother local geometry. The acquisition of patient geometry near the second trimester seems sufficient to predict the high strain location.

3.3 Cephalic Presentation

Comparison between left occipitoanterior and right occipitoposterior configurations has a last motivating result to evaluate the strain levels. An increase in maximal strain is observed with a posterior cephalic presentation (Fig. 6c). The maximum value changes from 109 to 142%. For the occiput posterior configuration, FE simulation shows that this level occurred later in time with R_s ratio above 0.92 against 0.78 previously. This result is caused by the rotation of the head that happens later on the kinematic. Since the face is closer to the pubis in the ROP presentation, it is necessary to consider a higher displacement magnitude on the back before the head deflexion, contrary to an anterior presentation where occipital bone is leaned on the pubic symphysis, leading to a more progressive rotation during head deflexion. Since such phenomena occur later, the critical area is located on the lower position of LAM, near the external anal sphincter that represents an area commonly injured during laceration of perineum. Similarly, the maximal strain location is more symmetrical on the LAM with that configuration since it is centered on the puborectal muscle with R_{lr} ratio about 0.47. On our fetal head model, occipital bone presents a more rounded shape compared to the frontal bone and could help to explain this difference on the quasi-symmetrical strain distribution. To conclude, the posterior presentation has higher strain levels, essentially caused by the rotation of the head that appeared later and the shape of the occipital bone affecting the LAM.

4 Discussion

Thanks to this study, we can notice that prediction of lesion risk during childbirth through a simulation tool involves several parameters related to numerical modeling, patient-specific morphology, and scenario type.

The damage evaluation on anatomical structures depends firstly on the quality of the anatomical representation. At a global scale, the reconstruction of a specific-patient follows a standard approach. The geometrical model is strongly conditioned by the MRI resolution. Moreover, the muscles structures, as well as ligaments, are difficult to segment and the 3D model needs substantial manual work to achieve characteristic simulation. The sustainable structures close to the LAM are also important to have a representative kinematic of the pelvic during delivery. At the local scale, the definition of muscle thicknesses provides also an essential step to predict the lesion risk. Taking thickness into consideration at any point of LAM allows us to identify the lower part of the muscle (puborectalis) as the most impacted area. These geometrical variations allow us to have a non-uniform distribution of strain over the LAM to offer a precise location of the damage at the most critical moment that corresponds to the appearance of the fetal head at the vaginal orifice.

In literature, the most critical cases are identified at the superficial level (skin), corresponding to the third and fourth degree perineal tears and are equivalent to an

avulsion of the external anal sphincter [6]. However, on the second degree, lesions appear in a deep level and more precisely on the puborectalis muscle. Our tool helps to predict this grade level as it gives strain mapping over the LAM. In this study, the inclusion of MRI at several months of pregnancy also brings interesting results in warning about risk of lesion. Considering no evolution of fetal head between 33 and 38 weeks of pregnancy, results are significantly equivalent when we compare the influence of LAM geometry. The maximal strain area is located on the same zone and we do not have a significant difference in strain level. The most influential factor considering the term is the size of the fetal head. To develop the refined FE model of a specific patient, we could consider an analysis of the pelvic floor at the second trimester to predict the risks. Simulation could be performed according to different sizes, shapes, and positions of fetal head before childbirth and thus prevent eventual damage to ensure a better medical follow-up.

Regarding the cephalic presentation, posterior position is more critical than the anterior position. This comparison is already observed in literature but the risk rate is not significant and corresponds to a trend [21]. Severe perineal lacerations may occur on the patient with higher rates with a posterior presentation than anterior one [22]. Third and fourth degree laceration occurs with 6.7% on anterior presentation and 18.2% on posterior one [23]. The simulations performed in this work allow us to quantify the injury risk in function of the general kinematic and the shape of the head. Thanks to the imposed trajectory, we could modify displacement magnitude to identify more accurately the influence of the rotation of the head and better understand the origin of the lesions.

In this study, some topics are not addressed such as the individualization of each fontanelle allowing the movement of skull to facilitate the fetal head descent. It was assumed that the simulations are performed with a rigid head with prescribed path that could cause an overestimation of strain levels. A comparison with no path could be used in future study to quantify the difference between the two approaches. Coccyx mobility observed during childbirth was not integrated but need to be investigated in future study as it has a significant role in pelvic floor mobility [24]. Muscle nonlinearity and anisotropy [15, 16, 25] could be also integrated in the model to identify more precisely the critical strains.

5 Conclusion

The knowledges on the occurrence of injury criteria are referenced but few personalized means exist to study the damage induced during delivery for a prediction of lesion risks. The FE method helps us to identify the most influential parameters. The local geometry is a major factor influencing the damage evaluation. Taking thickness variation into consideration is needed to better quantify risk areas on the LAM. Variations of strain levels depend also on the size of the head or cephalic presentation. All these results are in agreement with statistical and epidemiological data and could help to explain some clinical differences such as the perineal

lacerations induced by an anterior or posterior presentation of fetal head. Since the modeling of the parturient at the second trimester of pregnancy is sufficient to observe the maximal strain level, this developed approach could be used like a predictive tool to assess potential risks and adapt medical follow-up to the patient. The simulation protocol could be done on a semi-automated way to be a new tool evaluating damages on the pelvis during delivery and predicting patient risks.

Acknowledgments This research is a part of the project « MAMAN » financially supported by the University of Lille 2.

References

1. Mayeur O, Witz JF, Lecomte-Grosbras P, Brieu M, Cosson M, Miller K (2016) Influence of geometry and mechanical properties on the accuracy of patient-specific simulation of women pelvic floor. Ann Biomed Eng 44(1):202–212
2. Samuelsson EC, Arne Victor FT, Tibblin G, Svardsudd KF (1999) Signs of genital prolapse in a Swedish population of women 20 to 59 years of age and possible related factors. Am J Obstet Gynecol 180(2):299–305
3. Rortveit G, Brown JS, Thom DH, Van Den Eeden SK, Creasman JM, Subak LL (2007) Symptomatic pelvic organ prolapse: prevalence and risk factors in a population-based, racially diverse cohort. Obstet Gynecol 109(6):1396–1403
4. O'Boyle AL, O'Boyle JD, Ricks RE, Patience TH, Calhoun B, Davis G (2003) The natural history of pelvic organ support in pregnancy. Int Urogynecol J Pelvic Floor Dysfunct 14(1): 46–49
5. Rahn DD, Ruff MD, Brown SA, Tibbals HF, Word RA (2008) Biomechanical properties of the vaginal wall: effect of pregnancy, elastic fiber deficiency, and pelvic organ prolapse. Am J Obstet Gynecol 198(5):590–596
6. Sultan AH (1999) Clinical focus: obstetric perineal injury and faecal incontinence after childbirth – editorial: obstetrical perineal injury and anal incontinence. Clin Risk 5(6): 193–196
7. Kettle C, Tohill S (2008) Perineal care. BMJ Clin Evidence 2008:1–18
8. Dietz HP, Lanzarone V (2005) Levator trauma after vaginal delivery. Obstet Gynecol 106(4):707–712
9. Dietz HP, Gillespie AV, Phadke P (2007) Avulsion of the pubovisceral muscle associated with large vaginal tear after normal vaginal delivery at term. ANZJOG 47(4):341–344
10. DeLancey JOL, Kearney R, Chou Q, Speights S, Binno S (2003) The appearance of levator ani muscle abnormalities in magnetic resonance images after vaginal delivery. Obstet Gynecol 101(1):46–53
11. Chen L, Ashton-Miller JA, DeLancey JOL (2009) A 3d finite element model of anterior vaginal wall support to evaluate mechanisms underlying cystocele formation. J Biomech 42(10): 1371–1377
12. Parente MPL, Natal Jorge RM, Mascarenhas T, Fernandes AA, Martins JAC (2009) The influence of the material properties on the biomechanical behavior of the pelvic floor muscles during vaginal delivery. J Biomech 42(9):1301–1306
13. Ashton-Miller JA, Delancey JOL (2009) On the biomechanics of vaginal birth and common sequelae. Annu Rev Biomed Eng 11:163–176
14. van Delft K, Thakar R, Sultan AH, Schwertner-Tiepelmann N, Kluivers K (2014) Levator ani muscle avulsion during childbirth: a risk prediction model. BJOG 121(9):1155–1163

15. Li X, Kruger JA, Nash MP, Nielsen PMF (2010) Anisotropic effects of the levator ani muscle during childbirth. Biomech Model Mechanobiol 10(4):485–494
16. Li X, Kruger JA, Nash MP, Nielsen PMF (2010) Effects of nonlinear muscle elasticity on pelvic floor mechanics during vaginal childbirth. J Biomech Eng 132(11):111010–111015
17. Rubod C, Boukerrou M, Brieu M, Jean-Charles C, Dubois P, Cosson M (2008) Biomechanical properties of vaginal tissue: preliminary results. Int Urogynecol J Pelvic Floor Dysfunct 121(9):811–816
18. Chantereau P, Brieu M, Kammal M, Farthmann J, Gabriel B, Cosson M (2014) Mechanical properties of pelvic soft tissue of young women and impact of aging. Int Urogynecol J 25(11):1547–1553
19. Yeoh OH (1993) Some forms of the strain energy function for rubber. Rubber Chem Technol 66(5):754–771
20. Rubod C, Brieu M, Cosson M, Rivaux G, Clay JC, Gabriel B (2012) Biomechanical properties of human pelvic organs. J Urol 79(4):1346–1354
21. Salameh C, Canoui-Poitrine F, Cortet M, Lafon A, Rudigoz RC, Huissoud C (2011) Does persistent occiput posterior position increase the risk of severe perineal laceration? Gynecol Obstet Fertil 39(10):545–548
22. Pergialiotis V, Vlachos D, Protopapas A, Pappa K, Vlachos G (2014) Risk factors for severe perineal lacerations during childbirth. Int J Gynaecol Obstet 125(1):6–14
23. Ponkey SE, Cohen AP, Heffner LJ, Lieberman E (2003) Persistent fetal occiput posterior position: obstetric outcomes. Obstet Gynecol 101(5):915–920
24. Berardi M, Martinez-Romero O, Elías-Zúñiga A, Rodríguez M, Ceretti E, Fiorentino A, Donzella G, Avanzini A (2014) Levator ani deformation during the second stage of labour. Proc Inst Mech Eng 228:501–508
25. Dejun J, Ashton-Miller JA, DeLancey JOL (2012) A subject specific anisotropic visco-hyperelastic finite element model of female pelvic floor stress and strain during the second stage of labor. J Biomech 45(3):455–460

Abusive Head Trauma: Developing a Computational Adult Head Model to Predict Brain Deformations under Mild Accelerations

Nikini T. Puhulwelle Gamage, Andrew K. Knutsen, Dzung L. Pham, Andrew J. Taberner, Martyn P. Nash, and Poul M.F. Nielsen

1 Introduction

"Shaken baby syndrome" (SBS) is a well-known phrase used to describe a class of head injuries inflicted on young infants by their caregivers. As the name implies, it was thought for many years that these injuries were caused by violent shaking. However, it is now recognised that mechanisms involving impact may cause very similar injuries and hence the term "Abusive Head Trauma" (AHT) is now used, which does not require the medical practitioner to assume one specific mechanism of injury [1].

The injuries most commonly associated with AHT include intracranial bleeding (typically subdural) and bleeding into the retina, although a variety of other injuries may be sustained [2]. These injuries are not visible externally. Therefore, for a head injury to be diagnosed in an infant with no external signs of trauma, the infant must present symptoms of brain dysfunction (encephalopathy). These symptoms can be subtle, and vary from vomiting and lethargy to coma and acute collapse [3]. Internationally, the incidence of AHT is between 14 and 40 per year per 100,000 infants under the age of one [4].

N.T. Puhulwelle Gamage
Auckland Bioengineering Institute, The University of Auckland, Auckland, New Zealand

A.K. Knutsen • D.L. Pham
Center for Neuroscience and Regenerative Medicine, The Henry M. Jackson Foundation, Bethesda, MD, USA

A.J. Taberner • M.P. Nash • P.M.F. Nielsen (✉)
Auckland Bioengineering Institute, The University of Auckland, Auckland, New Zealand

Department of Engineering Science, The University of Auckland, Auckland, New Zealand
e-mail: p.nielsen@auckland.ac.nz

A. Wittek et al. (eds.), *Computational Biomechanics for Medicine*,
DOI 10.1007/978-3-319-54481-6_13

Uncertainties about the mechanisms of injury often become a central issue in criminal trials. This is particularly so for infants with no external signs of impact and no fractures of the ribs or long bones. In these infants, the classical "shaken babies", it may be argued that there was no trauma at all. In particular, it is often argued that shaking alone cannot cause serious brain injuries, and that the whole concept of SBS is fundamentally flawed. In these arguments, the lack of biomechanical evidence for shaking as a cause of injury often plays a key role [5]. It has become clear that further biomechanical research is needed to help determine the quantitative linkages between shaking an infant and the injuries that may result. Computational modelling of the infant head can help to address ambiguities surrounding the diagnosis of AHT.

The main aim of the AHT research project at the Auckland Bioengineering Institute is to ascertain if shaking alone can cause the injuries seen in AHT. In order to address this question, the problem has been separated into three parts. The first was to determine the mechanical coupling between the torso and the head. This involved determining how the head moved when the torso was shaken [6]. The second part was to use measurements of head motions to investigate the mechanical effects on the infant brain under these conditions. The third part was to link the mechanical indices identified and link them to the injuries seen in AHT.

In order to create an accurate computational infant head model the computational techniques used to create this model need to be validated. This paper outlines how an adult head model was created and validated using in-vivo experimental data. The computational techniques that were validated in this paper will then be used to create an infant head model, which could then be used to determine certain mechanical indices on the infant brain under a shaking motion.

2 Methods

A set of mild acceleration in-vivo adult head rotation experiments were conducted. The deformations of the brain under these rotational motions were measured and were used to validate a finite element (FE) model.

A healthy volunteer was placed supine into a magnetic resonance imaging (MRI) scanner with a rotational rig placed around their head. When a pulley was actuated, a latch was released allowing the head to rotate approximately 30°, guided by an off axis weight until a mechanical stop was reached. This protocol provided repeatable accelerations of approximately 260 rad·s^{-2}. These experiments were approved by the Internal Review Board at the National Institute of Health (USA) [7].

Tagged MR images were acquired using a novel approach that combined a modified tagged MRI pulse sequence with an MRI-compatible angular position sensor [7]. The imaging and the rotation were synchronised using a fibre optic sensor, which detected the release of the latch and started the MRI sequence. The tag lines were applied immediately at the start of the motion, and a second trigger was sent to the scanner when the shaft of the device rotated through approximately 29°,

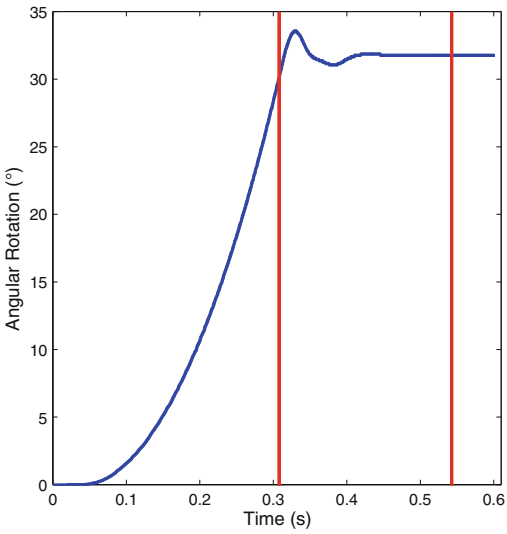

Fig. 1 The rotational displacement of the adult head. The first (*left*) *red line* shows when the data started to be acquired and the second (*right*) *red line* shows the end of the data acquisition

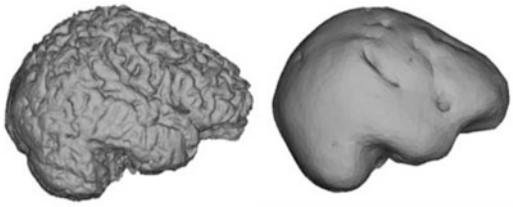

Fig. 2 *Left*: the original STL surface mesh that was obtained from ITK Snap. *Right*: the STL mesh after it had been modified with MeshLab

beginning the cine gradient echo acquisition from which the displacements were obtained.

To capture the full deformation of the brain, the experiments were repeated 120 times. Image displacements were computed using harmonic phase (HARP) analysis [8]. A filter radius was applied to create the HARP images. Two dimensional displacements of 14 axial slices throughout the adult brain were obtained. Starting at the base of the brain (brainstem), slices were regularly spaced at 10 mm intervals. This resulted in 13 slices and 59,478 points of measurement. Data for 13 time steps were collected, with the acquisition starting at 0.3074 s (first red line in Fig. 1) just before the mechanical stop and data collected every 18 ms until 0.5422 s (second red line). The 2D displacements were all measured relative to the first time step.

The rotational displacement of the whole head can be seen in Fig. 1. The first peak shows when the head came to a compliant stop. Once the rig contacted this stop, it would rebound slightly—an event evident in the decaying ripple after the first peak.

To determine the experimental error, rotational experiments were conducted on a gel phantom multiple times and the displacements throughout the gel, over time were measured. The variation in these results showed an experimental precision

error (uncertainty) of 1.5 mm. The bias error (accuracy) was not determined from these experiments. However, very low bias errors have been shown to occur for a similar MR imaging technique [9]. Therefore an experimental error of 1.5 mm will be used when analysing the results.

A computational FE model of the adult head undergoing mild acceleration rotational motions was created with ANSYS Workbench, using a fluid–structure interaction (FSI) model. A high resolution MR scan of the geometry of the volunteer's head was imported into the ANSYS Workbench environment. Volumes corresponding to the brain, brain stem, and the optic nerves of the volunteer were segmented from the model. ITK Snap (US National Institute of Health, [10]) was used to segment the images using active contour segmentation. This is a semi-automated segmentation process, where certain sections of the head could be segmented based on intensity levels, expansion force, smoothing force, and edge attraction force [10]. The segmented images were subsequently cleaned manually.

The cerebrospinal fluid (CSF) and the skull were not segmented from the MR images as the T1 weighted MRI intensity levels of the skull and the CSF could not be differentiated. Gravitational loading while the brain was being imaged could also alter the volume of the CSF. Because of this the CSF and skull had to be created manually. Once the entire brain had been segmented, the data were written to stereolithography (STL) files and imported into MeshLab (National Research Council (Italy)), a 3D mesh processing application. The STL surface mesh that was obtained from ITK Snap was cleaned, filtered, and reduced using MeshLab (see Fig. 2).

This processing of the initial STL mesh resulted in the fine folds of the brain (gyri and sulci) being smoothed out. This was acceptable as these folds were not thought to substantially influence the mechanical behaviour of the brain, but would overly complicate the final FE mesh geometry. This processing did cause the dimensions of the brain to decrease by approximately 2 mm in height and length. The STL files for the brain stem and the optic nerve were not processed in this way as they did not contain a complex outer surface.

Once the cleaned STL files had been created, they were saved as a ".XYZ" file, which contained the locations of all the nodes and the surface normals. The XYZ file of the brain was then used to create the CSF and skull of the adult head. MATLAB (The Math Works Inc., 2013) was used to project the nodes outwards to create the outer surface of the CSF layer and further extended to create the outer surface of the skull. The geometric models of the CSF and the skull were then saved as ".XYZ" files. MeshLab was used to create the outer surfaces of the CSF and the skull from the nodes and the surface normals. A Poisson surface reconstruction algorithm was used to create the surface from the point clouds. This model contained a 2 mm CSF layer and a 6 mm thick skull [11].

The falx cerebri and the tentorium cerebelli were added to the existing geometry. These structures could not be segmented using ITK Snap as they had similar MRI intensities as the surrounding tissue; instead, these structures were added manually using ANSYS ICEM (ANSYS Inc., Canonsburg, PA, USA). The outlines of the falx and tentorium were created using points and line segments. Faces were then inserted to create a final geometry. The longitudinal fissure and the transverse fissure were

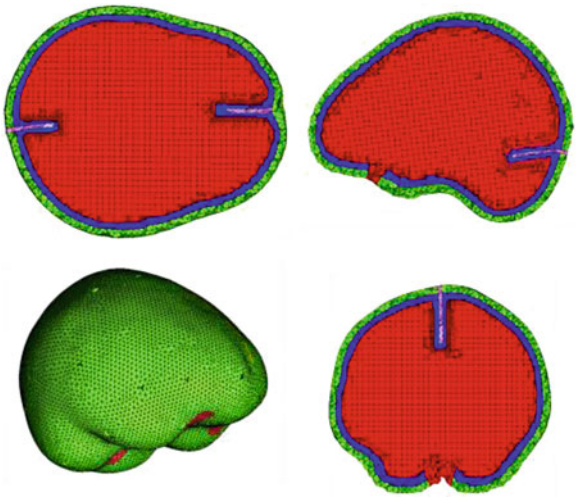

Fig. 3 The volume mesh of the adult head. *Top left*: transverse plane, *Top right*: Off-centred medial plane, *Bottom left*: Isometric view, *Bottom right*: Coronal plane. *Red* represented the brain, *blue* the CSF, green the skull, and pink the falx and tentorium

used to position the falx and the tentorium at the correct positions. These surfaces were also projected outwards by 2 mm to create the CSF layer between the brain and the falx cerebri and the tentorium cerebelli. The sizes of the falx cerebri and the tentorium cerebelli were estimated from the MRI scans and were consistent with those reported in the literature [11].

Once the anatomical surface model was created, a volume mesh was built using ANSYS ICEM. All surface meshes were imported into ICEM and an integrated volumetric mesh was created through an automated process. Tetrahedral meshes were used for the skull, CSF, falx, tentorium, optic nerves, and brainstem. The surface of the brain was described using tetrahedral elements. The main body of the brain was meshed using a hexahedral mesh. Figure 3 shows the mesh that was created by ICEM. The structural mesh (everything apart from the CSF) contained 24,831 elements, while the fluid component contained 85,504 elements. Once the geometry had been discretised, it was imported into ANSYS Workbench.

This workflow resulted in a model where the brain was contained inside a skull and surrounded by a 2 mm thick CSF layer. The falx cerebri and the tentorium cerebelli protruded into the skull, thereby separating the two hemispheres of the brain and the cerebellum. CSF was also present between the falx and brain, and between the tentorium and the brain. The optic nerves and the brainstem tether the brain to the skull, and both extend from the brain through the CSF to the outer surface of the skull. This arrangement is illustrated in Fig. 3, where the green elements represent the skull, blue elements represent the CSF, pink elements represent the falx and tentorium, and red elements represent the brain.

Table 1 lists the material properties that were assigned to each part of the model. The outer skull, falx, and tentorium were modelled using elastic material properties. The CSF was modelled using the standard fluid properties of density (ρ) and viscosity (η). The brain, optic nerves, and brainstem were modelled using a linear viscoelastic material property.

Table 1 The material properties that were used in the computational model

Anatomical structure	Material model
Brain	$G_0 = 0.038$ MPa, $G_\infty = 0.007$ MPa, $t_1 = 0.0014$ s [12–15]
Skull	$E = 7$ GPa, $\mu = 0.22$ [16, 17]
CSF	$P = 1000.59$ kgm^{-3}, $\eta = 0.78$ [18–20]
Falx/Tentorium	$E = 31.5$ MPa, $\mu = 0.23$ [14, 15, 21]

The rotational displacement of the head (Fig. 1) was used as a kinematic constraint on the FE model and was applied to the outer nodes of the skull. Two sets of contact conditions were applied in this model. A bonded contact condition was implemented between the outer edge of the optic nerves and the skull, and a frictionless contact condition was applied between the brainstem and the skull. The frictionless contact condition allowed the brainstem to move independently of the skull and the bonded contact condition of the optic nerve did not let the optic nerve to move independently of the skull. These constraints were assumed to provide a reasonable representation of the interactions between these anatomical structures. An FSI boundary was placed on the outer surface of the brain and the inner surface of the skull. This allowed the displacements from the solid solver to be transferred to the fluid domain (CSF) and the forces from the fluid solver were transferred to the solid domain (brain and skull). This was a simplified representation of the meninges layers but this proved to be sufficient to accurately model the deformation of the brain under mild angular rotations.

3 Results

The results from the FE model and the experimental model were compared to determine whether the FE model could reliably represent the deformation of the brain. Figure 4 shows the root mean squared (RMS) error between the resultant displacements magnitudes between all the points (59478) measured from the adult experiments and the predicted displacements from the corresponding points in the computational model. The time steps relate to the acquisition time of the tagged MRI images. The RMS error was seen to vary with the rotation of the brain.

Figure 5 shows the magnitude of the displacements and the errors associated at each time point. The error was calculated by taking the absolute differences between the measured and the predicted displacements. There was no obvious relationship between the absolute errors and the total displacement of the brain.

Figure 6 shows the relative errors between the measured and the predicted displacements. The relative errors were calculated by dividing the absolute differences between the measured and predicted displacements by the measured displacements. Time steps 2, 3, 4, and 6 have median relative errors below 0.1 and the other time steps had median relative errors that were above 0.1.

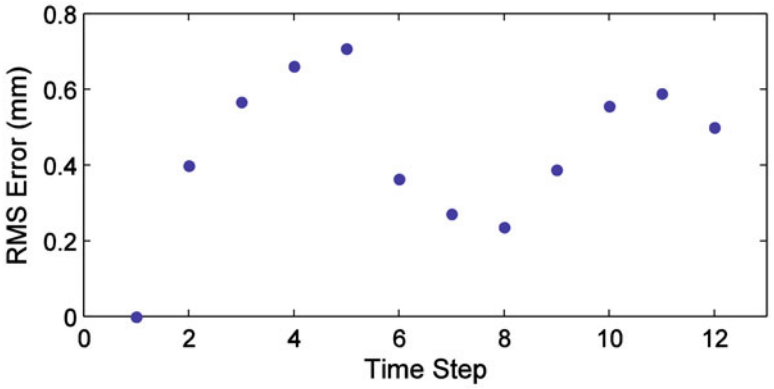

Fig. 4 RMS error between the experimental data and the FE model for each time step for the adult head model. The time steps were 18 ms apart from one another

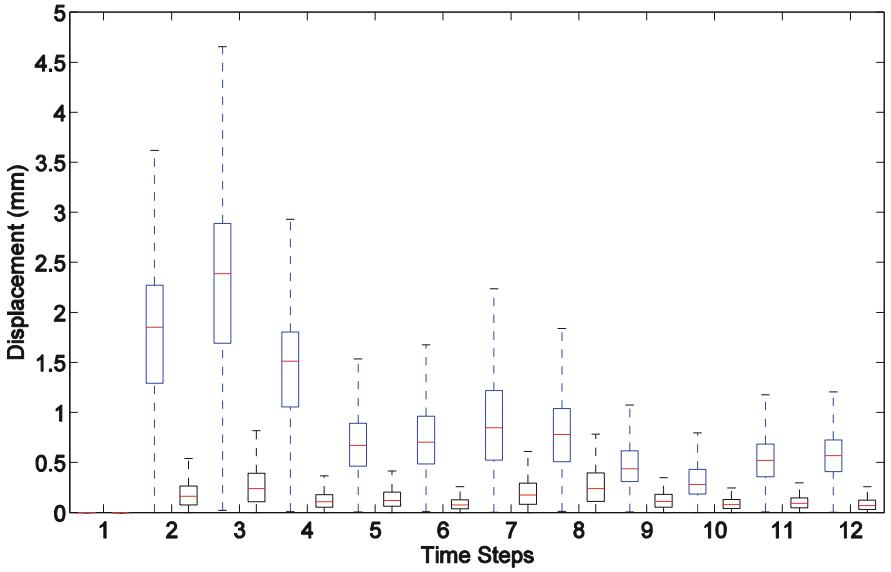

Fig. 5 Shows the displacement magnitudes (*blue*) from the measured displacement for each time step and the absolute errors (*black*) between the measured and the predicted displacement values. The time steps were 18 ms apart from one another

Figure 7 shows a slice (coronal plane of the brain) of the raw data from the experimental results (left), the FE model (middle), and their difference (right). The colours in these plots represent the x displacement (perpendicular to the plane shown) of the brain, with maximum value of 3.4 mm (red) and a minimum of −4.2 mm (blue). All the displacements measured were relative to the first time step. The following time steps show the displacement of the brain from just after the head

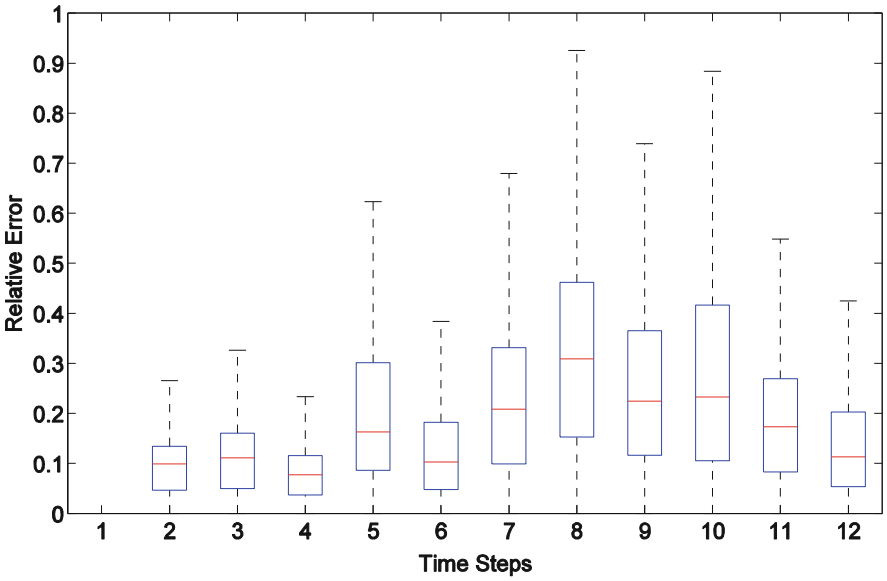

Fig. 6 Relative errors between the predicted and the measured displacements at each of the time steps, the time steps were 18 ms apart from one another

had hit a mechanical stop. The brain deforms the greatest amount during the start and settles as the experiments go on. Only the first six time steps are shown as the deformations were small in the remaining time steps.

4 Discussion

The main aim of this work was to validate a computational model that was used to predict the displacements of the adult human brain undergoing mild rotational accelerations. A volunteer underwent mild acceleration (max of 260 rad·s^{-2}) head rotations, where the 3D deformation of the brain was measured using a tagged MRI sequence. The motion of the volunteer's head was recorded and the rotational displacements were used to kinematically constrain the outer nodes of the FE model of the skull. The displacements of the brain under this rotation predicted by the FE model were compared to the displacements measured in the experiment.

The maximum and RMS error between the predicted displacements and the measured displacements at each time step are presented in Fig. 4. All RMS errors were below the experimental error of 1.5 mm. Thus, the FE model provides acceptable predictive accuracy.

A comparison of the measured displacements and the prediction errors is illustrated in Fig. 5. Acquisition commenced immediately prior to the impact with

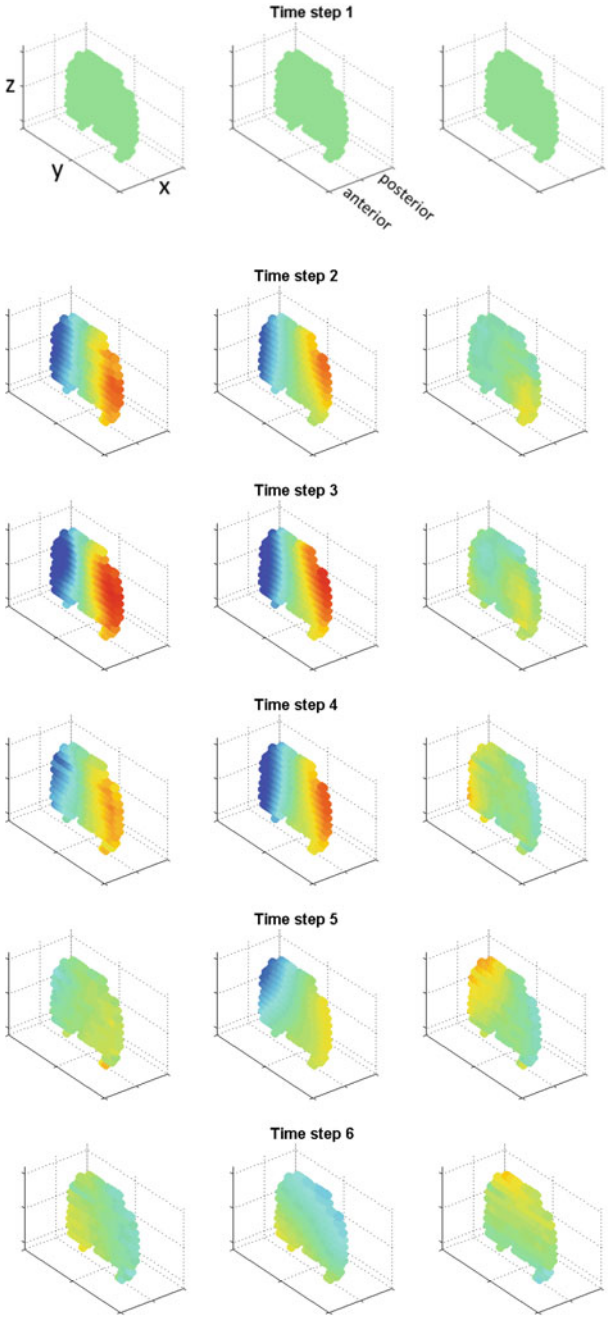

Fig. 7 Comparison of x-displacements from the experiments (*left*) and the FE model (*middle*), with the difference between the two (*right*), for the adult head FE model. The colours in these plots represent the *x* displacement of the brain, with maximum value of 3.4 mm (*red*) and a minimum of −4.2 mm (*blue*)

the mechanical stop, in order to capture the maximum displacements of the brain. This is evident as the first three time steps had median displacements of more than 1.5 mm. When the head ceased rotating, and the brain motion settled, the median displacements measured were below 1 mm. The median absolute error in the model predictions were below 0.3 mm, which was well below the experimental error, and much smaller than the overall displacement of the brain. The absolute errors were also relatively constant throughout the rotation of the head. Figure 7 also conveys this information. The relative errors between the predicted and the measured displacements at each of the time steps (Fig. 6) were small for time steps 2, 3, and 4. However, there were rather large relative errors at other time points. This was because of the small displacements (medians lower than 1 mm) at these time steps coupled with the relatively constant absolute errors throughout the experiment. This combination would result in a high relative error and hence these errors do not detract anything from the predictive capabilities of the computational model. These results provide confidence in the computational model that was used to predict the displacement of the brain under mild acceleration rotations.

This paper has detailed the construction of an FE model that was used to predict the displacements of the adult human brain undergoing mild rotational accelerations. The computational techniques required to predict the displacement of the brain were validated using in-vivo measurements of human brain displacements. In future, these computational techniques will be incorporated into an FE model of an infant head in order to predict the mechanical effects on the infant brain under a shaking motion. The dynamic stresses, strains, and the motion of the brain in relation to the skull will be used to help ascertain whether injuries could result from particular shaking incidents.

Acknowledgements The work presented in this paper could not have been completed without the assistance of the Image Processing Core lab at the Center for Neuroscience and Regenerative Medicine in Bethesda, MD. A special thank you must be given to Deva Chan, for her expert assistance with interpretation of the experimental data used in this project.

References

1. Christian CW, Block R (2009) Abusive head trauma in infants and children. Pediatrics 123:1409–1411
2. Chiesa A, Duhaime A-C (2009) Abusive head trauma. Pediatr Clin N Am 56:317–331
3. Minns R, Busuttil A (2004) Patterns of presentation of the shaken baby syndrome. Br Med J 328:766
4. Sieswerda-Hoogendoorn T, Boos S, Spivack B, Bilo RA, van Rijn RR (2012) Educational paper: abusive head trauma part I. Clinical aspects. Eur J Pediatr 171:415–423
5. Tuerkheimer D (2009) The next innocent project: shaken baby syndrome and the criminal courts. Washingt Univ Law Rev 87(1):1–58
6. Lintern TO (2014) Modelling infant head kinematics in abusive head trauma. Doctoral thesis, University of Auckland, Auckland, New Zealand. Retrieved from http://hdl.handle.net/2292/22988

7. Knutsen AK, Magrath E, McEntee JE, Xing F, Prince JL, Bayly PV, Butman JA, Pham DL (2014) Improved measurement of brain deformation during mild head acceleration using a novel tagged MRI sequence. J Biomech 47:3475–3481
8. Osman NF, Kerwin WS, McVeigh ER, Prince JL (1999) Cardiac motion tracking using CINE harmonic phase (HARP) magnetic resonance imaging. Magn Reson Med 42:1048–1060
9. Bayly P, Ji S, Song S, Okamoto R, Massouros P (2004) Measurement of strain in physical models of brain injury: a method based on HARP analysis of tagged magnetic resonance images (MRI). J Biomech Eng 126(4):523–528
10. Yushkevich PA, Piven J, Hazlett HC, Smith RG, Ho S, Gee JC, Gerig G (2006) User-guided 3D active contour segmentation of anatomical structures: significantly improved efficiency and reliability. NeuroImage 31:1116–1128
11. Hiatt JL, Gartner LP (2009) Textbook of head and neck anatomy. Lippincott Williams and Wilkins, Philadelphia
12. Al-Bsharat AS (2000) Computational analysis of brain injury. Doctoral thesis, Wayne State University, MI, USA. Retrieved from http://elibrary.wayne.edu/record=b2760872~S47
13. Chen Y (2011) Biomechanical analysis of traumatic brain injury by MRI-based finite element modeling. Doctoral thesis, University of Illinois, Champaign, IL, USA. Retrieved from https://www.ideals.illinois.edu/bitstream/handle/2142/29640/CHEN_YING.pdf?sequence=1
14. Tse KM, Lim SP, Tan VC, Lee HP (2014) A review of head injury and finite element head models. Am J Eng Technol Soc 1:28–52
15. Zhang L, Yang KH, King AI (2001) Comparison of brain responses between frontal and lateral impacts by finite element modeling. J Neurotrauma 18:21–30
16. Zoghi-Moghadam M, Sadegh AM (2009) Global/local head models to analyse cerebral blood vessel rupture leading to ASDH and SAH. Comput Methods Biomech Biomed Engin 12:1–12
17. Horgan TJ, Gilchrist MD (2004) Influence of FE model variability in predicting brain motion and intracranial pressure changes in head impact simulations. Int J Crashworthiness 9:401–418
18. Brydon HL, Hayward R, Harkness W, Bayston R (1995) Physical properties of cerebrospinal fluid of relevance to shunt function. 1: the effect of protein upon CSF viscosity. Br J Neurosurg 9:639–644
19. Bloomfielda IG, Johnstona IH, Bilstonb LE (1998) Effects of proteins, blood cells and glucose on the viscosity of cerebrospinal fluid. Pediatr Neurosurg 28:246–251
20. Kuchuk VI, Shirokova IY, Golikova EV (2012) Physicochemical properties of water-alcohol mixtures of a homological series of lower aliphatic alcohols. Glas Phys Chem 38:460–465
21. Willinger R, Kang HS, Diaw B (1999) Three-dimensional human head finite-element model validation against two experimental impacts. Ann Biomed Eng 27:403–410

Computation of Brain Deformations Due to Violent Impact: Quantitative Analysis of the Importance of the Choice of Boundary Conditions and Brain Tissue Constitutive Model

Fang Wang, Zhengyang Geng, Sudip Agrawal, Yong Han, Karol Miller, and Adam Wittek

1 Introduction

Traumatic brain injuries have been recognised as important public health and socio-economic problems affecting millions of people world-wide [1, 2]. Although the exact mechanisms of such injuries are still a subject of debate, brain deformation or strain has been pointed out in the literature as possible key biomechanical cause [3]. As direct measurement of strains during impact is extremely difficult for ethical and technical reasons, in practice, predicting brain responses through mathematical modelling is often the best possible solution [3]. Such prediction has been the subject of substantial research effort which resulted in numerous brain models implemented using the finite element method [3–9]. There are differences between such models in terms of geometry, constitutive models and constitutive constants for the brain tissues, and the way the brain–skull interface (tissues located between the brain and skull that determine boundary conditions of the brain) is modelled.

Constitutive behaviour of the brain tissues has been a subject of numerous experimental studies [9–13]. In contrast, as pointed-out by Wittek et al. [14], there is very little quantitative information about the mechanical behaviour of the brain–skull

F. Wang (✉) • Z. Geng • Y. Han
School of Mechanical and Automotive Engineering, Xiamen University of Technology, Xiamen 361024, China
e-mail: wangfang83715@163.com

S. Agrawal • A. Wittek
Intelligent Systems for Medicine Laboratory, School of Mechanical and Chemical Engineering, The University of Western Australia, Perth, WA, Australia

K. Miller
Intelligent Systems for Medicine Laboratory, School of Mechanical and Chemical Engineering, The University of Western Australia, Perth, WA, Australia

Institute of Mechanics and Advanced Materials, Cardiff University, Cardiff, UK

A. Wittek et al. (eds.), *Computational Biomechanics for Medicine*,
DOI 10.1007/978-3-319-54481-6_14

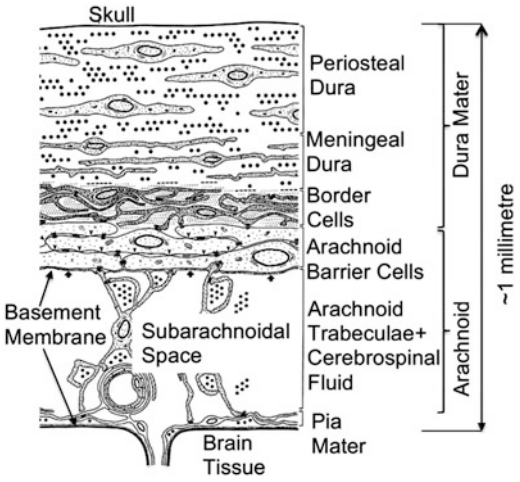

Fig. 1 Anatomical structures of brain–skull interface. Modified from Haines et al. [29]

interface and boundary conditions of other body organs. However, the importance of representation of boundary conditions in computational biomechanics models of the brain has been confirmed in several studies [6, 15, 16].

Constitutive properties of meningeal layers forming the brain–skull interface have been studied by Jin et al. [17–19]. However, direct representation of complex anatomical structure of the brain–skull interface (Fig. 1) would require quantitative data about the interactions between tissue layers within the brain–skull interface and necessitate very fine spatial discretisation resulting in very large number of small elements. Therefore, various simplifying approaches have been used in computational biomechanics models for predicting the brain responses under transient loads. For instance, Al-Bsharat et al. [20] used a layer of solid elements to model subarachnoidal cerebrospinal fluid CSF, with a frictionless sliding interface between arachnoid membrane and dura. Zhang et al. [4] selected sliding contact allowing no separation to represent the brain–skull interface. Miller et al. [21] compared the results obtained using 2-D computational biomechanics models with the experimental data obtained using pig brain and found that a sliding contact interface between the brain and skull was more suitable to predict the distribution of brain axonal injury. Similar approach (frictionless contact) was suggested by Agrawal et al. [22] for representing brain–skull interactions under compression at low loading speeds compatible with neurosurgery. In contrast, Claessens et al. [23] suggested that no-slip interface allowing no relative movement between the brain surface and skull exhibited a better agreement with the experiments than sliding contact. Some head–brain models include direct representation of key anatomical structures/tissues (cerebral meninges and CSF) of the brain–skull interface. Examples include the model by Yang [24], Total HUman Model for Safety THUMS by Toyota Motor Corporation and Toyota Central R&D Labs [25, 26], models developed at Wayne State University [4, 27], and SIMon model [28].

As none of the currently used approaches for modelling the brain–skull interface in computational biomechanics models for prediction of brain responses under transient loads and understanding mechanisms of traumatic brain injury has been accepted as a "gold standard", answering the question about effects of assumptions and simplifications when modelling the brain–skull interface remains an important and challenging research topic. Building on the previous research effort by Kleiven et al. [6] and Wittek and Omori [15], this study contributes to answering this question by quantifying the effects of approach for modelling the brain–skull interface and constitutive model of the brain tissues on predicting the brain deformations due to transient loads compatible with automotive impacts. We focus on the maximum principal strain and shear strain within the brain as they were proposed as possible measures/criteria for evaluation of brain injury risk [27]. We used the head–brain model from Total HUman Model for Safety THUMS Version 4.0 by Toyota Motor Corporation and Toyota Central R&D Labs [25, 26].

2 Methods

2.1 Head–Brain Model

We used previously validated head–brain model from Total HUman Model for Safety THUMS Version 4.0 [25, 26]. The THUMS brain model includes representation of key tissues and anatomical components of the brain: grey mater, white mater, falx, subarachnoidal cerebrospinal fluid (CSF), dura, arachnoid and pia (Figs. 2 and 3). The brain parenchyma is discretised using under-integrated eight-noded hexahedral elements. Dura, arachnoid and pia mater are represented using layers of four-noded shell elements with linear elastic constitutive model. No sliding between the skull and dura and between dura and arachnoid is allowed (tied contacts are used). The subarachnoidal CSF is modelled as a layer of eight-noded hexahedral solid elements (Fig. 3) with fluid-like properties (i.e. the deviatoric stress component in the CSF is solely due to viscosity).

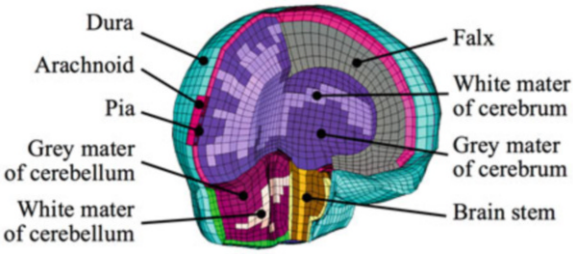

Fig. 2 THUMS Version 4.0 brain model

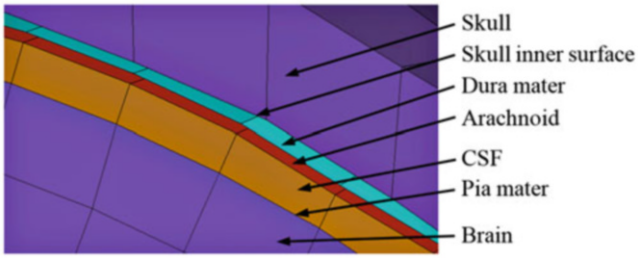

Fig. 3 Brain–skull interface representation in THUMS Version 4.0 brain model

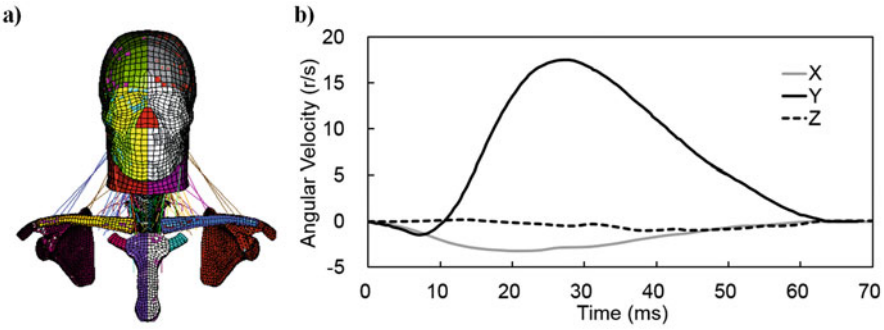

Fig. 4 (**a**) THUMS (Version 4.0) head–brain model with the cervical spine and the first (T1) and second (T2) thoracic vertebrae used in this study. T1, T2, scapula, collar bones and sternum were fully constrained to provide a base for the cervical spine **(b)** Head angular velocity—time histories measured in the experiments (cadaver test No. C755-T2) by Hardy et al. [30]. These time–histories were used as the head loading (prescribed angular velocity) in this study. X, Y and Z axes originate at the head gravity centre as shown in Fig. 5

Loading and Model Set-Up

We studied the effects of approach for modelling the brain–skull interface on predicting the brain responses under transient loads by modelling the experiments on human cadaver head–neck complexes conducted by Hardy et al. [30]. We selected these experiments as Hardy et al. [30] reported quantitative results of displacement of selected points within the brain.

In the experiments by Hardy et al. [30], the human cadaver head–neck complexes were subjected to frontal and occipital impacts resulting in motion in sagittal plane. Therefore, the entire cervical spine together with the first (T1) and second (T2) thoracic vertebrae from the THUMS Version 4.0 model were included in the model used in this study (Fig. 4a). T1 and T2, scapula, and collar bones were fully (rigidly) constrained to form a base for the cervical spine.

Direct modelling of an impact to the cadaver head would require calibration of the contact interactions between the head and impactor as well as information to create patient-specific models of the skull and cervical spine. Such information is

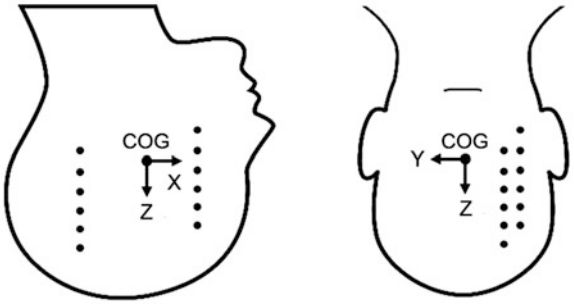

Fig. 5 Schematic representation of location of the markers (neutral density targets NDTs) implanted in the brain in the experiments by Hardy et al. [30, 31]. Based on Hardy et al. [31]

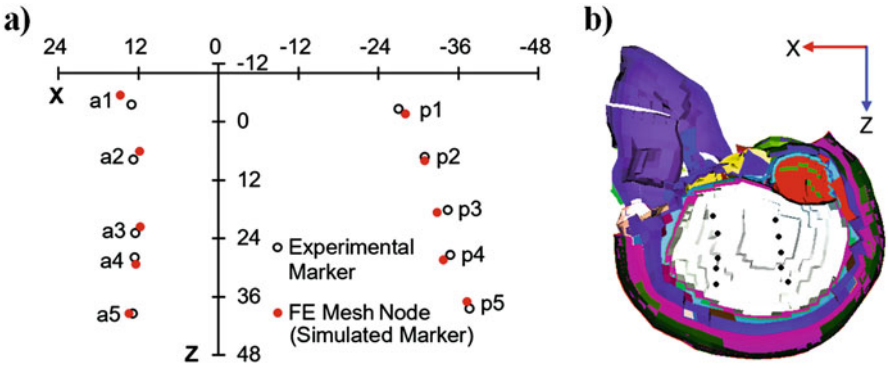

Fig. 6 (**a**) Initial position (in a coordinate system with origin at the head gravity centre COG, see Fig. 5) of the NDTs in the study by Hardy et al. [31], and (**b**) their representation (selected nodes) in the THUMS Version 4.0 finite element brain model in this study. X-Z coordinate system origin is at the head COG (see Fig. 5)

not available from the study by Hardy et al. [30]. Therefore, we directly defined the head kinematics by prescribing (at the head gravity centre) the head angular velocity–time histories measured in the experiments by Hardy et al. [30] (Fig. 4b). We used the time histories from cadaver test No. C755-T2 by Hardy et al. [30]. Position of the head gravity centre and head mass in the model were also taken from the data for cadaver test No. C755-T2 [30] (Fig. 5).

Analysed Brain Responses

To quantify the brain deformation under impact loading, Hardy et al. [30] applied X-ray to track the motion of twelve neutral density targets (NDTs) implanted within the brain (Fig. 5), and recorded the experimental output for ten of them (Fig. 6). We compared the trajectories and excursions of these targets with the computed trajectories and excursions of the brain model nodes located close to the targets (Fig. 6). Following [30], the excursions were defined as the differences between the maximum positive and negative displacements and the starting locations. Given limited accuracy of the data regarding the NDTs location in the experiment [30] and

complex geometry of the brain, it would be extremely difficult to modify the brain finite element discretisation to ensure that the analysed nodes are placed exactly at the NDTs' location. However, the positions of the NDTs and analysed nodes appear to be sufficiently close (Fig. 6) to justify quantitative comparison of their motion.

As strains within the brain have been proposed in the literature [27] as possible measures/criteria for evaluation of brain injury risk, we analysed the effects of the constitutive model of the brain tissues and approach for modelling the brain–skull interface on the maximum principal strain and shear strain within the brain parenchyma predicted using the computational biomechanics model. Although in biomechanical engineering studies, maximum values of strain or stress are often used to evaluate the risk of tissue rupture, prediction of the maximum strain values with computational biomechanics models implemented using finite element method can be mesh dependent and may be affected by localised phenomena/modelling artefacts. Therefore, following Garlapati et al. [32], we analysed quantile plots of the maximum principal strain and shear strain at the time when the maximum strain value was observed. Almansi strain measure was used.

2.2 *Investigation of Effects of Constitutive Modelling of Brain Parenchyma and Approach for Brain–Skull Interface Modelling*

Constitutive Model and Properties of the Brain Tissues

In the THUMS Version 4.0 brain model as well as many other models [8, 28] used in computational impact biomechanics, the constitutive behaviour of the brain parenchyma is often represented using a linear viscoelastic model. However, the experimental studies have clearly indicated non-linear stress–strain relationship of the brain tissues and proposed hyperelastic or hyperviscoelastic models to describe the tissue constitutive behaviour [11, 33, 34]. Following Miller and Chinzei [11], we used the Ogden hyperviscoelastic model as it accounts for the difference between the tensile and compressive stiffness of the brain tissue (Simulations 1, 2, 3 and 4 in Tables 1 and 2):

$$W = \frac{2}{\alpha^2}\int_0^t \left[G\left(t-\tau\right)\frac{\mathrm{d}}{\mathrm{d}\tau}\left(\lambda_1^{\alpha}+\lambda_2^{\alpha}+\lambda_3^{\alpha}-3\right)\right]\mathrm{d}\tau + K\left(J-1-\ln J\right), \quad (1)$$

$$G(t) = G_i + \left(G_0 - G_i\right)e^{\frac{-t}{\tau}}, \quad (2)$$

where W is the potential function, λ_i's are the principal stretches, G_0 is an instantaneous shear modulus, G_i is the relaxed shear modulus, τ is the characteristic time, α is the material coefficient which can assume any real value without restrictions [11, 35], K is the bulk modulus and J is the relative volume change.

Table 1 Constitutive models and parameters for the brain tissues used in this study. See Eqs. (1) and (2) for explanation of the symbols

	Linear viscoelastic model			Ogden hyperviscoelastic model			
Part	G_0 (Pa)	G_i (Pa)	τ(s)	G_0 (Pa)	α	G_i (Pa)	τ(s)
White matter cerebrum	1100	550	0.06	1100	–4.7	550	0.06
White matter cerebellum	1100	550	0.06	1100	–4.7	550	0.06
Gray matter cerebrum	850	425	0.06	850	–4.7	425	0.06
Gray matter cerebellum	850	425	0.06	850	–4.7	425	0.06

Table 2 Simulation matrix

	Modelling approach for brain–skull interface			
Brain tissue constitutive model	Original THUMS head/brain model (see Fig. 2)	Brain rigidly attached to the skull	Frictionless contact between the brain and skull	Cohesive layer (spring-like) between the brain and skull
Linear viscoelastic model	Simulation 1–2	Simulation 2–2	Simulation 3–2	Simulation 4–2
Ogden hyperviscoelastic model	Simulation 1	Simulation 2	Simulation 3	Simulation 4

As the brain tissue properties used in THUMS brain model have been reported to be somewhat beyond the range published in the literature [36], we used the properties (instantaneous shear modulus of 1100 Pa) that correspond to the highest strain rate applied in the experiments published by Miller and Chinzei [11, 33] (Table 1). As the experiments by Miller and Chinzei [11, 33] do not distinguish between the properties of grey and white mater, we followed the assumptions used in the original THUMS Version 4.0 brain model. The white mater in the cerebrum and cerebellum was assigned a shear modulus 25% greater than the grey mater (Table 1).

Models of the Brain–Skull Interface

In this study, four approaches for modelling the brain–skull interface were used (see Table 2). The brain–skull interface model used in THUMS (Version 4.0) head–brain model (Figs. 2 and 3) was treated as a base approach (Simulations 1 and 1–2 in Table 2). Three other approaches (Simulations 2, 2–2, 3, 3–2, 4 and 4–2 in Table 2) were introduced here to evaluate the effects of modelling of the brain–skull interface on prediction of deformations within the brain.

We started the analysis with two modelling approaches that can be regarded as representing limits of possible types of interactions between the brain and skull. In the first approach, the brain surface was rigidly attached to the skull through tied contact interface (Simulations 2 and 2–2 in Table 2). This approach allows no relative sliding and separation between the brain and skull, and has been reported by

Claessens et al. [23] as providing a good agreement with the experimental results. The second approach (Simulations 3 and 3–2 in Table 2) uses a frictionless sliding contact between the brain and skull, which allows not only tangential movement but also separation between the brain and skull. It has been successfully used in the studies on predicting the brain deformations due to craniotomy (surgical opening of the skull) by Hu et al. [37] and Wittek et al. [38], and recommended in the experimental study by Agrawal et al. [22] as providing a good representation of interactions between the brain surface and skull when the brain–skull interface is subjected to compression. Given the anatomical structure of the brain–skull interface (Fig. 1), one may expect that its actual behaviour should fall between the two modelling approaches just discussed.

The fourth approach for the brain–skull interface modelling used in this study (Simulations 4 and 4–2 in Table 2) relies on the experimental results by Mazumder et al. [39]. Mazumder et al. [39] quantified the mechanical behaviour of the entire brain–skull interface through sheep brain indentation and found that it exhibits spring-like behaviour. Mazumder et al. [39] proposed a value of 11.45 N mm^{-1}/mm^2 for the brain–skull interface stiffness. Therefore, in Simulations 4 and 4–2 (see Table 2), we represented the brain–skull interface using a layer of spring-type (no damping) cohesive elements with stiffness in the normal direction determined from Mazumder et al. [39].

Simulation Matrix

Eight computer simulations using the head–brain model shown in Fig. 2 with four different approaches for modelling the brain–skull and two constitutive models of the brain tissues were conducted here (Table 2). All the simulations were conducted using LS-DYNA 971 non-linear explicit dynamics finite element code by Livermore Software Corporation (Livermore, CA, USA; http://www.lstc.com). This code is widely used in both academia and industry for impact/injury biomechanics and car crash safety applications.

3 Results

The magnitude and general behaviour of trajectories of the nodes representing the markers (Neutral Density Targets NDTs) implanted within the brain in the experiments by Hardy et al. [30] were found to be strongly affected by the approach for modelling the brain–skull interface (Figs. 7 and 8, and Table 3). For the brain surface rigidly attached to the skull through a tied contact and linear viscoelastic model for the brain parenchyma (Simulation 2–2), magnitudes of the nodal trajectories were the smallest and exhibited large differences with trajectories of the markers experimentally determined by Hardy et al. [30] (Figs. 7b

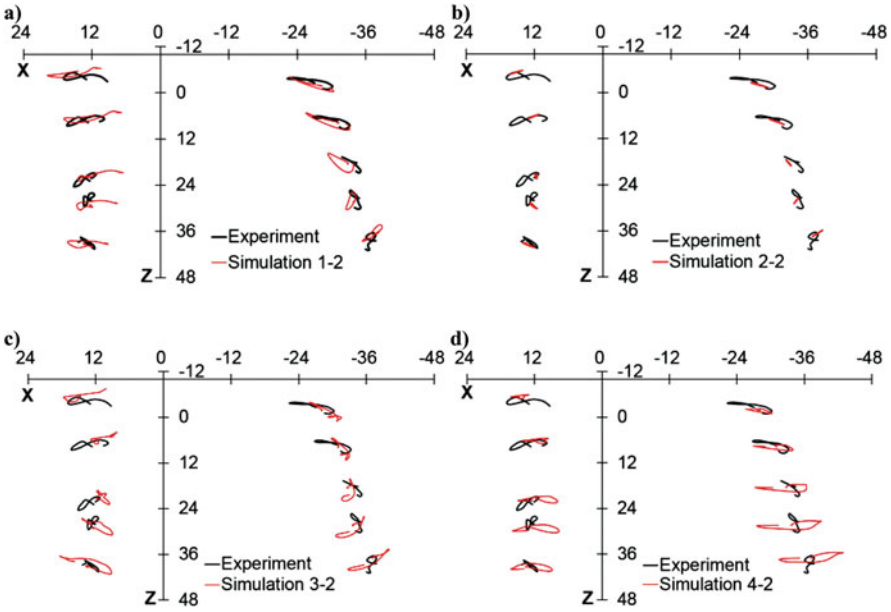

Fig. 7 Comparison of trajectories of nodes in THUMS model when varying the brain–skull interface modelling approach for linear viscoelastic model for brain tissue parenchyma and markers in the experiments by Hardy et al. [30]. The trajectories are given in the local head coordinate system (aligned with the Frankfort plane) with origin at the head COG (**a**) Simulation 1–2: original approach used in THUMS version 4.0 model (Fig. 2) (**b**) Simulation 2–2: brain rigidly attached to the skull (**c**) Simulation 3–2: frictionless sliding contact between the brain and skull (**d**) Simulation 4–2: brain–skull interface modelled using a layer of spring-type cohesive elements

and 8b). Large differences between the trajectories obtained using the computational biomechanics brain model and experimental results by Hardy et al. [30] were also observed for the brain–skull interface represented using a frictionless contact (Simulations 3 and 3–2 in Figs. 7c and 8c, and Table 3).

Comparisons of the nodal trajectories shown in Figs. 8 and 9 and excursions of the selected nodes (at location of NDTs a1, p1, a5 and p5 in Table 3) indicated that changing the constitutive model of the brain parenchyma from linear viscoelastic to Odgen hyperviscoelastic exerted appreciable effects on predicted deformations within the brain. For majority of the analysed ten nodes, the trajectories predicted using Odgen hyperviscoelastic model, rather than the linear viscoelastic model, tended to be closer to trajectories of the markers experimentally determined by Hardy et al. [30] (Figs. 8 and 9). This is also quantitatively confirmed by analysis of the experimentally observed and predicted excursions of NDTs a1, p1, a5 and p5 (Table 3).

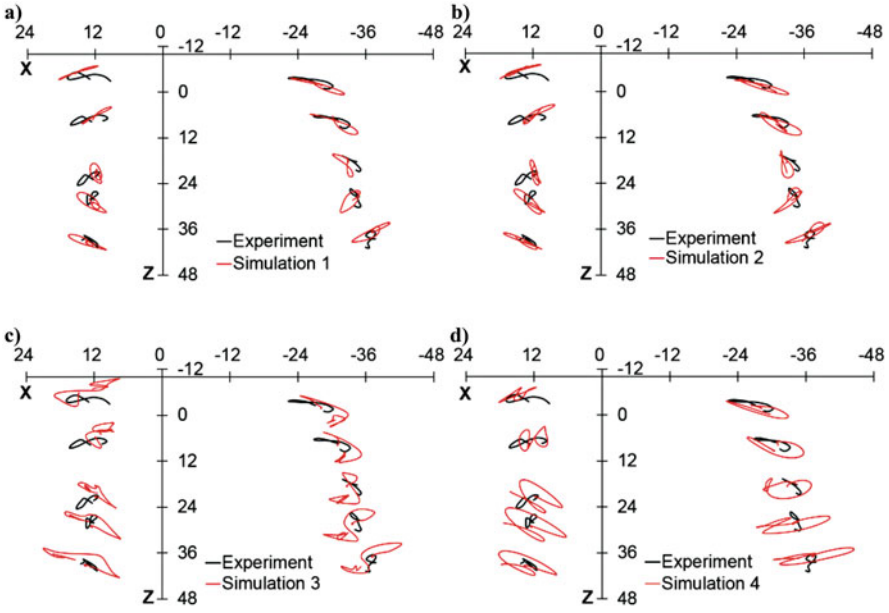

Fig. 8 Comparison of trajectories of nodes in THUMS model when varying the brain–skull interface modelling approach for Ogden hyperviscoelastic model for brain tissue parenchyma and markers in the experiments by Hardy et al. [30]. The trajectories are given in the local head coordinate system (aligned with the Frankfort plane) with origin at the head COG (**a**) Simulation 1: original approach used in THUMS version 4.0 model (Fig. 2) (**b**) Simulation 2: brain rigidly attached to the skull (**c**) Simulation 3: frictionless sliding contact between the brain and skull (**d**) Simulation 4: brain–skull interface modelled using a layer of spring-type cohesive elements

Analysis of the predicted maximum principal strain and shear strain within the brain led to observation consistent with those made when analysing nodal trajectories at selected locations within the brain. Appreciable differences in the predicted strain magnitude and distribution were observed when varying the approach for modelling the brain–skull interface (Figs. 9 and 10). The smallest strain was computed for the brain surface rigidly attached to the skull through a tied contact (Simulations 2–2 and 2). For this approach, the nodal trajectories also exhibited the smallest magnitude (compare Figs. 7b and 8b). The effects exerted when changing the constitutive model of the brain parenchyma from linear viscoelastic to Ogden hyperviscoelastic were clearly noticeable although much smaller than those observed when varying the approach for modelling the brain–skull interface (Figs. 9 and 10). The differences in the maximum strain computed when varying the constitutive model were of an order of 10% of the predicted maximum principal strain (Fig. 9) and up to around 40% for the maximum shear strain.

Table 3 Experimentally determined (by Hardy, 2007) and predicted in this study excursions of NDTs a1, p1, a2 and p2. See Figs. 5 and 6 for position of the NDTs and definition of axes X and Z. Simulations 1, 2, 3 and 4—Ogden hyperviscoelastic constitutive model; Simulations 1–2, 2–2, 3–2 and 4–2—linear viscoelastic model. See Table 2 for more complete description

NDT#		Hardy (2007) Experiment (mm)	Predicted Excursion (mm) Simulations 1–2	2–2	3–2	4–2	1	2	3	4
a1	X	3.48	5.11	1.57	3.05	1.52	3.71	3.09	4.37	0.83
		−4.27	−0.81	−0.46	−3.54	−1.69	−3.20	−4.14	−4.86	−3.1
	Z	0.78	1.49	0.72	1.46	0.62	2.26	2.02	3.17	1.60
		−1.66	−1.03	−0.22	−1.18	−0.41	−1.41	−1.65	−2.22	−1.80
p1	X	4.20	5.48	2.06	2.18	0.92	5.43	4.37	3.70	2.73
		−3.70	−2.30	−0.75	−2.84	−2.19	−4.20	−5.16	−4.77	−4.80
	z	1.95	1.39	0.38	2.26	0.74	2.34	2.44	4.27	2.50
		−1.05	−2.44	−0.9	−2.22	−0.49	−2.01	−1.39	−3.37	−0.91
a5	X	1.54	2.79	0.64	3.35	2.8	3.23	3.73	5.33	4.66
		−1.35	−4.27	−1.40	−4.19	−4.54	−3.45	−3.03	−5.90	−5.44
	z	1.23	0.85	0.84	1.80	1.02	1.99	1.84	−7.06	2.17
		−1.89	−0.97	−0.37	−2.28	−0.99	−2.02	−2.49	−3.76	−4.14
p5	X	1.22	1.98	0.52	2.13	5.86	3.75	4.65	2.10	5.95
		−0.49	−0.10	−1.23	−2.7	−5.55	−2.99	−3.34	−4.94	−7.12
	z	2.64	1.65	0.51	2.83	1.06	2.42	2.73	4.25	2.06
		−1.96	−2.63	−1.14	−2.26	−1.44	−2.69	−2.41	−3.58	−2.37

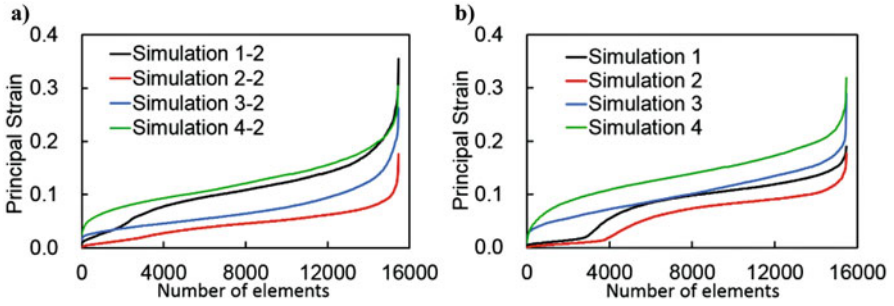

Fig. 9 Quantile plots of principal (Almansi) strain when varying brain–skull interface modelling approach, with (**a**) Linear viscoelastic and (**b**) Ogden hyperviscoelastic models for the brain tissues. For information about the simulations, see Table 2

4 Discussion

This study indicates that when applying computational biomechanics models to predict deformations within the brain under transient (impact) loads, the results are strongly affected by the method of modelling the brain–skull interface. Significant

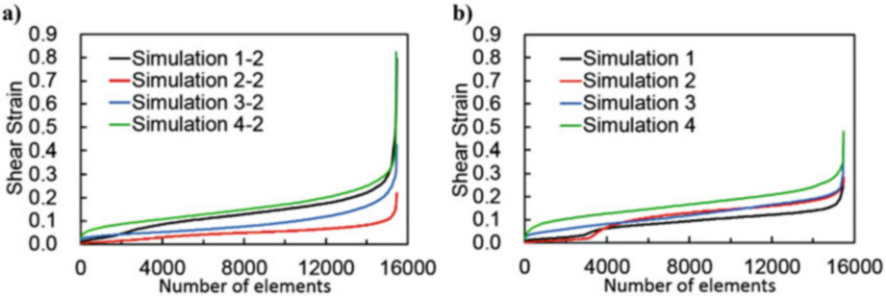

Fig. 10 Quantile plots of shear (Almansi) strain when varying brain–skull interface modelling approach, with (**a**) Linear viscoelastic and (**b**) Ogden hyperviscoelastic models for the brain tissues. For information about the simulations, see Table 2

effects were found in terms of kinematics of specific points within the brain (Figs. 7 and 8, and Table 3) as well as magnitude and distribution of brain tissue strain (Figs. 9 and 10). These results are consistent with the findings by Kleiven and Hardy [6, 15].

For the brain–skull interface represented as a "rigid connection" (tied contact) between the brain and skull, the maximum shear strains were around four times smaller than for the interface modelled using a layer of cohesive elements between the brain and skull, and approach originally used in THUMS Version 4.0 brain model that includes direct representation (solid elements with fluid-like properties) of the subarachnoidal cerebrospinal fluid CSF (Fig. 10). As strains within the brain have been proposed in the literature [27] as possible measures/criteria for evaluation of brain injury risk, the results obtained here highlight the importance of appropriately defining boundary conditions for the brain when applying computational biomechanics models in such evaluation.

Although providing a specific solution for brain–skull interface modelling is out of the scope of this study, comparisons of the calculated (using the biomechanical brain model) and experimentally obtained by Hardy et al. [30] trajectories and excursions of the selected points within the brain conducted here (Figs. 7 and 8, and Table 3) seem to suggest that such solutions should have the characteristics exhibited by the approach originally used in THUMS version 4.0 model (Fig. 2). This approach allows for movement between the brain outer surface and skull, while preventing complete separation between the brain and skull. Introduced here representation of the brain–skull interface as a layer of cohesive elements with spring-like properties also exhibits these characteristics. However, the mechanical properties for the cohesive elements were derived from the study by Mazumder et al. [39]. The study by Mazumder et al. [39] was conducted under loads compatible with neurosurgery. This may be one possible explanation for the differences between the modelling results obtained using these properties and experimental results by Hardy et al. [30] (Figs. 7 and 8). To the best of our knowledge, the behaviour of the brain–skull interface under conditions compatible with injury causing transients has not been investigated yet.

Changing the constitutive model of the brain parenchyma from linear viscoelastic to Ogden hyperviscoelastic exerted appreciable effects on the predicted kinematics of the selected points within the brain and brain tissue strain (Figs. 7, 8, 9, and 10, and Table 3). For the Ogden hyperviscoelastic model, the predicted trajectories of the selected points within the brain tended to be closer to the trajectories experimentally determined by Hardy et al. [30] than when the linear viscoelastic model was used (Figs. 7 and 8). This observation suggests that accurate prediction and analysis of brain trauma requires constitutive models of the brain tissues compatible with non-linear formulation of solid mechanics, such as hyperelastic/hyperviscoelastic models, and accounting for the differences between the tensile and compressive stiffness of the brain tissue. To the best of our knowledge, such suggestion has not been made before.

Acknowledgements This work is financially supported by Xiamen University of Technology (Grant No. YKJ15006R) and Fujian Administration of Foreign (Overseas) Experts Affairs (Grant No. 2015-79). Sudip Agrawal was supported by Australian Postgraduate Award programme and The University of Western Australia Safety-Net Top-Up Scholarship. All simulations using Toyota Total HUman Model for Safety THUMS Version 4.0 in this study were conducted at Xiamen University of Technology.

References

1. Peeters W, van den Brande R, Polinder S, Brazinova A, Steyerberg EW, Lingsma HF, Maas AI (2015) Epidemiology of traumatic brain injury in Europe. Acta Neurochir 157:1683–1696
2. de Almeida CER, de Sousa Filho JL, Dourado JC, Gontijo PAM, Dellaretti MA, Costa BS (2016) Traumatic brain injury epidemiology in Brazil. World Neurosurg 87:540–547
3. Yang KH, King AI (2011) Modeling of the brain for injury simulation and prevention. In: Miller K (ed) Biomechanics of the brain. Springer, New York, pp 90–110
4. Zhang L, Yang KH, Dwarampudi R, Omori K, Li T, Chang K, Hardy WN, Khalil TB, King AI (2001) Recent advances in brain injury research: a new human head model development and validation. Stapp Car Crash J 45:369–394
5. Yang J, Xu W, Otte D (2008) Brain injury biomechanics in real world vehicle accident using mathematical models. Chin J Mech 32:81–86
6. Kleiven S, Hardy WN (2002) Correlation of an FE model of the human head with local brain motion: consequences for injury prediction. Stapp Car Crash J 46:123–144
7. Miller K, Wittek A, Joldes G, Horton A, Dutta-Roy T, Berger J, Morriss L (2010) Modelling brain deformations for computer-integrated neurosurgery. Int J Numer Meth Bio 26:117–138
8. Mao H, Zhang L, Jiang B, Genthikatti VV, Jin X, Zhu F, Makwana R, Gill A, Jandir G, Singh A, Yang KH (2013) Development of a finite element human head model partially validated with thirty five experimental cases. J Biomech Eng 135:111002
9. Miller K (2011) In: Miller K (ed) Biomechanics of the brain. Springer, New York
10. Miller K, Chinzei K, Orssengo G, Bednarz P (2000) Mechanical properties of brain tissue in-vivo: experiment and computer simulation. J Biomech 33:1369–1376
11. Miller K, Chinzei K (2002) Mechanical properties of brain tissue in tension. J Biomech 35:483–490
12. Rashid B, Destrade M, Gilchrist MD (2013) Mechanical characterization of brain tissue in simple shear at dynamic strain rates. J Mech Behav Biomed 28:71–85

13. Bilston LE (2011) In: Bilston LE (ed) Neural tissue biomechanics: studies in mechanobiology, tissue engineering and biomaterials. Spinger-Verlag, Berlin
14. Wittek A, Grosland NM, Joldes GR, Magnotta V, Miller K (2016) From finite element meshes to clouds of points: a review of methods for generation of computational biomechanics models for patient-specific applications. Ann Biomed Eng 44:3–15
15. Wittek A, Omori K (2003) Parametric study of effects of brain-skull boundary conditions and brain material properties on responses of simplified finite element brain model under angular acceleration in sagittal plane. JSME Int J 46:1388–1398
16. Bayly PV, Clayton EH, Genin GM (2012) Quantitative imaging methods for the development and validation of brain biomechanics models. Annu Rev Biomed Eng 14:369–396
17. Jin X, Mao H, Yang KH, King AI (2014) Constitutive modeling of pia–arachnoid complex. Ann Biomed Eng 42:812–821
18. Jin X (2009) Biomechanical response and constitutive modeling of bovine pia-arachnoid complex. Dissertation, Wayne State University
19. Jin X, Yang KH, King AI (2011) Mechanical properties of bovine pia–arachnoid complex in shear. J Biomech 44:467–474
20. Al-Bsharat AS, Hardy WN, Yang KH, Khalil TB, Tashman S, King AI (1999) Brain/skull relative displacement magnitude due to blunt head impact, In: Proceedings of the 1999 43rd Stapp Car Crash Conference, San Diego, CA, USA
21. Miller RT, Margulies SS, Leoni M, Nonaka M, Chen X, Smith DH, D.F. Meaney (1998) Finite element modeling approaches for predicting injury in an experimental model of severe diffuse axonal injury. SAE Technical Paper, No. 983154
22. Agrawal S, Wittek A, Joldes G, Bunt S, Miller K (2015) Mechanical properties of brain-skull Interface in compression. In: Doyle B, Miller K, Wittek A, Nielsen PMF (eds) Computational biomechanics for medicine. Springer International Publishing, New York, pp 83–91
23. Claessens M, Sauren F, Wismans J (1997) Modeling of the human head under impact conditions: a parametric study. SAE Technical Paper, No. 973338, Washington, DC
24. Yang J (2011) Investigation of brain trauma biomechanics in vehicle traffic accidents using human body computational models. In: Wittek A, Nielsen PMF, Miller K (eds) Computational biomechanics for medicine. Springer, New York, pp 5–14
25. Shigeta K, Kitagawa Y, Yasuki T (2009) Development of next generation human FE model capable of organ injury prediction, In: International technical conference on the enhanced safety of vehicles (ESV), Stuttgart, Germany
26. Watanabe R, Miyazaki H, Kitagawa Y, Yasuki T (2011) Research of collision speed dependency of pedestrian head and chest injuries using human FE model (THUMS version 4), In: Proceedings of the 22nd Enhanced Safety of Vehicles (ESV) conference, Washington DC, USA
27. Mao H, Zhang L, Yang KH, King AI (2006) Application of a finite element model of the brain to study traumatic brain injury mechanisms in the rat. Stapp Car Crash J 50:583
28. Takhounts EG, Craig MJ, Moorhouse K, McFadden J, Hasija V (2013) Development of brain injury criteria (BrIC). Stapp Car Crash J 57:243
29. Haines DE, Harkey HL, Al-Mefty O (1993) The "subdural" space: a new look at an outdated concept. Neurosurgery 32:111–120
30. Hardy WN, Foster CD, Mason MJ, Yang KH, King AI, Tashman S (2001) Investigation of head injury mechanisms using neutral density technology and high-speed biplanar X-ray. Stapp Car Crash J 45:337–368
31. Hardy WN (2007) Response of the human cadaver head to impact. Dissertation, Wayne State Univesity
32. Garlapati R, Roy A, Joldes G, Wittek A, Mostayed A, Doyle B, Warfield S, Kikinis R, Knuckey N, Bunt S, Miller K (2014) More accurate neuronavigation data provided by biomechanical modeling instead of rigid registration. J Neurosurg 120:1477–1483
33. Miller K, Chinzei K (1997) Constitutive modelling of brain tissue: experiment and theory. J Biomech 30:1115–1121

34. Wittek A, Dutta-Roy T, Taylor Z, Horton A, Washio T, Chinzei K, Miller K (2008) Subject-specific non-linear biomechanical model of needle insertion into brain. Comput Method Biomech 11:135–146
35. Wittek A, Miller K, Kikinis R, Warfield SK (2007) Patient-specific model of brain deformation: application to medical image registration. J Biomech 40:919–929
36. Antona-Makoshi J (2013) Reanalysis of primate head impact experiments to clarify mild traumatic brain injury kinematics and thresholds. Dissertation, Chalmers University of Technology
37. Hu J, Jin X, Lee JB, Zhang L, Chaudhary V, Guthikonda M, Yang KH, King AI (2007) Intraoperative brain shift prediction using a 3D inhomogeneous patient-specific finite element model. J Neurosurg 106:164–169
38. Wittek A, Joldes G, Couton M, Warfield SK, Miller K (2010) Patient-specific non-linear finite element modelling for predicting soft organ deformation in real-time; application to non-rigid neuroimage registration. Prog Biophys Mol Biol 103:292–303
39. Mazumder MMG, Miller K, Bunt S, Mostayed A, Joldes G, Day R, Hart R, Wittek A (2013) Mechanical properties of the brain–skull interface. Acta Bioengin Biomech 15:3–11